Hydrodynamics and Heat Transfer in Shallow Fluidized Beds

by

Jyh-Shing Yang

Dissertation submitted to the Faculty of the

Virginia Polytechnic Institute and State University

in partial fulfillment of the requirements for the degree of

Doctor of Philosophy

in

Chemical Engineering

APPROVED:

Arthur M. Squires, Co-chairman

J. A. Liu, Co-chairman

George B. Wills

Thomas E. Diller

Gerhard H. Beyer

May, 1986

Blacksburg, Virginia

Hydrodynamics and Heat Transfer in Shallow Fluidized Beds

by

Jyh-Shing Yang

Co-chairmen: Arthur M. Squires, Y. A. Liu

Chemical Engineering

(ABSTRACT)

The use of shallow fluidized beds for heat exchange has been suggested because they give high bed-to-surface heat transfer rate and require very low bed pressure. However, in comparison with research on deep fluidized beds, only relatively few studies have been devoted to heat transfer in shallow beds, and results from the available literature are often inconsistent. This study represents an integrated research on the hydrodynamics and bed-to-surface heat transfer in shallow beds. The results from this study provide the quantitative basis for the design and efficient operation of shallow fluidized-bed heat-recovery system.

Based upon their physical appearance, shallow fluidized beds have been categorized into nine different types. A "phase diagram" (plot of superficial gas velocity versus static bed height) can be used to delineate the ranges of fluidization variables within which each type of shallow beds will be seen.

Pressure-drop data in gas flowing upward through a shallow bed reflect pressure recovery in jets formed immediatedly above a gas distributor at the bottom of the bed. Pressure-recovery data provide an effective means of distinguishing a shallow bed from a deep one, and suggest that the power consumption across a fluidized bed can be reduced dramatically by dividing a single deep bed into many multi-staged shallow beds.

A computerized light probe has been developed for measurements of particle volume-fraction distribution and its statical fluctuation (standard deviation). These data have been shown to quantatively define: (1).different types of shallow beds; (2).relative magnitude of solid mixing; (3).bed surface and bed height; and (4).jet penetration depth.

Based upon observations of the hydrodynamic behavior of shallow fluidized beds, three regions can be identified for heat-transfer applications: a jet-affected region at the bottom, a free-board region at the top, and, sandwiched between theses, a homogeneous region. Only heat-transfer data in the homogeneous region are sufficiently well-behaved to be subjected to quantitative correlation in terms of fluidization variables. For relatively coarse particles (Geldart's Group B particles) the vigor of solid mixing can be the most important factor in affecting the heat-transfer performance. Bed voidage and static electricity effects are found to be important for smaller and/or lighter particles (i.e., Geldart's Group A particles).

Acknowledgements

I would like to thank all the members of my graduate committee for their help and guidance throughout this study. Particularly, I am deeply indebted to Dr. A. M. Squires for his suggestions on the experiments and Dr. Y. A. Liu for his endless dedication on discussing the theories and their interpretations.

Most of this work was funded by the U.S. Department of Energy, Pittsburgh Energy Technology Center (PETC), under Grant No. All members of the Novel Fluid-Particle Research Laboratories at Virginia Tech deserve thanks for their assistance in completing my experimental work.

Finally, I am most grateful to my family for their continuing support and encouragement.

Table of Contents

CHAPTER 1 INTRODUCTION **1**

CHAPTER 2 LITERATURE REVIEW **6**

2.1 Fundamentals of Fluidization 6

2.1.1 General features of fluidization 6

2.1.2 Early history of fluidized beds 9

2.1.3 Applications of fluidized beds 11

2.1.4 Advantages and disadvantages of fluidized beds 14

2.1.5 Shallow fluidized beds 15

2.2 Basic Hydrodynamic Theories of Fluidization 18

2.2.1 Types of gas fluidization categorized by particle properties 18

2.2.2 Single particle properties 21

Particle shape factor, sphericity and mean diameter 21

Terminal and settling velocities of a single particle 23

2.2.3 Criteria for different fluidization regimes 29

Minimum fluidizing velocity 29

Minimum bubbling velocity and two-phase theory 32

Distinguishing bubbling and slugging beds 36
Slugging and choking in dilute phase 37
Turbulent fluidization 37
2.2.4 Gas and solid mixing in fluidized beds 38
2.2.5 Design of gas distributor 40
2.2.6 Jet penetration depth in fluidized beds 43
Definition of jets 43
Investigations of jet penetration 45
2.3 Heat Transfer between Particles and Immersed Surfaces in Fluidized Beds 50
2.3.1 Models for the bed-surface heat transfer 50
Limiting gas-film resistance model 52
Model of penetrating packets of emulsion 56
Discrete particle models 59
Modified packet models 62
Gas-convective model 65
2.3.2 Measurement of heat-transfer coefficient in fluidized beds 69
Evaporation of soaked porous material 69
Water/steam circulation system 70
Coaxial electric heater 71
Heating strips on a rod 72
2.3.3 Correlations for predicting heat-transfer coefficient in fluidized beds 79
2.3.4 Studies of heat transfer in shallow fluidized beds 83

CHAPTER 3 TYPES OF SHALLOW FLUIDIZED BEDS 91
3.1 Fluidized Bed System 91
3.1.1 Fluidized rigs 91
3.1.2 Air flow 92
3.1.3 Windbox 92

3.1.4 Distributors 96
3.1.5 Particles 98
3.2 Categorization of types of shallow fluidized beds 100
3.3 Phase diagrams 113
3.4 Mathematical models for predicting types of shallow fluidized beds 129
3.4.1 Distinction between type E and other types of shallow fluidized beds 129
3.4.2 Distinction between type F and type C beds 133
3.4.3 Distinctions between types A-B and between types B-C 137
3.5 Conclusions from study of phase diagrams 145

Chapter 4 PRESSURE DROP MEASUREMENTS IN SHALLOW FLUIDIZED BEDS 146
4.1 Orifice coefficients of the distributors 146
4.2 Manometer used for pressure studies 151
4.2.1 Manometer system 151
4.2.2 Basic theory for the manometer 151
4.2.3 Pseudo-first-order character of the manometer system 156
4.3 Experimental results for pressure drop across shallow beds 161
4.4 Theory and discussion for pressure ratio 174

CHAPTER 5 PRESSURE DISTRIBUTION IN SHALLOW FLUIDIZED BEDS 186
5.1 Fundamentals for the pressure distribution in shallow fluidized beds 186
5.2 Experimental method and conditions 188
5.3 General features of pressure distribution curves in shallow fluidized beds 189
5.4 Pressure distribution for all types of shallow fluidized beds 192
5.5 Variables affecting the pressure distribution curves 201
5.5.1 Effect of the amount of particles 201
5.5.2 Effect of gas velocity 204
5.5.3 Effect of particle size 208

5.5.4 Effect of particle density 208
5.5.5 Effect of distributor 211
5.6 Estimating bed expansion from pressure distribution curves 215
5.7 Jet penetration depth 224
5.7.1 Correlations for predicting jet penetration depth 224
5.7.2 Experimental conditions and results of the estimation of jet penetration depth .. 226
5.7.3 Comparison of correlations with experimental data 227
5.7.4 Conclusions for predicting jet penetration with use of pressure distribution curve 240

CHAPTER 6 PARTICLE VOLUME-FRACTION IN SHALLOW FLUIDIZED BEDS 241
6.1 The light probe 241
6.1.1 Original idea of the light probe 242
6.1.2 Design and calibration of light probe 242
Design of the light probe 242
The computer interfacing system 243
Calibration of light probe 252
Calibration of light probe using optical theory and particle volume-fraction 252
Calibration of optical probe with use of a vibrofluidized-bed system 254
Comparison of the two calibration techniques 261
Application of light probe and discussion of data 261
6.2 Particle volume-fraction data from the light probe 271
6.3 Particle volume-fraction curves for shallow beds of different types 273
6.4 Jet penetration heights obtained from particle volume-fraction curves 284
6.5 Effect of gas distributor on particle volume-fraction 290
6.6 Conclusions of the particle volume-fraction study 291

CHAPTER 7 HEAT TRANSFER IN SHALLOW FLUIDIZED BEDS 293
7.1 System for measuring heat-transfer coefficient 293

7.1.1 Design of heat probe 293
7.1.2 Obtaining heat-transfer data 296
7.1.3 Calculation of heat-transfer coefficient 298
7.1.4 Heat transfer in an empty column 301
7.1.5 Stability of the heat-transfer coefficient 304
7.2 Heat-transfer data for Group B particles 306
7.2.1 Heat transfer in homogeneous region 307
7.2.2 Heat-transfer data in jet region 323
7.2.3 Heat-transfer data in the free-board/cloud region 327
7.3 Heat transfer date from shallow fluidized beds of different sizes 330
7.4 Correlation of heat-transfer coefficient in shallow beds 334
7.5 Heat transfer of Group A particles in shallow fluidized beds 339

CHAPTER 8 SUMMARY AND RECOMMENDATIONS 348
Summary 348
Recommendations for further work 350

Nomenclature 352

Appendices 360
Appendix A. Pressure drop across a multi-staged shallow fluidized-bed system 361
Appendix B. BASIC program for the DT2801 data acquisition board in IBM PC 366
Appendix C. Derivation of the theoretical calibration curve for the light probe 372
Assumptions for the calibration 372
Derivation for the equations 372
Appendix D. The Pattern search program for the calibration of light probe 374
Appendix E. Error analysis for heat-transfer measurements 380
Appendix F. Experimental conditions for study of pressure drop across shallow beds .. 384

Bibliography 387

Vita 396

List of Illustrations

Figure 1. The shallow fluidized Fischer-Tropsch reactor 2

Figure 2. The fluidizing regimes as the gas velocity increases 7

Figure 3. Powder/particle classification in fluidization by Geldart 19

Figure 4. Drag coefficient versus Reynold number for single particle 24

Figure 5. The vertical jet and bubble in a fluidized bed 44

Figure 6. Heat-transfer coefficient versus gas velocity curve in a fluidized bed 51

Figure 7. The gas film model 55

Figure 8. The model of packets of emulsion 57

Figure 9. The isotherms near a single spherical particle 60

Figure 10. Using the evaporation of soaked porous material to measure the heat-transfer coefficient 74

Figure 11. Using the water/steam circulation system to measure the heat-transfer coefficient 75

Figure 12. Using the coaxial electric heater to measure the heat-transfer coefficient . . . 76

Figure 13. Using the heating strips on a rod to measure the heat-transfer coefficient . . . 77

Figure 14. Fluidization system for studies of shallow fluidized beds 93

Figure 15. Calibration of the orifice meter 94

Figure 16. Design of the windbox 95

Figure 17. Illustration of a type A bed 102

Figure 18. Illustration of a type B bed 103

Figure 19. Illustration of a type C bed 104

Figure 20. Illustration of a type D bed 105

Figure 21. Illustration of a type E bed 106
Figure 22. Illustration of a type F bed 107
Figure 23. Illustration of a type G bed 108
Figure 24. Illustration of a type H bed 109
Figure 25. Illustration of a type I bed 110
Figure 26. Phase Diagram for particle P-A-1 and distributor D-1 114
Figure 27. Phase Diagram for particle P-A-2 and distributor D-1 115
Figure 28. Phase Diagram for particle P-A-3 and distributor D-1 116
Figure 29. Phase diagram for particle P-A-1 (with laminated distributor) 118
Figure 30. Phase diagram for particle P-A-2 (with laminated distributor) 119
Figure 31. Phase diagram for particle P-A-3 (with laminated distributor) 120
Figure 32. Phase diagram for particle P-G-1 (with laminated distributor) 121
Figure 33. Phase diagram for particle P-G-2 (with laminated distributor) 122
Figure 34. Phase diagram for particle P-G-3 (with laminated distributor) 123
Figure 35. Phase diagram for particle P-G-4 (with laminated distributor) 124
Figure 36. Phase diagram for particle P-S-1 (with laminated distributor) 125
Figure 37. Phase diagram for particle P-C-1 (with laminated distributor) 126
Figure 38. Minimum fluidizing velocity and minimum smoothly fluidizing velocity 130
Figure 39. Top view of a type E bed with varying amounts of particles 132
Figure 40. Prediction of the minimum smoothly fluidizing velocity 134
Figure 41. Experimental and predicted critical static bed heights 139
Figure 42. Orifice coefficient versus gas velocity for different distributors 149
Figure 43. Design of pressure probe and manometer system 152
Figure 44. A typical second-order manometer system 153
Figure 45. The averaged response ratio versus time-constant ratio 158
Figure 46. Time constant for the manometer under first-order assumption 160
Figure 47. Pressure recovery ratio versus static bed height for distributor D-1, particle P-A-3 163

Figure 48. Pressure recovery ratio versus static bed height for distributor D-1, particle P-S-1. 164

Figure 49. Pressure recovery ratio versus static bed height for distributor D-1, 1.5 m/s. 165

Figure 50. Pressure recovery ratio versus static bed height for distributor D-6, 1.0 m/s. 166

Figure 51. Pressure ratio versus static bed height for distributor D-1, 0.5 m/s. 167

Figure 52. Pressure recovery ratio versus static bed height for particle P-A-3, 1.5 m/s. for perforated distributors 168

Figure 53. Pressure recovery ratio versus static bed height for particle P-A-3, 1.5 m/s. for laminated distributors 169

Figure 54. Experimental data comparing with the least-square fitted curves for pressure recovery ratio data 173

Figure 55. Predicted recovered pressure versus experimental data for all particles . . . 181

Figure 56. Predicted recovered pressure versus experimental data for Master Beads . 182

Figure 57. Predicted recovered pressure versus experimental data for glass beads . . . 183

Figure 58. Predicted recovered pressure versus experimental data for sands 184

Figure 59. Number of data points versus the percentage error of the predicted wall friction. 185

Figure 60. A typical pressure distribution curve. 190

Figure 61. Pressure distribution curve for a type A bed 193

Figure 62. Pressure distribution curve for a type B bed 194

Figure 63. Pressure distribution curve for a type C bed 195

Figure 64. Pressure distribution curve for a type D bed 196

Figure 65. Pressure distribution curve for a type F bed 197

Figure 66. Pressure distribution curve for a type G bed 198

Figure 67. Pressure distribution curve for type A, B and C beds 200

Figure 68. Pressure distribution curves for different amounts of particles 202

Figure 69. Percentage of maximum pressure versus probe elevation for different static bed heights 203

Figure 70. Pressure distribution curves for beds having a small amount of particles . . 205

Figure 71. Pressure distribution curves for beds having a medium amount of particles 206

Figure 72. Pressure distribution curves for beds having a large amount of particles . . . 207

Figure 73. Pressure distribution curves for beds having different sized particles 209

Figure 74. Pressure distribution curves for beds having different kinds of particles 210

Figure 75. Pressure distribution curves for beds of activated carbon 212

Figure 76. Pressure distribution curves for beds with perforated distributors 213

Figure 77. Pressure distribution curves for beds with different types of distributors ... 214

Figure 78. Three hydrodynamic curves for determining bed height 216

Figure 79. A set of pressure distribution curves for estimating jet penetration 228

Figure 80. Experimental jet penetration ratio versus prediction by Yang and Keairns correlation 230

Figure 81. Experimental jet penetration ratio versus prediction by the correlation of Blakes et. al. 231

Figure 82. Experimental jet penetration ratio versus prediction from the correlation of this study 232

Figure 83. Predicted and experimental jet penetrations for three sets of data 237

Figure 84. Predicted and experimental jet penetrations 238

Figure 85. Predicted and experimental jet penetrations for the same distributor 239

Figure 86. The light probe arrangement 244

Figure 87. Detail of the construction of the light probe 245

Figure 88. Electronic circuit for the light probe 246

Figure 89. Interface system between light probe and IBM PC 249

Figure 90. Flow diagram for obtaining output from light probe via IBM PC 250

Figure 91. Fluctuation of particle volume-fraction versus time 251

Figure 92. Calibration curve of light probe from optical theory 255

Figure 93. Comparison of actual and calculated particle weight from optical theory ... 256

Figure 94. Particle volume-fraction distribution on the amplitude-frequency plane 258

Figure 95. Calibration curves for Master Beads using the vibro-bed system 260

Figure 96. Comparison of proposed calibrational equation with the data from vibro-bed system 262

Figure 97. Comparison of two techniques for calibrating the light probe 264

Figure 98. Comparison of calibration curves for Master Beads and sands 265

Figure 99. Typical particle volume-fraction versus probe elevation with different amounts of particle 266

Figure 100. Typical particle volume-fraction versus probe elevation with different distributors 267

Figure 101. Typical particle volume-fraction versus probe elevation for Master Beads of different sizes 268

Figure 102. Sample curves of fluctuation ratio and particle volume-fraction 270

Figure 103. Particle volume-fraction and fluctuation curves for a type A bed 274

Figure 104. Particle vloume-fraction and fluctuation curves for a type B bed 275

Figure 105. Particle vloume-fraction and fluctuation curves for a type C bed 276

Figure 106. Particle vloume-fraction and fluctuation curves for a type D bed 277

Figure 107. Particle vloume-fraction and fluctuation curves for a type F bed 278

Figure 108. Particle vloume-fraction and fluctuation curves for a type G bed 279

Figure 109. Particle vloume-fraction and fluctuation curves for a type H bed 280

Figure 110. Particle vloume-fraction and fluctuation curves for different types of bed .. 281

Figure 111. Particle volume-fraction curves for beds having different distributors 286

Figure 112. Particle fluctuation curves for beds having different distributors 287

Figure 113. Design of heat probe 295

Figure 114. The temperature read-out system for the heat probe 297

Figure 115. Position of the thermocouples on the heat probe 299

Figure 116. Heat-transfer coefficient versus probe height in empty bed 302

Figure 117. Heat-transfer coefficients for particle P-A-2 with distributor D-1 308

Figure 118. Heat-transfer coefficients for particle P-A-2 with distributor D-4 309

Figure 119. Heat-transfer coefficients for particle P-A-2 with distributor D-7 310

Figure 120. Heat-transfer coefficients for particle P-A-1 with distributor D-1 311

Figure 121. Heat-transfer coefficients for particle P-A-3 with distributor D-1 312

Figure 122. Heat-transfer coefficients in homogeneous region versus particle diameter 316

Figure 123. Heat-transfer coefficients in the homogeneous region versus open area ratio of distributors 318

Figure 124. Heat-transfer coefficient data for beds with screen distributors at u = 1.5 m/s 320

Figure 125. Heat-transfer coefficient data for beds with screen distributors at u = 2.0 m/s 321

Figure 126. Heat-transfer coefficient data for beds with screen distributors at u = 2.5 m/s 322

Figure 127. Percentage increase in heat transfer in jet-affected region 324

Figure 128. Heat-transfer coefficients data for fluidized beds of different sizes 331

Figure 129. Comparison of heat-transfer coefficients for dry and wet fluidizing air 333

Figure 130. Comparison of correlations for heat-transfer coefficient 337

Figure 131. Comparison of the predicted and experimental heat-transfer data 338

Figure 132. Heat-transfer data for a Group A powder from Abu Bakar's thesis 340

Figure 133. Heat-transfer data for FCC powder obtained with dry and wet air at u = 0.1 m/s 342

Figure 134. Heat-transfer data for FCC powder with dry and wet air at u = 0.2 m/s . . . 343

Figure 135. Heat-transfer data for FCC powder at several gas velocities 345

List of Tables

Table 1. Specifications of different regimes for fluidized beds 10

Table 2. Comparison of shallow and deep fluidized beds 16

Table 3. Features of the Groups of particles categorized by Geldart 20

Table 4. Equations for the calculation of Reynold number at terminal velocity 26

Table 5. Equations for the calculation of minimum fluidizing velocity 33

Table 6. Comparison of gas distributors for fluidized beds 41

Table 7. Comparison of the most common ways to measure the heat-transfer in fluidized beds 78

Table 8. Summary of representative investigations on shallow fluidized-bed heat transfer 84

Table 9. Specifications of distributors used in this study 97

Table 10. Specifications of particles used in this study 99

Table 11. Descriptions of the types of shallow fluidized beds 101

Table 12. Specifications of boundaries for different types of shallow fluidized beds ... 127

Table 13. "Minimum smoothly fluidizing gas velocity" for type E beds 135

Table 14. Prediction of critical static bed height for type F shallow beds. 138

Table 15. The prediction of the boundary for type A and B beds. 143

Table 16. Prediction of boundary between type B and C beds. 144

Table 17. Orifice coefficients and pressure drops across different distributors 148

Table 18. Response time of the manometer system 157

Table 19. A typical set of data of pressure ratio versus static bed height 162

Table 20. Data for the least-square fitting of orifice design equation 172

Table 21. Correlation coefficients for friction factors in shallow beds. 177

Table 22. Correlation coefficients for friction factors versus different dimensionless groups 178

Table 23. Bed expansion ratios for different particles and gas velocities 218

Table 24. Bed expansion ratios for beds having different distributors 219

Table 25. Bed expansion ratios for beds having different static bed heights 220

Table 26. Experimental Bed expansion ratios and values calculated from equations 5.3 and 5.4 221

Table 27. Jet penetration depth estimated from pressure distribution curves 229

Table 28. Symbols for all data in the figures comparing correlations for jet penetration 233

Table 29. Constants for the three correlations for jet penetration 234

Table 30. Constants of three sets of data for predicting jet penetration 236

Table 31. Elements and functions of the light probe 247

Table 32. Comparison of two techniques for calibrating the light probe 263

Table 33. Comparison of the techniques of measuring jet penetration depths 285

Table 34. Jet penetrations evaluated from volume-fraction and from pressure-distribution data 288

Table 35. Comparison of experimental and predicted Nusselt numbers in an empty bed 303

Table 36. Stability of heat-transfer coefficient with variation in probe surface temperatures 305

Table 37. Heat transfer coefficients in homogeneous region for different static bed heights 313

Table 38. Heat-transfer coefficients in homogeneous region for different particles 317

Table 39. Heat-transfer coefficients in the homogeneous region for different distributors 319

Table 40. Percentage increase in heat-transfer coefficient in jet region 325

Table 41. Percentage increase in heat-transfer coefficient in jet region for different distributors 328

Table 42. Percentage increase of heat-transfer coefficients in free-board region for different particles 329

CHAPTER 1 INTRODUCTION

The late professor Douglas Elliott at the University of Aston in Birmingham, England, discovered that heat-transfer coefficients to an extended surface placed in a fluidized bed a few inches deep could be astonishingly high (Squires, 1976; Al Ali, 1976). Stone-Platt Fluidfire Ltd., the firm founded by Elliott, has built waste-heat-recovery equipment using the shallow-bed heat transfer phenomenon for recovering waste heat from a hot gas. However, because the hydrodynamic features of shallow fluid beds are significantly different from traditional deep beds, shallow-bed heat transfer mechanisms are still not well understood.

For the exploratory development of a new concept in indirect liquefication of coal, Liu et. al. (1983) offered an alternative to the Koelbel slurry reactor for conducting Fischer-Tropsch synthesis with low H_2:CO gas. Figure 1 on page 2 shows the schematic drawing of this new concept of a dry shallow fluidized-bed system for Fischer-Tropsch synthesis.

In the proposed concept, two gas streams are to be fed to the system: "Fluidizing-Gas" (F-Gas) is furnished at a low flow rate to a shallow fluidized bed having fine particles of (Fischer-Tropsch) catalyst, and "Supernatant-Gas" (S-Gas) is furnished at a higher flow rate to a space above the shallow bed. This arrangement can be designed to provide a relatively long dwell-time of catalyst in F-Gas (which is relatively rich in hydrogen) and a short dwell-

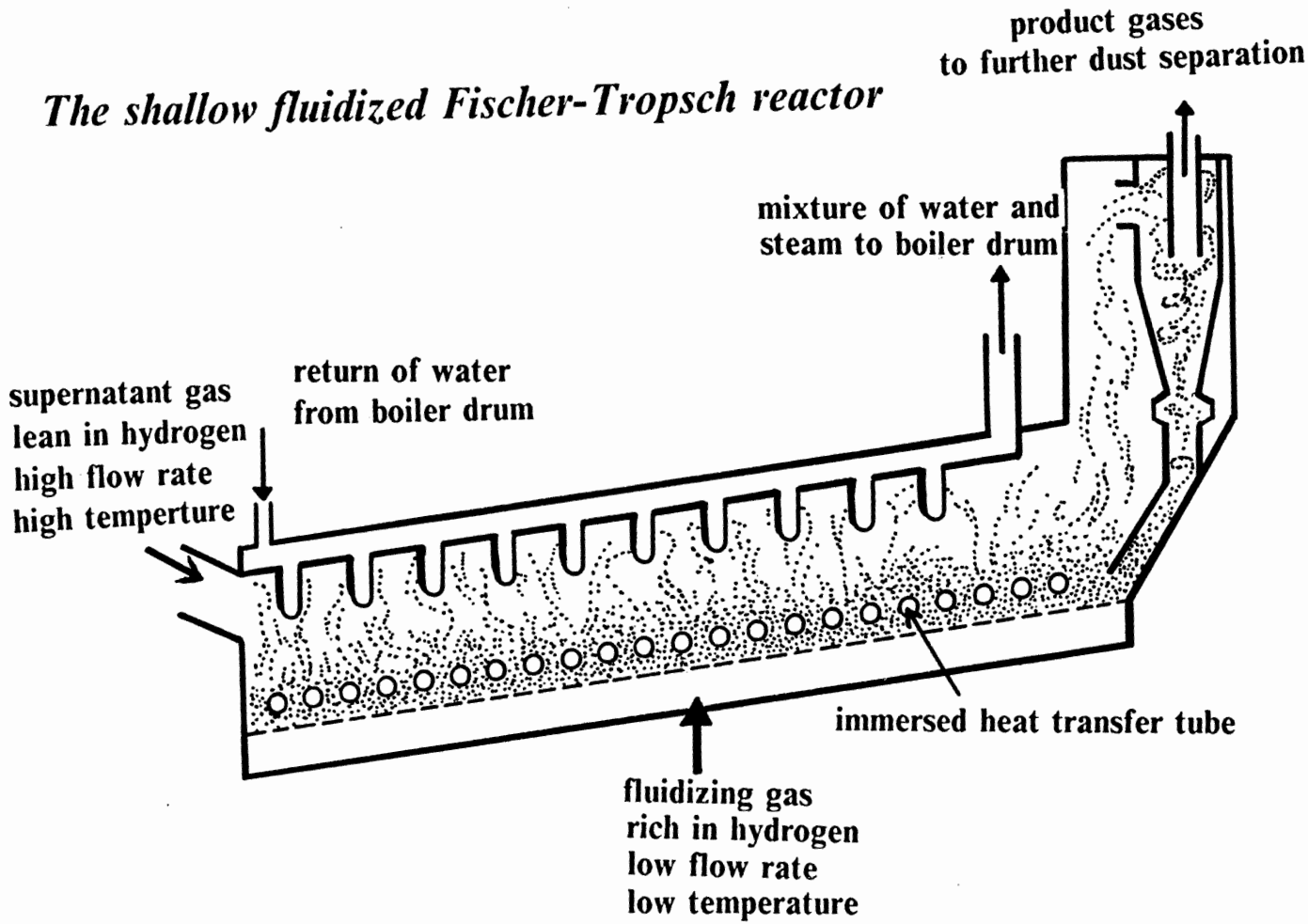

Figure 1. The shallow fluidized Fischer-Tropsch reactor

time of catalyst in S-Gas (having a low H_2:CO ratio). For details of Fischer-Tropsch reaction mechanisms, see the dissertation by Whiting (1985).

Heat from the exothermic Fischer-Tropsch reaction is removed from the system by two sets of tubes containing boiling water: horizontal tubes placed near the bottom of the shallow fluidized bed, and vertical tubes entering the supernatant space from above. The bed is inclined at an angle to the horizontal in order to facilitate the leftward return flow of catalyst in the dense zone.

Both hydrodynamic and heat transfer data are required for the construction of this conceptual shallow fluidized bed reactor. Hydrodynamic study of the shallow fluidized bed can provide the following design information:

1. Pressure drop across the system (vertically and horizontally), and, therefore, the power required to operate the system.

2. Gas/solid mixing and particle concentration in the bed. This will enable a designer to estimate the dwell-times of catalyst in F-Gas and S-Gas, information required for exercising a degree of control, more or less, over rates of chain initialization and chain propagation in the overall Fischer-Tropsch reaction scheme.

3. Possible types of shallow fluidized beds. Both static bed height and superficial gas velocity can affect the hydrodynamic mechanism. Useful operational ranges for these variables in a shallow fluidized bed can be determined only after exploring all possible combinations of these two variables.

4. Jet penetration depth. We can either put the heat transfer tubes in the jet region to increase the heat transfer coefficient or remove the tubes from that region to minimize erosion.

Heat transfer studies on the shallow fluidized beds are needed for designing heat-removal tubes in the proposed Fischer-Tropsch reactor. Heat transfer mechanisms are usually dominated by hydrodynamic features of the bed.

A design similar to proposed shallow fluid bed reactor for the Fischer-Tropsch reaction can also provide a "HeatTray" for use as a heat exchanger (e.g., to recover waste heat from a dirty gas) (see Boyd, 1984). The "HeatTray" is particularly well suited, for example, for the convective section of a coal-fired steam boiler, or for recovery of waste heat in a hot gaseous discharge from an industrial operation. It might be suited for use in a dry cooling tower, discharging low-level heat to the environment.

This study explores hydrodynamics and heat transfer in shallow fluidized beds. The hydrodynamic study breaks down into the following four major parts:

1. Distinctions of different types of shallow fluidized beds -- The hydrodynamic properties and characteristics of each type are examined and compared. The possible applications for different types of shallow beds can also be proposed according to their specific features.

2. Pressure drop across the shallow fluidized beds -- This will enable us to estimate the power required for the blower to fluidize the bed. Comaparisons between deep and shallow beds can also be made, based on the power required. Furthermore, the possibility for the operation of multi-staged shallow beds can also be considered provided that the pressure drop data are well understood.

3. Pressure distribution in the shallow fluidized bed -- Pressure measurements provide us the cheapest and easiest way to infer hydrodynamic phenomena in fluidized-bed studies. Although it is primary, the pressure distribution can give us some important information on the hydrodynamic features of the shallow fluidized bed such as: the jet penetration depth, the height of the bed, the qualitative description of particle density as a function of position in a shallow fluidized-bed, as well as the solid mixing pattern.

4. Particle volume-fraction distribution -- We have developed two new calibration methods of a light probe that can give quantitative information about particle volume-fraction distribution data in shallow beds. With the help of a computer interfacing system, particle density fluctuations can also be recorded. Solid mixing, jet penetration , and free-board particle density can all be evaluated from the light probe data.

To facilitate the design of shallow fluidized-bed reactors, heat-transfer studies have been carried out. Together with information from hydrodynamic studies, categorization of shallow fluidized beds according to the heat-transfer data can be achieved. Variables in determining heat-transfer coefficients can also be grouped in accord with their effects in the hydrodynamic studies.

CHAPTER 2 LITERATURE REVIEW

2.1 Fundamentals of Fluidization

2.1.1 General features of fluidization

Suppose that air is caused to flow upward through a vertical cylinder containing a certain quantity of fine solid particles sitting on a porous base plate (gas distributor). The schematic diagram for the pressure drop versus a gradually increase gas velocity can be shown as Figure 2 on page 7.

When the low flow rate of air percolates through the quiescent particles, the pressure drop across the rig will be linearly proportional to the superficial gas velocity according to Darcy's law. If the gas velocity is increased to a point at which the upward drag force is equal to the downward gravitational force, the particles will begin to move apart, while the bed expands upwards and takes on the appearance of a liquid. The superficial gas velocity under this condition is called the "minimum fluidization velocity", u_{mf}, and its value is dependent on the properties of gas and particles. Beyond this velocity, usually to a good approximation, the

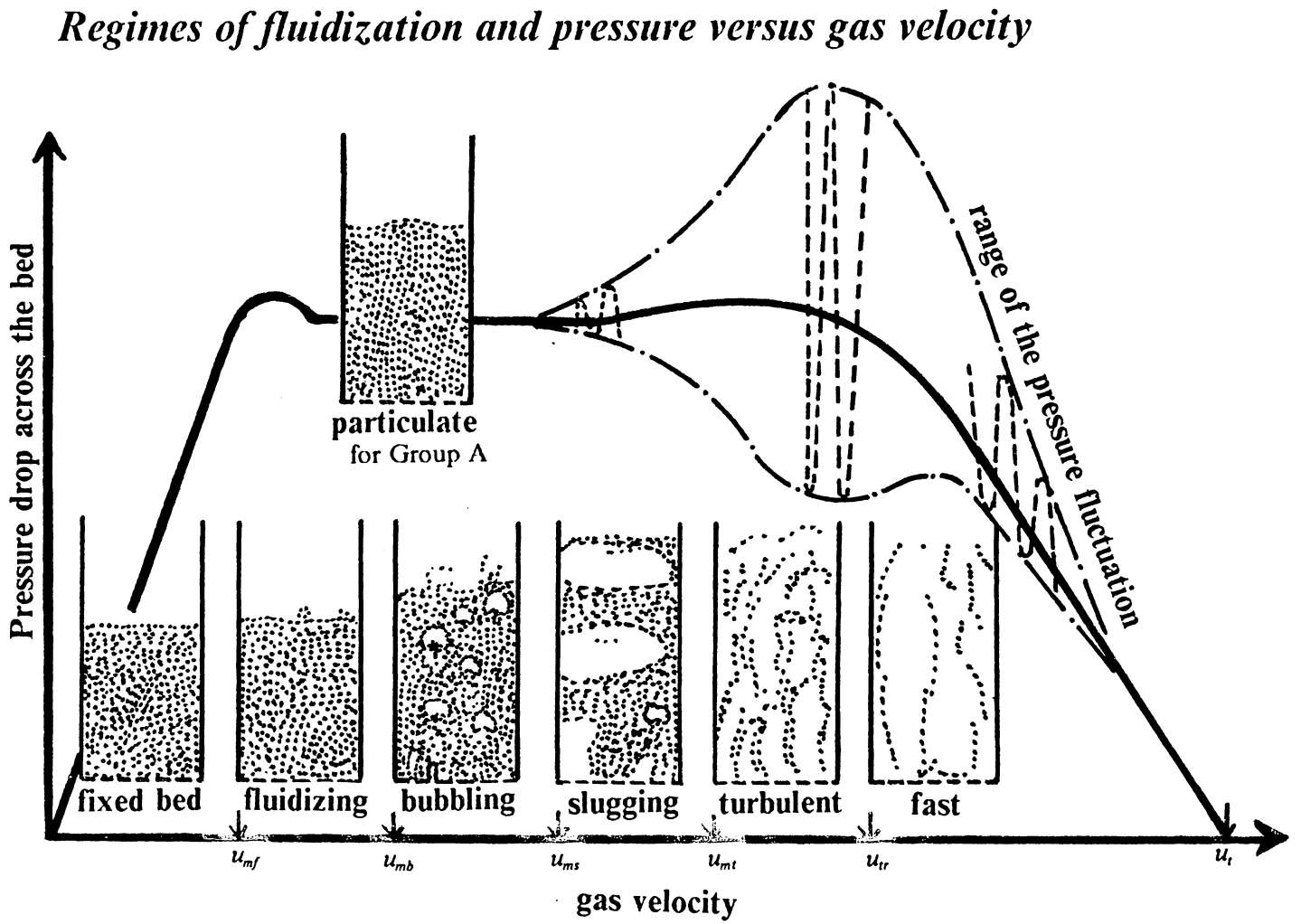

Figure 2. The fluidizing regimes as the gas velocity increases

pressure drop across the bed will be approximately equal to the total weight of the particles per unit area. However, in practice, in an experiment in which air flow is increased gradually past minimum fluidization, it usually occurs that the pressure drop slightly overshoots before upward drag forces upon the particle mass manage to break the interlocked particles apart, so that they move freely as a "fluidized" bed displaying the expected pressure drop.

For most liquid-solid and gas-powder systems, a bed expands smoothly in a homogeneous manner when the upward superficial fluid velocity moves a little beyond u_{mf}. This situation is termed particulate fluidization. The top surface of the bed is well defined, and the pressure drop across the bed counter-balances the total weight of the particles. In most liquid-solid systems, particulate fluidization persists as liquid velocity increases without limit, until all of the particles are swept away from the top of a container. In most gas-powder systems, if the gas velocity is increased above u_{mb}, the minimum bubbling velocity, voids appear within the powder mass, forming near the distributor and rising as "bubbles." Bubbles bursting at the surface generate pressure fluctuations and throw particles into the free-board space above the bed.

It should be noted that for gas-particle systems where the particles are large, particulate fluidization does not appear; there is no velocity interval over which the particle mass gradually swells, before bubbles appear (i.e. $u_{mb} = u_{mf}$ for large-particle systems).

A further increase in gas velocity leads to more vigorous bubbling with bigger and bigger bubbles until at a certain velocity, u_{ms}, (the starting slugging velocity), the bubbles almost fill the cross-section of the column. The bed is then said to be "slugging," a condition characterized by the bed diameter and bed depth in addition to the properties of the gas-particle system. The rising and collapsing of the large bubbles in a slugging bed drives the top surface up and down, sometimes over a considerable distance, and will also cause the pressure drop across the bed to fluctuate at a large amplitude.

The pressure drop across the bed fluctuates more violently as the gas flow rate is further increased, and surges created by erupting bubbles become more frequent until the regime

of turbulence is reached. The bed then will display a uniform degree of turbulence with intense local mixing characterized by many small voids and particle clusters that dart to and fro.

Still higher gas velocities result in more and more particles becoming transported from the top of the fluidized bed, while particles inside the bed aggregate in clusters. This situation has been termed "fast fluidization." No distinguishable upper surface can be observed. Table 1 on page 10 summarizes the features and descriptions of the regimes of fluidized beds.

2.1.2 Early history of fluidized beds

Originating in the 1920's and 1930's, two distinct fluidization practices were developed: (1). a "German" practice for treating coarse solids, and (2). an "American" practice for dealing with fine powder (Squires et al. 1985). The first successful fluid bed for coarse solids can be traced back to December 1921, when Fritz Winkler observed a bed of coarse particles of coke levitated and set in boiling motion by a raising current of steam. In 1922, he filed patent applications for two processes using a new chemical engineering unit operation, the "fluidized bed" -- one for producing activated carbon, the other one for the gasification of powdered coal (Squires, 1982). Warren K. Lewis and Edwin R. Gilliland of Massachusetts Institute of Technology were the first to fluidize fine powders. From December 1938, they blew clay powder upward through pipes at gas velocities up to about 3 m/s (Squires, 1984). Their work provided the fundamental data used by developers of fluid catalytic cracking (FCC) of gas oil to produce gasoline. Two other early applications are worthy of note: the development of fluidized-bed roasters in 1947 (FluoSolids system by Dorr-Oliver Company), and the application of this and similar systems for the drying and calcination of limestone and fine powders.

Table 1. Specifications of different regimes for fluidized beds

Regimes of a fluidized bed as gas velocity increases

gas velocity	fluidizing regime	features	notes
$0 < u \leq u_{mf}$	Fixed bed	1.particles are quiescent. 2.gas flows through spaces smoung particles. 3.follow Darcy's Law.	
$u_{mf} < u \leq u_{mb}$	Particulate	1.bed expends homogeneously. 2.surface is well-defined. 3.pressure drop is steady.	does not exist for gas-large-particle system.
$u_{mb} < u \leq u_{ms}$	Bubbling	1.voids form near the gas distributor, rise and grow as bubbles. 2.pressure drop fluctuates by the passing of bubbles.	bubbling, slugging, turbulent and fast regimes are often collectively called aggregative fluidization.
$u_{ms} < u \leq u_{mt}$	Slugging	1.bubbles asmost fill the cross-section of the bed. 2.bed diameter and depth will affect the fluidization. 3.pressure drop fluctuates vigorously.	amplitude of the pressure fluctuation can be as high as 80% of the average pressure drop; this regime may not exist for shallow beds.
$u_{mt} < u \leq u_{tr}$	Turbulent	1.small voids and prticle clusters dart to and fro. 2.bed surface is difficult to distinguish. 3.local mixing is intensive.	
$u_{tr} < u \leq u_t$	Fast	1.no upper surface. 2.particles are transported out of the top.(entrained)	bed voidage can be 75-90%; usually, $u_{tr}/u_t \cong 0.5/0.75$

u_{mf} = minimum fluidization velocity.
u_{mb} = minimum bubbling velocity.
u_{ms} = starting slugging velocity.
u_{mt} = starting turbulent fluidizing velocity.
u_{tr} = starting fast fluidizing velocity.
u_t = terminal velocity of the particles.

2.1.3 Applications of fluidized beds

The path to commercialize a fluidized process has usually been complex if not indeed painful (Squires, 1984; Kunii and Levenspiel, 1969). However, many research and development efforts in the past decades have provided a wide variety of applications. In these developed processes, the fluidized bed usually furnishes as a more efficient, convenient, and economical way for treating relatively large quantities of solids than alternate methods. Occasionally, one or more of the advantageous features of fluid beds (e.g. rapid mixing, uniform temperature, easy control of temperature or other process variables, easy supply of feed solids and easy discharge of solid products or spent catalysts) has been exploited in fluidized processes. Some fluid-bed applications are:

1. **Transportation** Usually, the "fluidity" of fluidized solids can be as good as that of liquids. Therefore, particles can flow according to the direction of applied driving force (by gravity or pressure force) after being fluidized. This type of transportation has a modest power consumption and usually has no moving parts. It is especially suitable for transporting dry fine particles such as cement, flour, resins, grains and soda ash. (For details, see Engineering Equipment Users' Association, 1963).

2. **Heat exchange** Because of their unique ability to rapidly transfer heat and maintain a uniform temperature, fluidized beds have been generally accepted as superb devices for heat exchange. They are especially suitable for the recovery of the heat from hot combustion gases. Hot gases are often used as the fluidizing gas, and the heat can be released to the particles directly before being transferred to the immersed cooling tubes.

3. **Fluid catalytic cracking** Many successful FCC processes have been developed after the first commercial unit, the SOD Model I (Standard Oil Development Company Model I) was built (Squires, 1983; Kunii and Levenspiel, 1969). Theoretically, the endothermic reaction

of the cracking of vaporized heavy hydrocarbons into lower-molecular-weight compounds can be efficiently carried out in a fluidized bed. By continuously circulating the suspended and flowing solids between reactor and regenerator, a fluidized-bed system can furnish the large amount of heat needed in the reactor and also regenerate the FCC catalyst rapidly by burning off carbon, generating heat.

4. **Particle growth, coating and drying** Since fluidized beds provide a easy way of handling and transporting large quantity of particles, they are often chosen when processes of physical interaction between particles and gas are concerned. Materials can be either transferred onto the particle surface (coating and particle growth) or driven out of the particles (drying). There are a number of processes in which the growth of bed particles may result. Usually, these involve the manufacture of salts such as ammonium sulfate, sodium cyanide, sodium hydroxide, uranyl nitrate, sodium sulphite,... etc. (see Kunii and Levenspiel, 1969; Wall et al. 1975; Hanway, 1970). Coating processes are commonly applied for the coating of plastic materials on metal surfaces. Fluidized-bed coating is especially applicable when the rate of growth is slow and therefore thin coated layers are required (for details, see Nienow and Rowe, 1985). Fluid beds can also provide heat at a high rate, thereby affording not only a high vaporization rate for drying of particles, but also a good control of the drying temperature. Fluidized-bed dryers usually give a better product quality and often require a smaller fuel consumption than comparable conventional dryers (Beeken, 1960).

5. **Mixing of particles** Traditional techniques for solid mixing usually require high power consumption and long operation time. Fluidized beds provide a way for fast and homogeneous mixing of particles. However, the degree of mixing and the rate of approach to uniformity will depend on the hydrodynamic features of the fluidized bed.

6. **Coal combustion** After a steady decline in its use during the past 30 years, coal has again become attractive as a fuel because of the political uncertainties and the price in-

security surrounding oil. Atmospheric-pressure fluid-bed combustion (AFBC) of coal has increased dramatically in recent years. An advantage of AFBC is its ability to burn low-grade fuels, such as oil shales and coal high in mineral matter, that are unsuitable for the conventional pulverized-coal boiler (Squires, 1985; Broughton and Howard, 1983). It is worthwhile to mention that the AFBC can also use limestone to absorb sulfur during the combustion process to remove sulfur compounds and thereby improve the quality of the waste gas.

7. **Coal gasification** Winkler's gas generator was the first fluidized-bed gasifier, operating commercially in 1926. Since then, many coal gasifiers utilizing the idea of fluidization have been developed for different applications and services. (For details, see Squires, 1983).

8. **Other applications of fluidized beds** There are many other chemical processes involving the applications of fluidized beds, such as:

   a. Sizing of particles.

   b. Chemical adsorption.

   c. Oxidation (production of ethylene oxide, alkyl chlorides, etc.)

   d. Fischer-Tropsch synthesis.

   e. Polymerization.

   f. Fluid catalytic reforming.

   g. Activation of charcoal.

   h. Calcining and clinkering.

i. Reduction of metal oxide.

j. Recovery of precious metals from ores.

2.1.4 Advantages and disadvantages of fluidized beds

Compared with other solid-fluid contacting methods available for use in chemical processes (such as fixed beds and moving beds), fluidized beds do provide better mixing patterns in most cases. However, the development of satisfactory methods for describing the hydrodynamic and heat-transfer phenomena has always been a difficult task for the study of fluidized beds. The advantages of fluidized beds in comparing with other chemical processes can be summarized as follows:

1. Because of the smooth flow of particles, the handling and control of the system is easy.

2. The rapid solid mixing gives a uniform bed temperature.

3. The removal and replacement of (catalyst) particles is easier than in a fixed-bed reactor.

4. The process is suitable to large-scale operations.

5. Heat and mass transfer rates between gas and particles are high.

6. High heat-transfer rates between the bed and an immersed surface are good.

However, there are some disadvantages for fluidized beds:

1. Flow of gas is difficult to describe.

2. Solids may have non-uniform residence time in the fluidized bed.

3. Chemical and mechanical problems created by presence of bubbles make the system complex to analyze and design.

4. Some types of particles fluidize poorly (e.g., those that are too small, too sticky or waxy, too spiky, too malleable, too putty-like).

5. Erosion of walls or internals may be a problem. This is especially noticeable when the gas velocity is high.

6. Entrainment and elutriation (the carrying-out of small particles by the fluid) make it necessary to replace particles and can lead to problems in connection with particle recovery.

7. Power consumption of the fluid-flow system must be considered.

A detailed comparison of fluidized beds with respect to other types of gas-solid reacting system can be found on page 10 of Kunii and Levenspiel's textbook (1969).

2.1.5 Shallow fluidized beds

Following the pioneering studies of heat transfer in a shallow gas-fluidized bed by the late Professor Douglas E. Elliott, many researchers have studied the applications of shallow fluidized beds (see Atkinson, 1974; Al-Ali, 1976; Huang, 1983). Table 2 on page 16 gives a comparison of key features of deep and shallow fluidized beds. Advantages and disadvantages of shallow fluidized beds in comparison with deep beds are summarized:

Advantages of shallow fluidized beds:

1. Pressure drop across a shallow bed is low.

Table 2. Comparison of shallow and deep fluidized beds

Comparison of key features of deep and shallow fluidized beds

Key Features	Deep Beds	Shallow Beds
Bed pressure drop	large	small
Bed expansion (%)	20-40	50-250
Transport disengaging height	more than 1 meter	usually < 1 meter
Heat-transfer coefficient ($W/m^2{}^\circ K$)	150-500	150-800
Bed slugging	common	seldom occurs
Bubble size (maximum)	about 1 m	about 0.1 m
Entry effect	usually not significant	often important
Bed temperture	usually uniform	gradients can occur
Multistage design	seldom practical	fairly easy and applicable
Bed scale-up	difficult due to slugs, especially for small beds.	relatively easy

2. Heat-transfer coefficient between a shallow bed and its immersed heating surface is high.

3. Slugging seldom occurs in a shallow bed.

4. Scale-up of a shallow bed and multistage shallow-bed design are relatively easy.

5. Gas-solid contact is good in a shallow bed.

6. Bubbles do not have a sufficient chance to grow up in a shallow bed.

Disadvantages of shallow beds are:

1. Jets can penetrate through the whole bed and create a by-pass for the gas flow.

2. It is hard to get uniform gas flow and temperature distribution in a shallow bed.

3. The applicable reaction region is small in shallow beds.

2.2 Basic Hydrodynamic Theories of Fluidization

2.2.1 Types of gas fluidization categorized by particle properties

Various attempts have been made to devise criteria that would categorize the features of fluidization (Zenz and Othmer, 1960; Simpson and Rodger, 1961; Harrison et al. 1961). Most of the criteria are based on dimensionless groups such as Froude number, Reynold number, Galileo number and the density ratio (particle density versus fluid density); see Wilhelm and Kwauk (1948); Romero and Johanson (1962). In recent years, the classification suggested by Geldart (1973) has been widely accepted as an easy and relatively accurate method of predicting how a given powder will behave when fluidized by gas.

Geldart divided particles for gas-solid fluidization systems into four recognizable groups, characterized by the density difference ($\rho_s - \rho_f$) and average particle diameter. Figure 3 on page 19 shows the powder/particle classification diagram for fluidization by air, while Table 3 on page 20 lists the features and specifications of the four categories proposed by Geldart. The characteristics of Geldart's particle "Groups" can be summarized as follows:

1. **Group A particles** -- Particles in this group are of small mean size and/or low particle density. Frequently, beds of powders in this group will expand considerably before bubbling commences; i.e., there is a velocity range just beyond minimum fluidization within which one observes particulate fluidization, as described earlier in Section 2.1.1. A bed of Group A particles collapses slowly (e.g., at a rate of 3 to 6 mm per second) when gas flow is suddenly stopped.

2. **Group B particles** -- Group B particles begin to bubble at gas velocities just in excess of their minimum fluidizing velocities. They are typically materials with $d_p = 150 - 500\,\mu m$

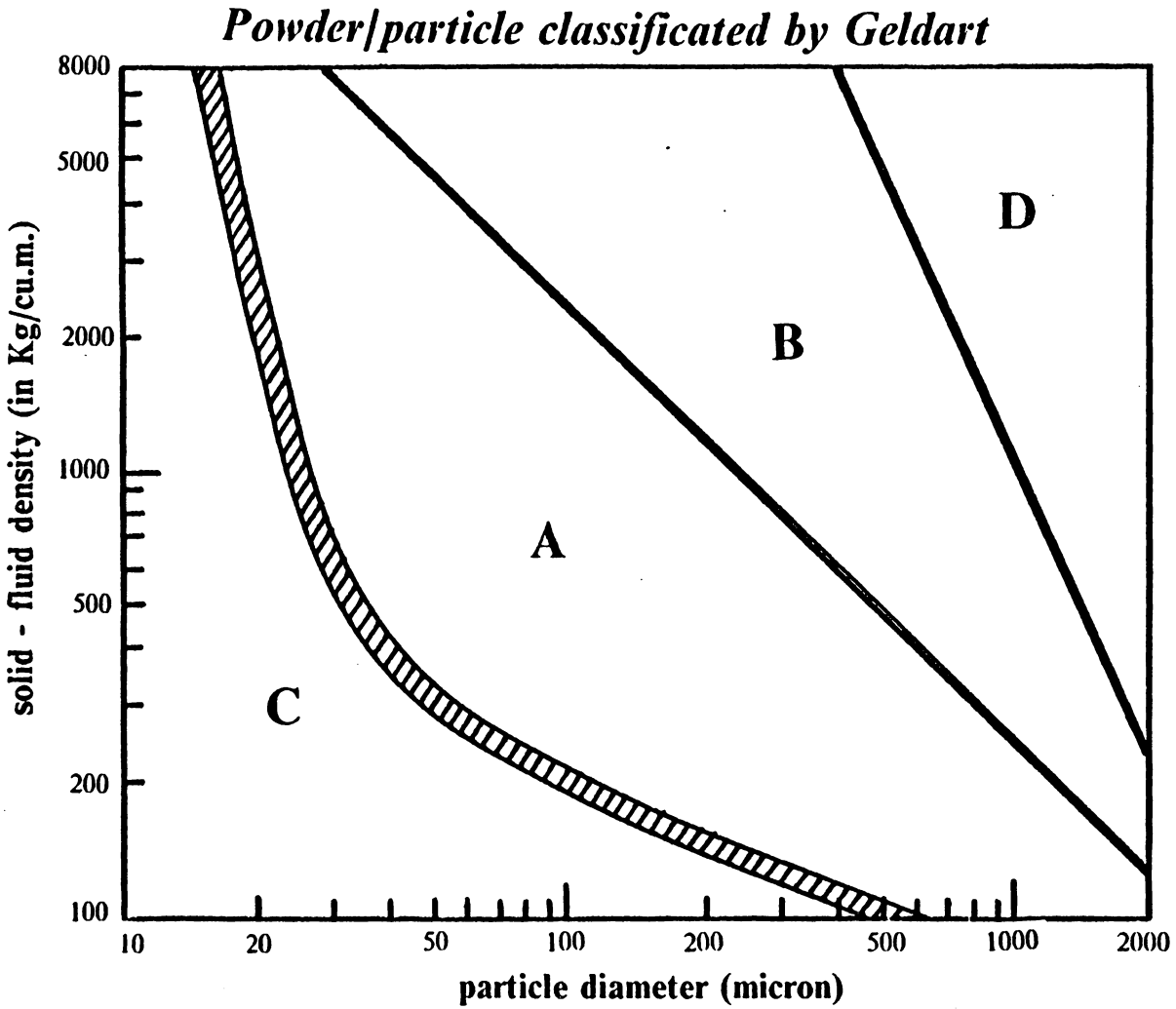

Figure 3. Powder/particle classification in fluidization by Geldart

Table 3. Features of the Groups of particles categorized by Geldart

Features of the four particle groups proposed by Geldart

Features/ specifications	Particle Group A	B	C	D
recognizable features	dense phase expand after minimum fluidi- zation	bubbles appear at the minimum fluidization velocity	difficult to fluidize	can form stable spouted bed
typical particle	cracking catalyst	beach sand	flour	lead shoot
bed expansion	high	small	very small	very small
collapse rate	slow	fast	slow	fast
bubble size	small	large	slugging	large
bubble velocity	fast	medium	none	slow
solid mixing rate	very high	medium	poor	low
gas exchange rate	high	medium	none	very low
mode of slugging	axi-symmetric	axi-symmetric (at low u) asymmetric (high u)	channels	asymmetric
spouting	none	for shallow bed	none	for bed deeper than 0.3 m
heat transfer between bed and immersed subject	high	medium	very low	low

and densities in the range of 1500-4000 Kg/m^3. Dense-phase void fraction remains substantially constant, close to its value at the minimum fluidization velocity.

3. **Group C particles** -- Cohesive powders of very small size (usually $d_p < 30 - 40\,\mu m$) belong in this category. When the gas flow is passing through a bed of particles of this kind, either plug flow (for small diameter bed) or channeling (for large bed) will occur. However, fluidization can often be made acceptable by using mechanical stirrers or vibrators.

4. **Group D particles** -- Fluidized particles that are either of very large size or of very high density fall in this category. Normally, the gas velocity in the dense phase is high, beyond the velocity of a typical bubble upward.

2.2.2 Single particle properties

Particle shape factor, sphericity and mean diameter

Consider a particle of any shape having a volume of V_p and a surface area A_p. We can define an equivalent-volume sphere as a standard of comparison, i.e. a sphere whose volume is V_p --

$$(\frac{\pi}{6})\, d_p^3 = V_p$$

or,

$$d_p = (\frac{6\,V_p}{\pi})^{\frac{1}{3}} = 1.24\,V_p^{\frac{1}{3}}$$

Usually, d_p is termed the normalized diameter of the particle.

The particle shape factor λ can be defined as the surface area A_p divided by the surface area of the equivalent-volume sphere --

$$\lambda = \frac{A_p}{A_s} = \frac{A_p}{(\pi d_p^2)}$$

Frequently, the inverse of shape factor, namely, the sphericity φ_s is used in fluidization studies. For any particle--

$$0 \leq \varphi_s = \frac{1}{\lambda} \leq 1$$

Note that $\varphi_s = 1.0$ for a perfect sphere. The calculated sphericities of several different solids are given by Kunii and Levenspiel (1969) at page 65.

In fluidization engineering, people usually use mixtures of particles of different particle sizes. Several different "mean diameters" can be defined:

Median diameter d_p(me)

= diameter of the particle such that all particles smaller than the given particle constitute one-half of the weight of the particle mass.

Arithmetic mean diameter $d_p(\text{am}) = \frac{\Sigma d_p}{N}$

Geometric mean diameter $d_p(\text{gm}) = (d_{p1} \times d_{p2} \times ..... \times d_{pn})^{\frac{1}{N}}$

Surface mean diameter $d_p(\text{sm}) = (\frac{\Sigma d_p^2}{N})^{\frac{1}{2}}$

Volume mean diameter $d_p(\text{vm}) = (\frac{\Sigma d_p^3}{N})^{\frac{1}{3}}$

Terminal and settling velocities of a single particle

The steady flow of a fluid passing around a submerged spherical particle will exert a drag force, F_D, which is associated with the kinetic behavior of the fluid. Many authors (e.g. Bird et al. 1960; Clift et al. 1978) define a dimensionless quantity C_D, known as the drag coefficient, to relate the drag force with the Reynold number --

$$C_D = \frac{F_D}{K_v A_c} = f(Re) \qquad [2.1]$$

where

F_D = drag force exerted on a single particle, N.

C_D = drag coefficient, dimensionless.

K_v = characteristic kinetic energy per unit volume = $(\rho_f u^2)/2$, $\frac{kg}{ms}$.

A_c = characteristic area of the particle = $(\pi d_p^2)/4$, m^2.

Re = Reynold number = $(\rho_f d_p u)/\mu_f$, dimensionless.

Clift et al. (1978) gave a detailed list of recommended correlation equations for C_D as functions of (Re). Figure 4 on page 24 shows the schematic diagram in conjunction with some physical definitions and explanations. (for details, see Clift et al. 1978)

For the free fall of a spherical particle in a fluid, the particle will eventually reach a steady-state terminal velocity, u_t, at which the drag force is just counter-balanced by the gravitational force less the buoyancy force. This can be expressed mathematically by the following equation --

$$F_D = (\rho_s - \rho_f)\frac{\pi d_p^3 g}{6} \qquad [2.2]$$

for $u = u_t$

Equations 2.1 and 2.2 can be combined to give

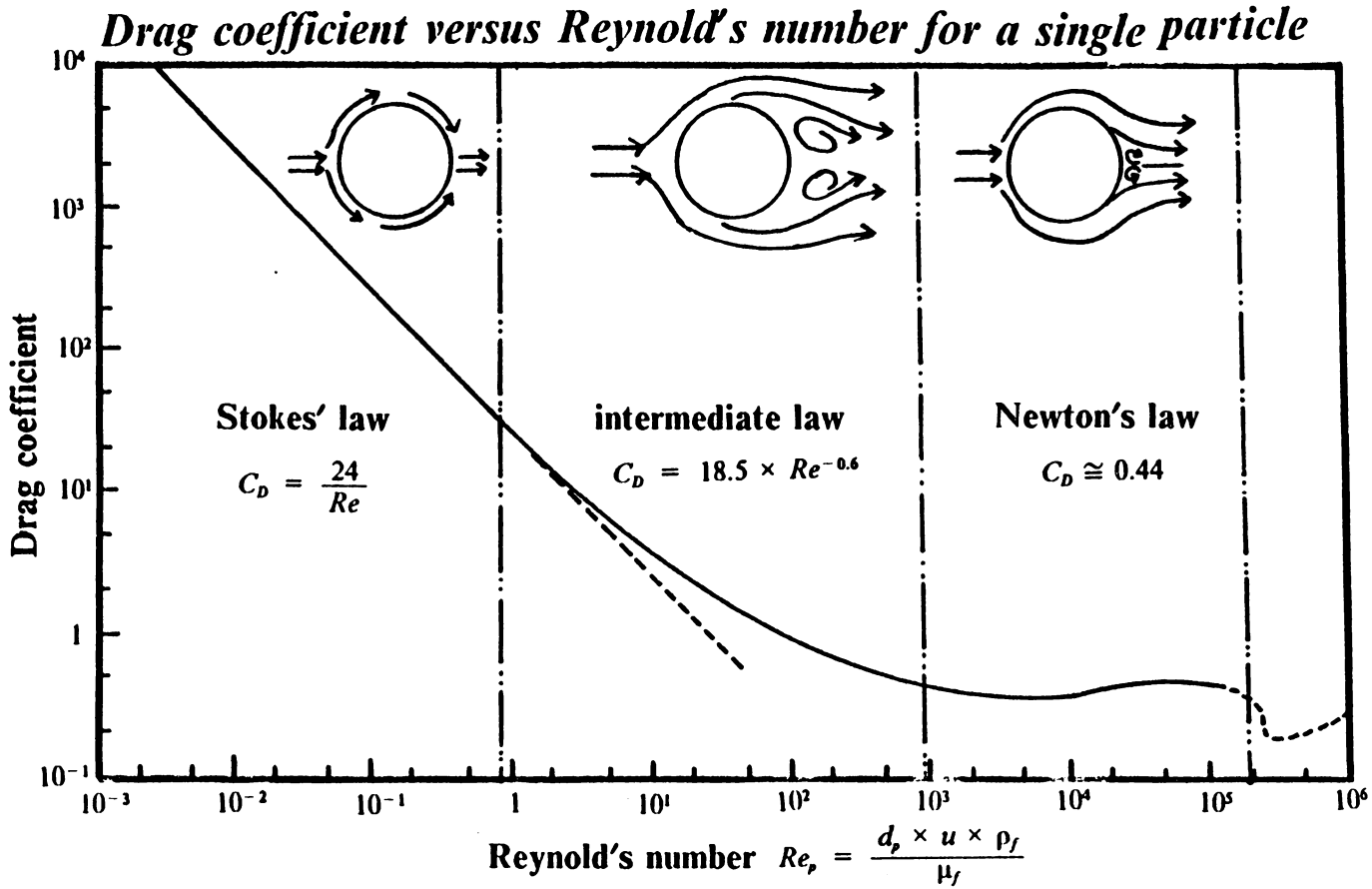

Figure 4. Drag coefficient versus Reynold number for single particle

$$F_D = C_D \left(\frac{\rho_f u_t^2}{2}\right)\left(\frac{\pi d_p^2}{4}\right) = \frac{\pi g (\rho_s - \rho_f) d_p^3}{6} \qquad [2.3]$$

After rearrangement, Equation 2.3 can be further rewritten to have the following form--

$$Re_t^2 C_D = N_D \qquad [2.4]$$

where

$$Re_t = \frac{\rho_f d_p u_t}{\mu_f}$$

$$N_D = g d_p^3 \frac{(\rho_s - \rho_f)}{\mu_f} \frac{4}{3}$$

Since the values of Re_t and C_D are interdependent according to Equation 2.1 and the equation for the calculation of C_D and Re_t has usually been specified as a function of N_D -- a variable depends only on the static properties of the fluid-particle system. Table 4 on page 26 (adapted from Clift, et al., 1978) lists the correlations for Re_t as functions of N_D in different ranges. The terminal velocity, u_t, can be easily calculated from those correlations in conjunction with the relations that define Re_t and N_D.

For non-spherical particles, the shape of the particles will not only affect the value of the terminal velocity but also determine how the particles fall. Since the particle shape varies from case to case, it has been always difficult (if not impossible) to identify an unambiguous way to find the terminal velocities for irregular particles. However, there are basically three settling regimes which can be characterized by the physical appearance and the Reynold number of the freely falling particles:

1. Low Reynold number (Re has the order of magnitude of 1)-- An irregular particle will keep its original orientation and settle steadily but not vertically. It can also display "side-slipping" behavior.

Table 4. Equations for the calculation of Reynold number at terminal velocity

Equations for the calculation of Reynold number at terminal velocity

$N_D \leq 73$ $Re_t \leq 2.73$	$Re_t = (\frac{N_D}{24}) - 1.7569 \times 10^{-4} N_D^2 + 6.925 \times 10^{-7} N_D^3 - 2.3027 \times 10^{-10} N_d^4$
$73 < N_D \leq 580$ $2.73 < Re_t \leq 12.2$	$\log(Re_t) = -1.7095 + 1.33438\,\omega - 0.11591\,\omega^2$
$580 < N_D \leq 1.55 \times 10^7$ $12.2 < Re_t \leq 6.35 \times 10^3$	$\log(Re_t) = -1.81391 + 1.34671\,\omega - 0.12427\,\omega^2 + 0.006344\,\omega^3$
$< N_D \leq 5 \times 10^{10}$ $6.35 \times 10^3 < Re_t \leq 3 \times 10^5$	$\log(Re_t) = 5.33283 - 1.21729\,\omega + 0.19007\,\omega^2 - 0.007005\,\omega^3$

$\omega = \log(N_D)$ $\qquad N_D = g\, d_p^3 \frac{(\rho_s - \rho_f)}{\mu_f} \frac{4}{3}$

2. Intermediate Reynold number (Re has the order of magnitude of 1 to 100) -- The particle will settle steadily and vertically with preferred orientation that has the maximum projected area perpendicular to the direction of motion. Heywood (1962) proposed an algorithm for estimating the terminal velocities of particles at intermediate Reynold numbers.

3. High Reynold number (Re has the order of magnitude over 100) -- Due to wake shedding, the particle can oscillate so much that secondary motions often occur. The terminal velocity becomes especially difficult to determine even if capability for performing wind tunnel measurements is available.

When a falling particle is in an assemblage, its settling velocity is usually decreased because of an increasing drag force. Two effects contribute for the increased drag: (1) displacement of the fluid caused by the particles; (2) disturbances and wakes introduced by neighboring particles. The hindered settling velocity, u_{hs}, of a single particle in an assemblage can be estimated by the Richardson-Zaki correlation (Richardson and Zaki, 1954) --

$$u_{hs} = u_t \varepsilon^n \qquad [2.5]$$

$$n = 4.65 + 20 \times \delta_R$$

for $Re_t \leq 0.2$;

$$n = Re_t^{-0.03} (4.4 + 18 \times \delta_R)$$

for $0.2 < Re_t \leq 1.0$;

$$n = Re_t^{-0.1} (4.4 + 18 \times \delta_R)$$

for $1 < Re_t \leq 200$;

$$n = 4.4 \times Re_t^{-0.1}$$

for $200 < Re_t \leq 500$;

$n = 2.4$

for $500 < Re_t$

where

Re_t = Reynold number for the terminal velocity. (from Table 4 on page 26)

ε = voidage of the particle assemblage.

$\delta_R = \frac{d_p}{D_b}$

d_p = particle diameter, m.

D_b = diameter of the container, m.

Heywood (1962) proposed the following algorithm for the determination of the terminal velocity for a free-falling, irregular particle having an intermediate Reynold number:

1. Calculate:

   A_p^* = maximum horizontal area (determined by using a microscope).

   K_s = volumetric shape factor. = (volume of the particle)/(d_p^3)

   d_A = characteristic diameter. = $2\,(\frac{A_p^*}{\pi})^{0.5}$

2. Estimate N_D after substituting d_A for d_p.

3. Calculate Re_t and hence u_t using Table 4 on page 26

4. Modify the u_t to u_t^*, the actual terminal velocity, by

   $u_t^* = K_A\, u_t$

Clift et al. (1978) gave the diagram of K_A which could be determined by the system's static parameter N_D and the volumetric shape factor K_s.

2.2.3 Criteria for different fluidization regimes

Minimum fluidizing velocity

The superficial gas velocity at which the bed starts taking on the appearance of a liquid is called the "minimum fluidization velocity", u_{mf}, and its value depends on the physical properties of the fluidizing gas and particles.

The experimental determination of minimum fluidization velocity is usually based on schematic diagram of the pressure drop versus gas velocity. By extrapolating the straight fixed-bed line to its intersection with the constant pressure-drop line (see the previous section and Figure 2 on page 7), we can reliably estimate the minimum fluidization velocity. However, in commercial practice, because of danger from particle choking (in a deep bed) and segregation (in a bed with a wide size distribution), it is usually not recommended that a fluidized bed be operated close to the minimum fluidization condition.

Many empirical expressions have been proposed to estimate the minimum fluidization velocity, u_{mf} , in terms of the physical properties of the fluidizing gas and particles. The most commonly used theoretical derivation is based on extending the relationship between gas velocity and pressure drop in a packed bed to the point where the particles are fluidized. A generalized equation for describing the relationship between gas velocity and pressure drop has been proposed by Ergun (1952) --

$$\frac{\Delta P}{H} = \frac{150\,(1-\varepsilon_s)^2}{\varepsilon_s^3}\,\frac{\mu_f u}{(\varphi_s\, d_p)^2} + \frac{1.75\,(1-\varepsilon_s)}{\varepsilon_s}\,\frac{\rho_f u^2}{\varphi_s\, d_p} \qquad [2.6]$$

where

d_p = particle diameter, m.

ρ_f = density of the fluid, Kg/m^3.

ε = static bed porosity (void-volume fraction).

φ_s = sphericity of the particle, dimensionless

u = superficial gas velocity, m/s.

μ_f = viscosity of the fluid, $\frac{N\,s}{m^2}$.

ΔP = pressure drop across the bed, $\frac{N}{m^2}$.

H = bed height, m.

Ergun's equation can be applied with success to both laminar and turbulent flows. Note that for high gas velocity, the first term on the right-hand side drops out, and the equation reduces to the Burke-Plummer equation for turbulent flow. At low gas velocity, the second term on the right-hand side drops out, and the Blake-Kozeny equation for the laminar flow results (Bird et al. 1960)

By assuming that the total weight of the bed at onset of fluidization is supported by the drag force of the upwardly moving gas (Kunii and Levenspiel, 1969), the left-hand side of Equation 2.6 can be expressed as --

$$\frac{\Delta P}{H} = (1 - \varepsilon_s)(\rho_s - \rho_f) g \qquad [2.7]$$

where

ρ_s = particle density, $\frac{kg}{m^3}$.

g = gravitational constant, $9.8\frac{m}{s^2}$.

Combining Equations 2.6 and 2.7, we can get the expression for the minimum fluidization condition --

$$\frac{1.75}{\varphi_s \varepsilon_{mf}} \left(\frac{d_p u_{mf} \rho_f}{\mu_f}\right)^2 + \frac{150}{\varphi_s^2 \varepsilon_{mf}^3} \left(\frac{d_p u_{mf} \rho_f}{\mu_f}\right) = \frac{d_p^3 \rho_f (\rho_s - \rho_f) g}{\mu_f^2} \qquad [2.8]$$

where

u_{mf} = the minimum fluidization velocity, $\frac{m}{s}$.

ε_{mf} = the bed voidage at u_{mf}, dimensionless.

For convenience in calculating u_{mf}, Equation 2.8 can be further simplified to read --

$$Re_m = [\alpha_1^2 + \alpha_2 Ga]^{0.5} - \alpha_1 \qquad [2.9]$$

where

Re_m = Reynold number for u_{mf}, $= \frac{u_{mf} d_p \rho_f}{\mu_f}$, dimensionless.

Ga = Galileo number, $= \frac{d_p^3 \rho_f (\rho_s - \rho_f) g}{\mu_f^2}$, dimensionless.

$$\alpha_1 = \frac{300\,(1 - \varepsilon_{mf})}{7\varphi_s}$$

$$\alpha_2 = \frac{\varepsilon_{mf}^3 \varphi_s}{1.75}$$

Notice further that for air at 1 ATM and 20 °C as the fluidizing gas, Equation 2.9 can be simplified to --

$$u_{mf} = \frac{15}{d_p}[(\alpha_1^2 + \alpha_2 Ga)^{0.5} - \alpha_1]$$

and,

$$Ga = 3.6 \times 10^{-3} d_p^3 (\rho_s - 1.205)$$

Because Re_{mf} and Ga are clearly defined, Equation 2.9 has been commonly accepted for the calculation of u_{mf}. Unfortunately, the values of ε_{mf} and φ_s are unknown in most of the situations under which the evaluation of u_{mf} is necessary. Botterill (1983) points out that an error of 10% in the estimation of ε_{mf} will produce an error of 37% in the estimation of u_{mf} for laminar-flow regime, while the error would be 16% for turbulent-flow regime.

Wen and Yu (1966) proposed that in a wide variety of systems, the values of φ_s and ε_{mf} could not be totally independent. Consolidating data from more than two studies, they found that --

$$\frac{1}{\varphi_s \varepsilon_{mf}^3} \cong 14$$

and,

$$\frac{1 - \varepsilon_{mf}}{\varphi_s \varepsilon_{mf}^3} \cong 11$$

Therefore, α_1 and α_2 values in Equation 2.9 can be substituted by 33.7 and 0.0408 respectively. Part I of Table 5 on page 33 lists values of α_1 and α_2 that have been suggested by many investigators under different experimental conditions. Many other correlations having forms other than Equation 2.9 for calculating u_{mf} are also listed in Part II of Table 5 on page 33.

Some correlations in Table 5 on page 33 can be applied to the pressurized fluidized beds. For beds operated under high temperature, Botterill et. al. (1981) suggested that ε_{mf} increased with increasing bed temperature in the laminar-flow region. However, most of the correlations based upon room-temperature data can still be used for the transitional and turbulent regimes, provided that the effect of temperature elevation on the fluid viscosity is considered.

Minimum bubbling velocity and two-phase theory

Geldart and Abrahamsen (1980) proposed the following correlation for calculating minimum bubbling velocity based on the S.I. units --

$$u_{mb} = u_{mf} \frac{4.125 \times 10^{-4} \mu_g^{0.9} \rho_g^{0.1}}{(\rho_s - \rho_g)\, g\, d_p} \qquad [2.10]$$

For large particles (Groups B and D), this equation usually will give $u_{mb} < u_{mf}$, and it shall be taken as $u_{mb} = u_{mf}$. For Group A powders in the particulate regime, bed expansion can be calculated by the Richardson-Zaki correlation --

$$\varepsilon_f = \left(\frac{u}{u_t}\right)^{\frac{1}{n}} \qquad [2.11]$$

where n can be calculated by Equation 2.5.

Table 5. Equations for the calculation of minimum fluidizing velocity

Equations for the calucaltion of minimum fluidizing velocity

using the equation -- $Re_m = [\alpha_1^2 + \alpha_2 Ga]^{0.5} - \alpha_1$

Reference	α_1	α_2	d_p (μm)	Re_{mf}	%error	comments
Narsimhan (1965)	$4.29b$	$.57ab^2$	730-5200	10.9-495	46	$a = 3.65 \times 10^{-6} d_p^{-.55}$ $b = .231\log d_p + 0.15$
Wen and Yu (1966)	33.7	.0408	51-460	.001-4000	34	
Babu et. al. (1978)	25.2	.0649	50-2870	.02-170	21.3	
Grace (1982)	27.2	.0408	---	----	9.0	for pressure .1 - 7.0 M Pa.
Nakamura et. al. (1985)	33.95	.0465	200-4000	.08-1360	8.5	for pressure .1 - 4.9 M Pa.
Richardson (1971)	25.7	.0365	---	----	--	assuming $\varepsilon_{mf} \cong 0.4$

Twoomy and Johnston (1952) proposed a two-phase theory of fluidization of particles by gas. They suggested that all gas in excess of the minimum required flow to fluidize the bed passes upward in form of bubbles. Mathematically, the ideal two-phase theory can be expressed as --

Q_b (volume of bubbles) $= A_b(u - u_{mf})$

However, in recent years, workers are in general agreement that the ideal two-phase theory overestimates the visible bubble flow (see Grace and Clift, 1974). Therefore, a modified two-phase theory can be written as --

$$Q_b = A_b [u - u_{mf}(1 + n_b f_b)] \qquad [2.12]$$

where

n_b = a positive number, dimensionless.

f_b = the volume fraction of bed occupied by bubbles, dimensionless.

Lockett et al. (1967) showed the theoretical value of n_b to be 1 for idealized circular bubbles (two-dimensional) and 2 for perfect spherical bubble (three-dimensional). Their treatment was based on the assumption of a bubble acting as low-resistance short circuit for interstitial gas velocity: $2u_{mf}$ and $3u_{mf}$ for circular and spherical bubbles, respectively. However, many different values of n_b have been reported (see Grace and Clift, 1974). Grace and Harrison (1969) even found a n_b value of 4.3 in an experimental study of a two-dimensional fluidized bed.

Yates (1983) suggested that the two-phase theory cannot be sustained in beds of either coarse particles, where gas bypassing appeared, or fine particles, where dense-phase expansion occured. It is still debatable how gas flow should be divided between bubbles and dense phase. However, the two-phase theory does provide a valuable basis for developing chemical reaction models in fluidization research.

One of the earliest hydrodynamic treatments of bubbles was given by Davidson and Harrison (1963), who proposed the following assumptions --

1. The bubbles are circular in two-dimensional beds and spherical in three-dimension beds.

2. The pressure inside a bubble is constant.

3. The fluidized-bed material can be treated as incompressible fluid of zero viscosity.

4. The interstitial gas flow obeys Darcy's law for incompressible viscous fluid.

They suggested the following equations for the gas velocity-field around a spherical bubble --

$$U_r = \frac{1}{r^2 \sin\theta} \frac{\partial \Phi_f}{\partial \theta}$$

$$U_\theta = \frac{1}{r \sin\theta} \frac{\partial \Phi_f}{\partial r}$$

$$\Phi_f = (u_b - u_g)\left(1 - \frac{R_c^3}{r^3}\right) \frac{r^2 \sin^2\theta}{2}$$

$$R_c = R_b \left[\frac{u_b + 2u_g}{u_b - u_g}\right]^{\frac{1}{3}}$$

where

U_r = flow velocity in the r-direction, $\frac{m}{s}$.

U_θ = flow velocity in the θ-direction, $\frac{m}{s}$.

Φ_f = the stream function, dimensionless.

R_c = cloud radius of the bubble, m.

R_b = radius of the bubble, m.

They solved the above equations and proposed stream lines as well as pressure distribution curves for different $\frac{u_b}{u_g}$ ratios (see also Kunii and Levenspiel , 1969).

Distinguishing bubbling and slugging beds

Davidson and Harrison (1963) proposed a chart for estimating a maximum stable bubble size and the condition for bubbling and smooth fluidization. However, they suggested that unless the rising velocity of the bubble (u_b) exceeds the terminal velocity of the particles (u_t), the bubble keeps growing without limit and will not break down. They also gave the following equation to estimate the rising velocity of a single bubble --

$$u_b = 0.711\sqrt{g\,d_b} \qquad [2.13]$$

where d_b is the diameter of the sphere of equivalent volume of the bubble. Some theories have been suggested for calculating the coalescence and growth of bubbles (see Kunii and Levenspiel, 1969). Unfortunately, there is still no universally accepted way to estimate the maximum size that a bubble will grow in a particular fluidizing system. However, Kunii and Levenspiel (1969) suggested --

1. The geometry of the vessel and its internals may limit the size of bubbles.

2. The maximum stable bubble size proposed by Davidson and Harrison (1963) gives us a limitation on the size a bubble can grow.

As long as the bubbles grow to the size of the cross-section area of a fluidized bed, slugging occurs. Davidson and Harrison (1963) suggested that for a slugging bed --

$$u_{sl} = 0.35\sqrt{g\,D_b}$$

where u_{sl} is the rising velocity of the slug and D_b is diameter of the bed. The averaged voidage in a slugging bed can also be calculated by --

$$\varepsilon_{sl} = \frac{u - u_{mf}}{(u - u_{mf}) + 0.35\sqrt{g\,D_b}} \qquad [2.14]$$

Slugging and choking in dilute phase

In a vertical pneumatic transport line, it is possible to operate the system so that very dilute solids are conveyed (usually, $\varepsilon_f \cong 0.9$). If the solid concentration accumulates or gas velocity decreases, a transition to slug flow occurs. This is called "choking" and represents the upper limit for the operation of the pneumatic transport line. Smith (1978) suggested that the maximum propagation velocity for a slug shall be

$$u_{sl}^{*} = u_t n (1 - \varepsilon_f) \varepsilon_f^{n-1} \qquad [2.15]$$

This is the modification of the Richardson and Zaki equation and n is the exponent suggested by Richardson and Zaki (1954). Therefore, when

$$0.35 \sqrt{g D_b} < u_t n (1 - \varepsilon_f) \varepsilon_f^{n-1}$$

the choking/slugging will not occur.

Turbulent fluidization

Lanneau (1960) was probably the first one to recognize the existence and potential advantage of turbulent fluidized beds, although he did not create this term, nor did his work arouse much interest at the time. By fluidizing 30-150 μm cracking catalysts, he found a gradual change of the bed to a condition of increasing homogeneity if the superficial gas velocity was increased well beyond a slugging velocity. Working with different powders (most of them were Group A) and capacitance probes, Kehoe and Davidson (1970) reported that turbulent fluidization occurs when --

$$u < 3u_{t,mim}$$

where $u_{t,mim}$ is the terminal velocity of particles belonging to the smallest cut. Many other investigations have also focused on the transition from bubbling to turbulent fluidization -- e.g. Thiel and Potter ,1977; Yerushalmi and Avidan, 1985.

2.2.4 Gas and solid mixing in fluidized beds

Potter (1971) gave a review on the use of diffusion and transfer-coefficient models to analysize solid mixing. His work enlarged upon two basic models --

1. Lewis et al. (1962) accounted for solid mixing in terms of an upward motion of solids with bubbles.

2. May (1959) suggested an unspecified diffusion process for solids mixing.

However, many hydrodynamic variables have to be evaluated in most of the models based on these two basic mechanisms. The considered variables are:

1. Bubble rising velocity.

2. Solid displacement by bubbles.

3. Solid and gas exchange between dense phase and bubbles.

4. Distribution of bubble and dense phases.

5. Coalescence rate of bubbles.

Unfortunately, complex assumptions have to be proposed before any of those properties can be calculated by the existing models or correlations.

Liu and Gidaspow (1981) adapted the basic equations for one-dimensional transient flow

1. Continuity equation in gas phase --

$$\frac{\partial \varepsilon_f \rho_g}{\partial t} + \frac{\partial (\varepsilon_f \rho_g u_g)}{\partial x} = 0$$

2. Continuity equation in solid phase --

$$\frac{\partial [(1 - \varepsilon_f)\, \rho_s]}{\partial t} + \frac{\partial [(1 - \varepsilon_f)\, \rho_s u_s]}{\partial x} = 0$$

3. Continuity equation for the mixture --

$$(u_s - u_g) \frac{\partial (u_s - u_g)}{\partial x} - f_\beta (u_s - u_g) - g = 0$$

4. Momentum equation for the mixture --

$$\frac{\partial}{\partial t}[\varepsilon_f \rho_g u_g + (1 - \varepsilon_f)\, \rho_s u_s] + \frac{\partial}{\partial x}[(\varepsilon_f \rho_g u_g^2) + (1 - \varepsilon_f)\, \rho_s u_s^2] + \frac{\partial P}{\partial x} = \rho_{mx} g + f_w$$

where

f_β = friction coefficient, dimensionless.

ρ_{mx} = density of the solid-gas mixture, $\frac{kg}{m^3}$.

f_w = friction force between the gas and the fluidized bed wall, N.

u_s = solid velocity, $\frac{m}{s}$.

After the linearization of the above equations, they proposed a set of analytical solutions by using principles of non-equilibrium thermodynamics. They found that experimental data for the distribution of tracer particles matched the proposed hyperbolic diffusion equation quite well. Van Deemter (1985) gave a detailed review of solid and gas mixing in fluidized beds.

2.2.5 Design of gas distributor

In most fluidized beds, the type of gas distributor used will strongly influence the quality and characteristics of the fluidization, especially when the bed is shallow. Most of the distributors used in distillation equipment can be adapted for fluidizing operations. However, to fulfill the basic fluidizing functions, a gas distributor has to --

1. Support the total weight of the particles inside the bed.

2. Prevent the particles from leaking to the windbox or the pipeline below the distributor.

3. Stabilize a uniform flow of gas into the bed.

4. Minimize the size of the gas bubbles created above the distributor.

Table 6 on page 41 compares various gas distributors most commonly used for fluidization operations.

Experience shows that distributors should impose a sufficient pressure drop to achieve uniform flow through the openings. However, too high a pressure drop may significantly increase the pumping power consumption, usually a major cost factor. Fakhimi and Harrison (1971) and Zabrodsky (1966) have suggested the estimation of P_D (the pressure drop across the distributor) in terms of the minimum fluidization velocity, particle density, bed voidage and superficial gas velocity. Botterill(1975) gave a rule of thumb to estimate the pressure drop across the distributor plate:

[I] for deep beds--

(1). $\frac{P_D}{P_B} \cong 0.15$ when $\frac{u}{u_{mf}} \cong$ 1-2

Table 6. Comparison of gas distributors for fluidized beds

Types of distributors used in the fluidization

Type of distributor	Cost	P_D	Mechanical strength	Jet	Running cost	Comments
wire mesh	1	1	1	2	1	1. for laboratory scale only. 2. does not have enough mechanical strength. 3. not recommended for shallow beds.
perforated plate	1	1	2	3	1	1. very common for laboratory scale. 2. number/size of holes can be adjusted to give the best performance. 3. can have more than one layer.
packed layer	2	3	2	1	2	1. inlet gas has to be absolutely clean. 2. the gas will mix well before entering the bed.
grate bars	2	1	2	3	1	1. give less uniform gas flow. 2. can be located above the other type of distributor to break down the bubbles.
sintered/waved metal plate	3	4	3	1	2	1. give small bubbles. 2. can have strong mechanical strength.
porous ceramic plate	3	4	2	1	2	1. high resistance to chemical corrosion. 2. might be eroded by the particles.
nozzles or bubblecaps	4	2	3	2	4	1. prevent solids from falling to the windbox (the angle of repose has to be considered.) 2. not recommended unless special performance is required.
pipe grid	4	2	2	3	2	1. good to be used to introduce reactant gas.

Note-- 1: very low; 2: low; 3: mediate; 4: high.

P_D = pressure across the distributor.

(2). $\frac{P_D}{P_B} \cong 0.015$ when $\frac{u}{u_{mf}} \cong > > 1$

[II] for shallow beds--

$$\frac{P_D}{P_B} \cong 1.0$$

where

P_D = pressure drop across the distributor, $\frac{N}{m^2}$.

P_B = pressure drop across the bed, $\frac{N}{m^2}$.

u = superficial gas velocity, $\frac{m}{s}$.

u_{mf} = minimum fluidization velocity, $\frac{m}{s}$.

However, an earlier recommendation proposed by Agarwal et al. (1962) suggests that $\frac{P_D}{P_B}$ be 0.1 with a minimum P_D in all cases of about 350 mm of water.

Since there are so many possibilities and uncertainties in the design of distributors, only good judgment and experience can tell which type of distributor and what range of pressure drop are best for a given application (Kunii and Levenspiel, 1969). However, some suggestions can be summarized from the literature --

1. The design of windbox can affect the performance of the gas distributor.

2. Usually, metallic distributors are recommended for their mechanical strength and their high resistance to the erosion (Kunii and Levenspiel, 1969).

3. For a perforated plate, the orifice diameter should be no larger than three times the average particle diameter to reduce the particle seepage beneath the distributor (Botterill, 1975).

4. The height of the entrance effect (highly dependent upon orifice spacing, fluidizing velocity, and particle properties) has to be taken into consideration for multi-orifice distributors (Whitehead, 1971; Fakhimi et al., 1983).

2.2.6 Jet penetration depth in fluidized beds

Definition of jets

A major function of the distributor in a fluidized bed is to provide a uniform flow of gas in the form of gas bubbles at a reasonable pressure drop. Under certain conditions, distorted gas "bubbles" are observed immediately above and connected with the distributor holes. The literature often refers to such distorted bubbles as "jets", although a distinction between jets and bubbles has yet to be properly defined. Recently, Rowe et al. (1979) have proposed distinctions based on temporal rather than shape characteristics. In their opinion, only permanent voids, irrespective of their shapes, are properly called jets; and any void showing an intermittent leakage (discharge) of gas through the boundary is, for these authors, a bubble.

Other investigators have presented different views of jets and bubbles. For example, Figure 5 on page 44 illustrates a picture of a vertical jet and bubble in a fluidized bed published by Merry (1975) and based, in part, upon motion pictures of jets by Markhevka et al. (1971). According to this picture, the bottom region of the jet is conical and bubbles form periodically in a regular pattern at the end of the jet. The upper ellipsoidal part of the jet, above the conical region, elongates, takes on the form of a bubble, and separates from the jet. The jet then collapses, and the cycle is repeated so that the jet region expands before and during bubble growth and contracts after bubble separation in a rhythmic pulsating cycle. In the figure, the jet penetration depth is defined as the vertical distance between the orifice and the lower edge of the bubble at the moment of bubble separation from the jet. Since this distance

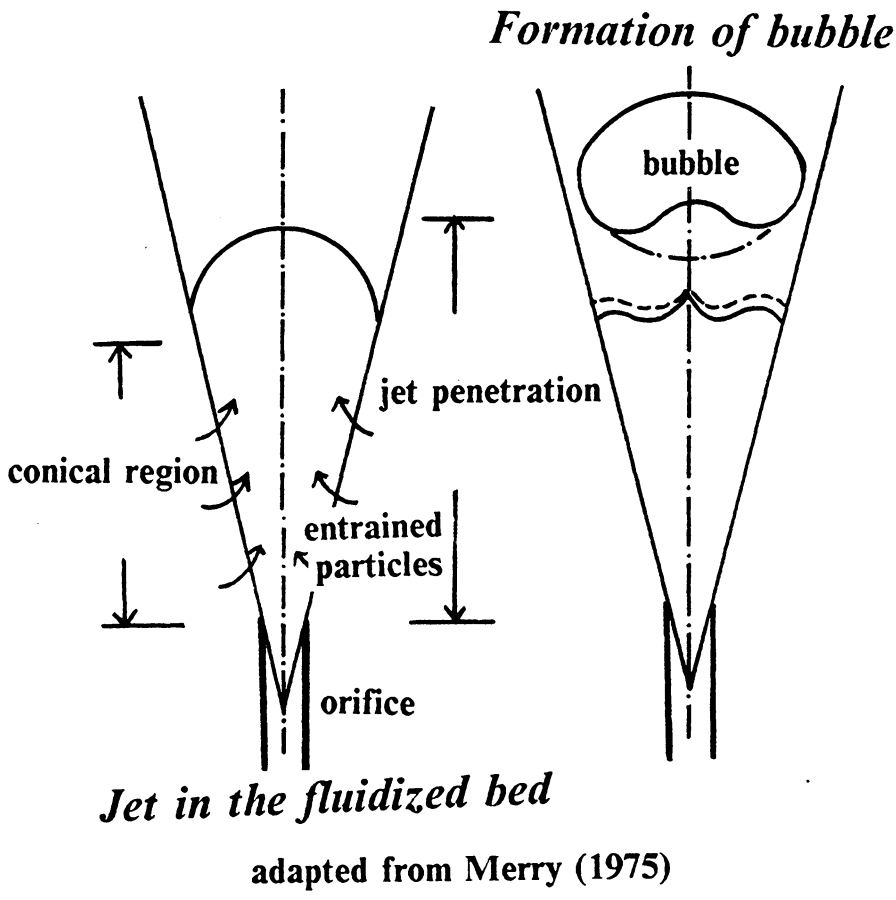

Figure 5. The vertical jet and bubble in a fluidized bed

is the maximum distance attained by the jet region, it necessarily defines the mean maximum jet height. Further, because of the pulsating nature of the jet, it is not unlikely that the actual maximum jet length varies by 20% about this mean value.

The jet phenomenon is of fundamental importance to the performance of fluidized-bed reactors. In the simplest fluidized bed, the fluidizing gas passes through the distributor holes in the form of jets; and it is important to know how far such jets will penetrate into the bed. If a high-velocity jet impinges on vessel internals, such as immersed heat-transfer tubes, it sandblasts the internals, eroding them with possibilities for disastrous results. For a bed in which a chemical reaction is occurring, much of the chemical conversion may occur in the jet region near the distributor plate, especially when the reaction is fast. For shallow beds with small static bed heights, the jet region may often occupy a significant portion of the bed height. This makes the jet penetration a key factor in controlling heat transfer and solid mixing characteristics of shallow fluidized beds.

Investigations of jet penetration

Bakker and Heertjets (1960) studied the porosity distribution in a fluidized bed. Their results suggested the appearance of three zones in a fluidized bed:

1. a zone directly above the distributor, called the sieve-effect zone, in which the porosity decreased with the bed height;

2. a zone of approximately constant porosity, extending to the static height of the bed; and

3. a zone with increasing porosity, above the static bed height.

Although the focus of this previous study was not on the sieve-effect zone, some trends could be observed from the reported data:

1. the voidage increased with increasing superficial air velocity;

2. the height of the sieve-effect zone was affected by the type of distributor plate used and the weight of the bed;

3. for small bed weights, the sieve-effect zone occupied the entire height of the bed, and the zone with constant voidage disappeared.

This work verified the existence of the jet region and demonstrated implicitly its importance in shallow beds.

Basov et al. (1969) investigated the structure of a nonuniform fluidized bed by using a radioscope. They found that formation and development of jets in a fluidized bed was of a pulsating nature, and that the frequency of the pulsation did not depend on the sizes of particles in the bed. Six distributors with different open areas and hole diameters were used to study the effect of distributor design on the jet region. Their conclusions can be summarized as follows:

1. Three different zones were observed within the bed, which is consistent with the results from Bakker and Heertjets (1960), and the voidage increased with increasing fluidizing gas velocity.

2. The jet zone near the distributor plate was characterized by a sharp variation in porosity; however, instead of showing a constantly decreasing voidage right above the distributor, their results showed a maximum voidage at certain points above the distributor plate.

3. The height of the jet zone depended on the distributor design and the fluidizing gas velocity, but not on the overall height of the fluidized bed.

4. For distributors with the same open area fraction and under the same gas velocity, those with the smallest hole size showed a rather smooth variation of porosity and a relatively

low extent of gas pulsation. In the jet zone, the distributor with the largest hole size showed a sharp change in porosity and a higher degree of gas pulsation.

Behie et al. (1970) studied the momentum dissipation of a jet in a fluidized bed. The jet was formed by a nozzle in the center of the distributor plate, and auxiliary air was used to fluidize a bed of FCC powder. Six nozzles with different sizes were studied, and gas velocities through the nozzles ranged from 30.5 to 91.5 m/s. The momentum flux in the center of the bed was measured along the axis of the bed by a pitot tube. A typical curve of momentum flux versus the distance above the nozzle showed a sharp decrease of the momentum in the region near the plate. This might well be the reason for the rapid mixing observed in jet region. The momentum flux curve started to level off from a certain point above the nozzle, an effect which the authors explained as a result of residual momentum carried by gas bubbles. The results also showed that when the nozzle diameter or the nozzle velocity increased, this level-off point would move further away from the plate. Although the authors did not specifically mention the jet penetration depth, it would be reasonable to approximate the jet penetration depth by the distance of their jet-momentum level-off point from the distributor plate. The authors also suggested that by relating the extent of erosion of a given bed internal structure, such as an immersed heat-transfer tube, one could use the momentum flux curve to estimate the minimum elevation of the internal structure permissible if erosion is to be avoided.

In a later study, Behie et al. (1971) compared the jet-momentum flux measurements from a single-orifice plate to those from a multiple-orifice plate. Results with the multiple-orifice plate showed considerable scatter and revealed the effect of interference between multiple jets on jet penetration. This observation clearly suggests that one should be careful in applying an experimental correlation for jet penetration to a system different from that in which the data for the correlation were obtained.

Merry (1975) studied the vertical jet penetration in a two-dimensional water fluidized bed. Lead shot with density of $11700 \frac{Kg}{m^3}$ was used as the fluidized medium so that aggregative

fluidization could be simulated. The bed was 300-mm wide and 12-mm thick with a single central vertical jet nozzle 19-mm in width. On either side of the nozzle, the bed was incipiently fluidized with a water supply separate from the jet water supply. A theoretical analysis of jet penetration depth based on a three-dimensional system was given. The resulting correlation suggested jet penetration to be independent of the viscosity of the fluidizing medium. The authors also compared their correlation with the reported data for a number of two- and three-dimensional beds, and concluded that the difference in jet penetrations between two- and three-dimensional beds was not significant. For detailed discussion of the correlations see Chapter 5.

Wen et al. (1982) developed a new optical probe to measure the jet penetration in a three-dimensional bed. They suggested that jets would exist only when there were some dead zones (defluidized regimes) on the distributor plate, and these dead zones would diminish with increasing fluidization velocity. Therefore, above a certain gas velocity, the dead zones would disappear, the jets would no longer exist, and bubbles would form directly above the orifices of a distributor plate. Based on their experimental results, the authors also suggested that the bed geometry had a significant effect on the jet height and recommended that results obtained from two-dimensional or semicircular beds should not be extrapolated to three-dimensional beds. An experimental correlation for estimating the jet penetration depth was also proposed by the authors (see Chapter 5).

In summary, a number of general conclusions from the published literature on jet penetration depth can be stated as follows:

1. The jet region is characterized by fairly rapid solid mixing and a high frequency of gas pulsation through the orifice of the distributor plate. The extent of solid mixing and gas pulsation increases with increasing gas velocity. The voidage in the jet region is generally larger than that in the main body of the fluidized bed.

2. The effects of such variables as particle size, distributor design, bed geometry, particle weight, and gas properties on the jet penetration characteristics are not yet clearly un-

derstood, with many apparently conflicting observations being reported in published studies. Further, most of previous investigations were done in deep beds; and little is known about the quantitative effects of operating variables on jet penetration in shallow beds, particularly for those with bed internals such as immersed heat-transfer tubes.

3. It is doubtful whether the fluidization behavior for systems with multiple-orifice distributor plates can be predicted from experimental results obtained from systems with single-orifice distributor plates. Also, it is not always reliable to employ a two-dimensional bed to simulate the situation in a three-dimensional bed.

2.3 Heat Transfer between Particles and Immersed Surfaces in Fluidized Beds

Although the average particle-fluid heat-transfer coefficients based on the total particle surface area are not large (usually between 6 and 23 W/m^2-K), a fluidized bed is capable of exchanging heat very effectively with the fluidizing gas because the large area exposed by the particles (the surface to volume ratio can be as high as 5000 m^2/m^3). (see Juveland et al. 1966; Botterill, 1975). In practice, attainable heat-transfer coefficients between a immersed surface and fluidizing particles can reach to about 400 W/m^2-K under normal fluidizing conditions.

Many models and correlations relate bed-to-surface heat-transfer coefficients to a range of operating variables (see later sections). Unfortunately, most of the correlations are of limited applicability because they require knowledge of parameters not generally available. However, many hydrodynamic properties mentioned earlier can fulfill the requirement of those models or correlations and therefore provide us with an estimate of heat-transfer coefficients.

2.3.1 Models for the bed-surface heat transfer

Figure 6 on page 51 shows a typical curve of the bed-to-surface heat-transfer coefficient (h_f) versus superficial gas velocity (u). It can be seen that the heat-transfer coefficient increases slowly but remains relatively low if the upward gas velocity through a fixed bed is progressively increased. The heat-transfer coefficient increases dramatically after the bed is fluidized ($u \geq u_{mf}$), reaches a maximum (h_{max}) at a optimalized velocity of u_h^*, and decreases thereafter.

Many of the available models have been based on the particular behavior of the heat transfer curves and are directed to the prediction of u_h^*. Although a variety of models of the

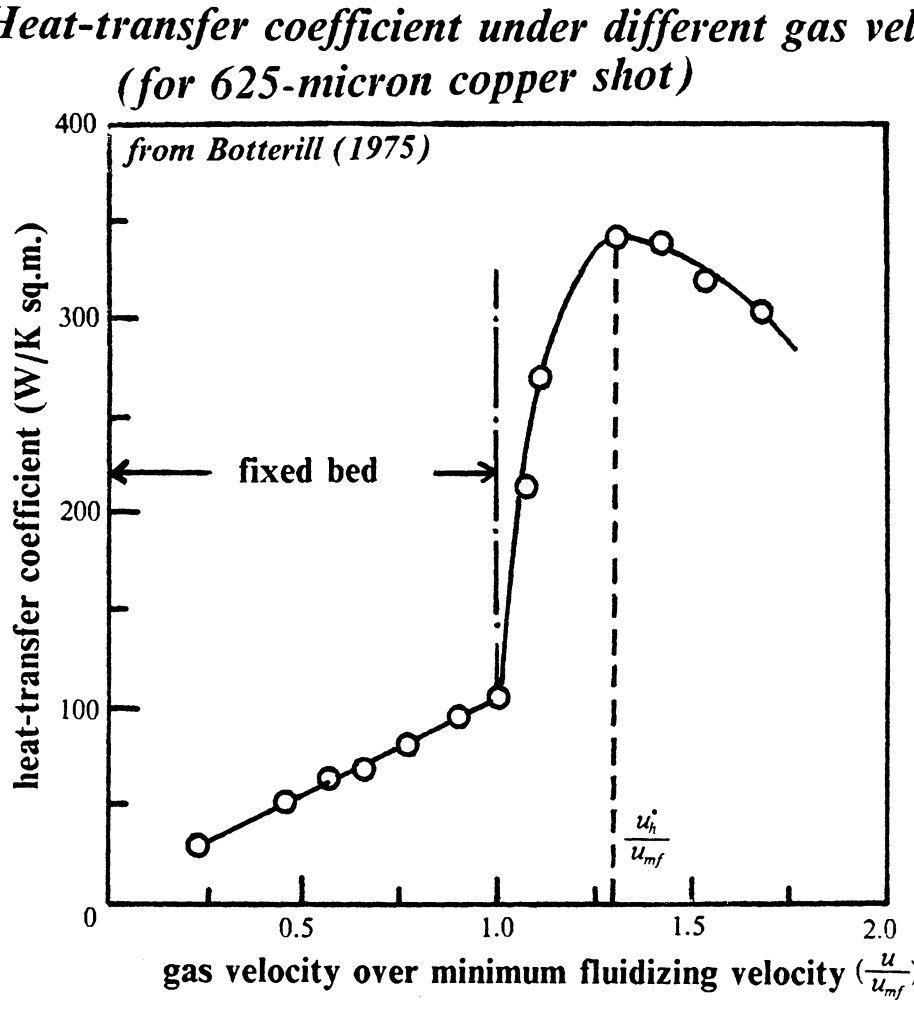

Figure 6. Heat-transfer coefficient versus gas velocity curve in a fluidized bed

mechanism of heat transfer has been suggested, none of the models is recognized as universally valid. However, each model can be used to interpret experimental results over a certain range of operation. In trying to understand the models suggested by the existing literatures, it is important to note that different mechanisms may dominate under different operating conditions, bed geometries, and surface locations (Kunii and Levenspiel, 1969). Furthermore, to our knowledge, none of the developed models has been used reliably for predicting commercial-scale heat-transfer behavior. Therefore, the assumptions and limitations of each model have to be checked carefully before it can be used.

Limiting gas-film resistance model

Dow and Jakob (1951) suggested a steady-state model for the heat transfer from a vertical tube wall to a fluidized bed. This model was based on two experimental findings:

1. The bed was isothermal apart from a narrow layer near the wall and a small region above the gas distributor.

2. The particles moved downward in the narrow region next to the wall.

They assumed the presence of a very thin gas layer adjacent to the heat-transfer surface. The heat conducted from the surface is picked up by the downflow of particles through this postulated gas layer. The particles flow down to a mixing region at the bottom of the bed, at which thermal equilibrium is attained. Using this mechanism, a correlation which fitted the experimental data with errors in the range of ± 10% was proposed --

$$\frac{h_f d_t}{k_g} = 0.5 \left(\frac{d_t}{L}\right)^{0.65} \left(\frac{d_t}{d_p}\right)^{0.17} \left(\frac{\rho_s C_s}{\rho_g C_g}\right)^{0.25} \left(\frac{d_t G}{\mu_g}\right)^{0.8} \qquad [2.16]$$

where

h_f = heat-transfer coefficient in the fluidized bed, W/m^2K .

d_t = diameter of the heat transfer tube, m.

k_g = thermal conductivity of the gas, $W/m\,K$.

L = length of the heat transfer tube, m.

d_p = averaged diameter of the particles, m.

ρ_s = density of the particles, $\frac{kg}{m^3}$.

ρ_g = density of the gas, $\frac{kg}{m^3}$.

C_s = heat capacity of the particles, $J/kg\,K$.

C_g = heat capacity of the gas, $J/kg\,K$.

G = mass flow rate of the gas, $\frac{kg}{s}$.

μ_g = viscosity of the gas, $N/m\,s$.

Unfortunately, this correlation has two drawbacks:

1. It can be applied only for particulate fluidization (in which there is no bubbling, slugging or channelling).

2. The correlation predicts that the heat-transfer coefficient will always increase with increasing gas velocity instead of reaching a maximum and then falling.

However, combining the above correlation with the traditional film theories for heat and mass transfer, the heat-transfer coefficient can be given by --

$$h_f \propto \frac{1}{R_g} = \frac{k_g}{\delta_f} \qquad [2.17]$$

where

R_g = thermal resistance in the film, $m\,K/W$.

δ_f = thickness of the gas film, m.

The decrease of the film thickness caused by the particle motion near the surface can explain the higher heat-transfer coefficients in fluidized beds than anything that would be expected in an empty vessel (see Baeyerns and Goosens, 1973).

Levenspiel and Walton (1954) assumed the existence of a laminar boundary layer similar to that present in a single-phase flow in a tube. They proposed a scouring model (see Figure 7 on page 55) by suggesting that the boundary layer was broken and renewed whenever solid particles impinge upon it. As shown in Figure 7 on page 55, the distance between successive layers is --

$$d_L = \frac{\pi d_p}{6(1 - \varepsilon_f)} \qquad [2.18]$$

where

d_L = distance between successive layers, *m*.

d_p = diameter of the particle, *m*.

ε_f = voidage of the fluidized bed, dimensionless.

The average thickness of the gas film was then determined by the boundary theory and was used to calculated the heat-transfer coefficient.

Wasan and Ahluwalia (1969) extended the model proposed by Levenspiel and Walton (1954) to include the effect of the contact between the fresh packets of fluid and the surface of the boundary film. By assuming that the heat-transfer coefficient is controlled by film thickness, thermal conductivity of the fluid, and unsteady-state conduction of the edge of the film, they proposed two correlations: one for laminar flow and the other for turbulent flow. However, there were large discrepancies between experimental and predicted values.

Van Heerden et al. (1953) suggested that the convective heat transfer between the wall and particles were dominated by effects of moving particles. Wicke and Fetting (1954) adapted this idea and developed a model which suggests that heat from the wall is first transferred by conduction through a thin gas film. The heat is then picked up by solids moving near the surface before it is passed to the core of the bed through particle mixing. Wicke and Fetting

The gas-film model

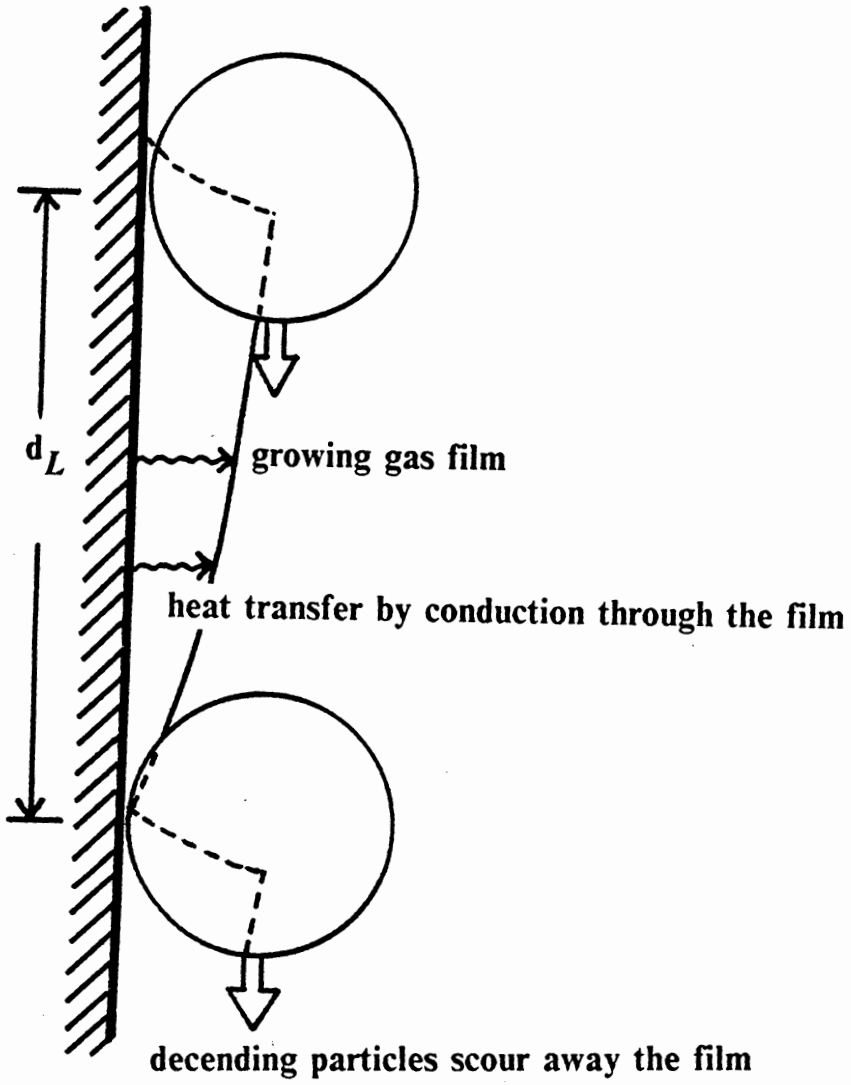

Figure 7. The gas film model: Adapted from Levenspiel and Walton (1954)

derived an equation based on their model and demonstrated satisfactory agreement between predicted and experimental values. Unfortunately, a lot of variables such as thickness of the gas film, thickness of solid layer, and solid superficial velocity have to be determined before their equation can be applied. These variables are difficult to obtain either experimentally or theoretically.

Model of penetrating packets of emulsion

Mickley and Fairbanks (1955) proposed this model by postulating that unsteady-state heat transfer occurs when the packets of emulsion (mixture of gas and solids) come into contact with the surface. The homogeneous packets emulsion are replaced by fresh emulsion from the bulk of the bed after being swept away by the upward motion of bubbles. Figure 8 on page 57 illustrates the features of this model.

Considering that a packet of particles from the bed at temperature T_b comes into contact with a flat surface of temperature T_s for a period of t, the rate of heat flow into the packet (q_i) is --

$$q_i = A_s (T_s - T_b) \sqrt{\frac{k_e \rho_e C_e}{\pi t}} \qquad [2.19]$$

where

A_s = area of the heat transfer surface, m^2.

k_e = thermal conductivity of the packet, $W/m\,K$.

ρ_e = density of the packet, $\frac{kg}{m^3}$.

C_e = heat capacity of the packet, $J/kg\,K$.

The local instantaneous heat-transfer coefficient is then given by --

$$h_i = \frac{q_i}{A_s (T_s - T_b)} = \sqrt{\frac{k_e \rho_e C_e}{\pi t}} \qquad [2.20]$$

The model of packets of emulsion

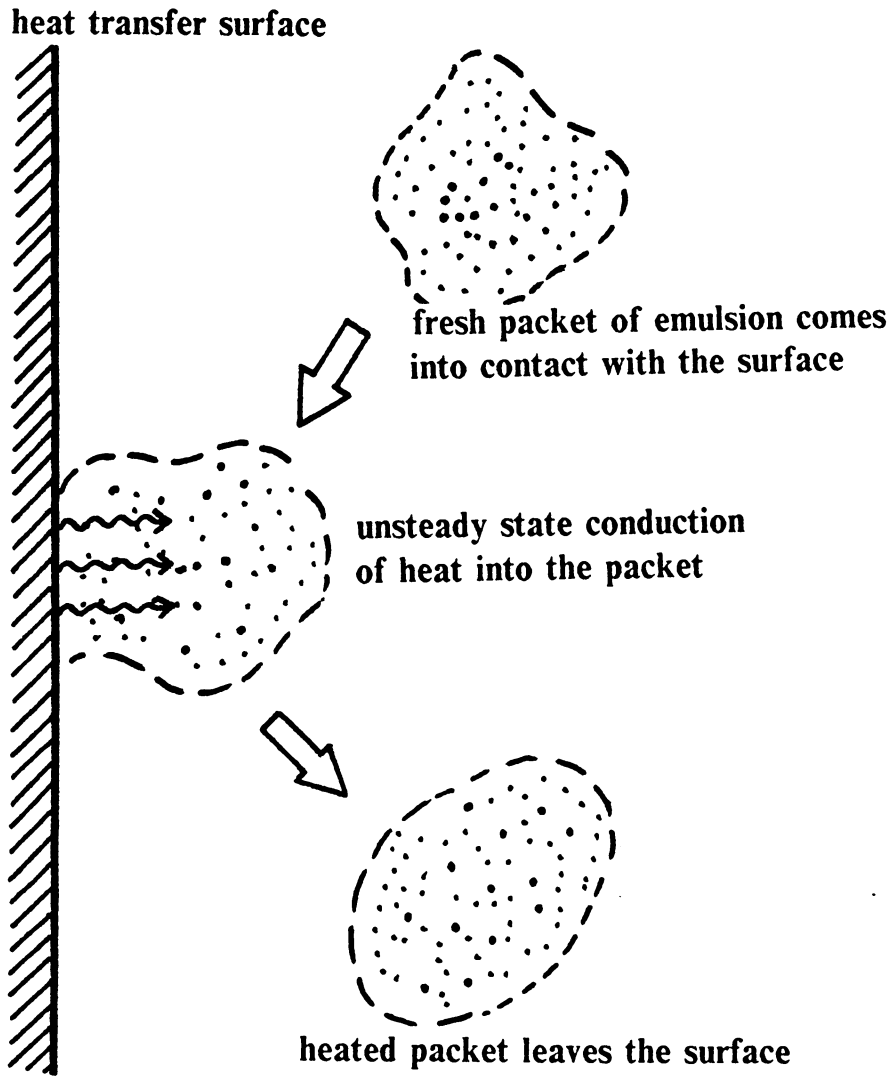

Figure 8. The model of packets of emulsion: Adapted from Mickley and Fairbanks (1955)

The local time-averaged heat-transfer coefficient, h_L, should reflect the variation of h_i as well as the contact time from one packet to another:

$$h_L = \int_0^\infty h_i \Phi(t)dt = \sqrt{\frac{k_e \rho_e C_e}{\pi}} \int_0^\infty t^{-0.5}\Phi(t)dt \qquad [2.21]$$

where $\Phi(t)$ is the frequency of occurrence in time of packets of age between t and $t + dt$. Mickley and Fairbanks (1955) observed that experimental values of h_L were directly proportional to $K_e^{0.5}$ as predicted by their model.

In a later study, Mickley et al. (1961) designed a low heat-capacity probe to determine frequency $\Phi(t)$ and instantaneous heat-transfer coefficient h_i. They reported discrepancies between predicted and experimental values of less than ± 20%. They attributed this error to --

1. Imprecise measurement of the fraction of time that the heat transfer surface was covered by the bubbles.

2. The difficulty in estimating average packet residence time.

Two crucial factors which can affect the prediction of the packet model significantly are the residence time distribution function $\Phi(t)$ and the thermal properties of the packets (k_e, ρ_e, C_e). The former is dependent on the experimental technique being used, while the latter is determined by the assumptions being made. By using an oscilloscope to record the temperature fluctuation of a thermocouple attached upon a heating tube in a fluidized bed, Agarwal and Ziegler (1970) found that the residence time distribution could be described by a gamma function. Pzkaynak and Chen (1980) designed a capacitance probe to determine the residence time distribution. They also made some assumptions in order to evaluate the properties of the emulsion packet, and compared the experimental data with the corresponding prediction of the packet model and found good agreement (± 15%).

The emulsion packet model has formed a strong basis for further understanding of fluidized-bed heat transfer. Most of the new models are based upon the modification of this model. However, the error caused by neglecting the gas convective component of the heat transfer can become significant when very large particles are used (see Baskakov and Suprun, 1972).

Discrete particle models

Botterill and Williams (1963) developed a single particle model for solving the unsteady state heat transfer between the surface of a spherical particle and its surrounding gas phase. They suggested the appropriate forms of the Fourier heat-transfer equations for thermal conduction within the solid, in the fluid phase, and across the boundary (between solid and fluid). The equations were solved numerically for various fluid and particle properties to give the isotherms. Figure 9 on page 60 gives three of the calculated isotherms for 200-μm glass beads in static air with different contacting times. The isotherms show that the heat transfer took place in the small region near the boundary of the particle and fluid. The numerical solutions of this model can be used to predict the effects of particle size as well as thermal conductivities of fluid and particles on the heat-transfer coefficient. The model was used to predicted the heat-transfer coefficients of a stirred fluidized bed, which can be treated as a constant residence-time system, and the error between model and experiment was less than $\pm$ 3%.

In a subsequent study Botterill et al. (1967) extended the model and considered the problem of heat transfer for a "chain" of two particles penetrating from heat-transfer surface into the bed. However, the predicted values from the extended model were higher than the experimental heat-transfer coefficients. They explained this discrepancy by suggesting the displacement of particles from the surface. In the calculations, they took the distance between the particle and the heat-transfer surface to be about 10% of the particle diameter.

Unsteady state heat conduction through a 200 micron spherical copper

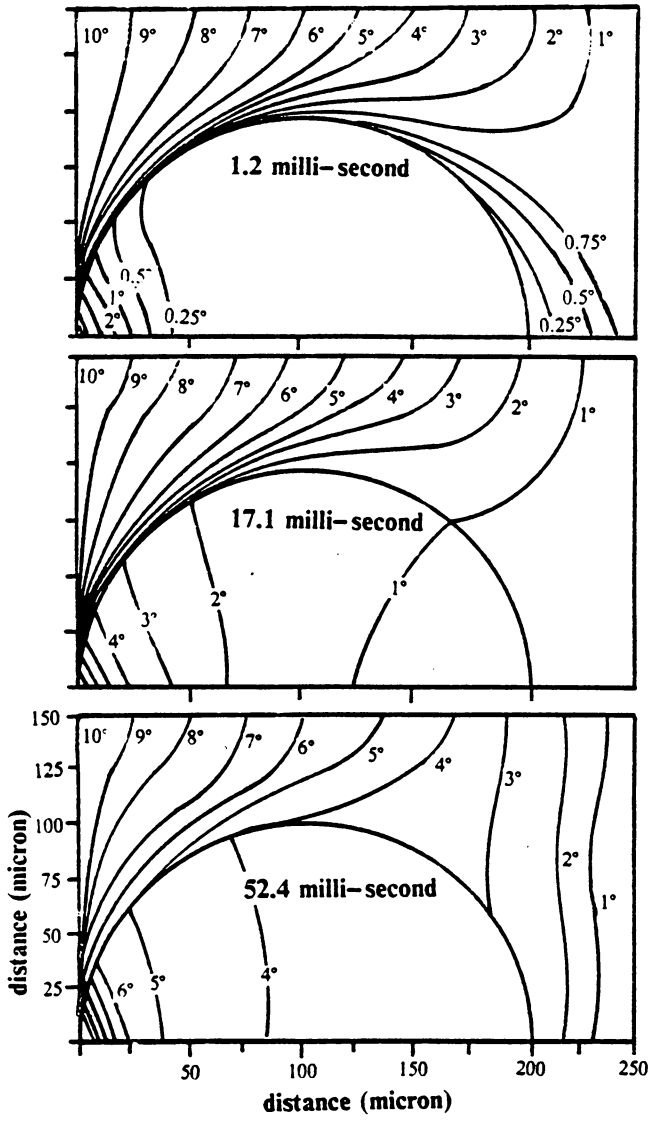

Figure 9. The isotherms near a single spherical particle: Adapted from Botterill and Williams (1963); for a 200 micron glass bead

Brusenback (1963) calculated the unsteady-state conduction from a heated surface to a chain of four particles. Gabor (1970) extended this model further by calculating the heat conduction through a particle string of indefinite length. Although this model predicted the heat-transfer coefficient quite well (with an error range of ± 20%), the numerical procedure used to solve the set of differential equations is complex. There are two additional drawbacks for this model:

1. The calculation can only be performed for spherical particles arranged in a hexagonal pattern viewed from the heated surface.

2. The gas gap between the surface and the first particle layer and the gaps among particles have to be assumed. However, even Gabor himself questioned the existence and proposed values of these gaps.

Decker and Glicksman (1981) characterized the effect of the conductive resistance between the particles and the heat-transfer surface by suggesting a thermal time constant,

$$\tau_c = \frac{1}{36}\left(\frac{\rho_s C_p d_p^2}{k_g}\right) \qquad [2.22]$$

which is an indication of the response of a particle influenced by an adjacent heated surface. Comparing the contacting time τ between a particle and the surface, they concluded that --

1. If $\tau << \tau_c$, only the first layer of particles is affected. The surface-particle resistance dominates the heat transfer.

2. If $\tau >> \tau_c$, the first layer of particles approaches the surface temperature. Therefore, the resistance among the particles dominates.

3. For $\tau \cong \tau_c$, both effects are significant.

Modified packet models

A significant drawback of the packet model is that the properties of the emulsion packet have been assumed to be the same so long as the bed is fluidized. Many investigations have concentrated on the effect of the increase of voidage as the superficial gas velocity increases. Ernst(1960) classified the heat-transfer mechanisms into two types:

1. The steady-state transfer between the surface and the particles, in which the effect of void region is taken into account.

2. The unsteady-state heat transfer during the particle residence time.

Baskakov (1964) make similar assumptions and developed an expression for the contact resistance. Gel'perin and Ainshtein (1971) developed further the model suggested by Baskakov (1964) and considered--

1. The fraction of time (t_{fb}) that the heat transfer surface was covered by gas bubbles.

2. The contact resistance between the surface and particles.

3. The gas convective component, h_{conv}.

4. The radiative component, h_{rad}.

Mathematically,

$$h_f = h_b t_{fb} + (1 - t_{fb})(h_e + h_{conv}) + h_{rad} \qquad [2.23]$$

where

h_b = the heat-transfer coefficient between bubbles and the surface, W/m^2K.

h_e = heat-transfer coefficient between emulsion phase and the surface, W/m^2K.

However, h_{rad} is important only for temperatures over 1000 K. It can also be assumed that the heat transfer between surface and gas bubbles is similar to the convective term (i.e. $h_{conv} = h_b$). This may be valid for large-particle system. Therefore, we have --

$$h_f \cong (1 - t_{fb})\, h_e + h_{conv}$$

The resistance between particles and surface can be considered as the contribution of --

1. The resistance for the unsteady-state conduction.

2. The contact resistance.

Based on these considerations, Gel'perin and Ainshtein (1971) suggested that --

$$h_f \cong \frac{1 - t_{fb}}{R_k + 0.5R_e} \qquad [2.25]$$

by proposing that the convective term is not significant for the dense phase in a fluidized bed. The contact resistance R_k was taken as $\frac{\delta_m}{k_e}$, where δ_m is the extent of the contact zone adjacent to the surface, which is on the order of $\frac{d_p}{2}$, and k_e is the effective thermal conductivity of this contact zone. After calculating the h_f values, they found that the equation predicted experimental data very well for the range of $\frac{R_k}{R_e}$ between 0.1 and 0.5.

Koppel et al. (1970) examined the packet model and suggested two mechanisms for heat transfer:

1. There was direct exchange of heat between the packet and the wall through a contact resistance as visualized by Baskakov (1967).

2. In the transient heating of a particle at the wall, the particle also gained heat by convection from the approximately stagnant fluid adjacent to the surface.

Based on these mechanisms, two complex theoretical solutions for the heat-transfer coefficients were obtained, but their comparison with experimental data was poor. This is probably because of lack of satisfactory means for estimating residence time and bulk density of the packets.

Yoshida et al. (1969) adapted the idea of film-penetration theory for gas adsorption to modify the packets of the emulsion model. They considered that a thin layer of emulsion of thickness (l_e) comes to contact with a heated surface for a period of time (t_e) before being replaced by a fresh packet of emulsion. With the assumption of random and uniform surface renewal mechanism, Yoshida et al. (1969) proposed a series of equations for predicting heat-transfer coefficients. Unfortunately, their experimental values deviated widely ($\pm$ 50%) from the prediction of those equations. This is probably due to the difficulty in estimating the thickness of the emulsion layer (l_e).

Yasutomi and Yokota (1977) extended the model proposed by Yoshida et al. (1969) by assuming that the emulsion element consists of two layers. The first layer is much the same as the one suggested by Yoshida et al. (1969) with $l_e = \frac{1}{2} d_p$. The second layer has an infinite thickness and follows the first layer. Mathematical equations had been derived by Yasutomi and Yokota (1977) for this model. They tested the prediction of the equations and found good agreement with experimental data. They also compared their model with the equations suggested by Baskakov (1964), Koppel et al. (1970), and Yoshida et al. (1969).

Groosens and Hellinckx (1973) also proposed a simple equation --

$$h_f = \frac{1.08\, \rho_s C_s d_p}{6\, t_c} \qquad [2.26]$$

by suggesting a model of unsteady-state transfer for packets of particles and gas penetrating into the boundary layer adjacent to the heat transfer surface. The physical properties of the

particles such as density, diameter, and heat capacity are all taken into account in this equation. However, the evaluation of the dimensionless residence time, t_c , has been a difficulty.

Gas-convective model

Xavier and Davidson (1978) developed a model to predict the heat-transfer coefficients for slugging beds. The assume that --

$$h_f = h_{cond} + h_{conv} \qquad [2.27]$$

For the conductive term h_{cond}, they adapted the Mickley and Fairbanks' (1955) packet model. As bubbles pass upward and stir the dense phase, the instantaneous value of h_{cond} is determined by the properties and temporary residence time of the packets.

$$(h_{cond})_i = [\frac{\rho_s(1 - \varepsilon_{mf})\, C_e K_e}{\pi\, t}]^{\frac{1}{2}} \qquad [2.28]$$

The time-averaged value over a time period of τ is --

$$h_{cond} = \frac{1}{\tau}\int_0^{\tau}(h_{cond})_i\, dt = 2\,(\frac{\rho_s(1 - \varepsilon_{mf})\, C_e K_e}{\pi\, \tau})^{0.5} \qquad [2.29]$$

However, the heat transfer surface is covered only a fraction (i.e.,$1 - f_b$) of the time by bubbles, during which there is little or no heat transfer due to thermal conduction. It is suggested that --

$$1 - f_b = 1 - \frac{\text{bubble volume}}{\text{bed volume}} = \frac{u_B}{u - u_{mf} + u_B} \qquad [2.30]$$

where u_B is the rising velocity of the bubbles. Therefore, h_{cond} can be modified to --

$$h_{cond} = 2\left[\frac{\rho_s(1-\varepsilon_{mf})\,C_e K_e}{\pi\,\tau}\right]^{0.5}\left(\frac{u_B}{u-u_{mf}+u_B}\right) \qquad [2.31]$$

In most fluidized beds, it is very difficult to define the average residence time (τ) of particle packets at a heat-transfer surface. However, Xavier and Davidson (1978) suggested that for a slugging bed --

$$\tau = \frac{L}{u-u_{mf}} \qquad [2.32]$$

where (L) is the length of the heat-transfer tube. Now the heat transfer coefficient for the conduction can be calculated as --

$$h_{cond} = 2\left[\frac{k_e\rho_s(1-\varepsilon_{mf})\,C_e(u-u_{mf})}{\pi\,L}\right]^{\frac{1}{2}}\left(\frac{u_B}{u-u_{mf}+u_B}\right) \qquad [2.33]$$

They also adapted the equation suggested by Yagi and Kunii (1960) to evaluate the thermal conductivity of the particulate phase --

$$k_e = k_e^o + 0.1\,\rho_g C_p d_p u_{mf} \qquad [2.34]$$

where

k_e^o = thermal conductivity between the packed bed and motionless fluid

also,

$$k_e^o = k_g\left(\frac{k_s}{k_g}\right)^z$$

$$z = A^* + B^*\log_{10}\left(\frac{k_s}{k_g}\right)$$

$$A^* = 0.280 - 0.757\log_{10}\varepsilon_{mf}$$

$$B^* = -0.057$$

k_s = thermal conductivity of solids.

k_g = thermal conductivity of gas.

However, these equations can be applied only for slugging beds. For other regimes in a fluidized bed, they considered a gas film of thickness δ_m sandwiched between the packets and surface. Then heat can be carried by:

1. Unsteady-state diffusion between gas layer and particle phase packets.

2. Steady-state conduction through gas film.

Based on these, they proposed a correlation --

$$h_{cond} = C_1 \left[\operatorname{erfc}\left(\frac{C_2}{u - u_{mf}}\right)^{0.5} \exp\left(\frac{C_2}{u - u_{mf}}\right) - 1 \right] \left(\frac{u - u_{mf}}{u_A}\right) + C_3 \left(\frac{u - u_{mf}}{u_A}\right) \qquad [2.35]$$

$$C_1 = \frac{\delta_m k_e C_e u_B}{k_g L}$$

$$C_2 = \frac{k_g^2 L}{\delta_m^2 k_e \rho_e C_e}$$

$$C_3 = 2\, u_B \left(\frac{k_e \rho_e C_e}{\pi L}\right)^{\frac{1}{2}}$$

$$\rho_e = \rho_s (1 - \varepsilon_{mf})$$

$$u_A = u - u_{mf} + u_B$$

$$\delta_m = \frac{d_p}{4} \quad \text{-- for horizontal surfaces}$$

$$\frac{d_p}{10} < \delta_m < \frac{d_p}{6} \quad \text{-- for vertical surfaces}$$

For the convective term, h_{conv}, Xavier and Davidson (1978) used the model of Gabor (1970) --

for flat surface:

$$h_{conv} = [\frac{4\, k_e \rho_g C_e u_{mf}}{\pi L}]^{\frac{1}{2}} \qquad [2.36]$$

for cylindrical surface:

$$h_{conv} = [\frac{4\, k_e \rho_g C_e u_{mf}}{\pi L}]^{\frac{1}{2}} + \frac{k_e}{d_t} \qquad [2.37]$$

where d_t is the diameter of the cylindrical heat-transfer tube.

According to the equations for the gas-convective model, h_{cond} dominates the overall heat-transfer coefficient h_f for fine particles, but the importance of h_{conv} increases as the particle size increases. This model also predicts the general trend of the curve of h_f versus superficial velocity (see Figure 6 on page 51). However, this model and its related correlations are limited to the region in which the two-phase theory for bubbling or slugging beds applies.

Adams and Welty (1979) developed a gas-convective model for the heat transfer between an immersed horizontal cylinder and a fluidized bed of large particles. They proposed an interstitial channel model and solved the two-dimensional boundary layer equations numerically. The prediction was proven by Catipovic et al. (1982) to be in fair agreement ($\pm$ 20%) with experimental data.

2.3.2 Measurement of heat-transfer coefficient in fluidized beds

Many of the ways for measuring the heat-transfer coefficients in the fluid dynamic research have been adapted for study of fluidized beds. Generally, those techniques can be grouped into the following four categories:

Evaporation of soaked porous material

A porous material is cut into a desired shape and soaked with a volatile solution. After being exposed in a fluidized bed for a period of time, the porous material is weighed to give the amount of volatile solution being evaporated. From thermodynamic and mass-transfer theories, we can calculate the dew point of the solution and the mass-transfer coefficient for the vapor film around the porous material. Therefore, the heat-transfer coefficient can be evaluated by comparing the mass-transfer coefficient and the rate of evaporation on surface of the porous material.

The advantage of this method is that one can omit any measurement of surface temperature of the heat-transfer surface. It also provides a cheap and easy way for quickly estimating the heat-transfer coefficient. However, the estimation of dew point and mass-transfer coefficient can be inaccurate or difficult to obtain, especially if the volatile solution is one that is rarely used. Another drawback of this method is the unsteady-state character of the evaporation process, which may increase the complexity of mass-transfer calculation. Figure 10 on page 74 gives the schematic diagram of this method.

Water/steam circulation system

As shown in Figure 11 on page 75, a system of water or steam is circulated by the support of a pump and a reservoir. A desired section of the circulating tube passes through the bed to absorb or release heat, while other sections are covered by insulating material. The heat-transfer coefficient between the outer surface of the tube and the fluidized bed can be calculated after recording the following data:

1. temperature readings before and after the heat-exchange section.

2. bed temperature.

3. flow rate of the water or condensation rate of the steam.

4. the heat-transfer coefficient in the inner side of the tube, which can be estimated from handbooks for heat-exchanger design.

Compared with other techniques, this method provides the most direct way of measuring the heat-transfer coefficient. In many instances, it is also the method closest to a real case of a heat exchanger in a fluid bed. The tube section exposed in the fluidized bed can be arranged carefully to eliminate end effects, which has been a matter of difficulty for other techniques.

There are a few drawbacks for this technique:

1. The water or steam circulation system is expensive to build. It can also be expensive to operate the system.

2. Start-up of the circulation has to be controlled carefully to eliminate any possible error caused by unsteady-state operation.

3. The heat of friction, the energy generated by the pump, and the heat lost through the insulation can all cause experimental errors.

4. The film heat-transfer coefficient of the inner side of the tube can be hard to evaluate, especially when the water/steam flow pattern in the tube is not well-understood.

Coaxial electric heater

Figure 12 on page 76 shows the basic design of this most popular way of measuring the heat-transfer coefficients in fluidized beds. A cartridge heater is placed coaxially inside a metal tube (usually copper) to provide heat creating a temperature gradient between tube surface and fluidized bed. Thermocouples are fixed in the drilled holes or grooves to measure the surface temperature of the tube. After recording the temperature difference between the tube surface and the bed (ΔT) and the power generated by the heater (Q), the heat-transfer coefficient (h_f) can be calculated by --

$$h_f = \frac{Q}{\Delta T A_t} \qquad [2.38]$$

where A_t is the surface area of the tube.

The reason for the popularity of the technique can be visualized by examining its advantages --

1. It is easy and cheap to build the heating tube.

2. The power output of the cartridge heater can be adjusted to give a desired surface temperature on the metal tube.

3. It can be modified to measure the local heat-transfer coefficient.

However, there are also some difficulties in designing and manufacturing the coaxial heat tube --

1. The thermocouples used to monitor the surface temperature are difficult to install. Usually, the drilled holes or grooves will distort the heat-transfer pattern and therefore cause errors.

2. Heat losses towards both ends of the heating tube must be prevented.

3. There shall be absolutely no air gap between the cartridge heater and the metal tube. However, the difference between the thermal expansion ratios of both heater and tube materials can cause a problem (see Abu Bakar, 1981).

Heating strips on a rod

In this technique (see Figure 13 on page 77), thermal foils with thermocouples stuck underneath are fixed on the surface of an insulating rod. Electric power is supplied to heat the thermal foils to create a temperature difference. The approach to calculating a heat-transfer coefficient is much the same as that for the coaxial heater. This method has been used quite often in recent years due to the improvement on the quality of the heating foils (e.g. they are getting thinner, cheaper, and smoother).

The following special features of the heating strips also make this method attractive --

1. The temperature on the strips can be adjusted to simulate the heat-transfer pattern on a tube with a non-uniform temperature distribution.

2. Due to its thinness, the surface temperature of the foil can be measured accurately.

3. Since the foils are separated, the heat-transfer coefficient for each foil can be calculated. By carefully adjusting the size of the foil, the local heat-transfer coefficient can be evaluated easily.

However, there are some disadvantages for this technique --

1. The heat strips are difficult to be fixed upon a rod.

2. Power output for the foils is usually low (normally less than 10 Watt).

3. Due to the vigorous, rapid fluctuation of the local heat-transfer coefficient in a fluidized bed and the low heat capacity of the strips, controlling the temperature of the foils often becomes a difficult task.

Table 7 on page 78 compares the preceding four ways to measure the heat-transfer coefficients in fluidized beds. Some published references are also listed in the table. Since each technique has it own advantages and disadvantages, careful comparison has to be made before choosing a particular way of measuring heat-transfer coefficient in a fluidized bed.

Evaporation of soaked porous material for heat-transfer measurement

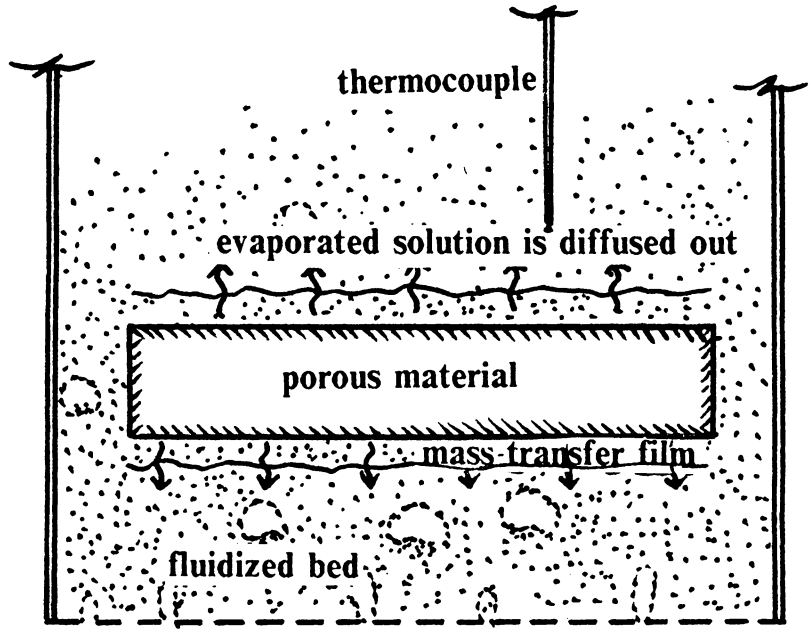

Figure 10. Using the evaporation of soaked porous material to measure the heat-transfer coefficient

Water/steam circulation system for heat-transfer measurement

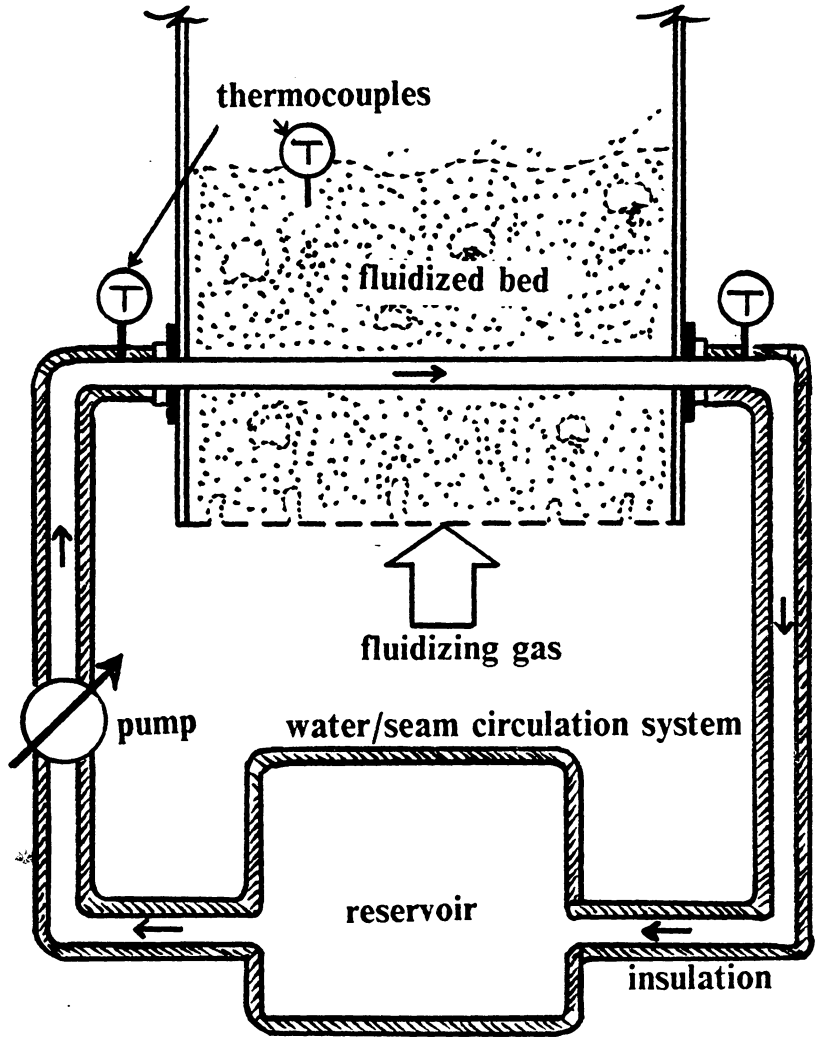

Figure 11. Using the water/steam circulation system to measure the heat-transfer coefficient

Coaxial electric heater for heat-transfer measurement

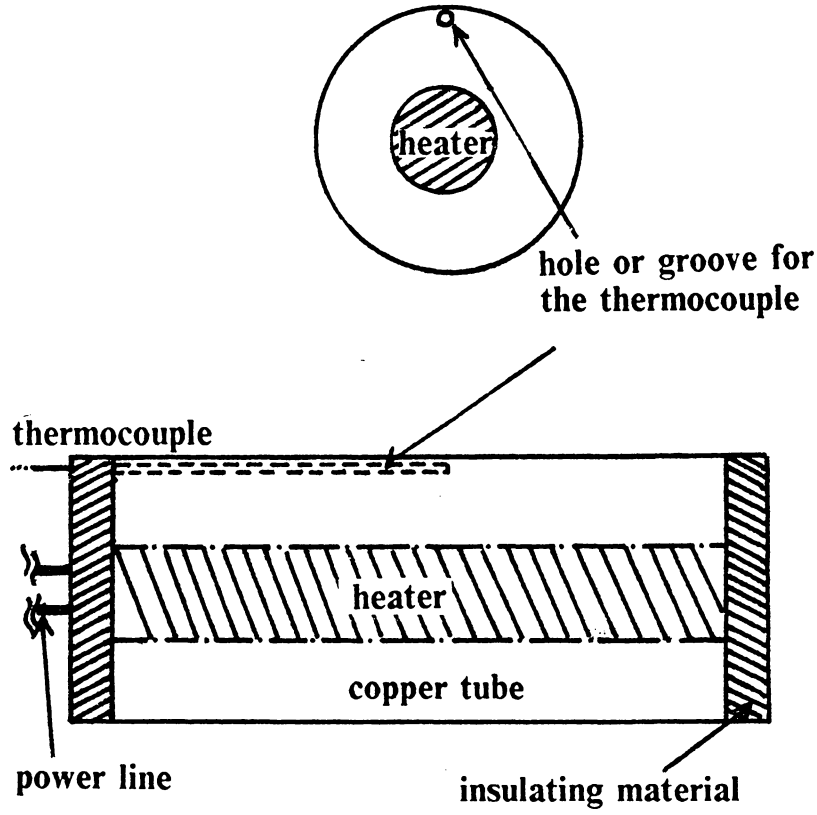

Figure 12. Using the coaxial electric heater to measure the heat-transfer coefficient

Heating strips on a rod for heat-transfer measurement

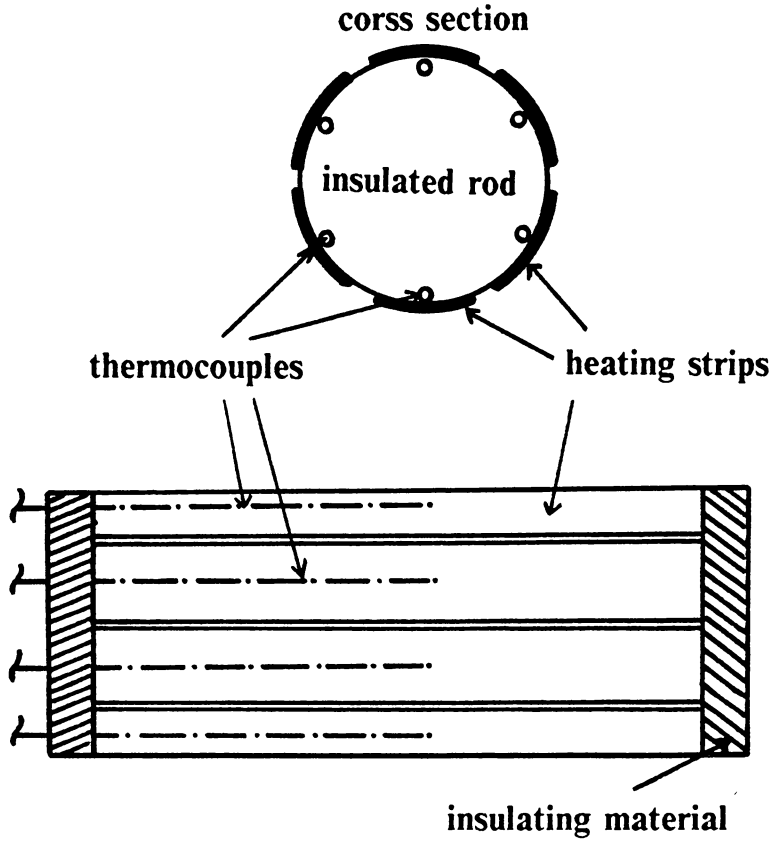

Figure 13. Using the heating strips on a rod to measure the heat-transfer coefficient

Table 7. Comparison of the most common ways to measure the heat-transfer in fluidized beds

Comparison of the most common ways to measure the heat-transfer coefficients in fluidized beds

Type of the measurement	Description	Data to be measured	Data to be evaluated	Advantages	Disadvantages
Evaporation of soaked material Ziegler et.al. (1964)	Porous material is cut into shape and soaked with the volatile solution. The porous material is allowed to be evaporated	1.bed temp. 2.conc. of the solution in the bed.	1.dew point of the solution under the bed temperature.	1.cheap. 2.easy to install 3.don't have to measure the temp. on the surface.	1.unsteady state operation. 2.difficult to evaluate the mass transfer coefficient. 3.the evaporation near the ends can cause the error.
Water/steam circulation Dow and Jakob (1951) Vakhrushev et. al. (1963) Al-Ali et. al. (1977)	System of water or steam is ciuculated A section of the tube passes through the bed to absorb or release heat	1.flow rate of water/seam. 2.temp. at up and down steam of the heat exchange 3.bed temp.	1.heat-transfer coefficient in the inner side of the transfer tube	1.close to the real application. 2.no end effect of the heat tube. 3.temp. are easy to measure.	1.expensive 2.difficult to operate 3.internal film coeff. is hard to evaluate. 4.heat of friction, heat generated by the pump can cause error.
Coaxial elec. heater Chen & Withers (1978) Denloye et.al. (1978) Grewal et. al. (1979)	A catridge heater is coaxial with a metal tube. Thermocouples are fixed in the holes or grooves to measure the surface temperature	1.bed temp. 2.surface temp. 3.the power generated by the heater.	none	1.easy to build 2.can be adjusted to measure the the locak heat transfer. 3.power output can be changed.	1.thermocouples are difficult to install. 2.heat lost at the ends has to be prevented. 3.contack between the heater and tube has to be good enough.
Heating strips on a rod Mickley et.al. (1961) Gel'perin et. al. (1966) Chandran et. (1980)	Thermal foils with thermoucouples sticked underneath them are fixed on the surface of an insulating rod.	1.bed temp. 2.temp. for each foil. 3.the power for each foil.	none	1.easy to be used to measure the the local heat transfer. 2.can simulate the nonuniform temp. on the tube. 3.surface temp can be measured accurately.	1.difficult to build. 2.power output is amall. 3.difficult to control the temp. of the foils.

2.3.3 Correlations for predicting heat-transfer coefficient in fluidized beds

Dozens of correlations have been proposed for predicting heat-transfer coefficients in fluidized beds. This unsatisfying situation arises simply as a result of the difficulty in attempting to create a universal model applicable to a wide range of fluidization conditions that are encountered: e.g., for coarse and fine particles; for bubbling, slugging, turbulent, and fast fluidization regimes. Grewal and Saxena (1983) summarized some of the more popular equations and compare calculated heat-transfer coefficients with experimental values. Most of the correlations that they considered give an error range of less than ± 50%. Many correlations proposed in recent years can give better predictions, in the range of ± 25% (e.g. see: Aerojet Energy Conversion Co., 1980; Xavier and Davidson, 1981; Martin, 1982).

Usually, the constants in most of the correlations are questionable due to the difficulty in collecting sufficient experimental data to verify the proposed equations. Therefore, it is suggested that experimental parameters used to derive a correlation must be checked and compared carefully before an attempt is made to use the correlation. A brief review on the proposed correlations will help us understanding the importance of some of the experimental parameters as well as the physical meaning of some dimensionless groups.

In one of the earliest studies on heat transfer in fluidized beds, Vreedenberg (1951, 1958) measured heat-transfer coefficients between a cool tube and a bed fluidized by hot air. Cracking catalyst and sand with particle diameter ranged from 63.5 μm to 316 μm were used as fluidized particles, and the static bed height was kept at 1.2 meters. After operating the bed under different air flow rates and various temperatures, he found that:

1. Heat-transfer coefficient increased when the air flow rate or bed temperature increased.

2. Heat-transfer coefficient increased when the particle size or tube diameter increased.

Based on experimental data, Vreedenburg proposed the following correlation --

$$(1) \quad Nu_t = 0.66\, Pr^{0.3} \left[Re_h \left(\frac{\rho_s}{\rho_g}\right) \left(\frac{1 - \varepsilon_f}{\varepsilon_f}\right)\right]^{0.44} \qquad [2.39]$$

for $Re_h < 2050$

$$(2) \quad Nu_t = 420\, Pr^{0.3} \left[Re_h \left(\frac{\rho_s}{\rho_g}\right) \left(\frac{\mu_f^2}{d_p^3} \rho_s^2 g\right)\right]^{0.3} \qquad [2.40]$$

for $Re_h > 2550$

For $2050 \leq Re_h \leq 2550$, a linear interpolation of the above two equations was suggested. He also proposed the use of correlation factor for the case of a tube bundle immersed in a fluidized bed. Note that the three dimensionless groups used in those equations are:

Pr = Pradtl number = $\frac{\mu_g C_g}{k_g}$.

Re_h = Reynold number based on the tube diameter.

Nu_t = Nusselt number based on the tube = $h_f \frac{d_t}{k_g}$

Zabrodsky (1966) proposed a correlation, based on the data collected by Ainshten (1959) for three different grades of sand with averaged diameters of 163, 224 and 258 μm. Zabrodski's bed had a porous distributor made of foamed fire clay. With a superficial air velocity ranging from 0.06 to 0.35 m/s and a fixed static bed height of 350-mm, he carried out about one hundred experiments. None of his data deviated from the following correlation by more than ± 10% --

$$Nu_p = 5.76\,(1 - \varepsilon_f) \left(\frac{Re_p}{\varepsilon_f}\right)^{0.34} Pr^{0.33} \left(\frac{H_t}{D_b}\right)^{0.16} \qquad [2.41]$$

where

Nu_p = the Nusselt number based on the particle diameter, dimensionless.

Re_p = the Reynold number based on the particle diameter, dimensionless.

H_t = elevation of the heat-transfer tube, m.

D_b = diameter of the fluidized bed, m.

This work was the first attempt to include the tube elevation in a correlation for heat-transfer coefficient.

Ainshtein and Gel'perin (1966) gave another correlation to predict the heat-transfer coefficient between a fluidized bed and a horizontal tube --

$$Nu_p = 4.38 \left(\frac{1 - \varepsilon_f}{\varepsilon_f}\right) \left[\frac{Re_p}{6 (1 - \varepsilon_f)}\right]^{0.32} \qquad [2.42]$$

However, the operating conditions for the data were not listed. Grewal and Saxena (1981) used data for 265-427 μm glass beads in a 305-mm by 305-mm square bed to check the above correlation. They found that the deviation was within ± 14%. Abu Bakar (1981) also suggested the correlation gave reasonably good predictions, especially when the superficial gas velocity was low.

Petrie et al. (1968) studied the heat-transfer coefficient for tube bundles in fluidized beds at relative high temperatures (400 to 770 C). They suggested the following equation --

$$Nu_t = 14 \left(\frac{G}{G_{mf}}\right)^{0.33} Pr^{0.33} \left(\frac{d_t}{d_p}\right)^{0.67} \qquad [2.43]$$

where G is the volumetric gas flow rate and G_{mf} is the value of G at the minimum fluidizing condition. The latter can be evaluated by the equation proposed by Leva (1959) --

$$G_{mf} = \frac{8.1 \times 10^{-3}}{\mu_f^{0.88}} \left[d_p^{1.85} \rho_g (\rho_s - \rho_g)\right]^{0.914} \qquad [2.44]$$

Petrie, et al. compared the correlation with their experimental data and found that the deviation was less than ± 43%. They also found that the heat-transfer coefficient for a single tube could be comparable to the data from a tube bundle if the space between tubes was greater than 45 particle diameters.

Based on the data for a variety of particles (ranged from 136 to 504 μm), Grewal and Saxena (1981) proposed the following equation for small particles --

$$Nu_p = 0.9[\frac{(.0127\ Ga)}{d_t}]^{0.21} (\frac{C_s}{C_g})^{45.5Ga^{-0.7}} \quad [2.45]$$

for $300 \leq Ga < 10{,}000$

where

Ga = Galieo number = $\frac{d_{p3}\rho_f(\rho_s - \rho_f)g}{\mu_g^2}$

C_s = specific heat of the particles, $J/kg\,K$.

C_g = specific heat of the fluidizing gas, $J/kg\,K$.

The also extended the equation to

$$Nu_p = 0.9\,[Ga\,\frac{0.0127}{d_t}]^{0.21} (\frac{C_s}{C_g})^{0.2}$$

for $75 < Ga < 20{,}000$

$d_p < 800\mu m$

and found that the prediction was generally within ± 20% of the existing data. Grewal and Saxena (1983) generalized the correlation to the case for horizontal tube bundles --

$$Nu_p = 0.9\,[Ga\,\frac{0.0127}{d_t}]^{0.21} (\frac{C_s}{C_g})^{0.2}\,C_b \quad [2.46]$$

where C_b is a correlation factor to be experimentally determined by the pitch of tube bundles and the tube diameter. For the case of $1.75 < \frac{P_t}{d_t} < 9.0$, they suggested that --

$$C_b = 1 - 0.21\,(\frac{P_t}{d_t})^{-1.75} \quad [2.47]$$

where P_t is the pitch distance of tube bundles. They found that the correlation predicted the heat-transfer coefficient for tube bundles within an astonishingly narrow range of ± 6%.

2.3.4 Studies of heat transfer in shallow fluidized beds

The use of shallow fluidized beds for heat exchange has been suggested since they require low bed pressure, reducing power consumption for a blower. Unfortunately, only relatively few studies have been performed on heat transfer in shallow beds, and results of the several studies are often inconsistent. This is thought to be due to the strong dependency of the heat-transfer mechanism on bed geometry, distributor design, and operating conditions. Table 8 on page 84 gives a summary of representative investigations on heat transfer from shallow fluidized beds to immersed heat- transfer surfaces.

Yuditskii and Zabrodsky (1966) investigated the heat transfer from a horizontal tube to a rectangular shallow bed having a cross-section of 325 mm by 55 mm. The particles used were sand (300, 710 , 1610 μm), a synthesis polymer MSN (710 μm), and CO-conversion catalyst, while the distributor was a perforated plate with open area ratio of 9% and hole diameter of 1.65-mm. The static bed height was either 35 or 70-mm; superficial gas velocity ranged from 0.5 to 4.0 m/s. A heater was used, 15.5-mm in diameter and 65-mm in length. Results of their investigation can be summarized as follows --

1. The heat-transfer coefficient increased monotonically with increasing air velocity when the heat tube was placed close to the grid (probably in a jet region).

2. As in most deep beds, finer particles gave higher heat-transfer coefficients. However, the heat-transfer coefficients for particles with diameters of 710 μm and 1610 μm were almost the same in the jet region.

3. Static bed height did not show a significant effect on the heat-transfer coefficient.

To study the heat transfer from bare and finned tubes to shallow fluidized beds, Atkinson (1974) used three different rigs: a circular column with an internal diameter of 534 mm, and

Table 8. Summary of representative investigations on shallow fluidized-bed heat transfer

Summary of representative investigations on shallow-bed heat transfer

Authors	Bed material and particle size	Bed geometry and dimension	Static bed ht. (mm)	Gas velocity (m/s)	Heat transfer surface	Probe elevation (mm)
Atkinson (1974)	Zircon sand silica sand steel shot	circular I.D.=534-mm rectangular	25-79	0.08-1.40	horizontal bare and finned tube (O.D.=10-50cm)	13-54
Pillai (1976)	silica sand silica carbide Zircon sand	circular I.D.= 0.1 and 0.14m	20-80	up to 1.5	sphere dia.= 5,6,10,15 mm	50% of bed ht.
Andeen and Glicksman (1976)	Sand	square 609 by 609-mm	5-30	0.3-2.4	horizontal bare tube (O.D.= 14.3 mm)	2 7.2-73
Al Ali and Broughton (1977)	snad aluminum	rectangular 600 by 150-mm	28-50	0.1-1.1	horizontal bare tube (O.D.= 14.3 mm	7.2-73
Abu Bakar (1981)	charcoal	circular I.D. = 278-mm	7-130	0.1-0.8	horizontal bare tube (O.D.= 30 mm)	44-93

two rectangular beds, 102 mm by 305 mm and 127 mm by 305 mm, respectively. Zircon sand (average diameter of 138μm) was used in most of the experiments, and the superficial gas velocity ranged from 0.1 to 1.5 m/s. The static bed height varied from 25 to 79 mm and the tube elevation ranged from 13 to 54 mm. The results showed high heat-transfer coefficients (500 to 700 W/m^2-K), but different rig geometries could cause variations in heat-transfer coefficient by as much as 25%, all other conditions remaining the same.

Pillai (1976) investigated the heat transfer between an immersed sphere and a shallow bed fluidized by hot air supplied from a pre-mixed gas combustion. Bed temperatures varied from 275 to 1100 C . Three different particles (silicon sand, silica carbide and zircon sand) ranging from 212 to 787 μm were used; superficial gas velocity was varied from 0.15 to 1.5 m/s. The distributor was a ceramic plate with a thickness of 25-mm. Heat-transfer coefficient was determined by a spherical probe with a thermocouple placed in its center. Since the spherical probe has a very low Biot number ($\frac{h_r R_s}{k_s}$, where R_s and k_s were the radius and thermal conductivity of the sphere, respectively), the temperature reading of the thermocouple was essentially very close to the surface temperature needed to calculate the heat-transfer coefficient.

The results can be summarized as follows --

1. Lower heat-transfer coefficients were found in the regions adjacent to either the wall or the grid plate. Probe elevation had no effect on the heat-transfer coefficient at other locations in the shallow beds.

2. The heat-transfer coefficient decreased when the static bed height increased.

3. A correlation was suggested --

$$Nu_p = 0.365 \left(\frac{T_b}{273}\right)^{0.82} Ga^{0.22} \qquad [2.48]$$

where T_b is the bed temperature in K.

Pillai suggested that two features affecting shallow fluidized-bed heat transfer were the violent coalescence of bubbles and the agitation caused by the jet region. These observations were consistent with those made by Yuditskii and Zabrodsky (1966).

Andeen and Glicksman (1976) used a square (609 mm by 609 mm) rig to study the heat-transfer coefficient between a tube row and a shallow bed. Sand with particle sizes of 360, 510 and 710 μm were used, while the superficial air velocity ranged from 0.2 to 2.0 m/s. The distributor was made of a 60-mesh brass wire cloth backed with one or two layers of cotton cloth. A coaxial electric heater having an aluminum tube of a 19.2-mm outside diameter and 19 thermocouples located on the surface was used to measure heat transfer. Static bed height ranged from 5 to 30-mm. Two basic observations were made --

1. With a fixed probe elevation (12.7 mm), the heat-transfer coefficient increased with increasing gas velocity to a maximum and then decreased, as in a deep bed.

2. The heat-transfer coefficient increased monotonically when 3/4 of the distributor was blocked off. The authors suggested that the production of jets by the blocking caused the gas stream to impinge directly on tubes and hence increased the heat-transfer coefficient. This is inconsistent with the observation of Yuditskii and Zabrodsky (1966).

Andeen and Glicksman (1976) compared their data with a few correlations proposed for the fluidized-bed heat transfer and found that none of them was able to give good prediction on their data. They modified the equation suggested by Vreedenberg (1958) by adding a factor to account for the voidage of the bed --

$$Nu_t = 900\,(1 - \varepsilon_f)\,[\,Re_h(\frac{\rho_s}{\rho_g})\,(\frac{\mu_g^2}{d_p^3\rho_p^2 g})]^{0.326}Pr^{0.3} \qquad [2.49]$$

The voidage of the bed was calculated by the correlation --

$$\varepsilon_f = \frac{1}{2.1}[0.4 + (\frac{200^u \mu_g}{d_p^2(\rho_s - \rho_g)\, t})^{0.33}] \qquad [2.50]$$

The deviation of experimental data from their model predictions was less than ± 5% .

Al Ali and Broughton (1977) used a rectangular rig (with dimension of 600-mm by 150-mm) having a pierced plate distributor to investigate the heat transfer from a horizontal copper tube (d_t = 14.3-mm) to a shallow fluidized bed. Sand (151, 253, 345 μm) and aluminum (1100 μm) were fluidized with a preheated air at velocities between 0.1 and 1.1 m/s. The static bed height varied from 28 to 50 mm while the probe elevation ranged from 7.2 to 73 mm. The results can be summarized as follows --

1. As long as the heat probe was fully immersed in the shallow fluidized bed, the heat-transfer coefficient was controlled by the superficial gas velocity and was almost independent of the static bed height and tube elevation.

2. The maximum value in the case of the heat-transfer coefficient versus gas velocity decreased as the static bed height was reduced. However, this was only significant for fine particles.

3. The heat-transfer coefficient would suddenly increase when the tube was place slightly above the static bed height. They attributed this phenomenon to a "cloud-zone effect."

4. The optimum operating gas velocity was suggested by --

   $0.28 \text{ m/s} < u_{opt} - u_{mf} < 0.44 \text{ m/s}$

5. The inconsistency in the literatures about the heat-transfer coefficients near the distributor (especially for shallow beds) can be attributed to bubble blanketing of the heat transfer surface in some cases.

Abu Bakar (1981) designed a sophisticated heating tube with a 277-mm length and a 30-mm outside diameter to measure heat-transfer coefficients in a shallow gas-fluidized bed. The fluidized rig was made of plexiglass with an inner diameter of 278 mm, and the gas flow rate could be increased to 0.15 m^3/sec.. Glass beads with an average diameter of 200 μm and three sizes of activated charcoal (165, 342, 480 μm) were used as the fluidizing medium. Distributors, having an open area percentage ranging from 0.64 to 4.72%, were made of 3.18-mm perforated plates with 74 μm screen placed on top of them to prevent the dumping of small particles.

Some observations can be summarized based on Abu Bakar's work --

1. Variations of heat-transfer coefficient can be attributed to the change of bed dynamics with bed height. However, the heat-transfer coefficient in the lower portion of the shallow beds always gave higher values.

2. When static bed height was 250 mm, the bed gave the highest heat-transfer coefficient. This was probably because the solid circulation rate was maximum at that bed height for this particular bed. This is in consistent with the observation of Merry and Davidson (1978), who found that the solid circulation was strongest when particles travelled up close to the walls and down in the middle of a bed having a depth of 255 mm.

3. The local heat-transfer coefficient distribution around a tube was more symmetrical for a shallow fluidized bed than for deep beds. This was explained as a possible consequence of more or less straight, upward paths of gas bubbles in shallow beds, leading to a uniformity in solid circulation.

Abu Bakar (1981) also checked his experimental data with some of the existing correlations -- i.e. Ainshtein (1959); Gel'perin et al. (1966); Vreedenberg (1958); Petrie et al. (1968); and Andeen and Glicksman (1978). He found that none of the correlations gave good agree-

ment with his data. However, by modifying the equation suggested by Andeen and Glicksman (1978), he proposed a correlation --

$$Nu_t = 1135\,(1 - \varepsilon_f)\,Pr^{0.3}\left(\frac{u\,d_t\mu_g}{d_p^3\rho_s g}\right)^{0.766}\left(\frac{h_t}{H_s}\right)^{0.145} \qquad [2.51]$$

where h_t is the elevation of the heat tube while H_s is the static bed height. The largest deviation between predicted and experimental values was about 20%. A specific feature of Abu Bakar's correlation is the presence of probe elevation (h_t). However, the existence of the ($\frac{h_t}{H_s}$) in the correlation may be questionable (see Huang, 1983).

In his thesis, Huang (1983) used three sizes of "Master Beads" (335, 630, 1260 μm), similar to solids used in the work reported here (see Section 3.1.5 in Chapter 3 for description of "Master Beads") to study heat transfer in shallow fluidized beds. The fluidized rig was a 101.6-mm circular glass column. The static bed height ranged from 10 to 40 mm and the tube elevation also varied between 10 and 40 mm. Some conclusions were suggested --

1. When the tube was in the jet region, the curve of the heat-transfer coefficient versus gas velocity showed a monotonically increasing tendency. This matched the observation of Yuditskii and Zabrodsky (1966).

2. The "cloud-zone effect" suggested by Pillai (1976) was observed. It was also found that this effect was more significant for shallower beds, smaller particles, and deeper jet penetration.

3. Away from the jet and cloud zones, both the tube elevation and the static bed height showed no significant effect on the heat-transfer coefficient.

4. The distributor design had a dominant effect on the overall behavior of shallow-bed heat transfer.

Some of Huang's data had been used for the primary evaluation of the heat-transfer study of the Master Beads.

CHAPTER 3 TYPES OF SHALLOW FLUIDIZED BEDS

3.1 Fluidized Bed System

3.1.1 Fluidized rigs

Figure 14 on page 93 shows a typical fluidized-bed system used in this work for hydrodynamic and heat-transfer studies. Although beds of different sizes have been studied, a 0.61-m (2 ft.) pyrex glass column with an inside diameter (I.D.) of 101.6 mm has been used in most experiments. A ruler with a reading range of 400 mm is attached on the outside wall of the fluidized column for convenience in measuring bed height during a fluidization experiment.

A plastic glass column having 0.61 m in length and 152.4 mm I.D. has also been used to provide data with bed size as a variable. Four rectangular columns, also with an identical height of 0.61 m, have also been employed. One dimension of those rectangular columns is

fixed at 101.6 mm, while the four widths are 38.1, 63.6, 101.6 and 152.4 mm respectively (1.5, 2.5, 4 and 6 inches). The fixed dimension (101.6 mm) has been selected to match the inside diameter of the circular rig.

3.1.2 Air flow

Air at room temperature has been used as the fluidizing medium. (Maximum available supply pressure = 35 psig.) A pressure regulator and a control valve are used to adjust the air flow for experiments. The pressure regulator (Model R550-13) and the connected air filter (Model F550-13) are manufactured by Perfecting Inc.. The fluidizing air velocity for the circular bed (101.6-mm I.D.) is measured by an orifice meter, which is calibrated by a standard rotameter. Figure 15 on page 94 gives the calibration curve for the volumetric air flow versus the pressure drop across the orifice.

For experimental rigs other than the 101.6-mm I.D. bed, the fluidizing air velocity is measured by two Schutte & Koerting Safeguard Rotameters (cat. no. 20-4200). The rotameters are calibrated by the manufacturers and have also been verified by flow meter.

3.1.3 Windbox

Figure 16 on page 95 shows the design of the windbox for the circular bed (101.6-mm I.D.). The design principle was that the pressure drop in the windbox will be smaller than that across the distributor, yet attention was paid to ensuring that the gas stream is dispersed with a reasonable degree of uniformity before it reaches and crosses the distributor plate beneath the fluidized bed. A pressure tap was located on the wall of the windbox for pressure drop measurements across the distributor.

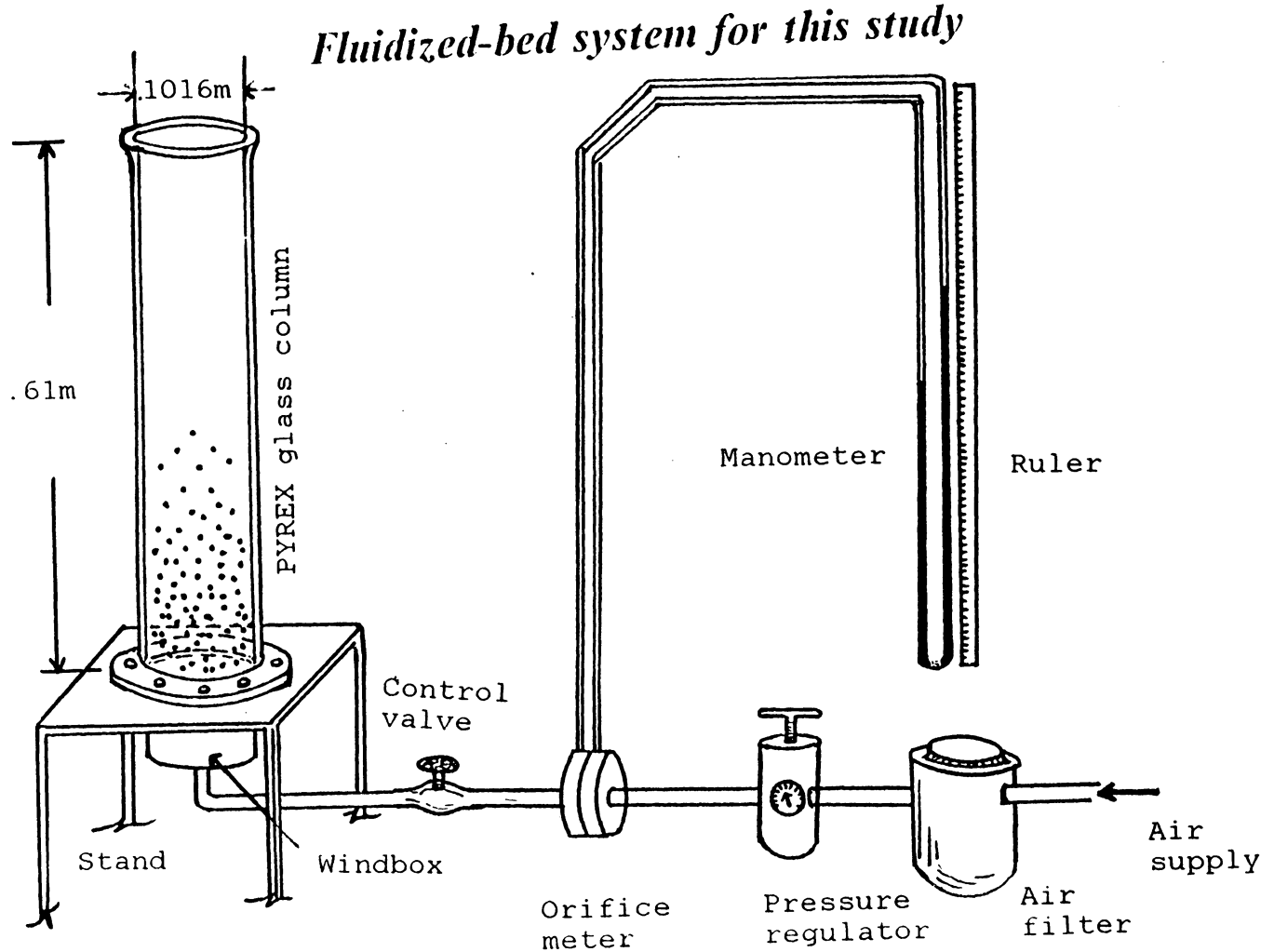

Figure 14. Fluidization system for studies of shallow fluidized beds

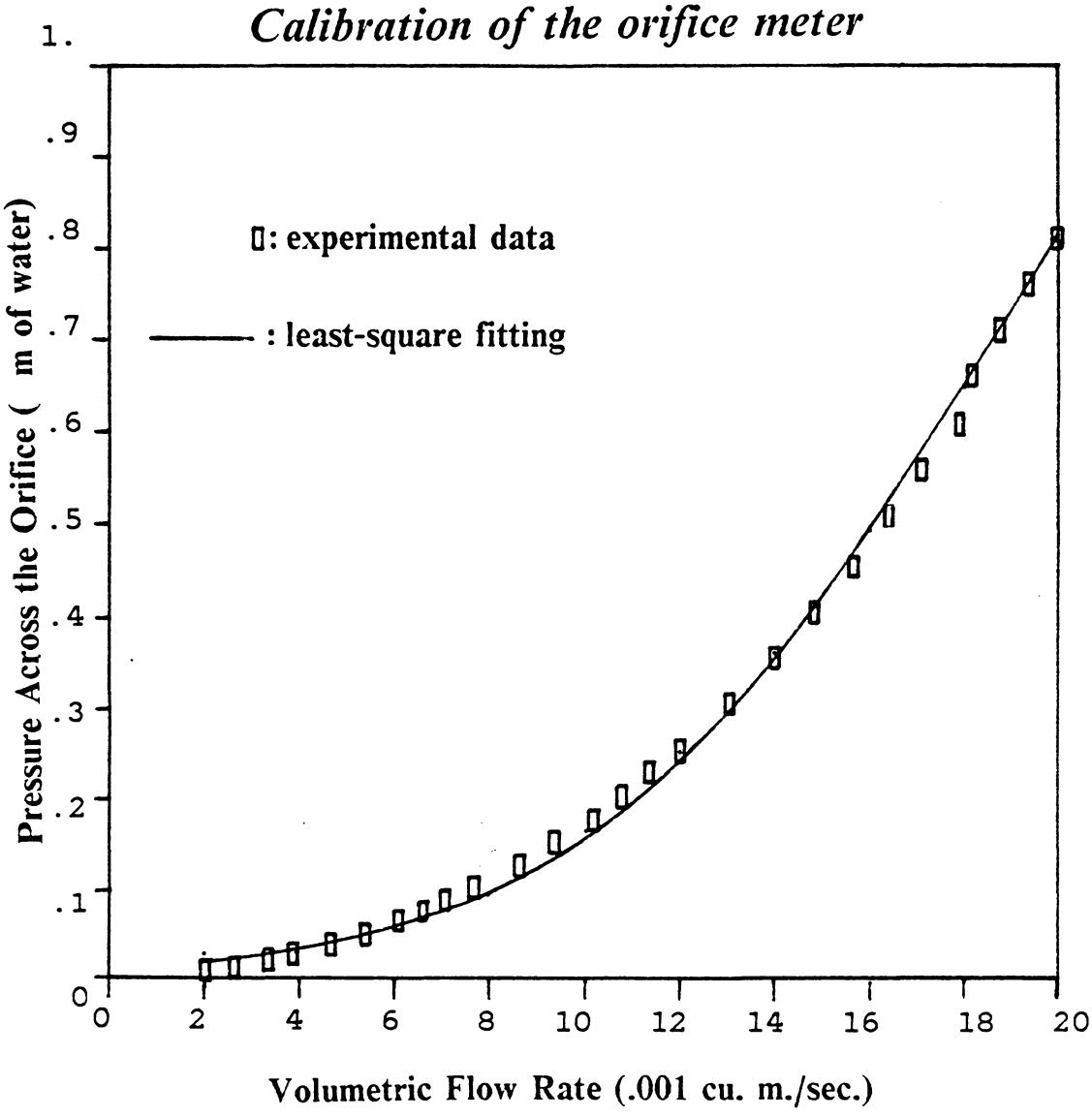

Figure 15. Calibration of the orifice meter

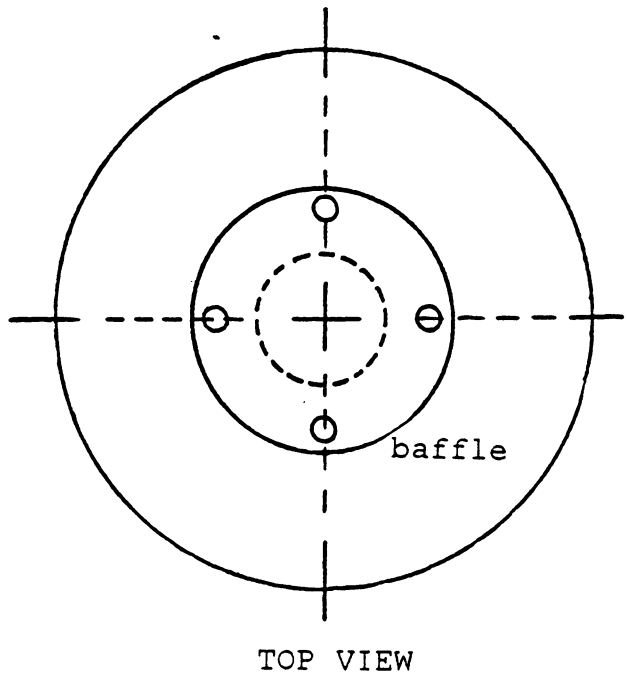

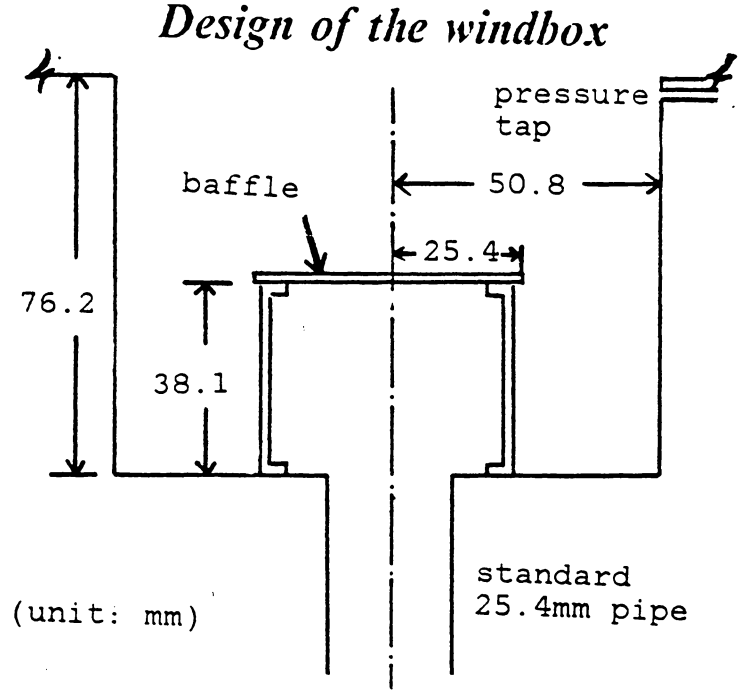

Figure 16. Design of the windbox

It is found that the distribution of the air flow in the 101.6-mm I.D. rig becomes non-uniform when the bed has a very large open-area distributor and is operated with a small inventory of particles. The windbox heights for all other beds, accordingly, has been increased to 304.8-mm (1-foot) to provide a sufficient space for the air flow to expand uniformly after it passes from the supply line and buffers. Notice that the cross-sectional areas of these latter windboxes have been tailored to match the rigs they support.

3.1.4 Distributors

Table 9 on page 97 shows the specifications of all of the gas distributors used in this study. According to their features, the distributors can be categorized into three types:

1. **Perforated plates--** Stainless-steel plates of 1.6-mm (1/16″) thickness are drilled with small holes at triangular pitch by the workshop of the Chemical Engineering Department at Virginia Tech.

2. **Laminated Plates--** Manufactured from stainless-steel by the Michigan Dynamic Division (of AMBAC Industrial Inc.). The two laminated plates comprise double layers (Cat. Dynapore 401430) and triple layers (Cat. Dynapore 407520), respectively.

3. **Screen plates--** These are "Micro-etch" stainless-steel screen from Buckbee-Mears Inc. (part nos. 8-7, 6-6, and 14-2 respectively). In comparison with the previous two types of distributors, the screen plates are thin (about 0.3 mm) and have larger percentages of open area.

In general, the perforated distributors are such that air flowing across them and into a fluidized bed will form "jet" or "voids" directly above the distributors. Our three perforated plates, with different open area ratios, have permitted us to study jet-penetration depths. The

Table 9. Specifications of distributors used in this study

Specifications for the distributors

Distributor label	Type	Open area (%)	Orifice diameter (mm)	Pitch distance (mm)
D-1	perforated	5.6	1.0	4.01
D-2	perforated	3.6	1.0	5.02
D-3	perforated	2.1	1.5	9.94
D-4*	laminated	4.2	---	---
D-5*	laminated	2.1	---	---
D-6**	screen	9.0	0.19	0.56
D-7**	screen	15.0	0.15	0.39
D-8**	screen	18.0	0.38	0.79

* Dynapore's 2 layers(401430) and 3 layers (407520) laminates.
** Micro-etch stainless-steel screen from Buckbee-Mears Inc., 6, (part no. 8.7, 6.6, and 14-2 respectively).
*** All are triangular-pitched except D-7 (which is rectangular-pitched).

screen distributors will produce small pressure drops (for their large open area ratios), and this can be an important advantage in respect to power consumption for providing fluidizing air.

3.1.5 Particles

Table 10 on page 99 lists the specifications of the particles used in this study. All particles are assigned labels for convenience of reference. Descriptions of those particles can be summarized as follows:

1. **"Master Beads"--** An inexpensive solid manufactured by the Material Division of Norton Co. for use in grinding and as a packing in deep oil and gas wells. Substantially spherical particles of this solid are non-dusting in a fluidized bed, since they have high body strength for impact and high wear resistance.

2. **Sands--** Building sands ranging from 100 to 1000 μm have been screened to provide the two categories used in this study.

3. **Carbons--** Activated carbon from the Carbon Department, Westvaco Chemical Division, -12+40 mesh (Cat. Nuchar WV-G 12-40),has been screened to provide the -20+40 mesh fraction used in this study. This size fraction of activated carbon has been selected to match the -20+40 mesh fractions of both Master Beads and sands.

4. **Glass beads--** "Technical quality glass beads" from Potters Industries Inc. can be categorized into two types: (i) type P (for P-G-1,P-G-2, and P-G-4), beads of regular glass; (ii) type H (for P-G-3) is of high lead content and with a high specific density, 4.49. All glass beads are of relatively high sphericity (above 0.8).

Table 10. Specifications of particles used in this study

Specifications of particles used in this study

label	type	mesh size	dia. (micron)	density (kg/cu.m)	porosity
P-A-1	Master bead*	-12+20	1260	3680	0.38
P-A-2	Master bead	-20+40	630	3680	0.38
P-A-3	Master bead	-40+60	335	3680	0.38
P-S-1	sand	-20+40	630	2870	0.44
P-S-2	sand	-40+50	359	2840	0.48
P-C-1	carbon**	-20+40	630	960	0.40
P-G-1	glass	-16+25	842	2500	0.38
P-G-2	glass	-20+30	705	2500	0.38
P-G-3	glass***	-30+40	484	4490	0.39
P-G-4	glass	-40+50	353	2500	0.39

* Master beads are products from Norton Co., the main constituent is bauxite (alumina).
** the activated charcoal.
*** high density glass.

3.2 Categorization of types of shallow fluidized beds

Our studies of the hydrodynamics and heat-transfer behavior of shallow fluidized beds has permitted us to classify such beds into nine different types according to physical appearance. Table 11 on page 101 lists the specifications for the nine types of beds, while Figure 17 on page 102 to Figure 25 on page 110 gives sketches of their appearance. Short descriptions of the nine types are given here:

1. **Type A bed** is similar to the familiar "deep" bubbling beds, having a bed surface that fluctuates up and down as a consequence of the escape of bubbles.

2. **Type B bed** starts from a shallower static bed than type A and exhibits a surface that sprays solids into the "free-board," the space above the bed. For type B beds, Elliott and his colleagues (Al Ali and Broughton, 1977) spoke of a "cloud phase" interposed between a denser, bubbling zone below and a "spray zone" above.

3. **Type C bed** stars from a much shallower static bed and exhibits a "dimpled" surface. The size of dimples increases with increasing static bed height. For a bed with a distributor that creates jets (e.g., a perforated plate), the position of dimples correlates with positions of the orifice holes of the distributor underneath. However, dimples still appear if this distributor is replaced by a laminated plate for which jets either do not exist or have no fixed position.

4. **Type D bed** displays swirling solids that reach higher elevations than a type-C bed, even though the amount of particles is smaller. A bed with higher gas jets (i.e., with a small open area ratio in a distributor with orifice holes) will fall into this type of behavior more easily than a bed with a laminated plate.

Table 11. Descriptions of the types of shallow fluidized beds

Types of Shallow Fluidized Beds

Type	Description	effect of jet	gas vel.	amount of particles	effect of windbox	distributor open area	effect of increasing gas velocity	increasing gas velocity will change to
A	the bed surfaces spray particles high (esp. for near the wall); this is like most deep beds.	no	high	large	no	not important	shift to type D when jet exists	no change
B	three zones --dense, cloud and spray regions can be identified 5mm < cloud zone < 20mm 10mm < spray zone < 30mm	no	medium	medium	no	not important	shift to type D when jets are high; shift to type A otherwise	type A
C	with small dimples on the bed surface; dimples are enlarged by increasing the bed height	some cases	low	small	no	small	shift to type B or type D	type B
D	the bed is swirling high with void regions in the bed.	yes	high	small	yes	small	shift to type G when amount of particle is small	type A for high vel.; B otherwise
E	a certain portion of the bed is not fluidized.	no	low	any	yes	large (usually)	shift to type F (no jet);C (with jets)	no change
F	the bed is very shallow but has a stable surface.	no	medium	small	yes	small	shift to type D for high jets; type D otherwise	no change
G	all particles are flying high but not swirling	yes	high	small	no	small	increase the swirling	type D
H	a few lines of particles are settling and swigging on the distributor; other particles are flying high.	yes	medium	small	no	small	shift to type G	type C or type F
I	the bed is "dead" except few particles are carrying high by the jets.	yes	low	small	no	small	shift to type H	type E or type F

The Shallow Fluidized Bed of Type A

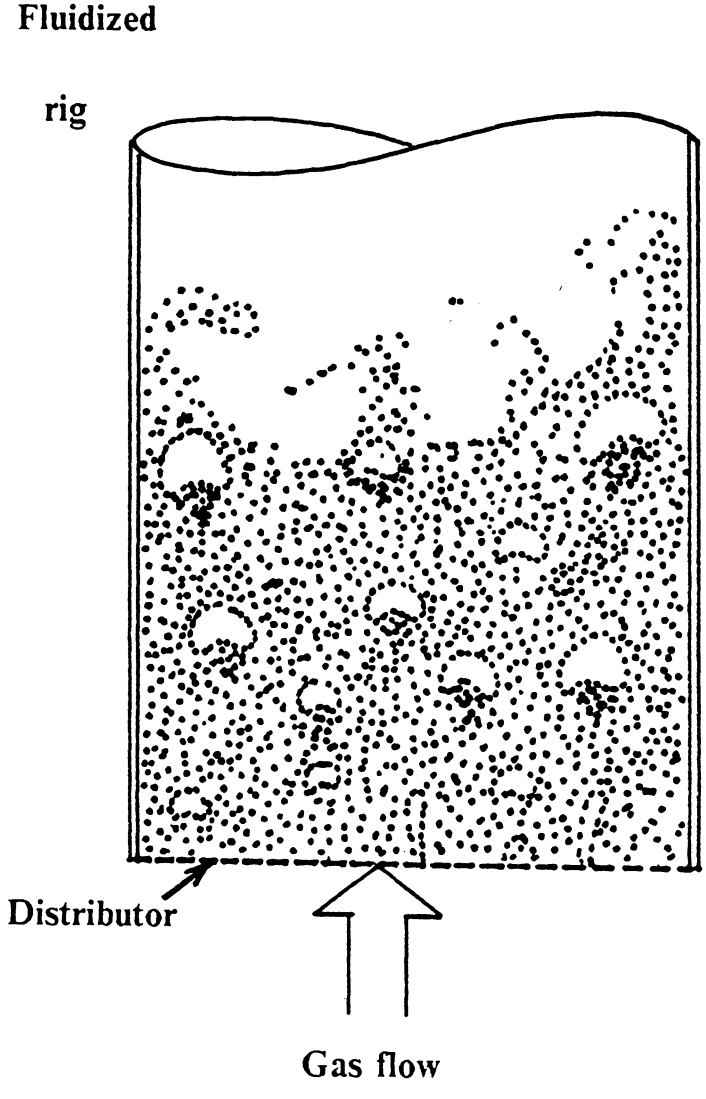

Figure 17. Illustration of a type A bed

The Shallow Fluidized Bed of Type B

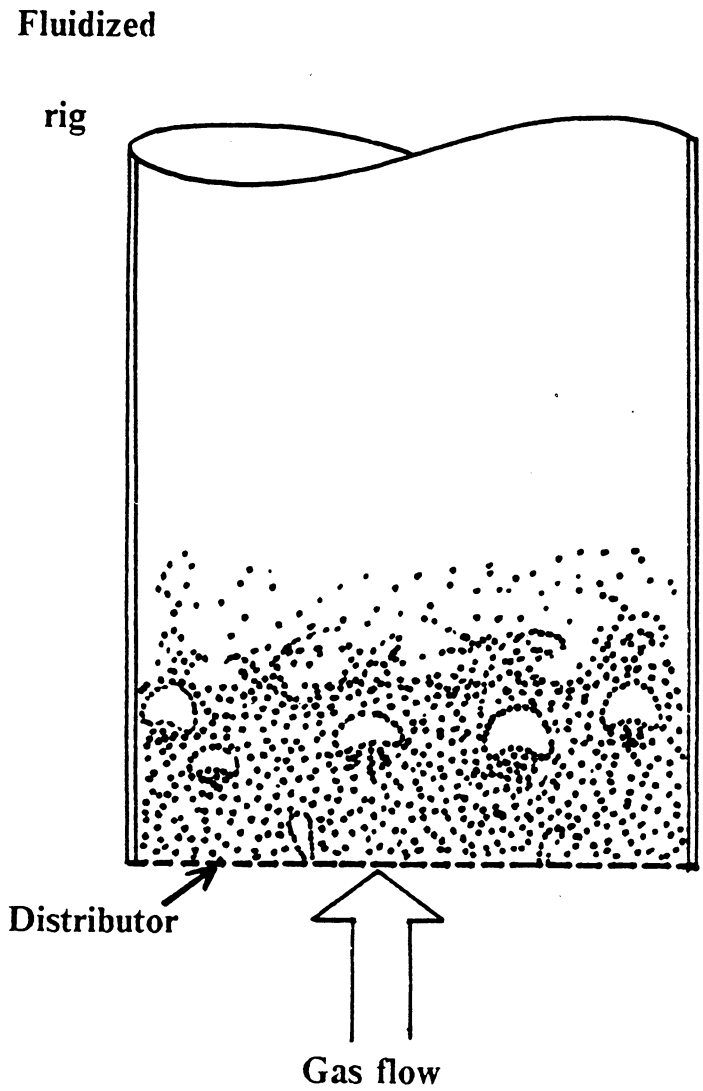

Figure 18. Illustration of a type B bed

The Shallow Fluidized Bed of Type C

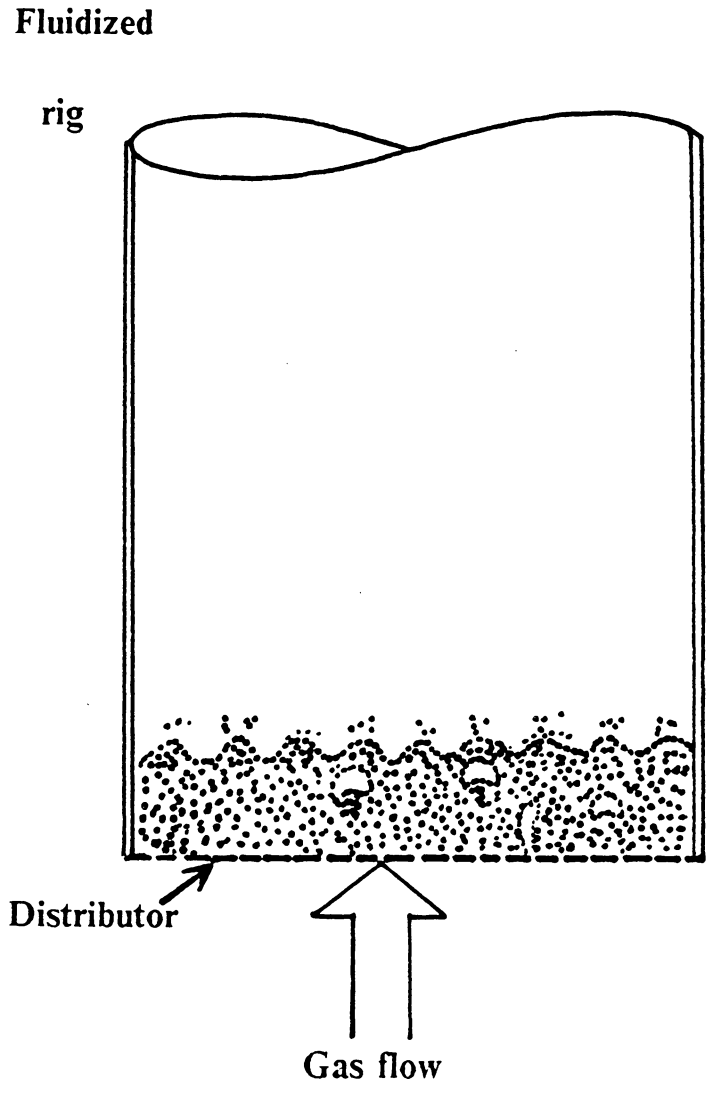

Figure 19. Illustration of a type C bed

The Shallow Fluidized Bed of Type D

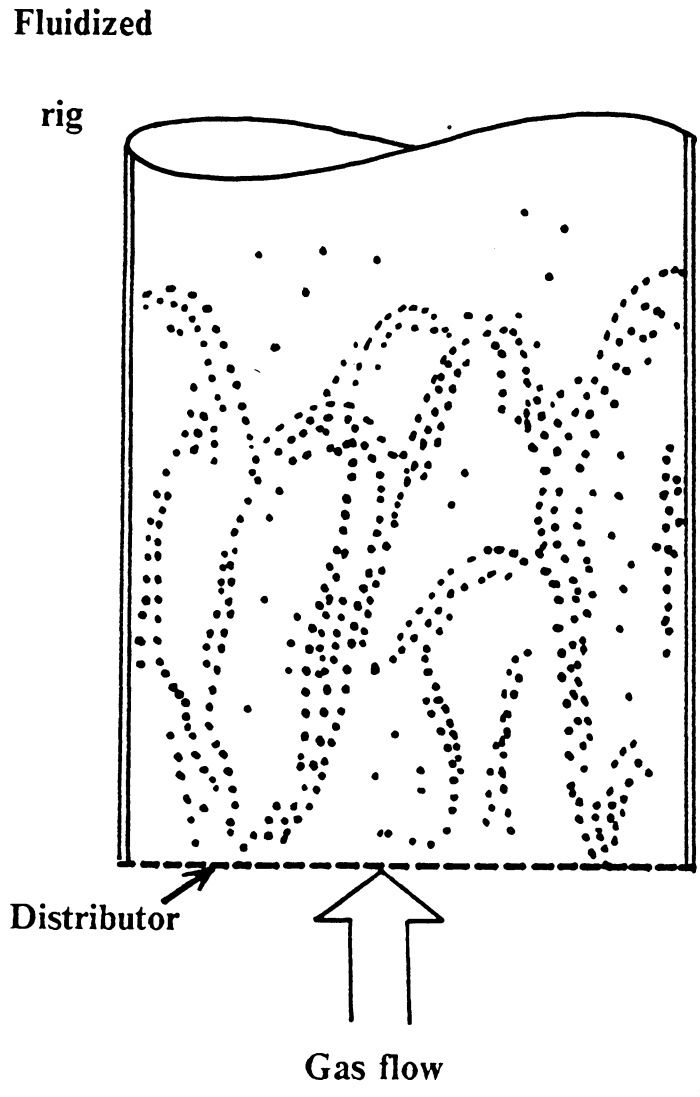

Figure 20. Illustration of a type D bed

The Shallow Fluidized Bed of Type E

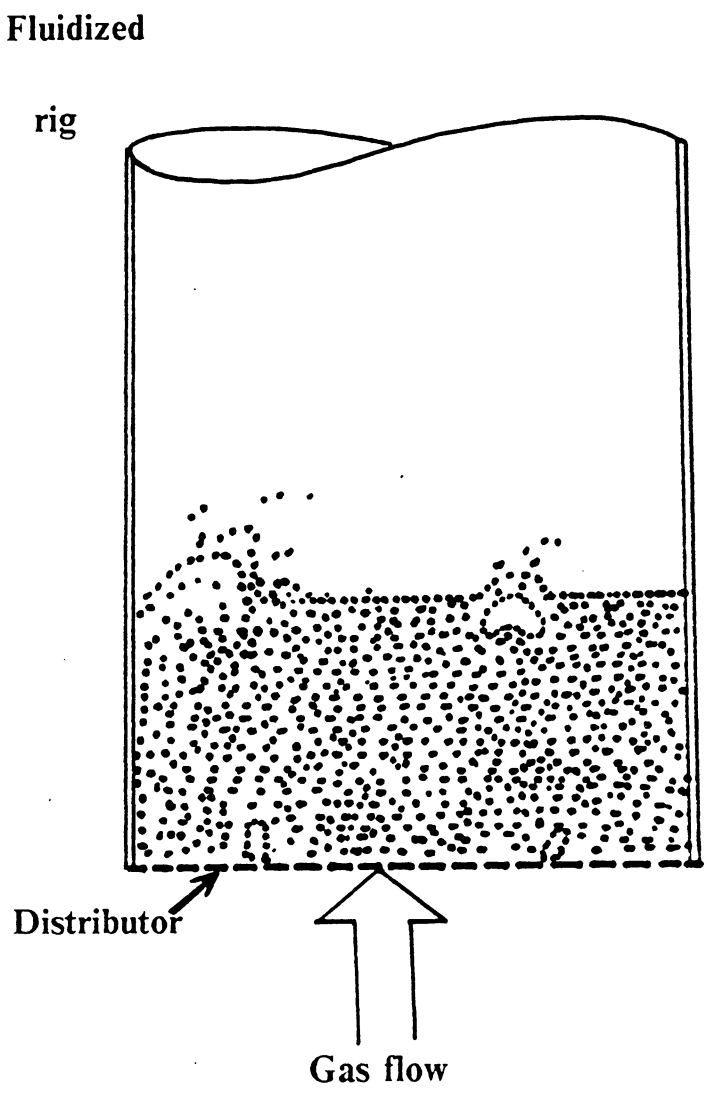

Figure 21. Illustration of a type E bed

The Shallow Fluidized Bed of Type F

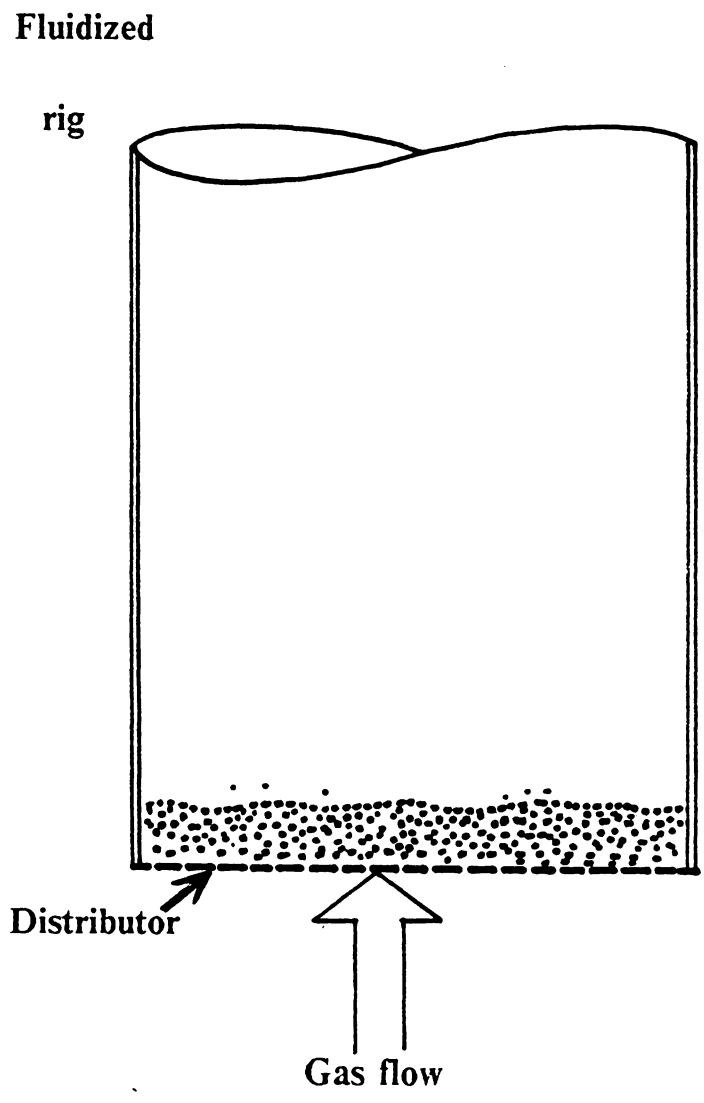

Figure 22. Illustration of a type F bed

The Shallow Fluidized Bed of Type G

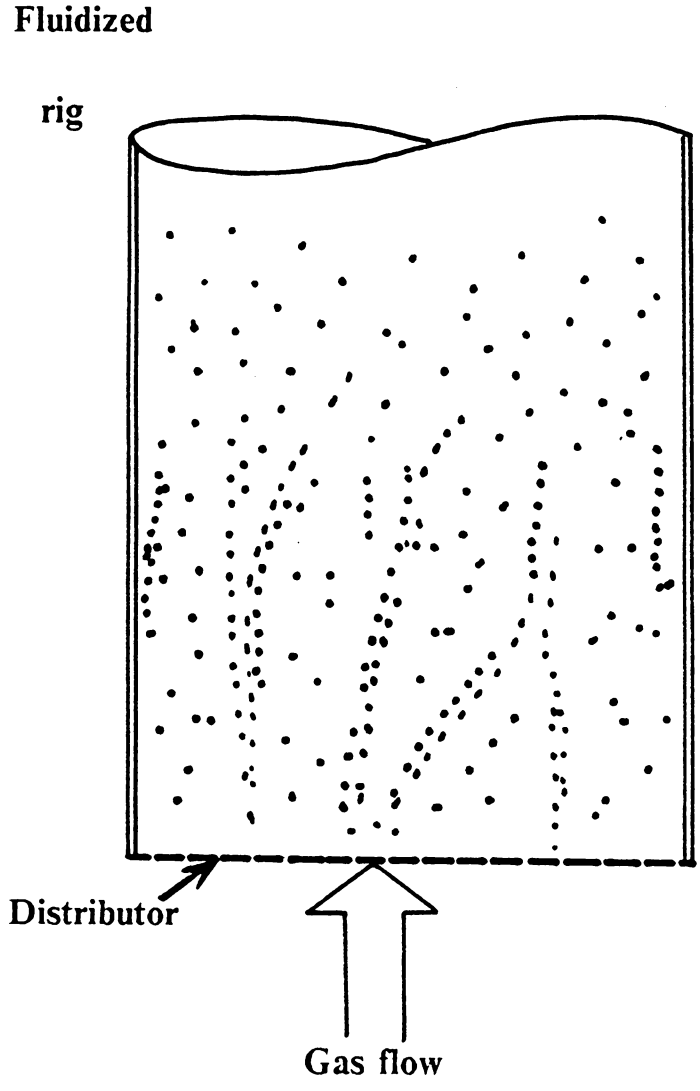

Figure 23. Illustration of a type G bed

The Shallow Fluidized Bed of Type H

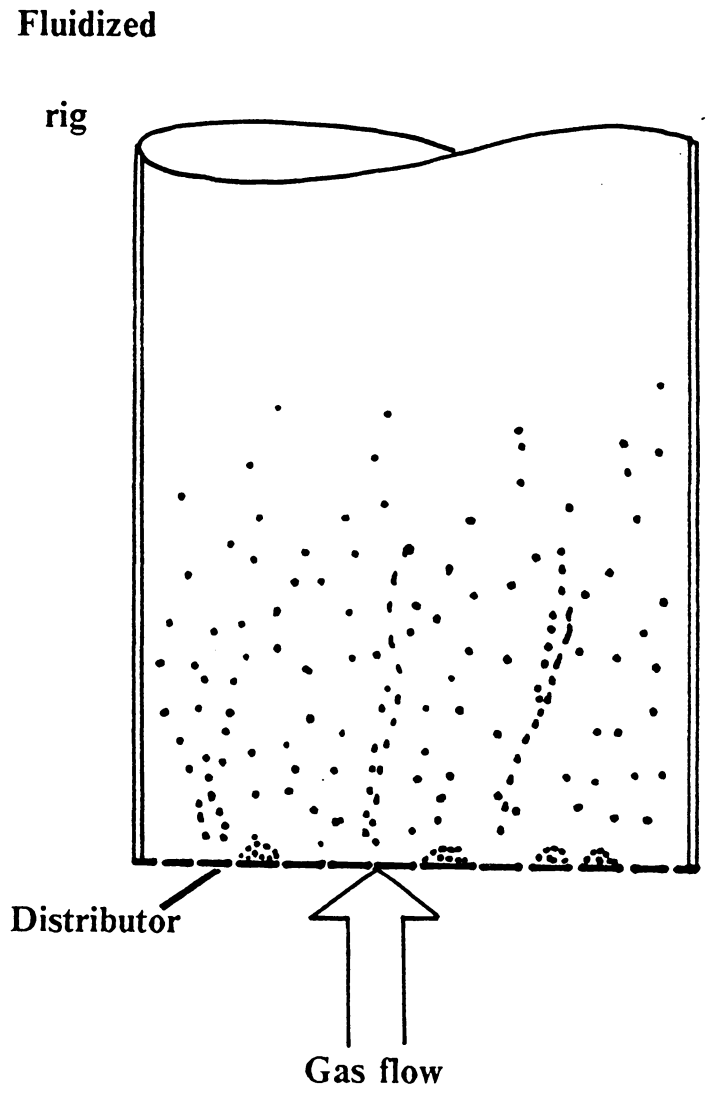

Figure 24. Illustration of a type H bed

The Shallow Fluidized Bed of Type I

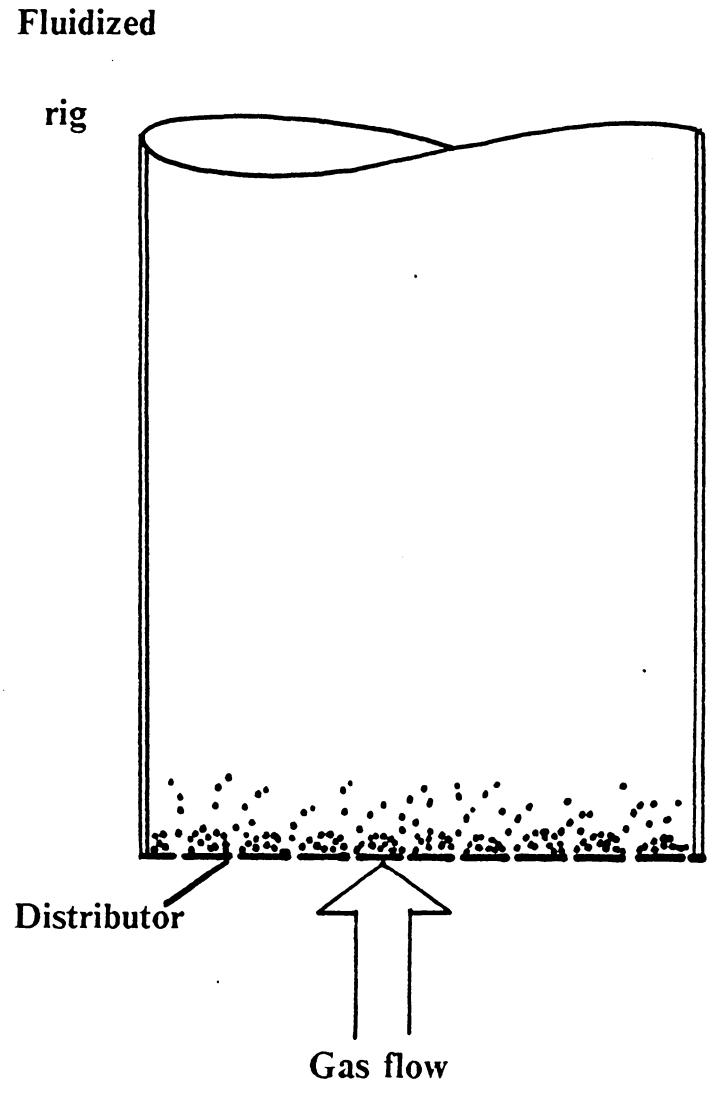

Figure 25. Illustration of a type I bed

5. **Type E bed** displays portions that are not fluidized. Risk of type E behavior is greater if the open area of the distributor is large.

6. **Type F bed** has a flatter surface than type C; the surface is "sharper," more clearly defined, an dimples are almost non-existing.

7. **Type G bed** is usually seen when the particle inventory is very small (usually, less than 20 grams in our work in the 101.6-mm circular column) and the bed is fluidized at a high gas velocity. There is no dense region, and the swirling exhibited by type D does not appear either.

8. **Type H bed** displays sinuous linear strands of particles that swirl back and forth upon the distributor. (The situation near the distributor is a bit like that one sees when light, dry, powdery snow is falling in a condition of high wind: one sees swirls of linear strands of snow particles near the ground. The fluid dynamics that cause particles to gather into swirling strands in turbulent gas flows, rich in shear, remain an intriguing but, so far as we are aware, an unstudied problem.) Some particles, not present in the strands, fly high above the distributor but display little swirl. Type H behavior appears when the particle inventory is small and a distributor of relatively large open area operates under a "medium" gas velocity.

9. **Type I bed** displays solids that are mostly "dead", but a high-velocity gas flow from the distributor carries a few particles to high elevations if the static bed height is sufficiently small.

These types of shallow fluidized beds can exhibit markedly different solid mixing and circulation patterns. We will return to this point when we discuss our particle volume-fraction distribution data. However, some points can be mentioned here that especially affect the potential utilization of several types of shallow beds:

1. In most applications of shallow fluidized beds, especially for heat transfer, only the beds in types A, B, C and D are applicable. Other types of beds are either too shallow, too dilute, or not sufficiently well-fluidized.

2. Type A can also reflect a characteristic of deep fluidized beds, viz., the rig wall will affect the bed surface when the bed diameter is small.

3. Due to high jet penetration, beds of types D and G can create erosion problems for heat-transfer tubes.

4. Beds of type F and G have relatively small inventories of particles and thus might be used as reactors for special chemical reactions (e.g. for a very fast and/or exothermic reaction).

5. Because of the existence of dead regions, the hydrodynamic properties for those beds of type E, H and I are not well-defined and not very interesting.

3.3 Phase diagrams

Figure 26 on page 114, Figure 27 on page 115, and Figure 28 on page 116 give three exemplary "phase diagrams" illustrating how "regions" of a plot of superficial gas velocity versus static bed height can fall into the respective types of shallow beds. The three figures are for three sizes of Master Beads fluidized on a common gas distributor (D-1, a perforated plate with 5.6% open area ratio) in experiments conducted in the 101.6-mm I.D. glass rig. We have found that these "Phase Diagrams" are substantially independent of the size and shape of the fluidized bed, unless a bed being used is "too narrow"; the 38.1-mm by 101.6-mm rectangular bed displayed a higher bed surface for a given inventory of particles per horizontal cross-sectional area than our other three rigs.

We have developed phase diagrams for each of the different kinds of gas distributors that we have studied. A few conclusions can be presented here:

1. At this stage of our research, we do not have experimental apparatus that will permit us to made sharply quantitative distinctions among the types of beds. What we can do with our existing equipment now is to rely on visual observation to distinguish the types and to draw sketches that illustrate their respective characteristic behaviors. However, careful scrutiny of particle volume-fraction distribution data may in the future provide better criteria for distinguishing among the nine types. We will return to this point in Chapter 6.

2. Existence of type D, G, H, I, and sometimes even F, is highly dependent upon the specific design of the gas distributor that is used. In other words, beds having jet-producing distributors will tend to display larger areas for those types in phase diagrams. However, for the same kind of particles, the phase diagram is fairly well-defined for beds with laminated and screen distributors that do not produce jets.

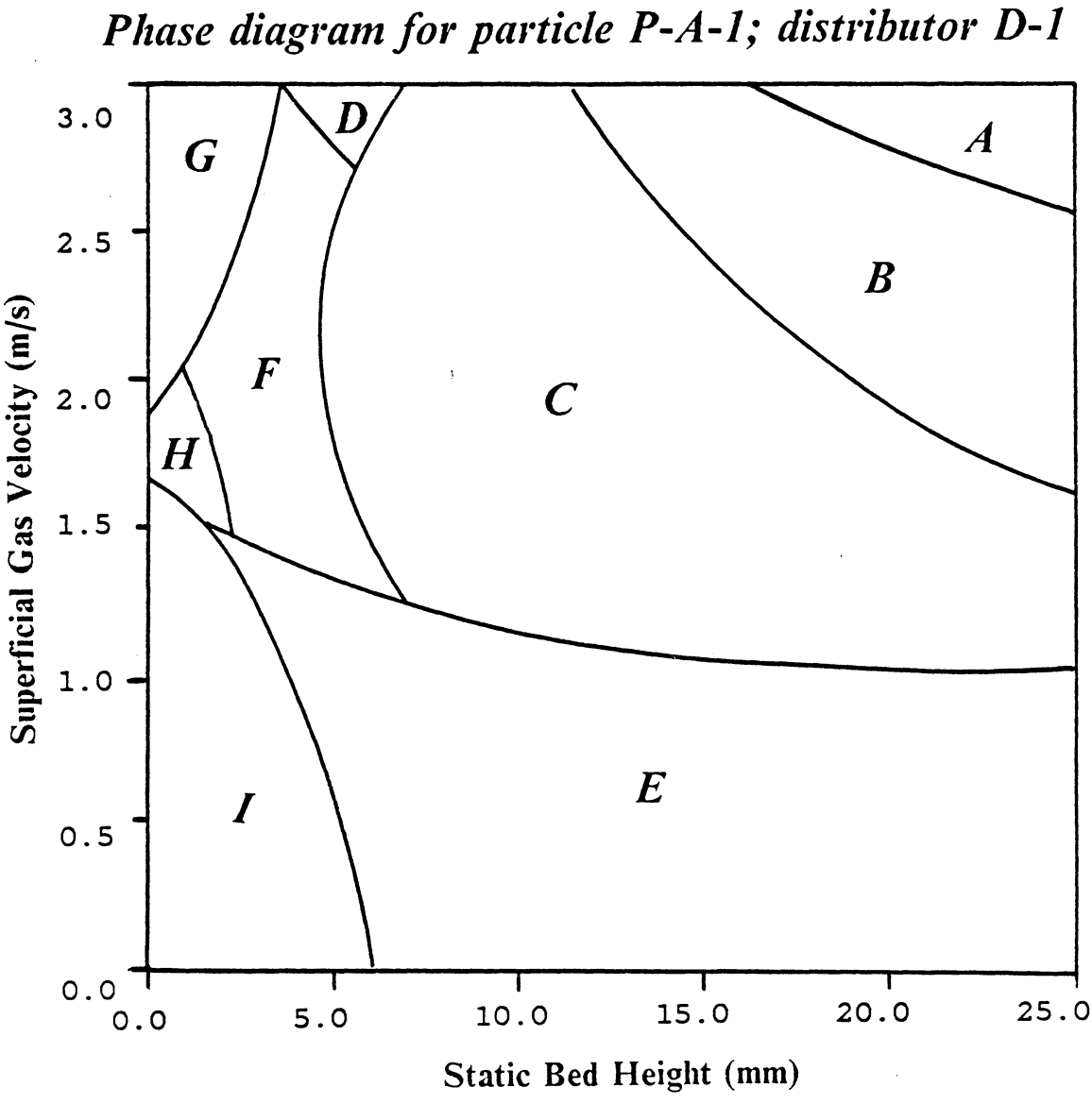

Figure 26. Phase Diagram for particle P-A-1 and distributor D-1: (1260-micron Master Beads in the bed having 5.6% open area distributor)

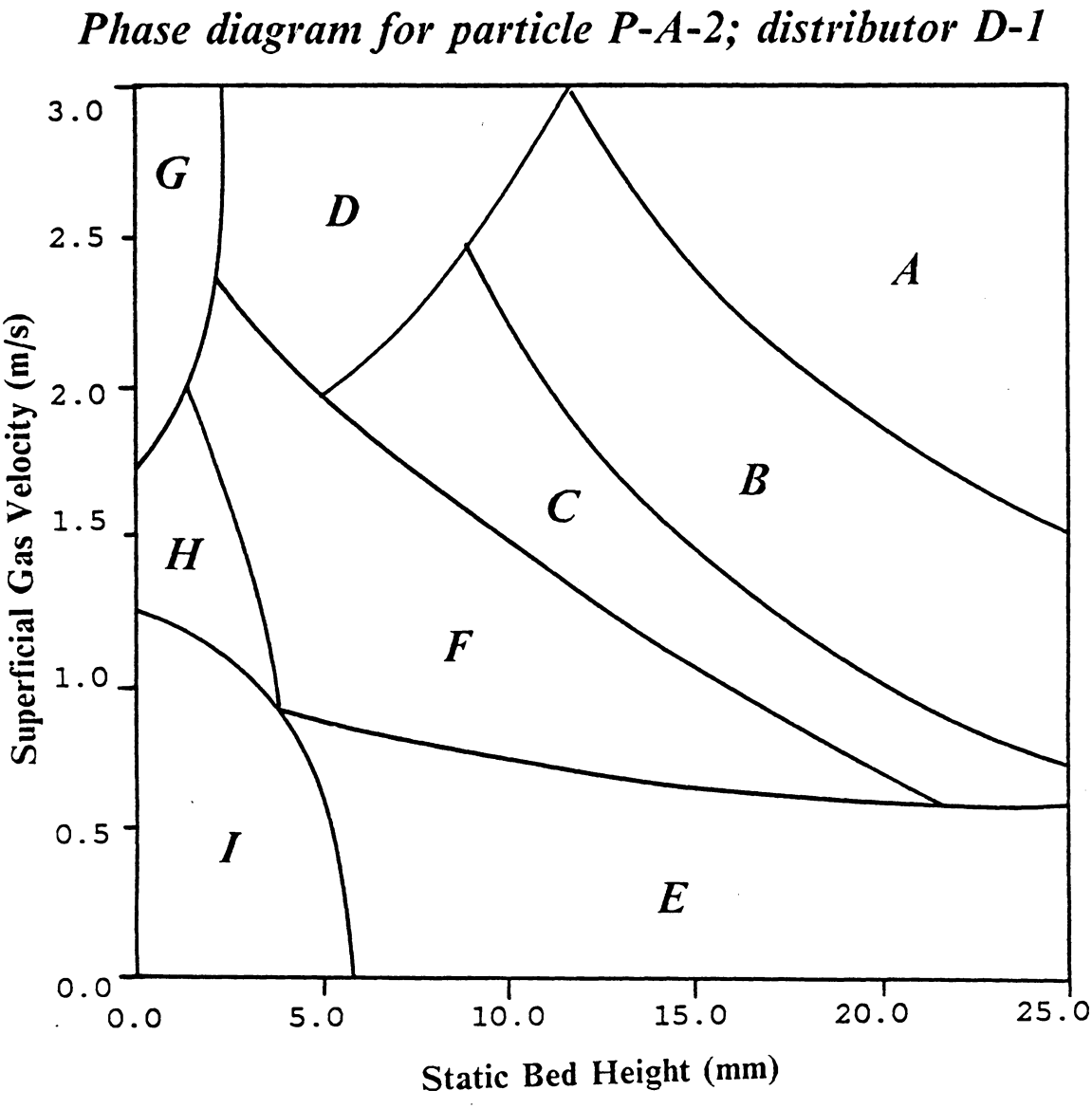

Figure 27. Phase Diagram for particle P-A-2 and distributor D-1: (630-micron Master Beads in the bed having 5.6% open area distributor)

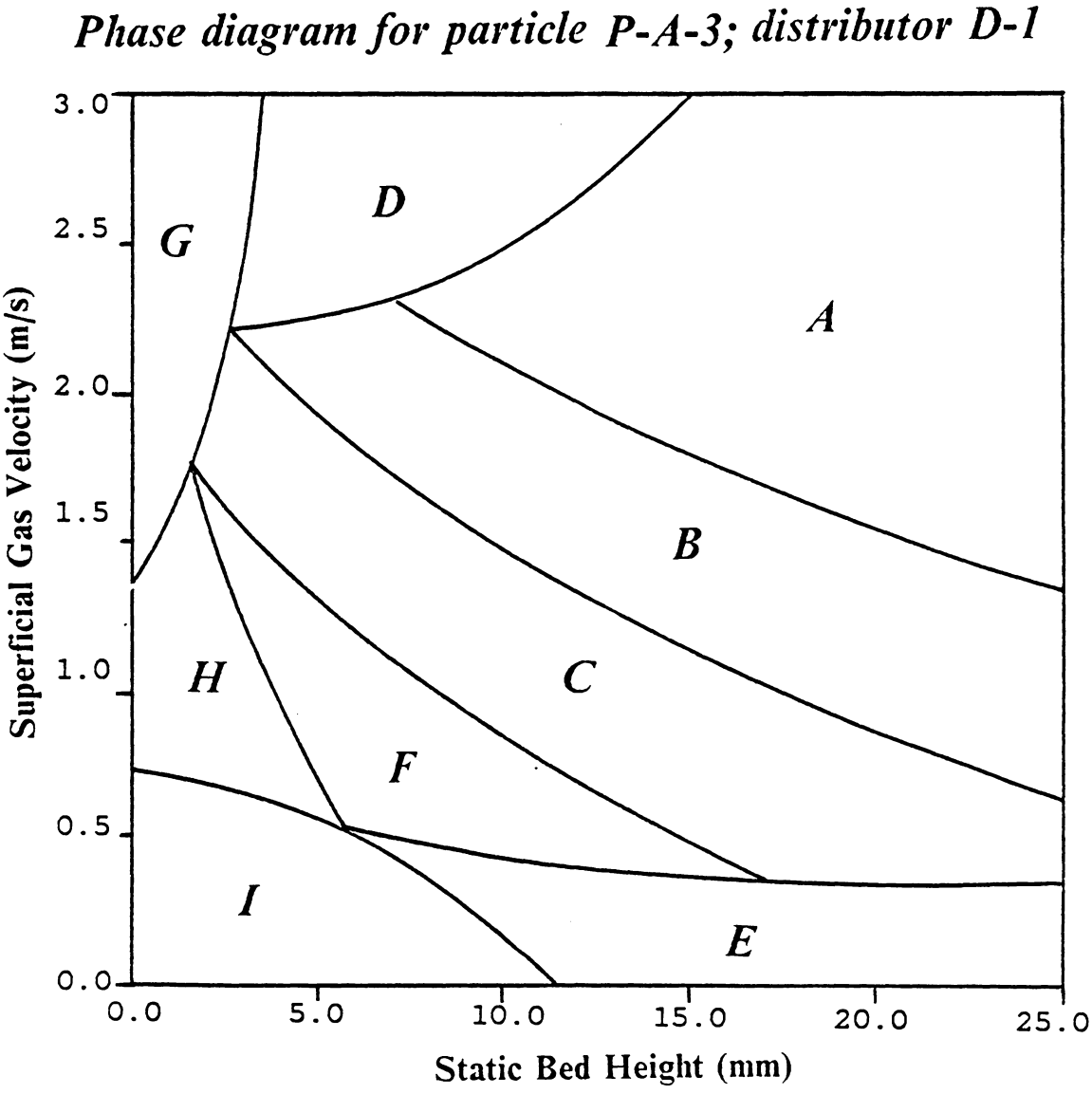

Figure 28. Phase Diagram for particle P-A-3 and distributor D-1: (335-micron Master Beads in the bed having 5.6% open area distributor)

3. A "phase diagram" does vary with physical properties of the fluidized particles. This will be the main point in the discussion that follows.

Figure 29 on page 118 to Figure 37 on page 126 present phase diagrams for all of the nine particles that we have studied in the 101.6-mm I.D. rig with a laminated gas distributor having 4.2% open area ratio (distributor D-4). These figures are chosen for discussion because of the uniqueness of the phase diagrams for beds having laminated distributors. For beds having jet-producing distributors, the phase diagram must be scrutinized case by case (based on the features of the distributor) and they usually cannot provide us with conclusions of much generality. However, useful conclusions concerning jet-existing beds can still be made if future data provides details of the hydrodynamic behavior of jets and bubbles.

Transition points between different types of beds are presented as triangular dots in Figure 29 on page 118 to Figure 37 on page 126. These points define boundaries between the types that can be expressed as straight lines without introducing too much error. Some observations can be summarized as follows:

1. Boundary lines between type E and other types are almost horizontal. Therefore, we can assign a definite superficial fluidizing gas velocity, u_f^*, below which the bed will fall into type E. (We will provide a name for this velocity shortly.)

2. Similarly, boundary lines between type F and type C are almost vertical and hence will provide us a specific static bed height H_s^*.

3. For the boundaries between types A and B or between types B and C, slopes and intercepts can be assigned as S_{ab}, I_{ab}, S_{bc}, and I_{bc} respectively, for the convenience of our study. (S represents 'slope'; I means 'intercept'; the subscripts define pairs of types whose boundaries are under consideration.)

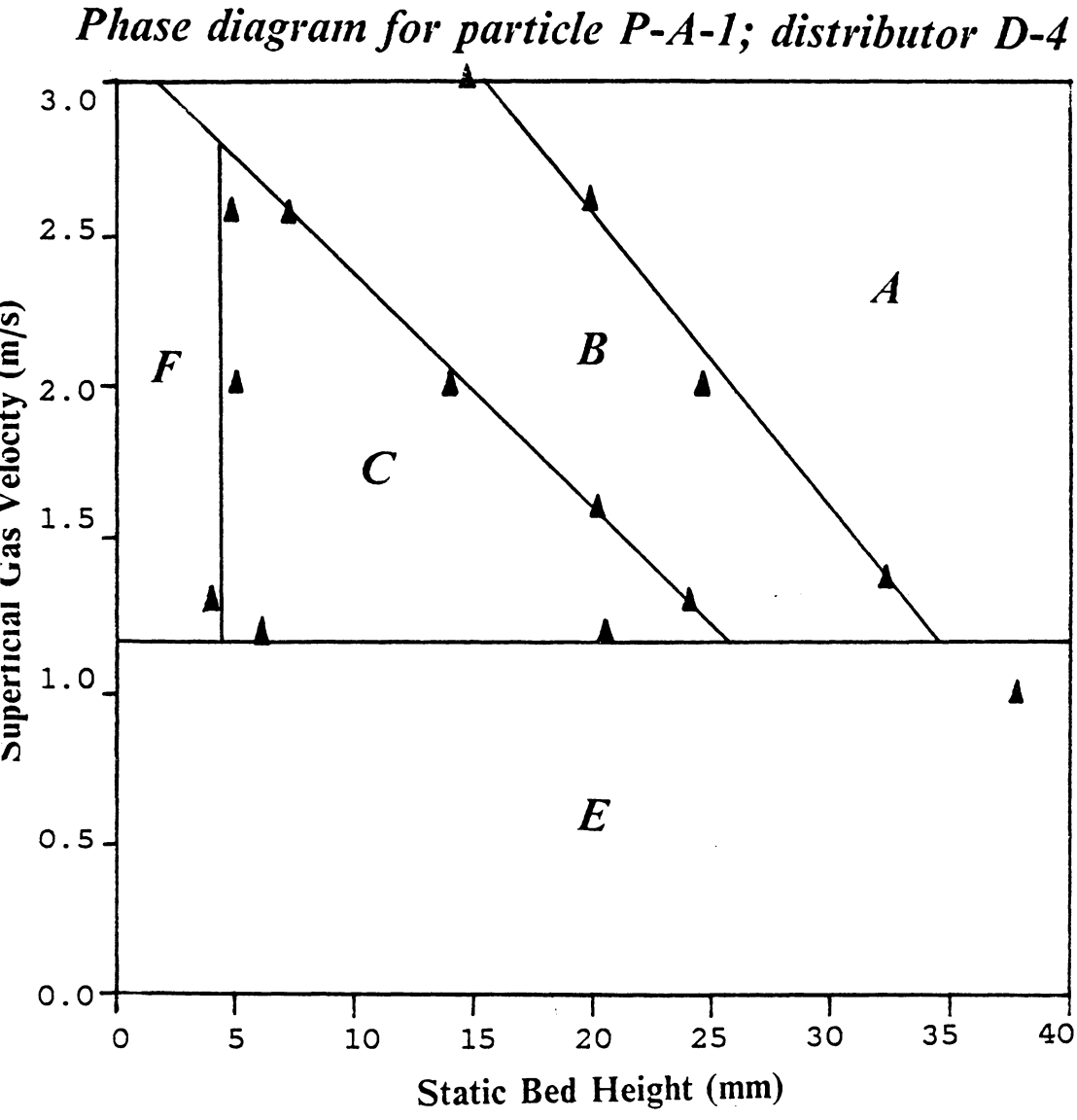

Figure 29. Phase diagram for particle P-A-1 (with laminated distributor)

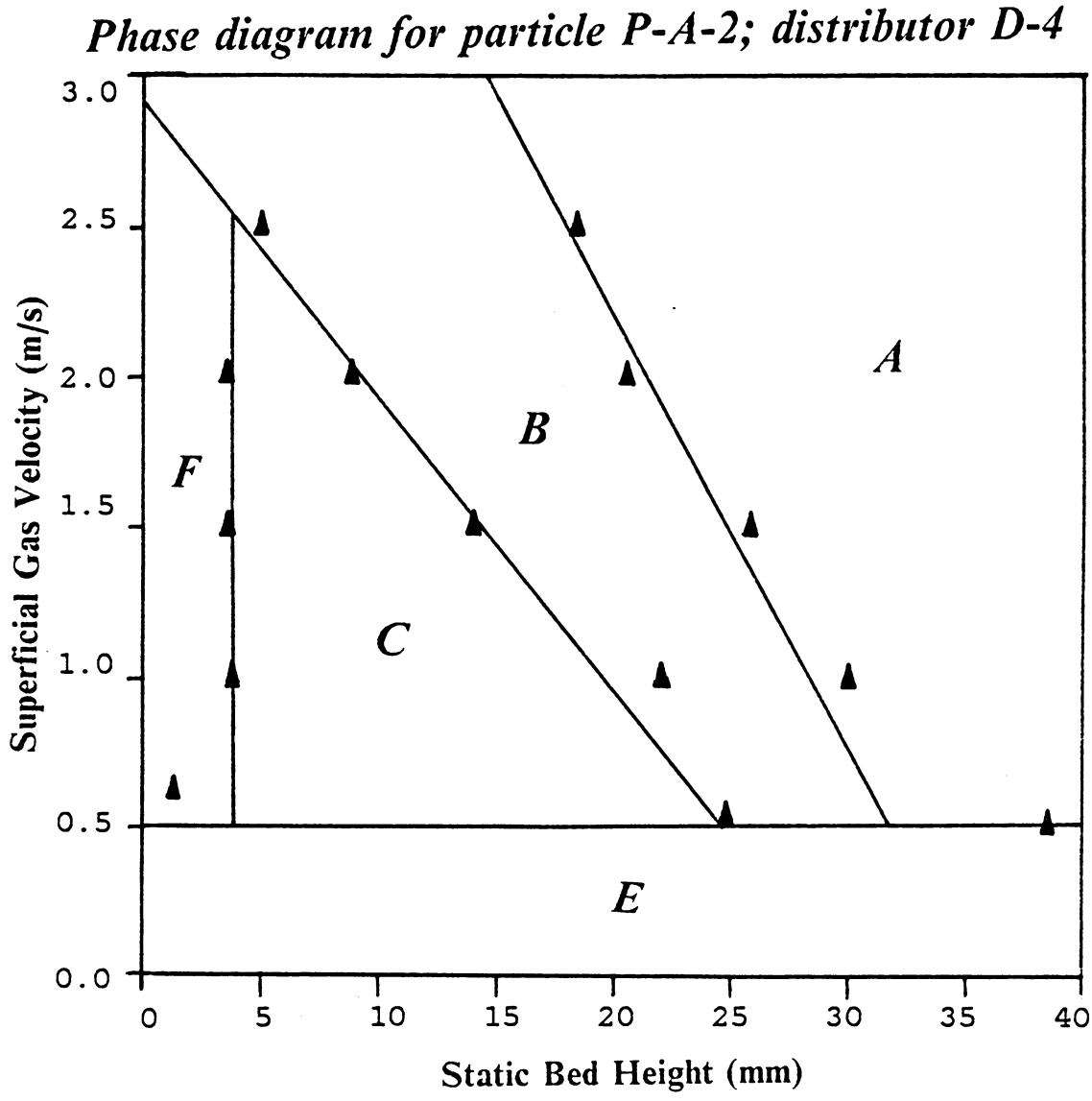

Figure 30. Phase diagram for particle P-A-2 (with laminated distributor)

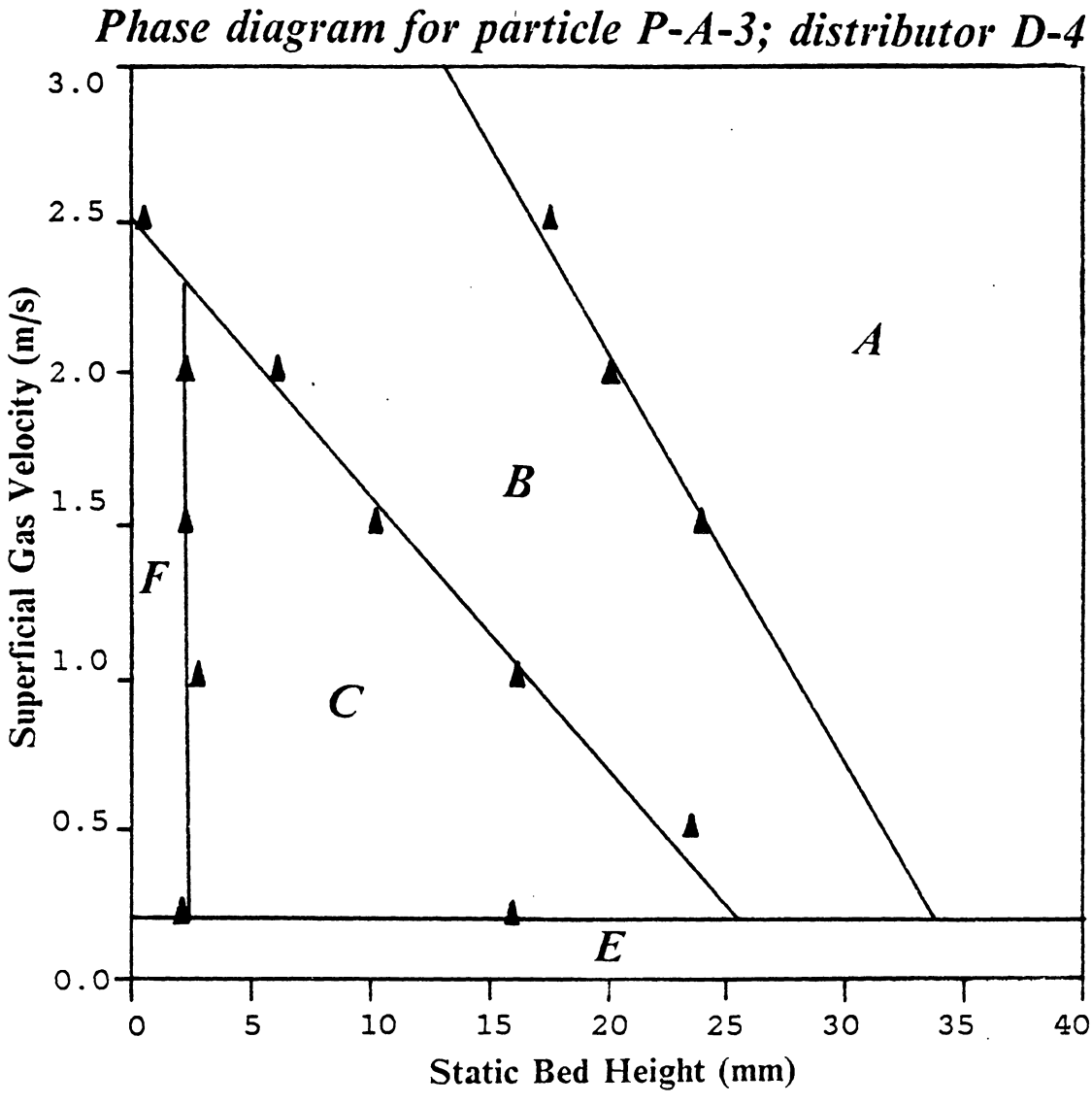

Figure 31. Phase diagram for particle P-A-3 (with laminated distributor)

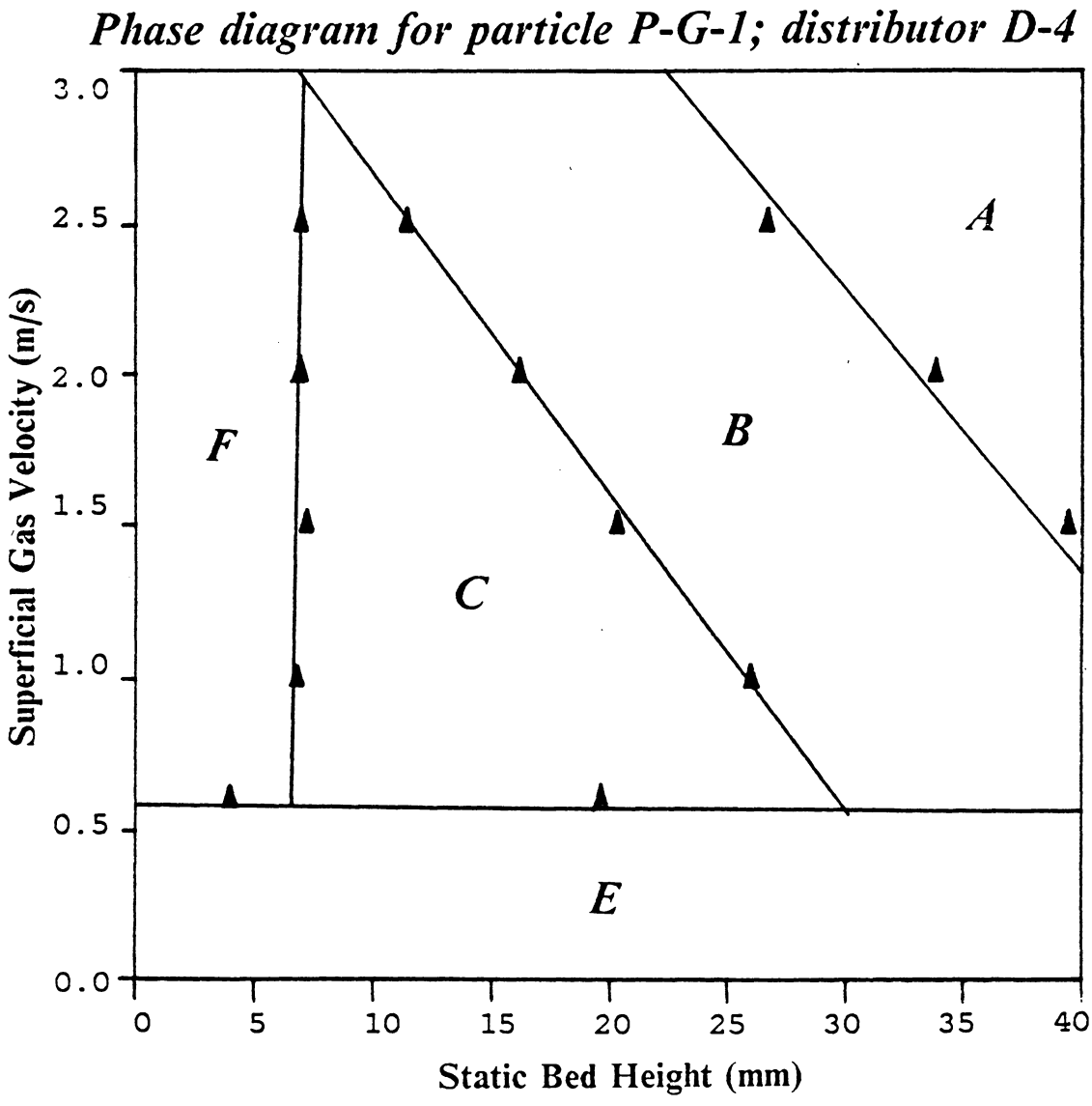

Figure 32. Phase diagram for particle P-G-1 (with laminated distributor)

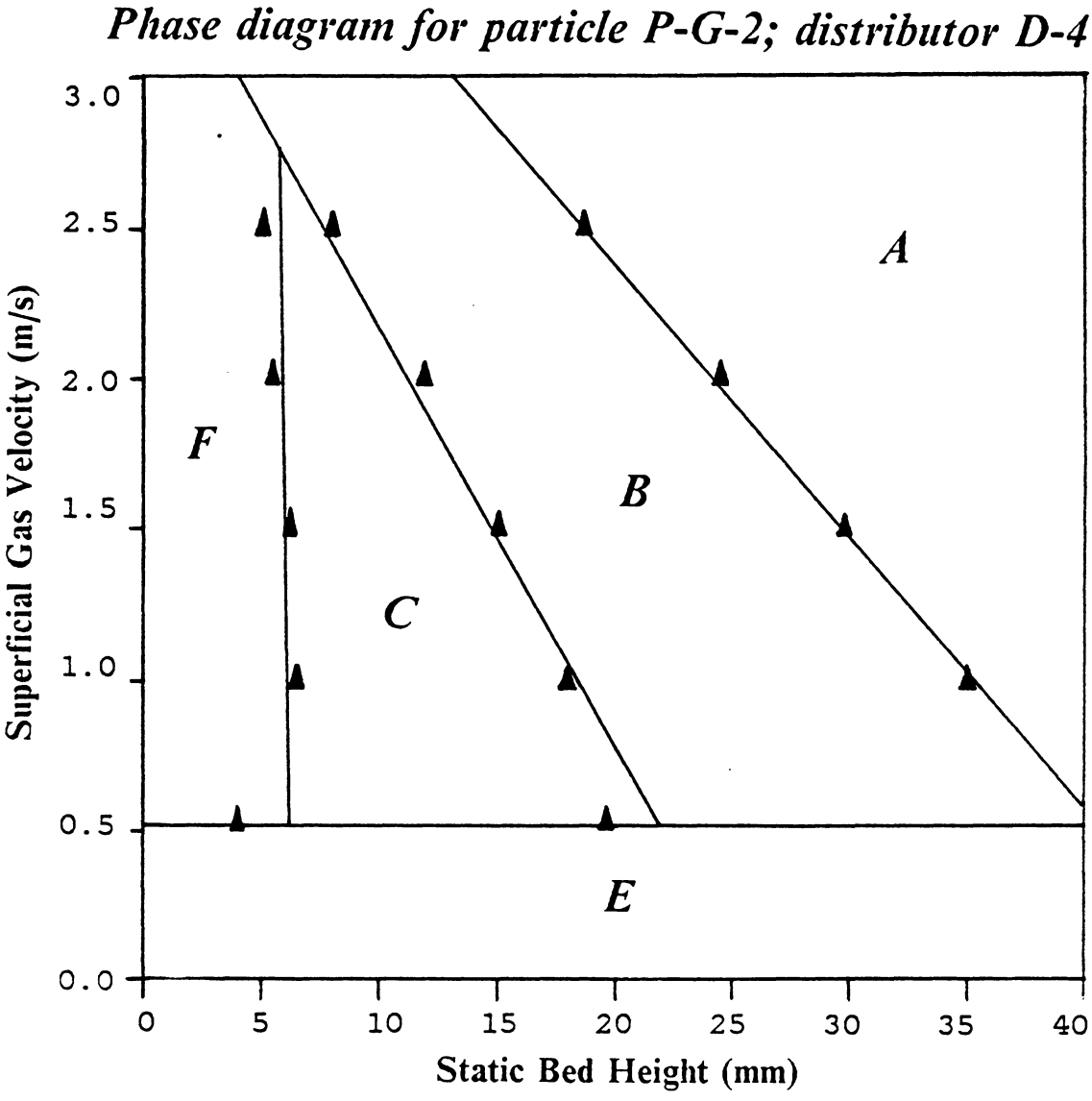

Figure 33. Phase diagram for particle P-G-2 (with laminated distributor)

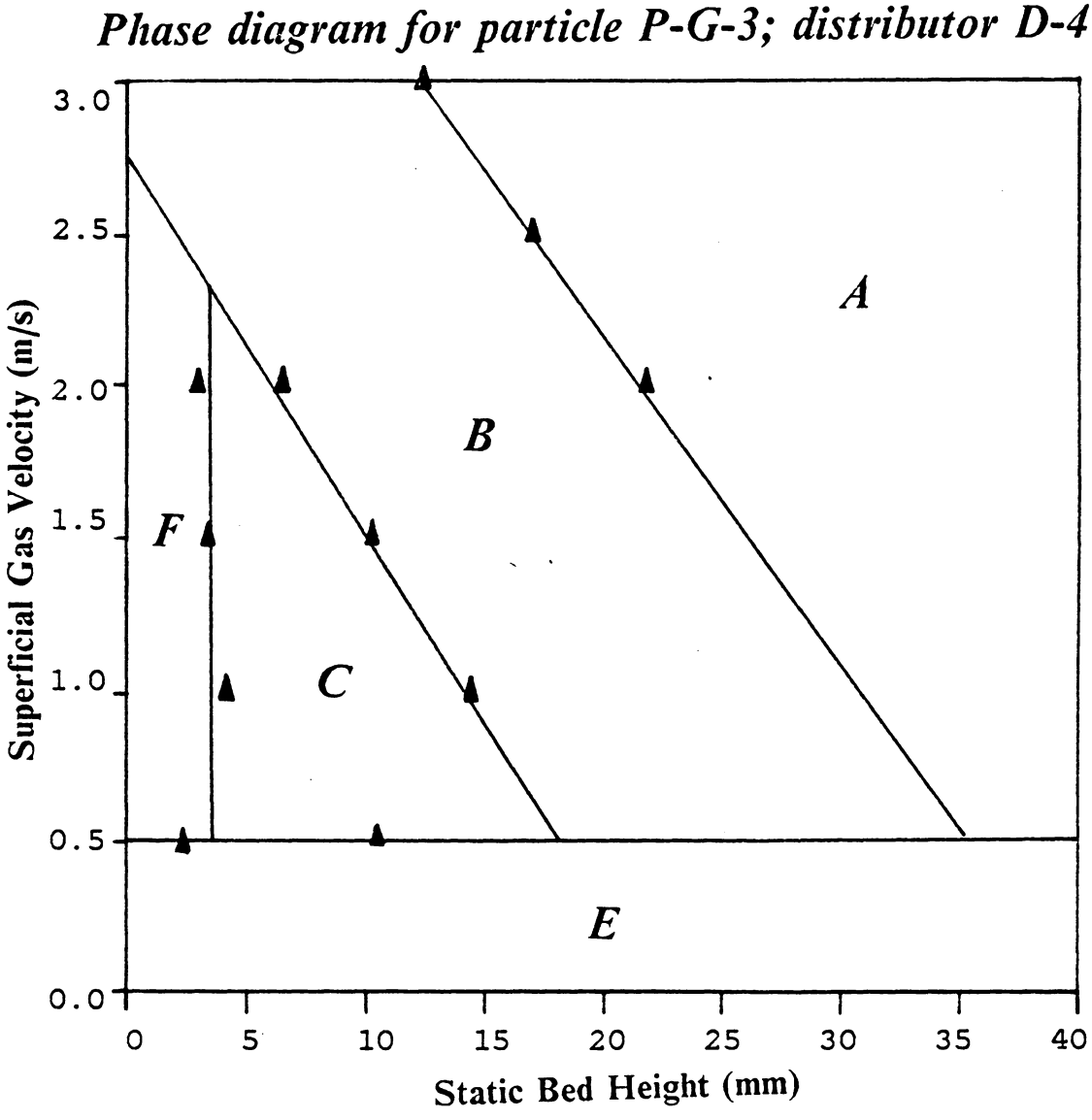

Figure 34. Phase diagram for particle P-G-3 (with laminated distributor)

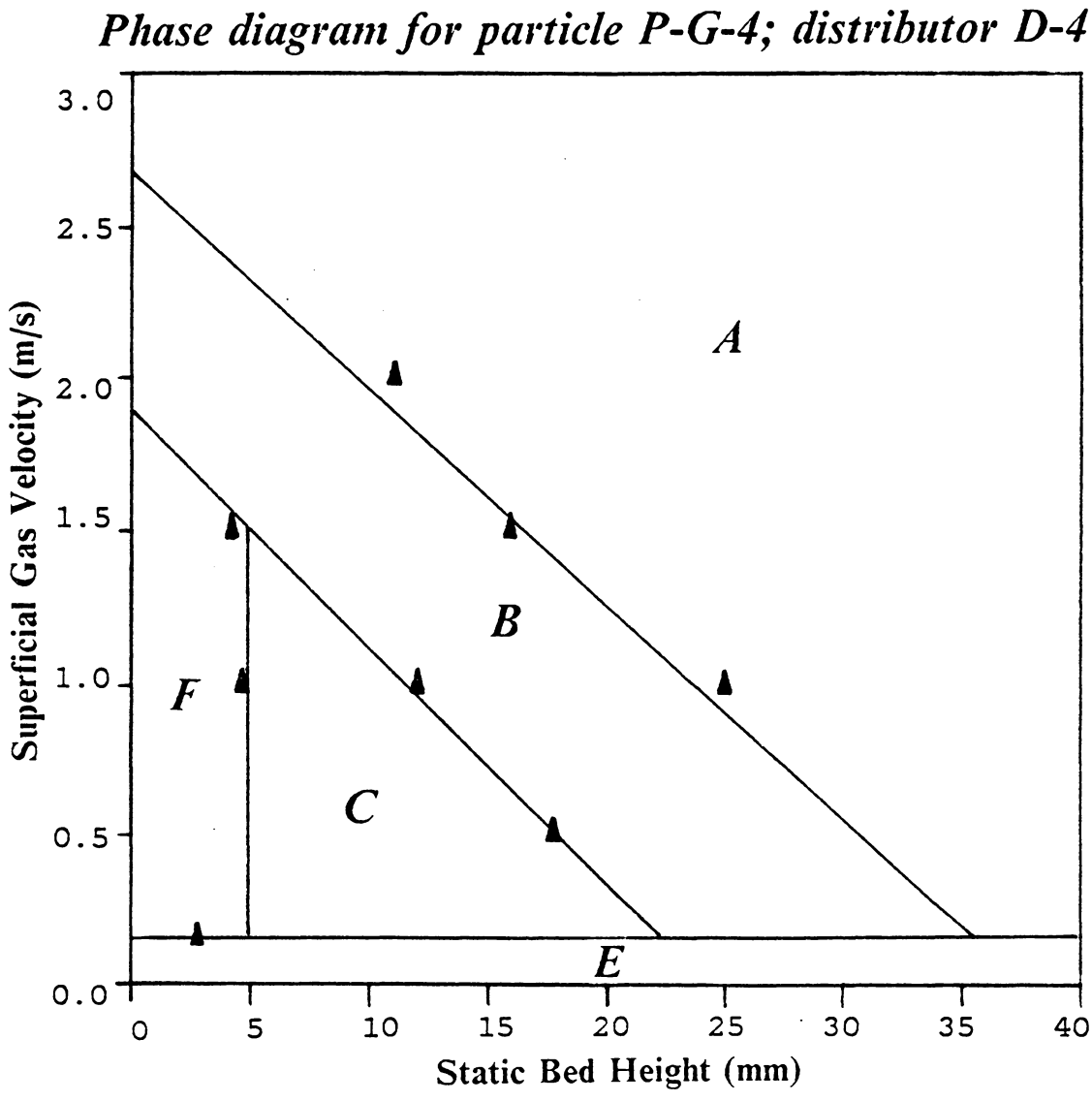

Figure 35. Phase diagram for particle P-G-4 (with laminated distributor)

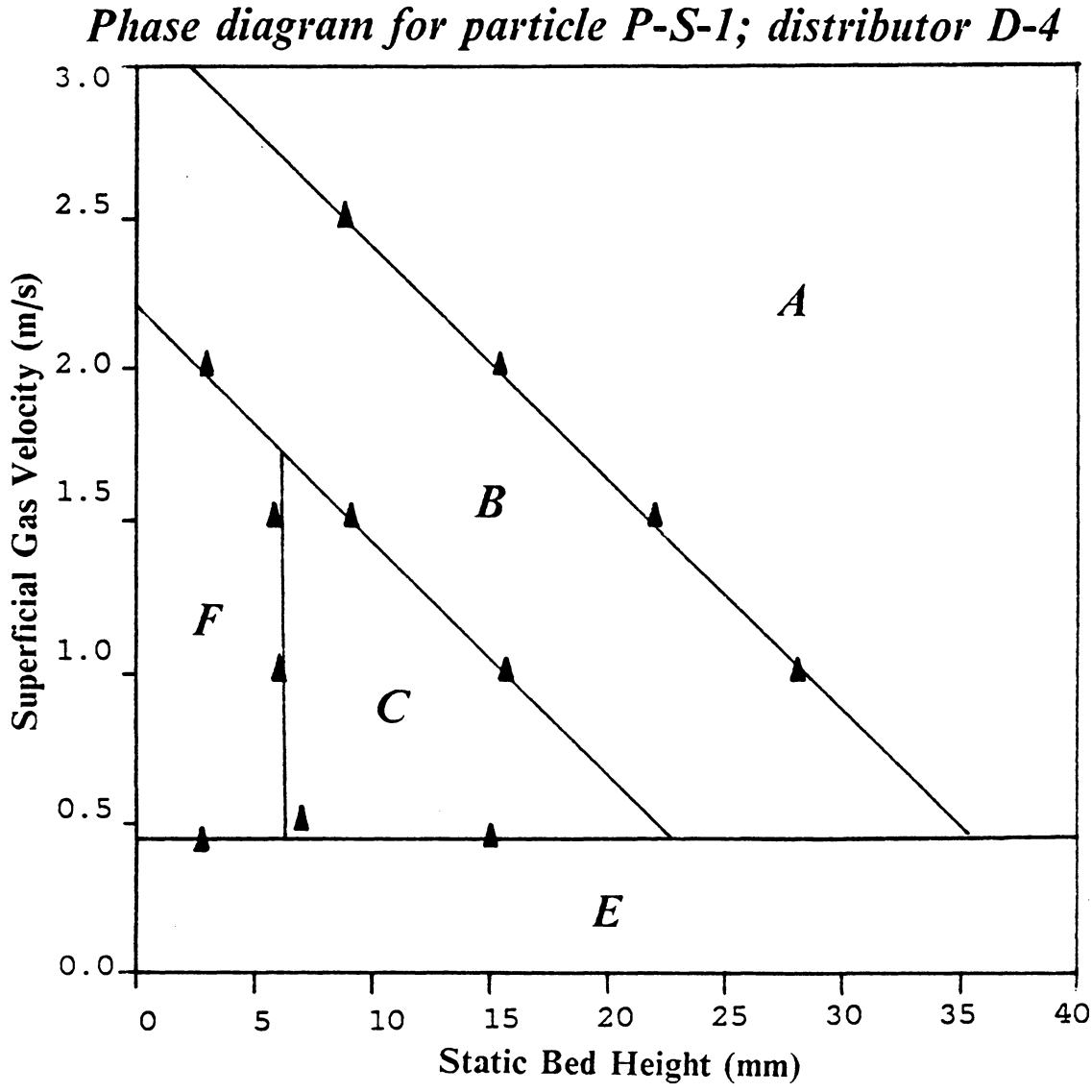

Figure 36. Phase diagram for particle P-S-1 (with laminated distributor)

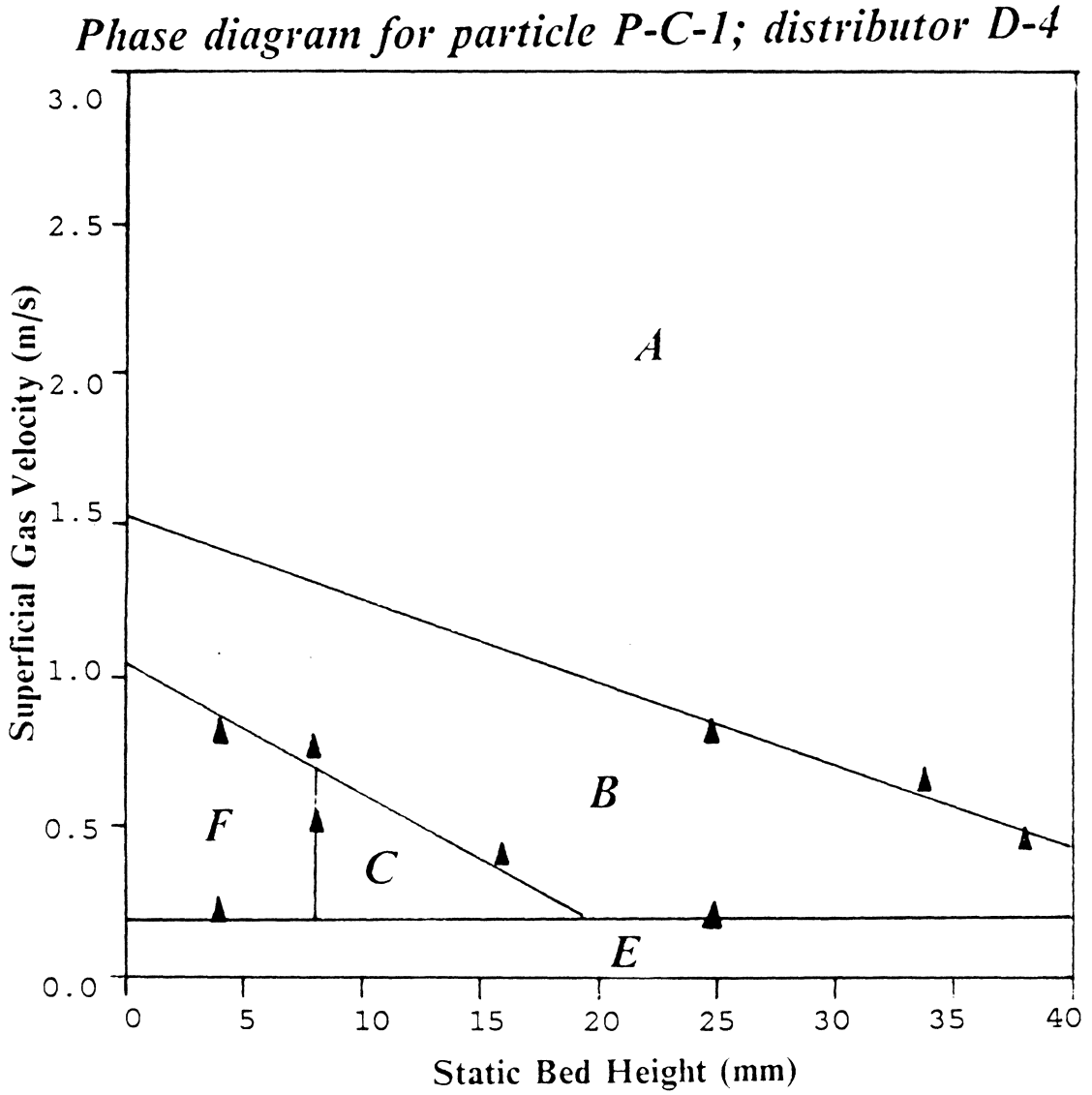

Figure 37. Phase diagram for particle P-C-1 (with laminated distributor)

Table 12. Specifications of boundaries for different types of shallow fluidized beds

Boundaries for different types of beds

Particle	u_f^*	H_s^*	S_{ab}	I_{ab}	S_{bc}	I_{bc}
P-A-1	1.12	4.6	-.094	4.398	-.074	3.074
P-A-2	0.57	3.6	-.122	4.629	-.087	2.827
P-A-3	0.21	2.4	-.151	5.082	-.088	2.498
P-G-1	0.60	7.0	-.078	4.610	-.105	3.685
P-G-2	0.52	5.6	-.092	4.239	-.150	3.736
P-G-3	0.50	3.5	-.106	4.315	-.127	2.816
P-G-4	0.15	4.8	-.069	2.700	-.073	1.830
P-S-1	0.44	6.3	-.078	3.198	-.079	2.229
P-C-1	0.20	8.1	-.025	1.439	-.035	0.975

Table 12 on page 127 lists all of the data obtained from the phase diagrams for Figure 29 on page 118 to Figure 37 on page 126. Linear regression has been used to find slopes and intercepts for the lines separating types A-B and types B-C. It was found that the straight-line assumption can predict the data points with a correlation coefficient of 0.9925 with respect to the experimental data. (The standard variation is as small as 2%). This is evidence for the validity of proposing that these boundaries may be represented by straight lines.

3.4 Mathematical models for predicting types of shallow fluidized beds

It would be worthwhile to interpret the boundary lines in our phase diagrams in terms of mathematical models based on existing hydrodynamic theories of fluidization. However, one must keep in mind the current imperfect status of fluidization theory. Whatever the models we can propose, they may still be in a rudimentary form.

3.4.1 Distinction between type E and other types of shallow fluidized beds

We begin by remembering that the definition of minimum fluidization velocity has an element of arbitrariness: "smooth" fluidization is not usually achieved until the superficial gas velocity has exceeded the theoretical minimum, u_{mf}, by an indefinite velocity increment, needed to "unlock" the particle mass. This has been the case in most of our experiments.

In all of our phase diagrams, boundaries between type E and other types of shallow fluidized beds are almost horizontal. As mentioned earlier, this suggests that there exists what we might term a "minimum smoothly fluidizing velocity", u_f^* , which provides a criterion for judging the status of shallow fluidized beds.

The existence of the u_f^* can also be understood with reference to a plot of pressure drop versus gas velocity as shown in Figure 38 on page 130. A generally accepted way of determining the minimum fluidizing velocity, u_{mf}, is to find the intersection (point b in Figure 38 on page 130) of the two segments (line a-b and line b-c in Figure 38 on page 130) in the plot of pressure versus gas velocity.

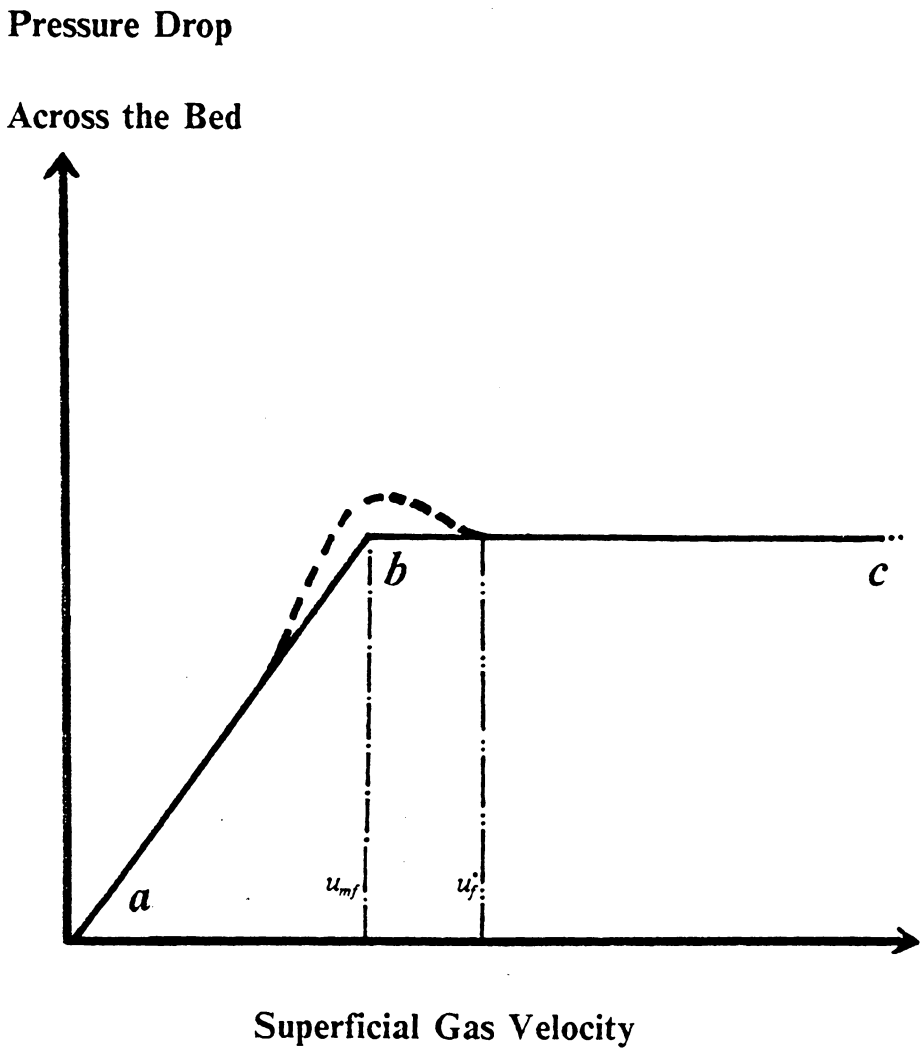

Figure 38. Minimum fluidizing velocity and minimum smoothly fluidizing velocity: Experimental technique via. the plot of bed pressure drop versus gas velocity

However, most experimental data reveal, not a curve as sharp and perfect as curve a-b-c (of Figure 38 on page 130), but rather a curve of pressure drop versus gas velocity having the shape of the dotted curve in Figure 38 on page 130. Therefore, there is reason for us to believe that the bed will reach a "smoothly fluidized" status only if the superficial gas velocity passes beyond the minimum fluidizing gas velocity by a definite interval, reaching a "minimum smoothly fluidizing velocity." u_f^* .

A simple model for predicting the u_f^* is to assume that--

$$u_f^* = B^* u_{mf} \qquad [3.1]$$

where B^* is a constant to be determined.

Table 13 on page 135 lists experimental values of u_f^* obtained from the phase diagrams as well as experimental values of u_{mf} determined by the procedure displayed in Figure 38 on page 130. The last column of Table 13 on page 135. gives values of B^* for all of our particles. The average value of B^* is 1.56 with an astonishing small deviation of 0.065, implying only a 4.2% averaged error in predicting B^*. Figure 40 on page 134 shows experimental values of u_f^* versus the predictions of Equation 3-1. The agreement illustrates the usefulness of the model that we are proposing.

Observing from the top of a type E bed, we found that the cross-sectional area of the bed can be divided into three regions: fluidized region, semi-fluidized region, and dead region. Figure 39 on page 132 shows sketches of those regions for a type E bed as the amount of particles is increased. It can be seen that the area of the semi-fluidized and dead regions will increase to a certain extent. However, the dead region will shrink after increasing to about half of the cross-sectional area. (In Figure 39 on page 132, the maximum extent of dead region occurs at particle weights between about 80 and 170 grams; 184.5 grams of Master Beads creates a 10-mm static bed height in the 101.6-mm I.D. bed). When the static bed height increases to a certain value, all regions of the bed are at least semi-fluidized. It is conceivable that some uses might be found for type E beds, fully semi-fluidized, with the advantage of low bed pressure drop.

Top view of a type E bed

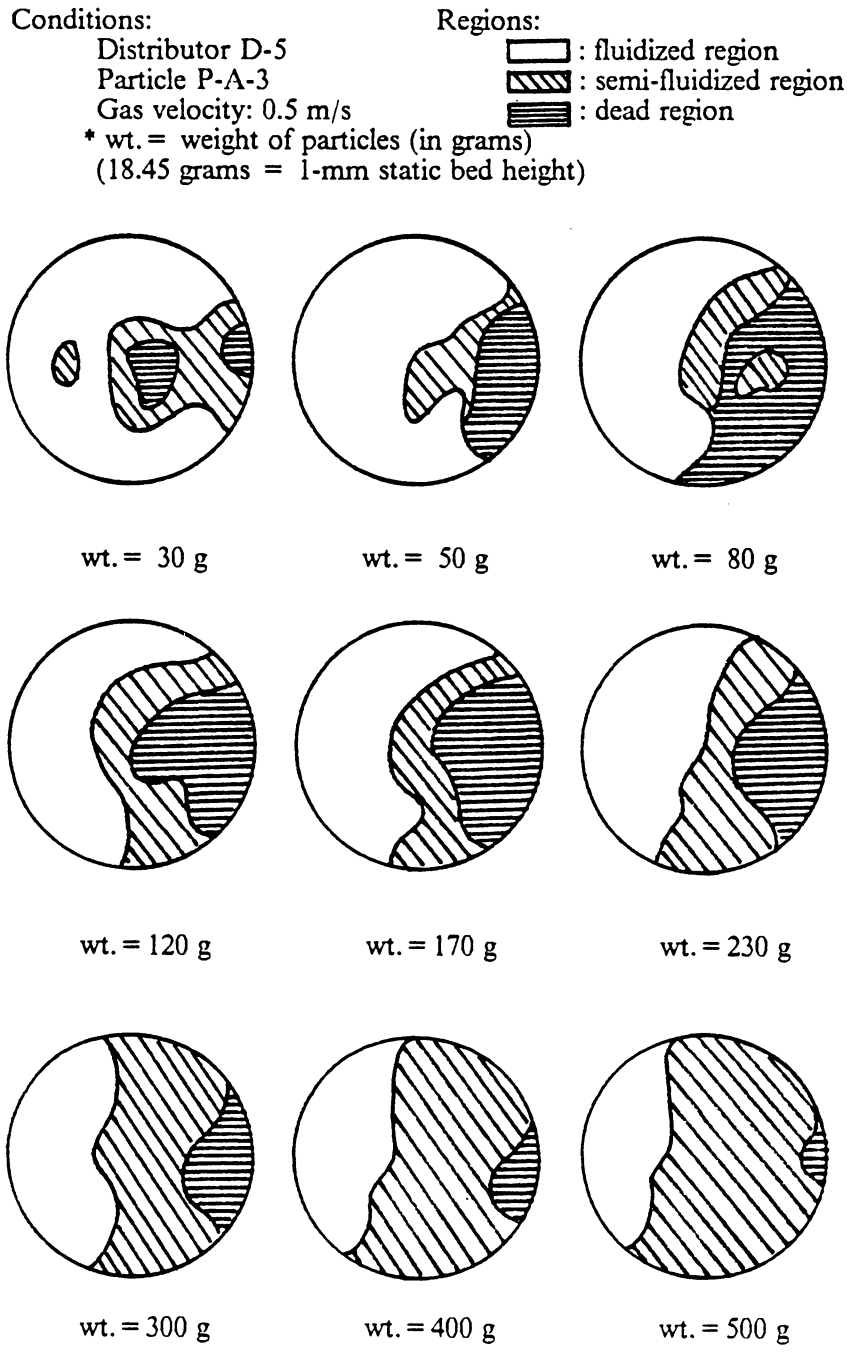

Figure 39. Top view of a type E bed with varying amounts of particles

3.4.2 Distinction between type F and type C beds

For a bed of type F, the bed surface is always so flat that the small dimples usually appearing in type C beds are not seen. This is probably due to the fact that most "small gas voids" rise through the relatively shallow particle layer in so short a time that they do not "consolidate" into "proper bubbles". We can propose a critical pressure drop across the bed, namely p^* , above which time of gas residence and the physical resistance to its upward flow force the voids into bubbles. From a physical point of view, this critical pressure drop will be less at a higher particle density or diameter.

It is difficult to propose a mathematical model for prediction p^* in terms of the physical properties of particles. However, the velocity of the gas stream passing through the bed can be used as an indicator of the resistance of the fluidizing medium and hence serves as a determining factor for p^*. A simple model can be proposed here:

$$p^* = c^* u_p \qquad [3.2]$$

where

u_p = the velocity of the gas stream passing through the fluidized bed, in $\frac{m}{s}$.

c^* = a constant, dimensionless.

From Kunii and Levenspiel's (1969), for Reynold number greater than 200--

$$u_p = c^{**} \sqrt{d_p (\rho_s - \rho_g)} \qquad [3.3]$$

where

c^{**} = a constant which is independent of the particle properties, dimensionless.

Therefore, we can have

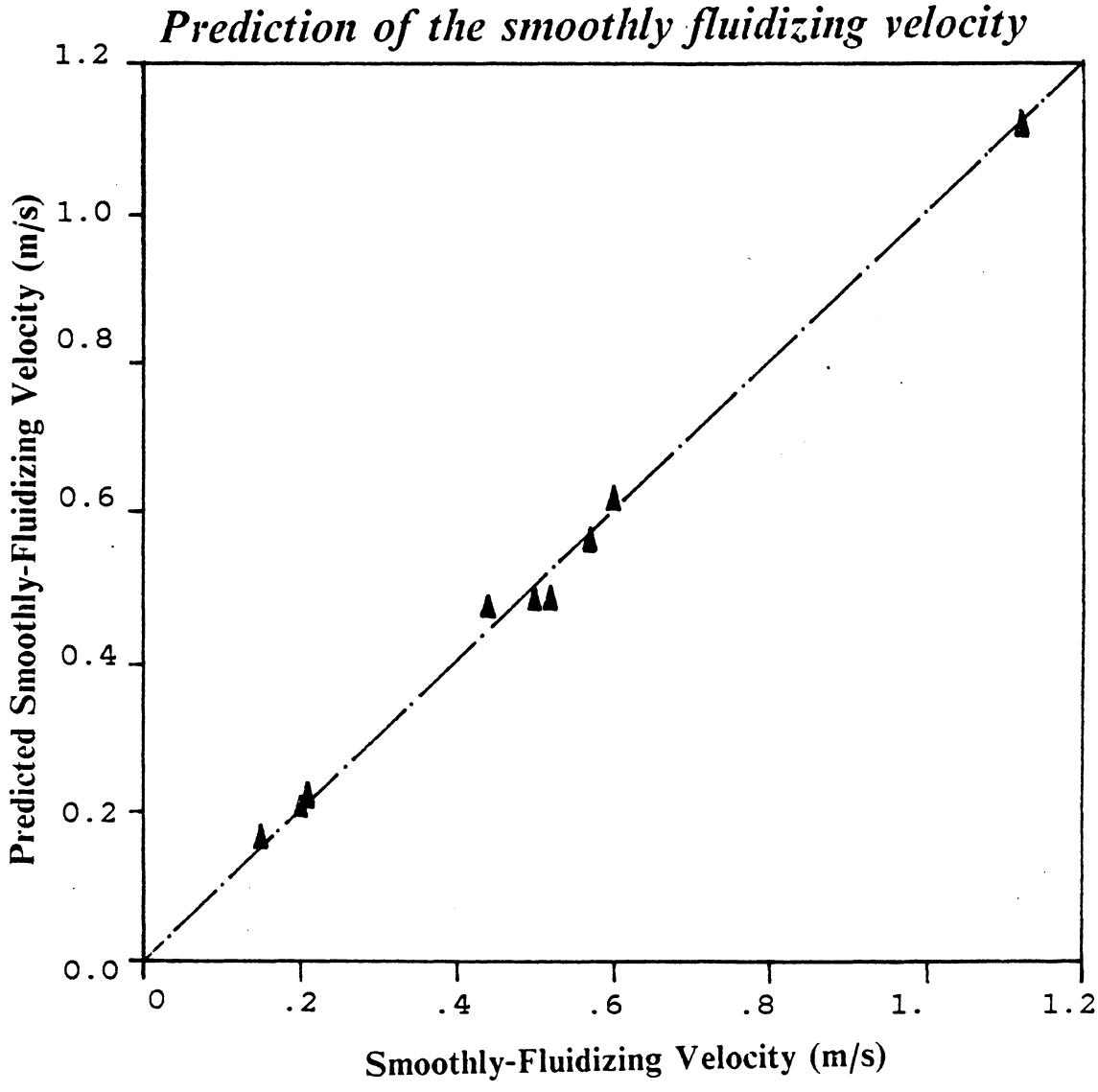

Figure 40. Prediction of the minimum smoothly fluidizing velocity

Table 13. "Minimum smoothly fluidizing gas velocity" for type E beds

The minimum "smoothly fluidizing" gas velocity for type E beds

Particle	u_{mf}	u_f^*	B^*
P-A-1	.71	1.12	1.58
P-A-2	.36	.57	1.58
P-A-3	.14	.21	1.50
P-G-1	.39	.60	1.54
P-G-2	.31	.52	1.68
P-G-3	.31	.50	1.61
P-G-4	.10	.15	1.50
P-S-1	.30	.44	1.47
P-C-1	.13	.20	1.54

Average = 1.56
standard deviation = 0.065
(4.2 %)

$$p^* = \Phi' \sqrt{d_p (\rho_s - \rho_g)} \qquad [3.4]$$

where

Φ' = a constant determined by the gravitational force, particle shape factor, and gas density.

For any porous medium, we have the following equation (see Kunii and Levenspiel, p. 72) --

$$\frac{p^*}{H_s^*} = (1 - \varepsilon_s)(\rho_s - \rho_g)\frac{g}{g_c} \qquad [3.5]$$

where

H_s^* = the static bed height with respect to p^*, m.

ε_s = static bed voidage, dimensionless.

Substituting Eq. 3.4 into Eq. 3.5, we obtain --

$$H_s^* = \frac{\Phi' g_c}{(1 - \varepsilon_s) g} \times \frac{d_p}{\sqrt{(\rho_s - \rho_g)}} \qquad [3.6]$$

In most of our work, the range of the superficial gas velocity for type F beds has been relatively small. Therefore, we can assume that the bed porosity ε_s does not change too much, to obtain the following --

$$H_s^* = \Phi \sqrt{d_p/\rho_s} \qquad [3.7]$$

where

$\Phi = \frac{\Phi' g_c}{(1 - \varepsilon_s) g}$, a "pseudo-constant", dimensionless.

$\rho_s \cong \rho_s - \rho_g$ for solid-gas system.

Table 14 on page 138 lists the experimental values of H_s^* and $\sqrt{d_p/\rho_s}$ for all of our particles. The correlation coefficient between H_s^* and $\sqrt{d_p/\rho_s}$ is 0.8675 -- a value indicating the validity of equation 3.7 for predicting H_s^* from particle density and diameter. The last column

of Table 14 on page 138 gives the Φ values, which have an average value of 9500 and a standard deviation of 3700. (Unfortunately, this represents about a prediction error of 38%, a bit too high). In summary, we write:

$$H_s^* = 9.5 \times 10^3 \sqrt{d_p/\rho_s} \qquad [3.8]$$

Figure 41 on page 139 shows experimental values of u_f^* versus values predicted by Equation 3.8.

3.4.3 Distinctions between types A-B and between types B-C

If we regard the Type B bed as an intermediate situation, the most obvious distinction between shallow fluidized beds of type A and C is the effect of the gas bubbles. For a normal type C or type B bed, the system has the following features:

1. The superficial gas velocity, u, is in an intermediate range.

2. Slugging does not exist (i.e. wall effect is unimportant).

3. Gas bubbles are not large enough to affect the time- averaged bed pressure distribution.

Therefore, the bed can be treated as a "relatively" homogeneous porous medium in comparison with conventional "deep" fluidized beds. The famous Ergun equation will describe the relationship between the pressure drop and the apparent bed height --

$$\frac{\delta P}{H} g_c = 1.75 \frac{(1-\varepsilon_f)}{\varepsilon_f^3} \frac{\rho_g}{\varphi_s} \frac{u^2}{d_p} f \qquad [3.9]$$

where

δP : pressure drop across the bed, $\frac{N}{m^2}$.

Table 14. Prediction of critical static bed height for type F shallow beds.

The prediction of critical static bed height for type F shallow beds

Particle	H_s^*	$\sqrt{\frac{d_p}{\rho_s}} \times 10^4$	$\Phi \times .001$
P-A-1	4.6	5.76	7.90
P-A-2	3.6	4.07	8.84
P-A-3	2.4	2.97	8.08
P-G-1	7.0	5.80	12.06
P-G-2	5.6	5.31	10.55
P-G-3	3.5	3.28	10.66
P-G-4	4.8	3.76	12.78
P-S-1	6.3	4.69	13.44
P-C-1	8.1	8.10	10.00

Average = 9.50
standard deviation = 3.70
(38 %)

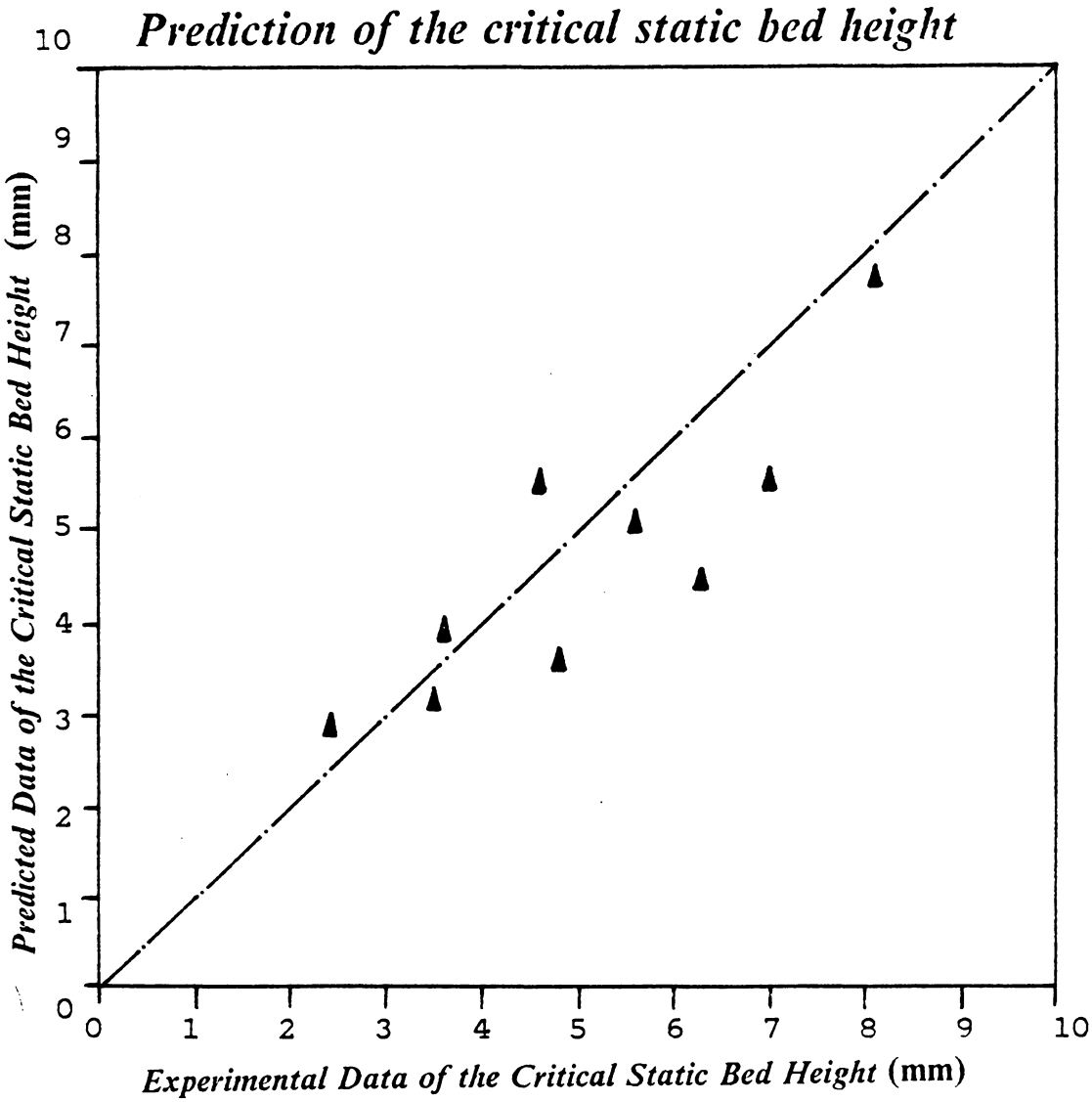

Figure 41. Experimental and predicted critical static bed heights: Experimental values of H_s^* versus the data predicted by Eq. 3.8

H : apparent bed height, *m*.

ε_f : porosity of the fluidized bed, dimensionless.

φ_s : spherical factor of the particles, dimensionless.

ρ_g : gas density, $\frac{kg}{m^3}$.

u : superficial gas velocity, $\frac{m}{s}$.

d_p : averaged particle diameter, *m*.

This result is based on the following assumptions:

1. The Reynold number with respect to the particle is large (> 100)

2. The porosity, ε_f, does not vary much in the bed.

3. The variable *f* is a correction factor due to presence of gas bubbles (i.e. *f* is an indicator of the fairness of the Ergun equation in this fluidizing system.)

From the hydrodynamic theory, we can also have the following expression for δP -- [see Kunii and Levenspiel ,1969]

$$\frac{\delta P}{H} g_c = (1 - \varepsilon_f)(\rho_s - \rho_g) g F \qquad [3.10]$$

where

ρ_s : density of the particles, $\frac{kg}{m^3}$.

g : gravitational force, 9.8 $\frac{m}{s^2}$.

F : correlation factor for bubbling, dimensionless.

Combining Equations 3.9 and 3.10, we obtain --

$$u^2 = \left(\frac{f}{F}\right)\left(\frac{g\,\varepsilon_f^3\,\varphi_s}{1.75\,\rho_g}\right) d_p (\rho_s - \rho_g)$$

$$= \Gamma' d_p (\rho_s - \rho_g) \qquad [3.11]$$

where

$$\Gamma' = (\frac{f}{F})(\frac{g\,\varepsilon_f^3\,\varphi_s}{1.75\,\rho_g})$$

Now, we can define a critical characteristic velocity, u_c, above which the effect of bubbling is so significant that Eq. 3.11 will not be valid any longer. Under this circumstance, we have --

$$u_c = \Gamma\sqrt{d_p \times \rho_s} \qquad [3.12]$$

In the equation,

Γ is determined by

(a). porosity of the bed.

(b). physical properties of the bubbles.

(c). depth of the bed.

since $\rho_g << \rho_s$, we can assume that $(\rho_s - \rho_g) \cong \rho_s$.

From general fluidization theory, the deeper the bed is the smaller will be the value of u_c that is required for bubbles to influence fluidization. This fact can be combined with the mathematical expression of Eq. 3.12 to obtain a simple model in which the bed height appears:

$$u_c = K(1 - \frac{H_s}{H_{s'}})\sqrt{d_p\,\rho_s} \qquad [3.13]$$

where

$$K(1 - \frac{H_s}{H_{s'}}) = \Gamma$$

K : a constant to be determined by the characteristics of the bed.

$H_{s'}$: theoretically critical static bed height beneath which $u_c = 0$.

By noting the similarity of the physical meaning of $H_{s'}$ with H_s^* in Eq. 3.7, we can propose a mathematical expression of $H_{s'}$ as follows--

$$H_{s'} = \sigma\sqrt{d_p/\rho_s} \qquad [3.14]$$

where σ is a constant.

Substituting Eq. 3.14 into Eq. 3.13, we obtain --

$$u_c = K\sqrt{d_p \rho_s} - (\frac{K}{\sigma})\rho_s H_s \qquad [3.15]$$

Therefore, in a phase diagram, i.e.the plot of u vs. H_s plot, the line separating type A from type B beds, will have

$$\text{slope} = S_{ab} = -(\frac{K}{\sigma})\rho_s \qquad [3.16]$$

$$\text{intercept} = I_{ab} = K\sqrt{d_p \rho_s} \qquad [3.17]$$

Table 15 on page 143 lists experimental data of S_{ab} and I_{ab} obtained from Figure 29 on page 118 to Figure 37 on page 126 together with the $\frac{-K}{\sigma}$ and K values calculated from the above two equations. Similar sets of data have also been found for S_{bc} and I_{bc}, based upon the same equations; these are presented in Table 16 on page 144. Only predictions of S_{ab} give satisfactory results from statistical point of view.

Checking the data on Table 16 on page 144, we can conclude that Equations 3.16 and 3.17 will not predict boundary lines separating types B and C beds. This can be explained by the fact that hydrodynamic theories we used in deriving Equations 3.16 and 17 are all based on a homogeneous view of fluidized beds. Since the main distinction between type B and C beds is not their homogeneity (both types B and C beds are homogeneous in comparison with type A bed), hydrodynamic theories other than those we used should be explored for defining the characteristics of the boundary lines that separate types B and C beds in the phase diagrams.

Table 15. The prediction of the boundary for type A and B beds.

The prediction of

S_{ab} and I_{ab}

Particle	S_{ab}	$(\frac{-K}{\sigma}) \times 10^{-5}$	I_{ab}	K
P-A-1	-.094	2.47	4.40	2.01
P-A-2	-.122	3.21	4.63	2.99
P-A-3	-.151	3.97	5.08	4.50
P-G-1	-.078	3.12	4.61	3.18
P-G-2	-.092	3.68	4.24	3.19
P-G-3	-.106	2.36	4.32	2.93
P-G-4	-.069	2.76	2.70	2.87
P-S-1	-.078	2.72	3.20	2.38
P-C-1	-.025	2.60	1.44	1.85
avearge	-.091	2.99	3.85	2.88
standard deviation	-.035	0.55	1.17	0.78
% of deviation	38%	18%	30%	27%

Table 16. Prediction of boundary between type B and C beds.

The prediction of

S_{bc} and I_{bc}

Particle	S_{bc}	$(\frac{-K}{\sigma}) \times 10^{-5}$	I_{bc}	K
P-A-1	-.074	1.95	3.07	1.40
P-A-2	-.087	2.29	2.83	1.83
P-A-3	-.088	2.32	2.50	2.21
P-G-1	-.105	4.20	3.69	2.54
P-G-2	-.150	6.00	3.74	2.81
P-G-3	-.127	2.83	2.82	1.91
P-G-4	-.073	2.92	1.83	1.95
P-S-1	-.079	2.76	2.23	1.66
P-C-1	-.035	3.65	0.98	1.25
avearge	-.091	3.21(2.87)*	2.63	1.95
standard deviation	-0.33	1.26(0.74)	0.88	0.51
% of deviation	36%	39%(26%)	34%	26%

* exclude the outlier for P-G-2.

3.5 Conclusions from study of phase diagrams

1. From the stand point of physical appearance, shallow fluidized beds can be categorized in nine different "types."

2. Different types of shallow fluidized bed can be expressed and distinguished on plots of superficial gas velocity versus static bed height, termed here "phase diagrams."

3. Among all of the types of shallow fluidized beds, only four of them are good for heat-transfer applications: types A, B, C and D. All other types are either too shallow or too dilute to be utilized effectively for this purpose.

4. Both particle properties and features of gas distributors affect the phase diagram. It has been found that changing the gas distributors among the laminated plates, which produce no jets, does not affect the phase diagram. On the other hand, for beds having perforated plates, the phase diagram is highly dependent on the features of distributors.

5. The existence of gas jets in the shallow fluidized beds does affect the hydrodynamics of some types of shallow beds. However, for the types of practical applicability (types A, B, and C), the effect of having jets on the physical appearance of the bed is significant.

6. We have proposed a minimum smoothly fluidizing velocity, which is shown to be about 1.6 times the classic minimum fluidizing velocity.

7. Hydrodynamic theory can be used to explain the existence of a few types of shallow beds on the phase diagrams. However, further efforts must emphasize work on theories of bubbles and voids in order to get more detailed and accurate models.

Chapter 4 PRESSURE DROP MEASUREMENTS IN SHALLOW FLUIDIZED BEDS

4.1 Orifice coefficients of the distributors

Throughout our studies on hydrodynamics and heat transfer of shallow beds, resutls obtained with perforated distributor plates deserve special attention for the following reasons:

1. Perforated distributors are commonly used in most fluidization research.

2. Utilizing a perforated distributor allows one to choose any specific orifice size and open area ratio.

3. A fluidized bed with a perforated distributor will display jets when the superficial gas velocity is high. The existence of jets will enable us to study many of the interesting hydrodynamic characteristics of the fluidized bed (especially when the bed is shallow).

Our perforated distributors were drilled in the mechanical shop of the Chemical Engineering Department at Virginia Tech. All of the orifices are arranged in a triangular pitch on 1.6-mm thick stainless steel plates. (See Table 9 on page 97 for the detailed specifications.)

For approximate or preliminary design of an orifice meter, the following equation has been proposed [see McCabe and Smith, 1981]--

$$u_o = C_o \sqrt{\frac{2\,g\,\delta P}{(1-\beta^4)\,\rho_f}} \qquad [4.1]$$

where

u_o = fluid velocity through the orifice, $\frac{m}{s}$.

β = ratio of orifice diameter to pipe diameter.

δP = pressure drop across the orifice meter ($\frac{N}{m^2}$)

g = gravitational constant (9.8 m^2/s)

ρ_f = density of the fluid. (1.205 Kg/m^3 for the air at S.T.P.)

Although different C_o values are reported, the above equation has frequently been used in designing multi-orifice distributor plates. The orifice coefficient, C_o , can be calculated by the following simplified equation based on Equation 4-1 and the fact that $\beta << 1$ for most of the cases--

$$u_o = 4.034 \times C_o \times \sqrt{\delta P} \qquad [4.2]$$

where

u_o is in m/s.

δP is in mm of water.

(for air at 20°C, 1 atm., only)

Table 17 on page 148 lists the orifice coefficients and the correspondent pressure drops across the three perforated (multi-orifice) gas distributors for different superficial gas velocities. Figure 42 on page 149 shows the plot of the orifice coefficient versus gas velocity for different types of gas distributor. A few conclusions can be summarized as follows:

Table 17. Orifice coefficients and pressure drops across different distributors

The orifice coefficients and the pressure drops across different gas distributors

* pressure drops are in mm of water

Gas velocity (m/s)	0.5	1.0	1.5	2.0	2.5	3.0
Distr. D-1						
Pressure drop	8.8	30.0	69.9	124.8	203.1	299.5
Orifice coefficient	0.74	0.80	0.79	0.79	0.77	0.75
Distr. D-2						
Pressure drop	18.1	69.9	156.7	284.8	459.8	704.7
Orifice coefficient	0.81	0.83	0.83	0.82	0.81	0.76
Distr. D-3						
Pressure drop	53.8	207.1	466.5	812.5		
Orifice coefficient	0.82	0.83	0.83	0.84		
Distr. D-4 (a laminated plate; for comparison)						
Pressure drop	12.4	48.9	115.9	206.4		
Orifice coefficient	0.84	0.84	0.82	0.82		

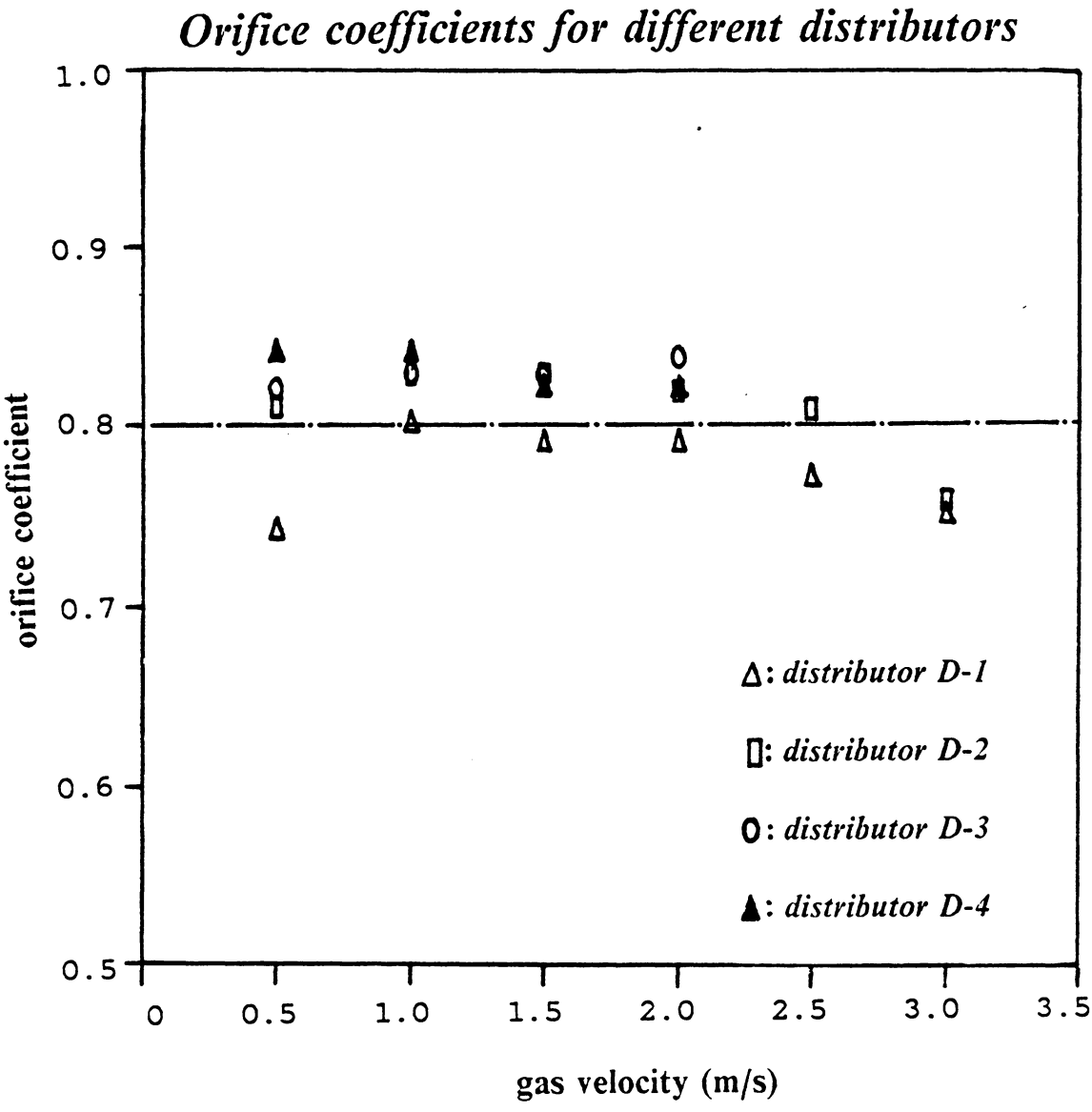

Figure 42. Orifice coefficient versus gas velocity for different distributors

1. The orifice coefficient C_o can be taken as 0.8 in designing a multi-orifice gas distributor for a fluid bed. The error in predicting pressure drop will be less than 8%.

2. For laminated plates (having very fine opening), C_o can be taken as 0.8 without introducing too much error.

3. C_o values will slightly increase as the open area ratio decreases.

4. Although the existence of particles inside the bed will affect the pressure drop across the multi-orifice distributor, it has been found that C_o values can be taken as 0.8 in Equation 4.2 for the beds with particles inside.

4.2 Manometer used for pressure studies

4.2.1 Manometer system

As shown on Figure 43 on page 152, a specially-designed pressure probe connected to a manometer filled with Meriam oil of a specific gravity of 0.827 has been used to measure the bed pressure drop and pressure distribution in shallow fluidized beds. The probe is made of 2-mm I.D. polyethylene tube. Pressure measurements are made through a hole drilled directly above the sealed end of the polyethylene tube, which is placed inside the fluidized bed. A 200-mesh screen is used to cover the hole to prevent fluidized particles from entering the manometer system.

4.2.2 Basic theory for the manometer

The force balance on the manometer depicted in the upper part of Figure 44 on page 153 can be expressed as--

$m \times a = \Sigma F$(summation of all of the forces)

= pressure force + potential force + friction force

or,

$$\frac{A_m L_m \rho_m}{g_c} \times \frac{d^2y}{dt^2} = A_m \delta P_m - 2y \rho_m A_m \times \frac{g}{g_c} - \mu_m K A_m \times \frac{dy}{dt} \qquad [4.3]$$

where

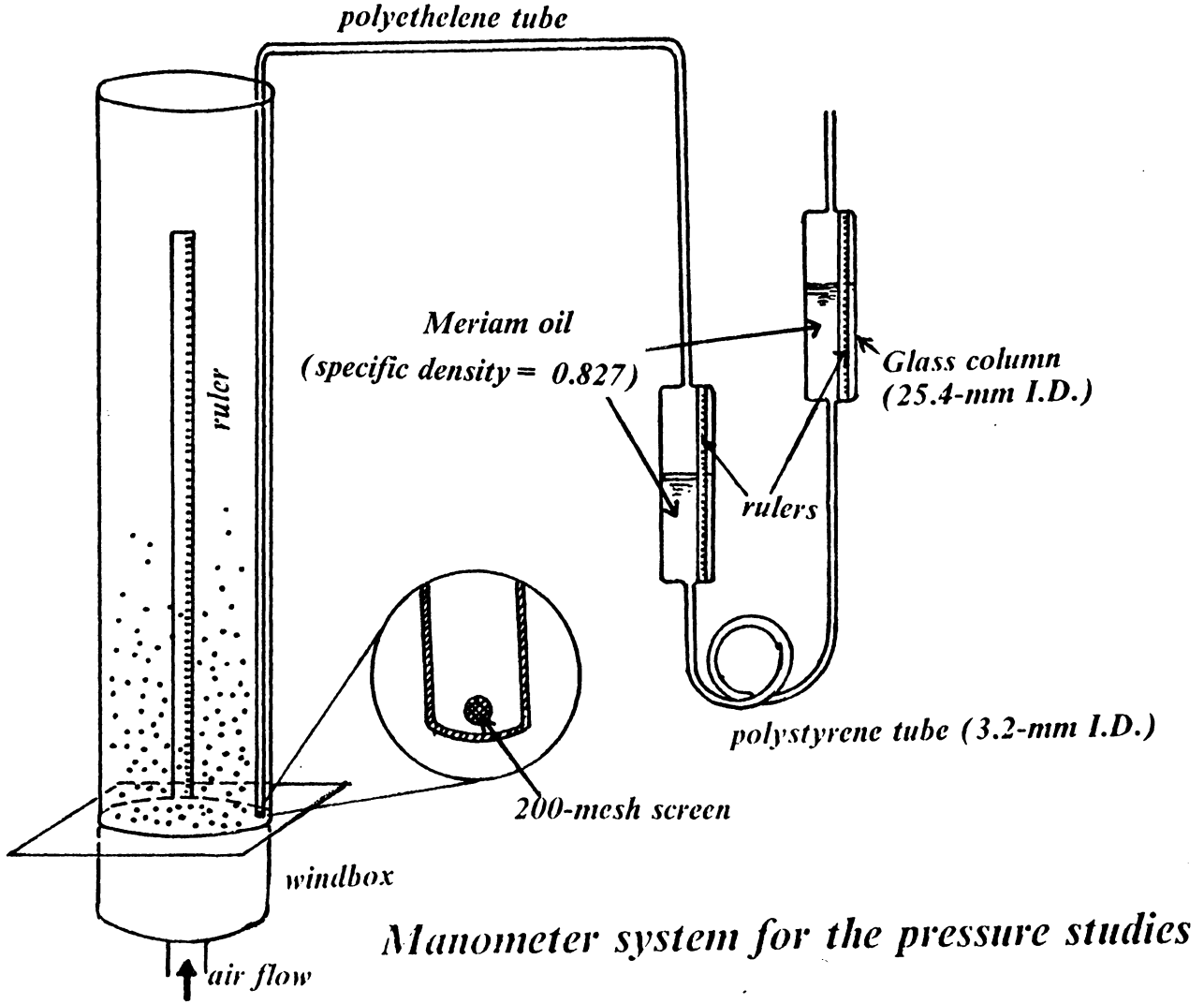

Figure 43. Design of pressure probe and manometer system

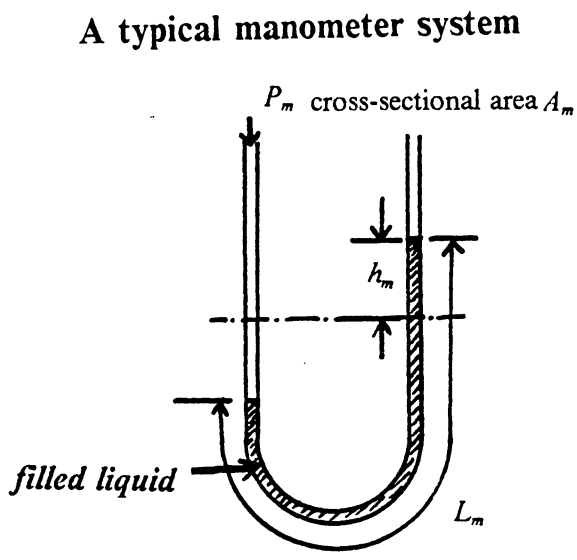

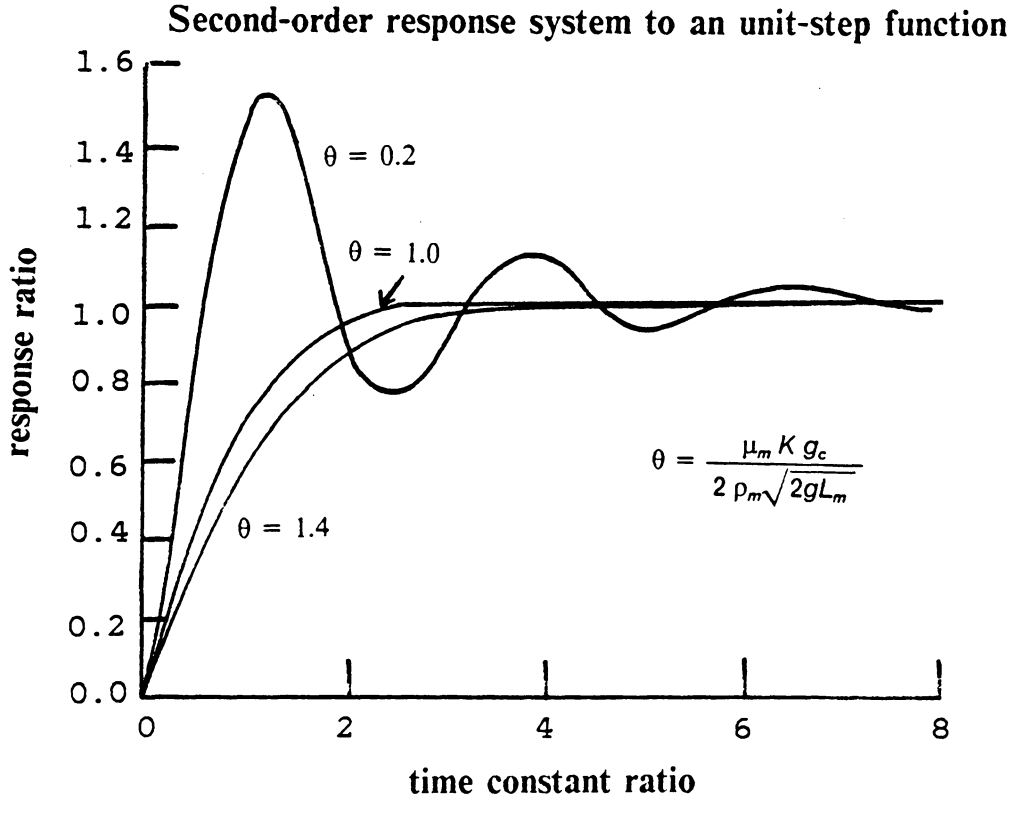

Figure 44. A typical second-order manometer system

m = total mass of the fluid in the manometer, N. ($= A_m L_m \rho_m / g_c$)

a = acceleration of the fluid, m/s^2.

A_m = cross-area of the manometer, m^2.

ρ_m = density of the fluid in the manometer, Kg/m^3 .

L_m = loaded length of the manometer, m.

g_c = gravitational constant, 9.8 $m/s^2\,Kg$.

δP_m = pressure difference applied to the manometer, $\frac{N}{m^2}$.

y = half of the height-difference of the two ends of the manometer, m.

μ_m = viscosity of the fluid in the manometer, $N\,s/m^2$.

K = resistance factor of the flow inside the manometer, dimensionless.

Equation 4.3 can be rearranged to read --

$$\frac{L_m}{2g} \times \frac{d^2y}{dt^2} + \frac{\mu_m K\, g_c}{2\,\rho_m\, g} \frac{dy}{dt} + y = \frac{\delta P_m\, g_c}{2\,\rho_m\, g} \qquad [4.4]$$

This can also be represented in the form --

$$\tau^2 \frac{d^2y}{dt^2} + 2\,\theta\,\tau \frac{dy}{dt} + y = P_a \qquad [4.5]$$

where

$$\tau = \sqrt{\frac{L_m}{2g}}$$

$$\theta = \frac{\mu_m K\, g_c}{2\,\rho_m \sqrt{2gL_m}}$$

$$P_a = \frac{\delta P_m\, g_c}{2\,\rho_m\, g}$$

Coughanowr and Koppel (1975) discuss the second-order response of a system having the general form of Equation 4.5. The response of a second-order system to a unit-step forcing function is displayed in Figure 44 on page 153. It can be seen that the response is non-

oscillatory and becomes more "sluggish" as θ-value increases above the value of 1. Actually, the response of $\theta > 1$ in a second-order system can be regarded as a result of two first-order systems in series (see Coughanowr and Koppel, 1975).

In our pressure-measurement experiments, the pressure at any specified point can fluctuate because of the vigorous solid mixing and also by the action of gas bubbles that move past the point. Therefore, a manometer having large value of θ will help us to "damp" the fluctuations and give us a meaningful time-averaged reading of the pressure. However, there is a penalty in an attempt to follow a fluctuating pressure in the form of a longer time lapse before a reading changes to a new stabilized value (e.g. compare the response curves for $\theta = 1.0$ and $\theta = 1.4$ in Figure 44 on page 153).

Design of the manometer in Figure 43 on page 152 has focused on increasing θ value in Equation 4.5. The bend connection, a thin connecting tube, and a contracting section are included for increasing the value of resistance factor K. The Meriam oil used to fill the manometer has a high viscosity and low density, two factors for further increasing the θ value.

With these design features in addition to an enlarged reading section on the manometer, we have found that the manometer can be treated as a sluggish second-order response system. This can be further confirmed by the following two observations:

1. The manometer never oscillates either when a step-change pressure difference is applied or when the pressure probe is inserted into an intensely bubbling fluidized bed with a rapidly fluctuating pressure.

2. The manometer damps a step-change pressure very slowly. For a 60-mm change in Meriam oil level, the manometer needs about 60 seconds to reach a stable reading.

Coughanowr and Koppel (1975) gave the following response equation for a step-change input function in a second- order response system:

$$Y(t) = 1 - e^{-(\theta t/\tau)} \times \left[\cosh\left(\frac{\Gamma t}{\tau}\right) + \left(\frac{\theta}{\Gamma}\right) \times \sinh\left(\frac{\Gamma t}{\tau}\right)\right] \qquad [4.6]$$

where

$\Gamma = \sqrt{\theta^2 - 1}$

t= time, in seconds.

τ = time constant, in seconds. = $\sqrt{\frac{L_m}{(2g)}}$

θ = a dimensionless group. (defined previously)

Y= y/(value of the step-change input).

For our manometer system, the time constant has been found to be 0.194 seconds when the filled section of the manometer, L_m, is 0.737 m. A rough evaluation of the above equation for our manometer system suggests that both ($\theta t/\Gamma$) and ($\Gamma t/\tau$) values are so large that a calculation of the experimental terms in Equation 4.6 is impracticable, swamping the computer program. Fortunately, Equation 4.6 can be simplified to --

$$Y(t) = 0.5\,(1 + \sigma_k)[e^{\Gamma}/e^{\theta}] \qquad [4.7]$$

by assuming that $\Gamma t/\tau > 20.0$ and setting $\sigma_k = \theta/\Gamma$.

4.2.3 Pseudo-first-order character of the manometer system

Table 18 on page 157 shows the response of the manometer after a pressure equivalent to 61-mm level of Meriam oil is applied to the system, while Figure 45 on page 158 gives a plot of the averaged Y(t) versus t/τ values. Substituting the data on Figure 45 on page 158 into the response equation proposed by Coughanowr and Koppel, Eq. 4.6, we find the θ value for our manometer to be approximately 34.0.

Figure 45 on page 158 also shows the second-order response curve of the manometer system for τ=.194 seconds and θ=34.0. It can be seen that the curve calculated from Equation 4.7 matches the experimental data very closely. This match demonstrates that the manometer system performs as a sluggish (with large θ value) second-order response system.

Table 18. Response time of the manometer system

Response time of the manometer system

with the pressure difference of 61-mm Meriam oil

pressure difference reading (mm)	raising time (seconds)					
	run1	run2	run3	run4	run5	average
50.8	2.79	2.80	2.88	2.80	2.78	2.81
40.6	5.98	5.91	5.87	5.94	5.75	5.89
30.4	9.71	9.69	9.65	9.57	9.54	9.63
20.4	14.97	14.71	14 83	14.96	15.08	14.91
15.2	18.31	18.34	18.55	18.26	18.57	14.41
10.2	23.78	23.57	23.55	23.64	23.44	23.60
5.0	31.29	31.00	30.95	31.56	30.85	31.13
2.5	39.82	40.22	39.41	38.96	38.33	39.35

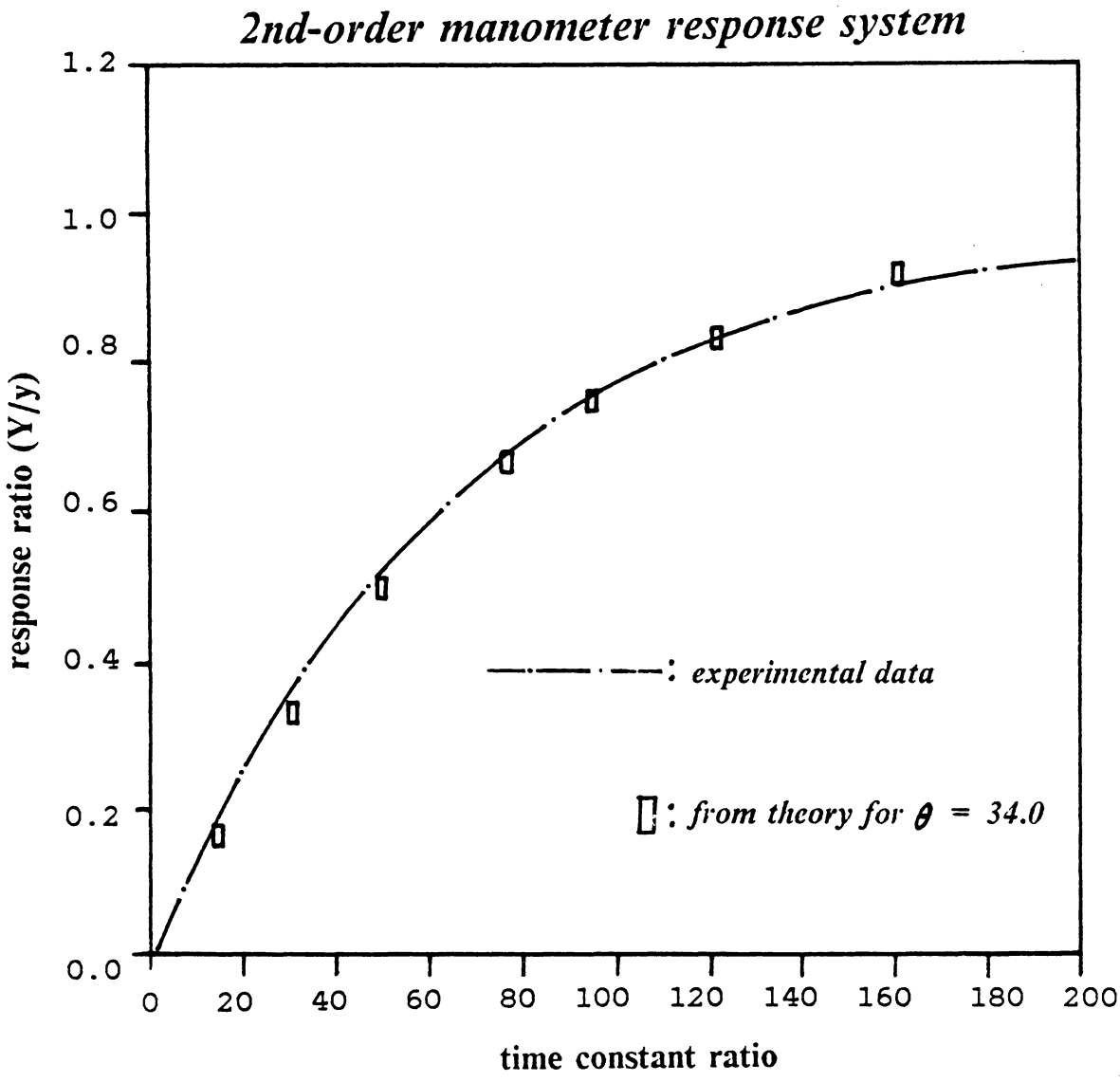

Figure 45. The averaged response ratio versus time-constant ratio

Since the system's behavior is so similar to a first-order response, we are able to apply a "pseudo-first-order" assumption to a good approximation. Figure 46 on page 160 shows the first-order time constant versus step-change in pressure difference across the manometer. In most of the experimental conditions for pressure measurements in this study, a sudden change in pressure difference can not exceed 20 mm of water. This implies that the time span for us to record the stabilized pressure difference has to be 35 seconds (about three times the time constant). Notice that the time delay has to be considered as a trade-off in order to eliminate pressure oscillations and fluctuations.

In most of our fluidized-bed experiments, gas bubbles create pressure disturbance and make the pressure measurement difficult. Fortunately, the bubble frequency is usually greater than 3 Hz, which means the roughly 10-second pseudo-first-order time constant of our manometer system will cover the disturbence of at least 30 bubbles. With its sluggish character in addition to the large reading cross-section, our manometer system has the ability to damp the pressure perturbation caused by gas bubbles and hence enables us to read the averaged pressure difference.

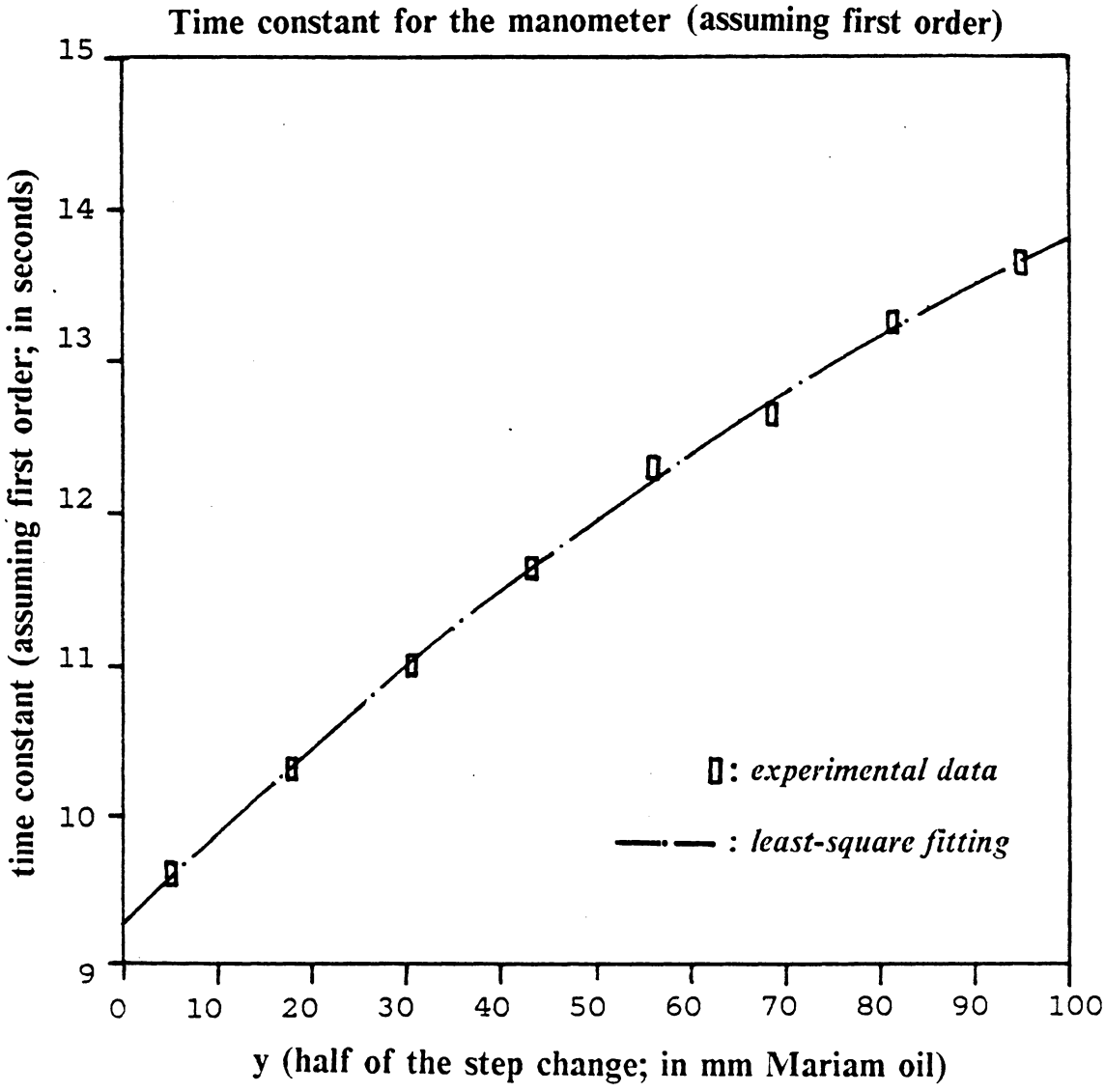

Figure 46. Time constant for the manometer under first-order assumption

4.3 Experimental results for pressure drop across shallow beds

Figure 43 on page 152 illustrates the experimental system for pressure drop measurements in a shallow fluidized bed; and the first few columns in Appendix F list the distributors, particles, and superficial gas velocities used. A set of typical pressure-drop data is listed in Table 19 on page 162, while Figure 47 on page 163 to Figure 53 on page 169 give some sample plots of pressure ratio versus static bed height under various experimental conditions. (For details on the specifications of particles and distributors, see Table 9 on page 97 and Table 10 on page 99). In these figures, the bed pressure-drop is expressed as a pressure ratio, defined as:

$$\text{pressure ratio} = \frac{\text{pressure drop across the bed}}{\text{static bed pressure}}$$

where "static bed pressure" represents the total weight of the fluidized particles divided by the cross-sectional area of the bed.

Some observations from the pressure drop study can be summarized as follows:

1. Pressure drop is "insignificant" for "very" shallow fluidized beds. Note the low pressure ratio for small static bed height in Figure 47 on page 163 to Figure 53 on page 169. This may constitute one of the key differences between shallow and deep fluidized beds.

2. At most experimental conditions, pressure ratios are below 0.8 for static bed heights less than 30 mm.

A typical set of pressure ratio versus static bed height data

Particle: P-A-2 (Master Beads)
Solid density = 3680 kg/m^3.
Particle dia. = 630 μ m.
Distributor: D-1
Open area ratio = 5.630 %
Jet diameter = 1.0 mm.
Pitch distance = 4.01 mm.
Bed: 101.6 mm. (4 inches) I.D.

PRESSURE RECOVERY-RATIO DATA:

Static bed ht. (mm)	u = 0.5 (m/s)	1.0	1.5	2.0	2.5
5.4060	0.187	0.255	0.255	0.153	-0.170
8.1090	0.420	0.465	0.511	0.443	0.250
10.812	0.528	0.605	0.605	0.579	0.485
13.515	0.654	0.695	0.688	0.647	0.565
16.218	0.664	0.732	0.732	0.721	0.607
18.921	0.715	0.774	0.774	0.735	0.671
21.624	0.762	0.796	0.796	0.783	0.711
24.327	0.764	0.817	0.821	0.791	0.738
27.030	0.807	0.841	0.838	0.804	0.739
29.733	0.830	0.861	0.842	0.821	0.768
32.437	0.843	0.869	0.849	0.817	0.781
35.140	0.831	0.862	0.862	0.831	0.783
37.843	0.866	0.873	0.864	0.837	0.796
40.546	0.858	0.874	0.865	0.829	0.802
43.249	0.864	0.879	0.864	0.832	0.803
45.952	0.860	0.878	0.858	0.833	0.813
48.655	0.882	0.882	0.865	0.836	0.806
51.358	0.875	0.882	0.860	0.837	0.819
54.061	0.899	0.886	0.860	0.831	0.814
59.467	0.912	0.890	0.862	0.845	0.834
64.873	0.901	0.891	0.866	0.856	0.844
70.279	0.904	0.893	0.872	0.862	0.853
75.685	0.895	0.900	0.879	0.870	0.862
86.497	0.919	0.903	0.884	0.881	0.861
97.310	0.900	0.901	0.891	0.873	0.861

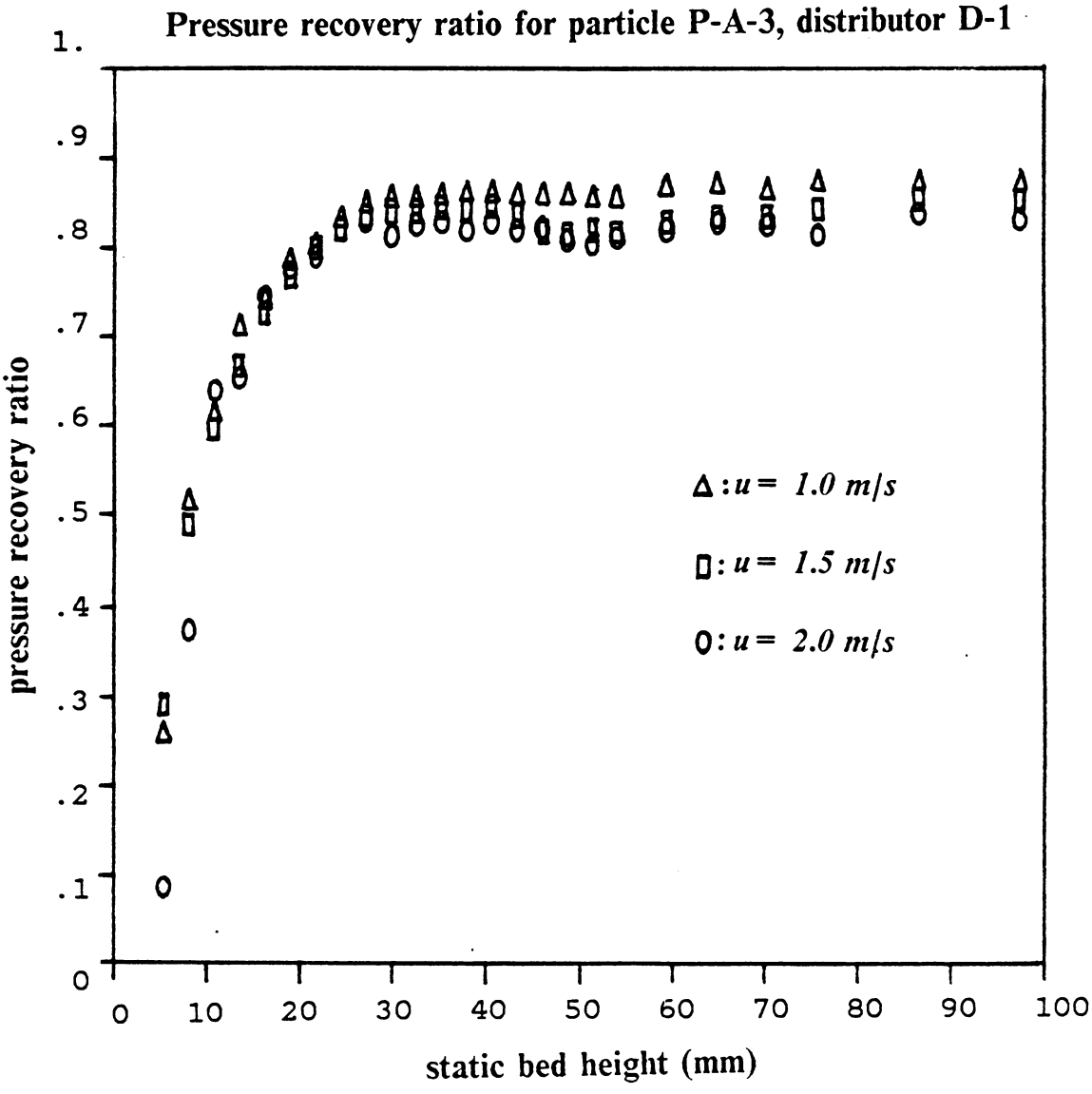

Figure 47. Pressure recovery ratio versus static bed height for distributor D-1, particle P-A-3: (335-micron Master Beads in the bed having 5.6% perforated distributor)

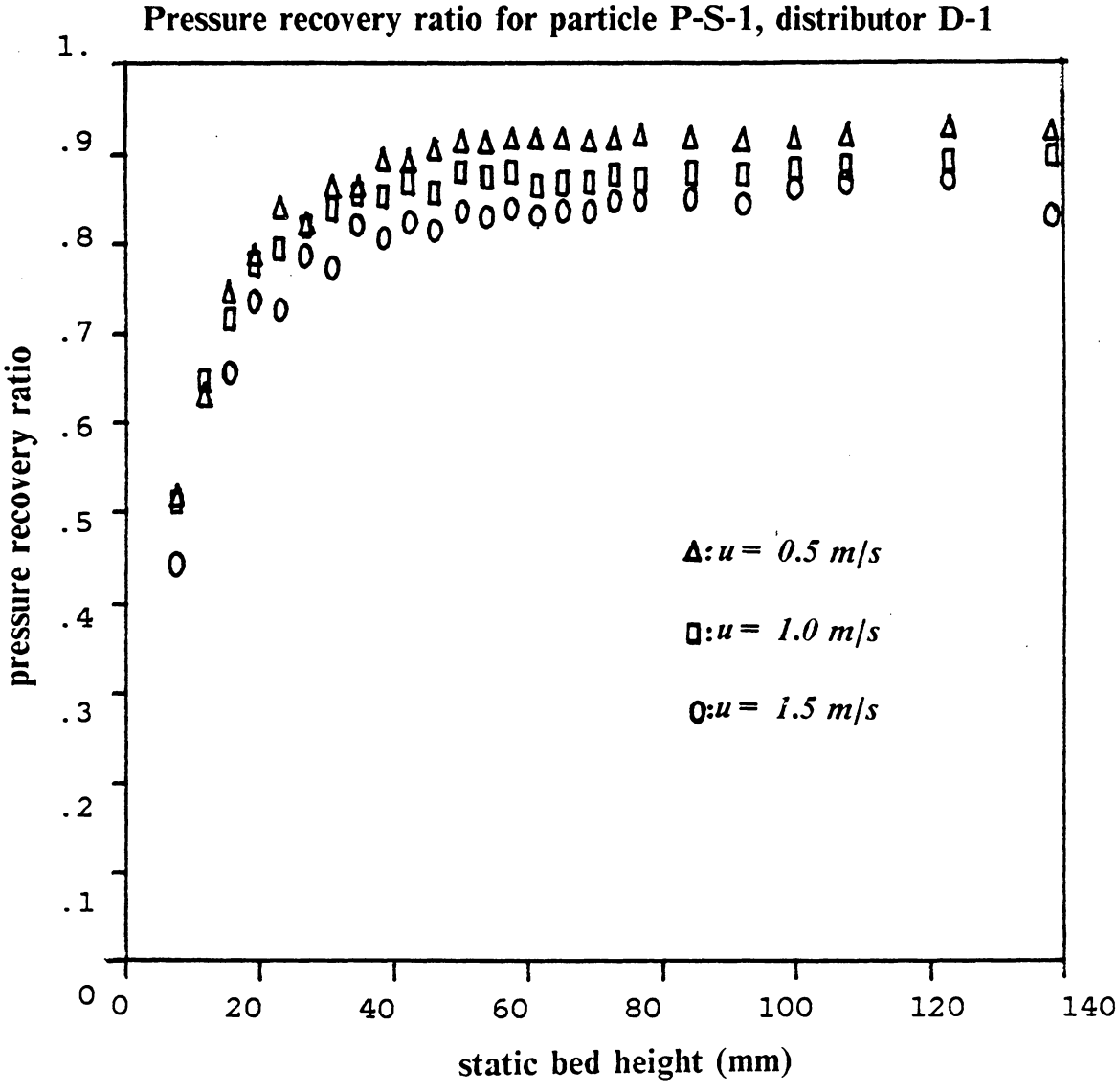

Figure 48. Pressure recovery ratio versus static bed height for distributor D-1, particle P-S-1.: (630-micron sands in the bed having 5.6% perforated distributor)

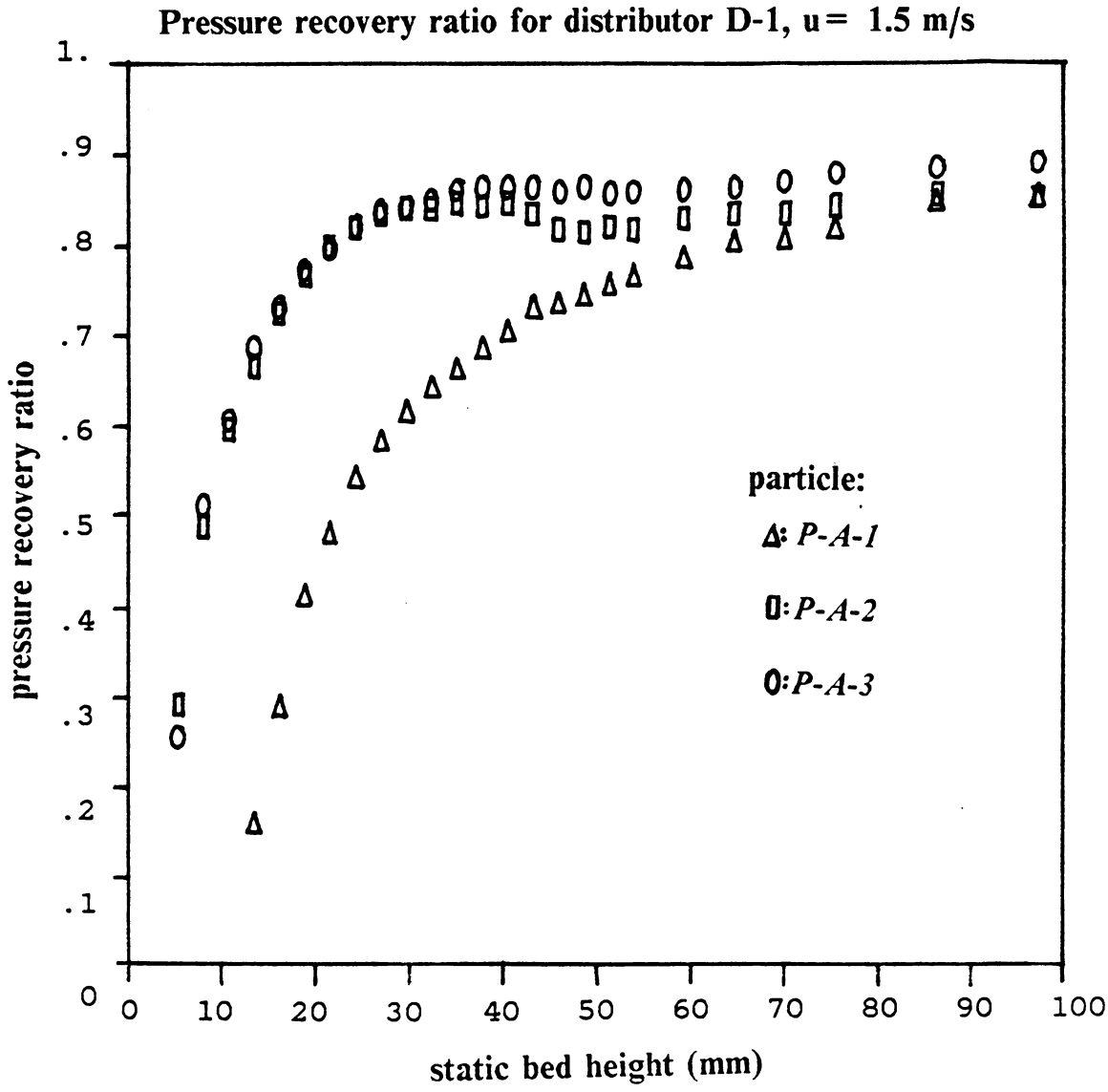

Figure 49. **Pressure recovery ratio versus static bed height for distributor D-1, 1.5 m/s.:** (5.6% perforated distributor with gas velocity = 1.5 m/s for different sized Master Beads.)

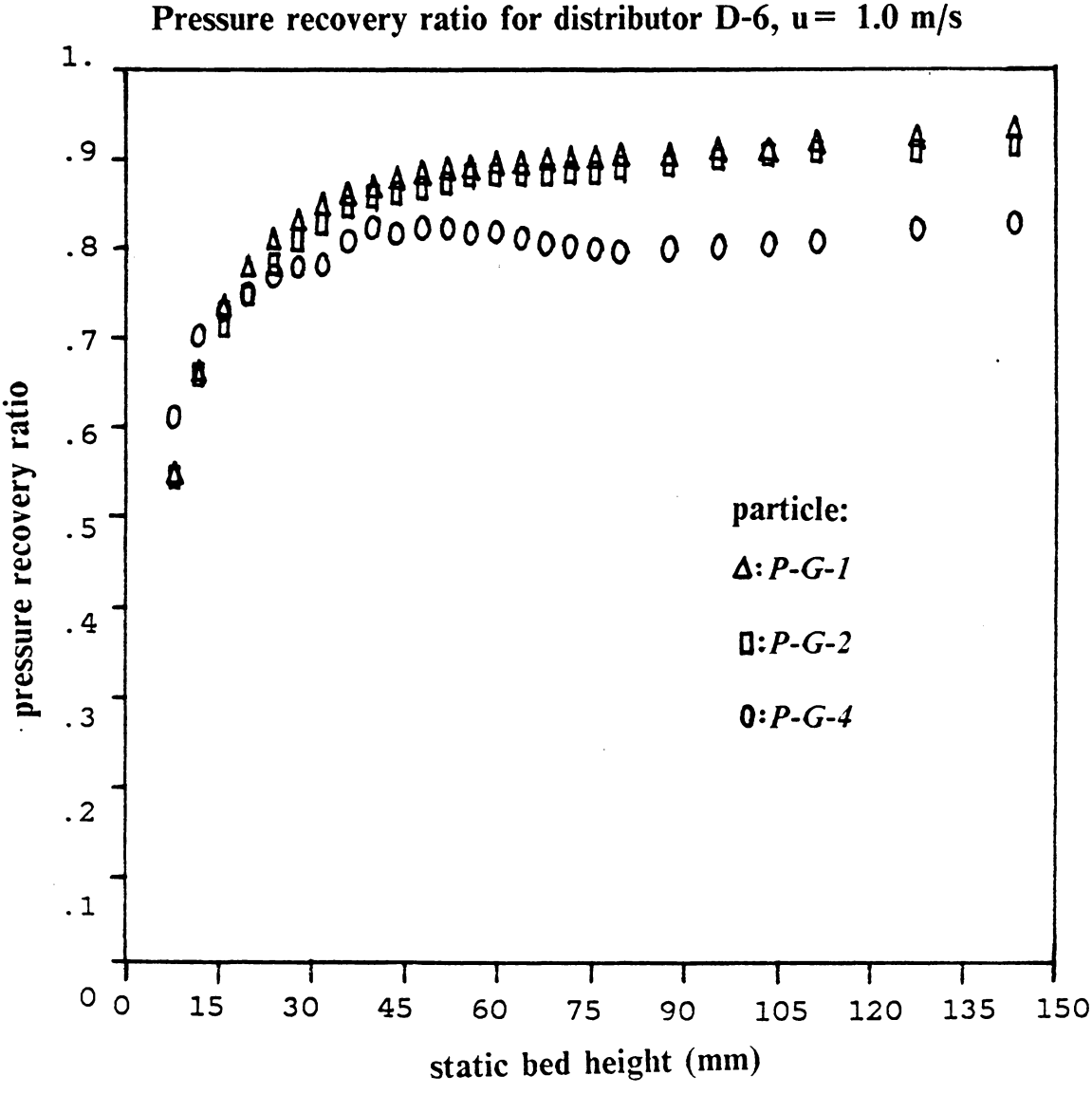

Figure 50. Pressure recovery ratio versus static bed height for distributor D-6, 1.0 m/s.: (9% open area laminated distributor for different sized glass beads.)

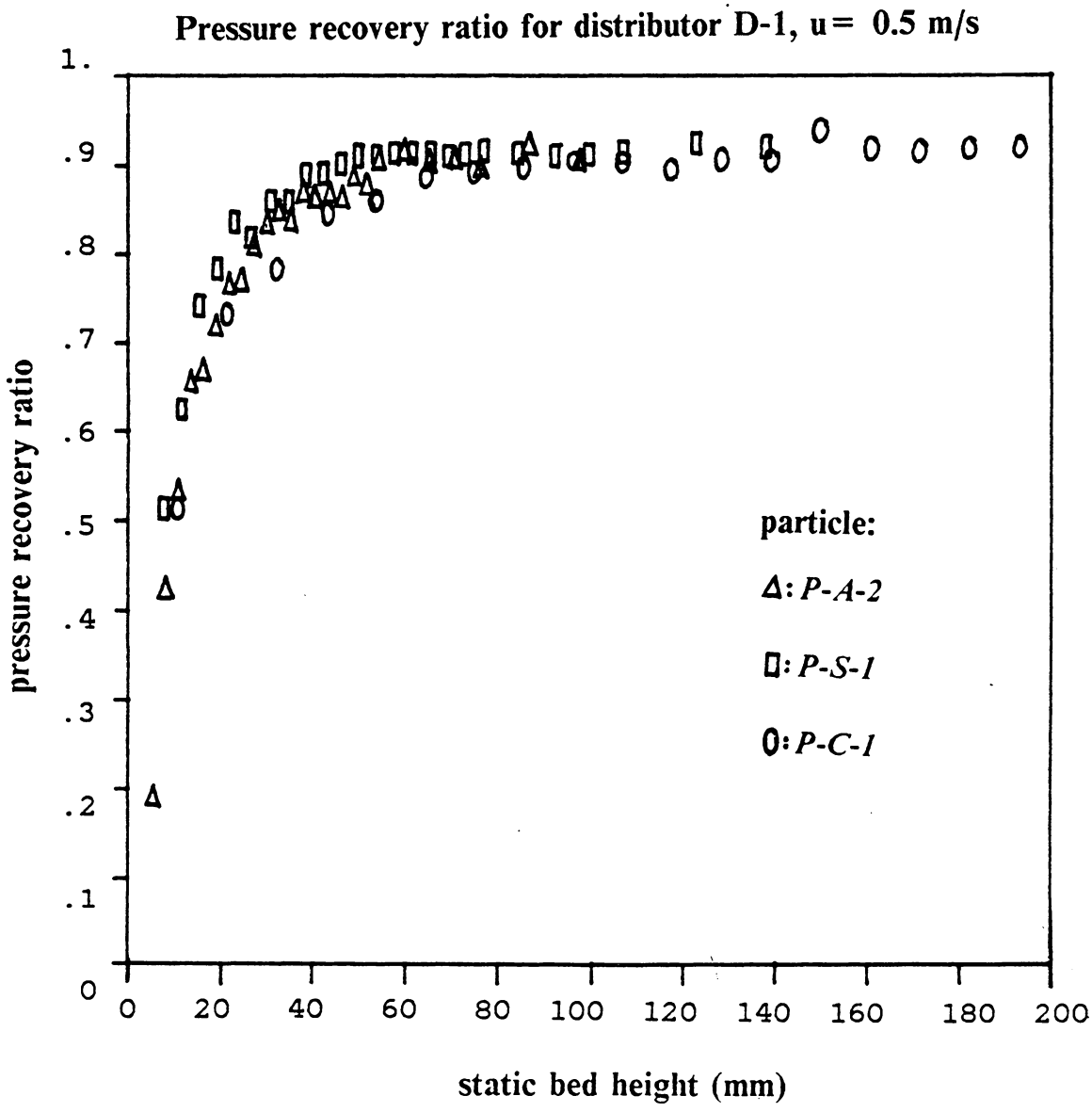

Figure 51. Pressure ratio versus static bed height for distributor D-1, 0.5 m/s.: (The bed having 5.6% perforated distributor with gas velocity = 0.5 m/s)

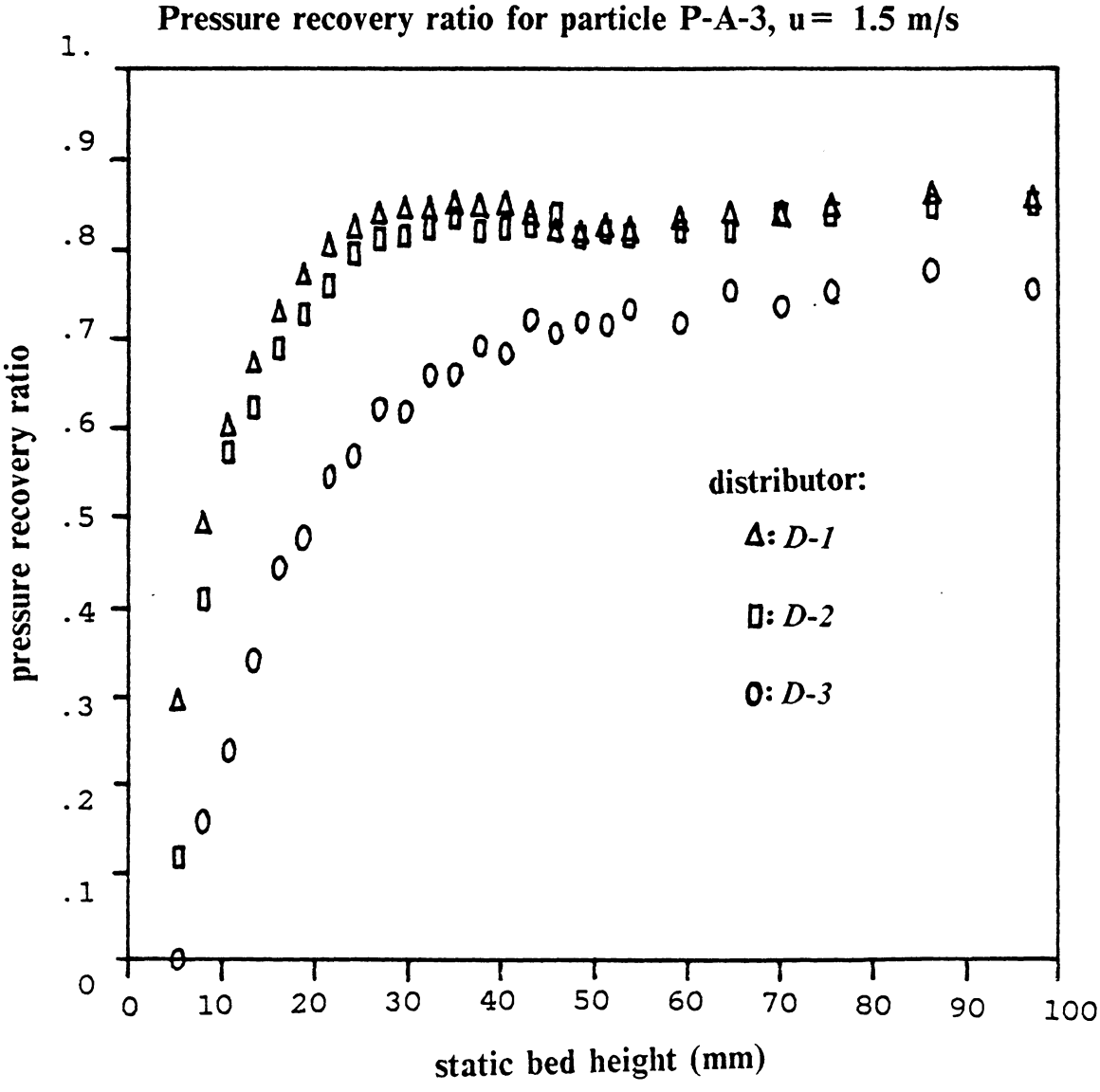

Figure 52. **Pressure recovery ratio versus static bed height for particle P-A-3, 1.5 m/s. for perforated distributors:** (335-micron Master Beads fluidized in the bed having gas velocity 1.5 m/s)

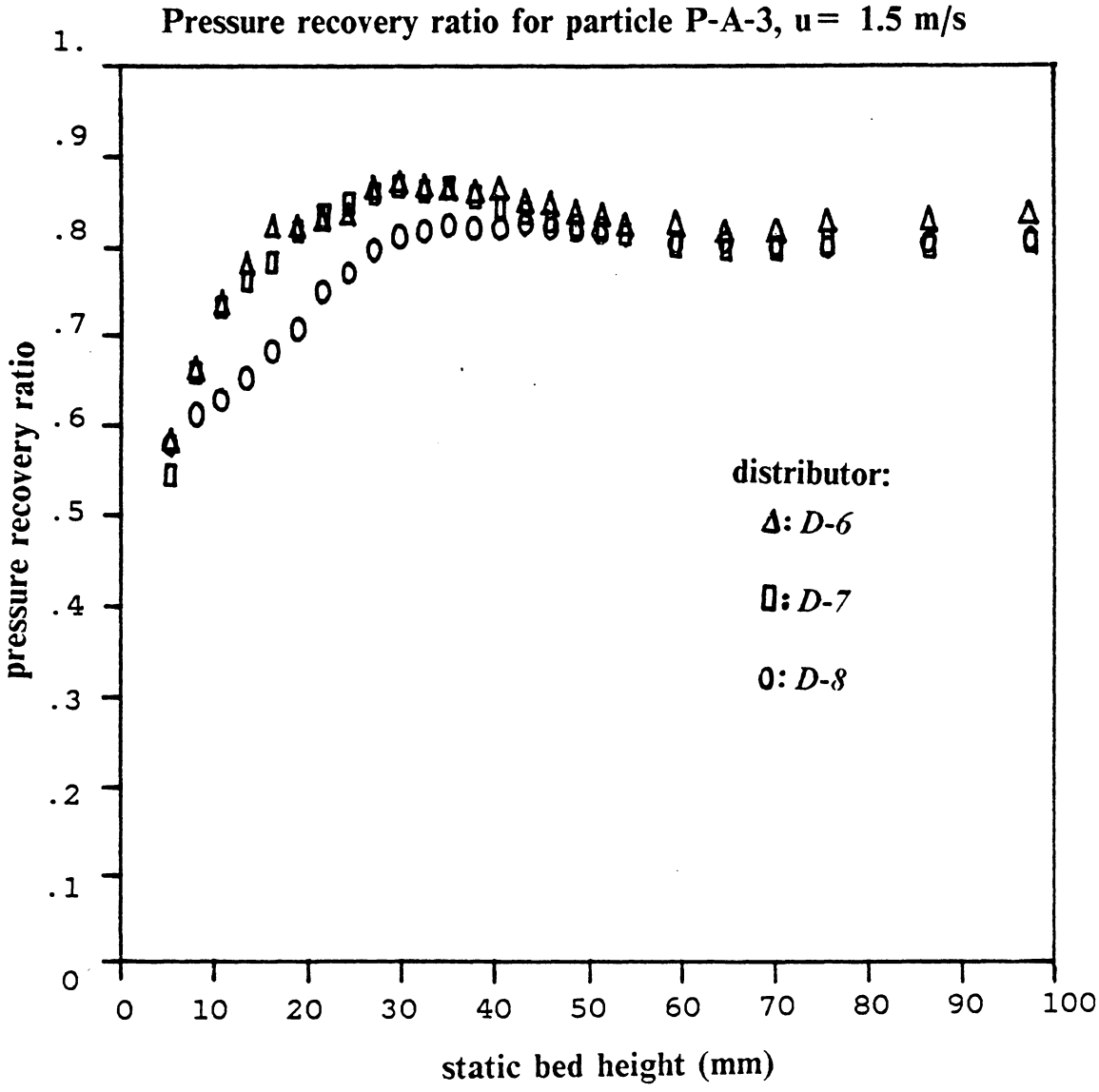

Figure 53. Pressure recovery ratio versus static bed height for particle P-A-3, 1.5 m/s. for laminated distributors: (the 335-micron Master Beads fluidized in the bed having gas velocity 1.5 m/s)

3. Increasing the open area percentage or increasing the superficial fluidizing velocity will generally decrease the bed pressure drop. However, for beds with distributors of large open area percentage, the bed pressure drop becomes essentially independent of superficial fluidizing velocity for a wide range of static bed heights. (See Figure 52 on page 168 and Figure 53 on page 169.)

4. For shallow beds of smaller particles, the bed pressure recovery ratio becomes essentially independent of superficial fluidizing velocity. (See Figure 47 on page 163)

5. The pressure recovery ratio increases with increasing particle size, especially when the bed is deep. (See Figure 49 on page 165)

6. Under fixed fluidizing conditions, a bed of particles of low density will display a small pressure recovery ratio when the bed is shallow. However, the pressure recovery ratio becomes independent of particle density as the bed height increases into a certain range. (See Figure 51 on page 167)

We have discovered that a very simple equation can be used to represent the relationship between the pressure recovery ratio and static bed height:

$$PR = \alpha - \frac{\beta}{H_s} \qquad [4.8]$$

where

PR = pressure recovery ratio.

H_s = static bed height.

α,β = two constants depending on experimental conditions (gas velocity, particle, and distributor).

A computer program utilizing the pattern (Hookes and Jeeves) search method (Bazaraa and Shetty, 1979) has been used to find a least-square fit of Equation 4.8 for all experimental

conditions. The last three columns of Appendix F list the fitted α and β values in conjunction with R-square values. (Notice that the R value represent the correlation coefficient between experimental data and values calculated from the least-square fitted correlation equation). Figure 54 on page 173 shows an example of experimental data and least-square fitted curves following Equation 4.8. Table 20 on page 172 lists values of R, R-square, and standard deviation of R-square for the data collected for all distributors. The average R value is 0.984 for all of the data, and we can conclude that Equation 4.8 gives a highly satisfactory description of the relationship between pressure recovery ratio and static bed height.

Table 20. Data for the least-square fitting of orifice design equation

The statistical information for the least-square fitting of Equation 4.1

Distributor label	No. of data set	R	R-square	sta. dev. of R-square
ALL	117	0.9844	0.9690	0.0398
D-1	25	0.9899	0.9800	0.0173
D-2	29	0.9918	0.9836	0.0129
D-3	24	0.9847	0.9696	0.0262
D-5	15	0.9718	0.9444	0.0562
D-6	12	0.9688	0.9355	0.0769
D-7	12	0.9852	0.9706	0.0402

Notes:

R : the correlation coefficient between the given and predicted data.
R-square : R^2, direct output value from SAS PROGRAMS.

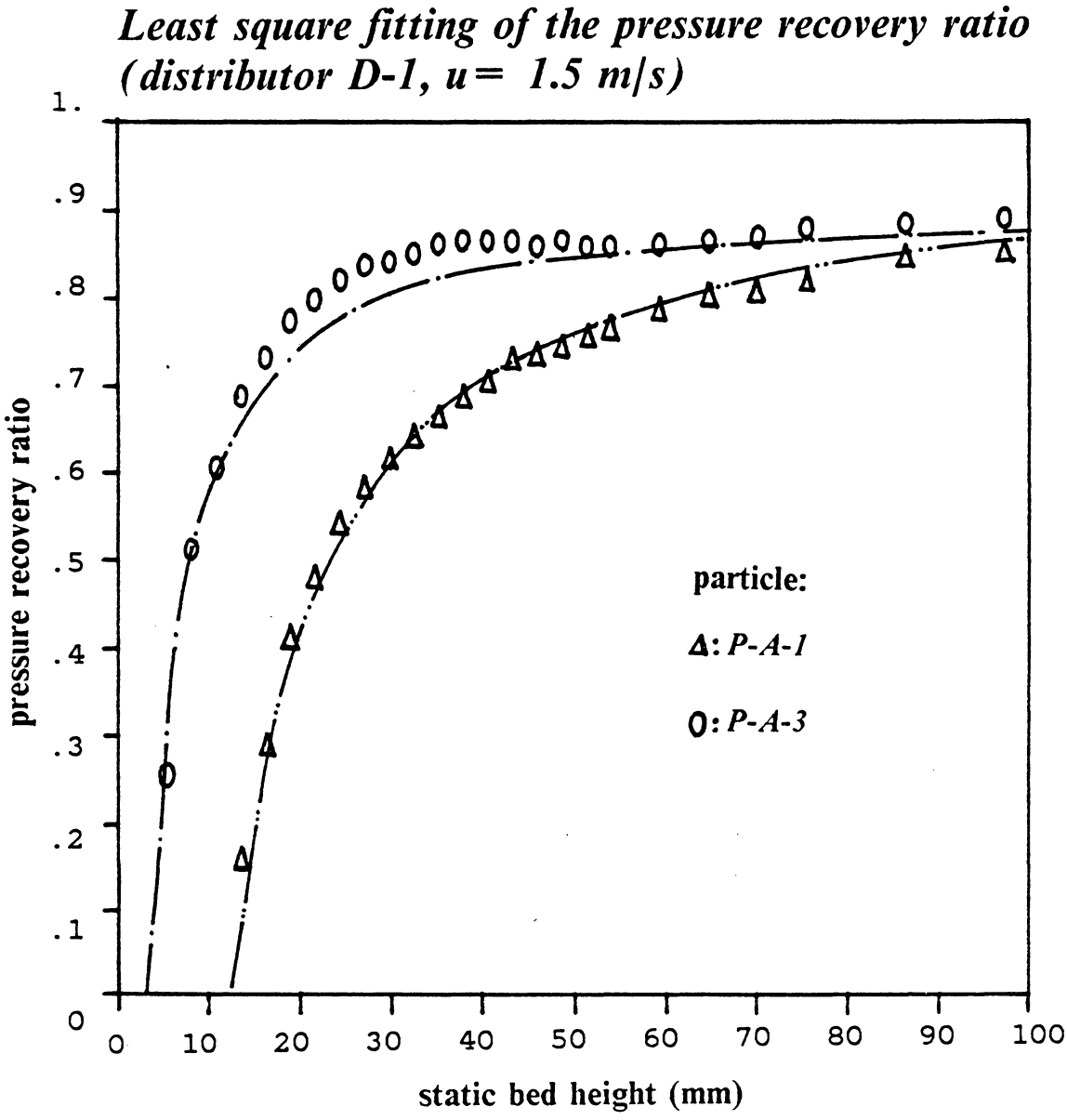

Figure 54. Experimental data comparing with the least-square fitted curves for pressure recovery ratio data

4.4 Theory and discussion for pressure ratio

A force balance on the fluidized particles will provide us a quantitative interpretation of the preceding experimental results. Briefly, the total weight of fluidizing particles must be equal to the sum of different forces supporting the particles. Specifically, one may write the following force balance equation for a fluidized bed:

total weight of fluidizing particles
= sum of supporting forces
= (pressure drop across the bed) × (bed area)
+ (pressure recovery in the jets) × (bed area)
+ bouncing force between the distributor and particles
+ shear forces between the bed wall and particles.

This can be expressed mathematically as --

$$\rho_p(1 - \varepsilon_s)A_bH_s = P_bA_b + P_rA_b + f_bA_b + \tau_w(\pi D)H_f \qquad [4.9]$$

In the equation, the different notations are defined as follows --

ρ_p = solid density, Kg/m^3

ε_s = static voidage of the bed, dimensionless.

A_b = cross-sectional area of the bed, m^2

H_s = static bed height, m

H_f = fluidized-bed height, m

P_b = measured pressure drop across the bed, N/m^2

P_r = pressure loss recovered in the jets (or in high-velocity air streams, however small and dispersed), N/m^2

f_b = bouncing force between the distributor and particles per unit area, N/m^2

τ_w = shear stress between the bed wall and particles, N/m^2

D = bed diameter, m

Rearranging Equation 4.9 gives the following --

$$\text{PR (pressure ratio)} = \frac{\text{(bed pressure drop)}}{\text{(static bed weight)}}$$

$$= \frac{P_b}{\rho_p(1-\varepsilon_s)H_s}$$

or,

$$\text{PR} = 1 - \tau_w \frac{\pi D H_f}{\rho_p(1-\varepsilon_s)H_s A_b} - \frac{P_r + f_b}{\rho_p(1-\varepsilon_s)H_s} \qquad [4.10]$$

Note that the fluidized bed height, H_f, can be related to the static bed height, according to --

$$H_f = H_s \times \frac{1-\varepsilon_s}{1-\varepsilon_f}$$

where ε_f is the bed voidage under fluidizing conditions. The above two equations can be combined and simplified to give --

$$\text{PR} = \alpha - \frac{\beta}{H_s}$$

where

$$\alpha = 1 - \frac{\tau_w}{\rho_p R_h(1-\varepsilon_f)} \qquad [4.11]$$

$$\beta = \frac{f_d}{\rho_p(1-\varepsilon_s)} \qquad [4.12]$$

and,

$$f_d = P_r + f_b$$

We define a new variable, f_d, the recovered pressure (from jet streams and from the bouncing of the particles). The above expression for PR has the same form as Equation 4.8. Notice that the bed diameter (D) should be replaced by four times the hydraulic radius (R_h) for a fluid bed in non-cylindrical equipment. The hydraulic radius can be taken as the cross-sectional area of the bed divided by the wetted perimeter. ($R_h = D/4$ for a cylindrical bed; see Bird et al. 1960.)

From values of α and β in Table 19 on page 162, we can calculate f_d and τ_w values according to Equations 4.11 and 4.12. All variables in those two equations are known from experiments except for ε_f. Fortunately, Staub and Canada (1978) proposed a generalized correlation for bed expansion ---

$$\frac{u}{\varepsilon_f} = \frac{(1 - \varepsilon_s)u_{mf}}{\varepsilon_s} + uC_o \qquad [4.13]$$

where u_{mf} is the minimum fluidizing velocity. Taking C_o as 1.05, Staub and Canada obtained voidage values agreeing with experiment with deviation of less than $\pm 12\%$. Because these authors investigated a wide range of gas velocities, their correlation has been used frequently in the subsequent literature.

Table 21 on page 177 lists correlation coefficients for f_d and τ_w versus all of the experimental variables and dimensionless groups. Notice that correlation coefficients for the logarithm of some of the variables are also listed for clarity of the comparison.

A computer package for statistical analysis (release 82.4 of SAS) has been used to study the possible correlations for f_d and τ_w by checking all variables and dimensionless groups. The R-square value has been used as an indicator for the validity of a given correlation provided that the dimensionless groups involved in the correlation follow reasonable physical

Table 21. Correlation coefficients for friction factors in shallow beds.

Correlational coefficients for f_d and τ_w versus R_e,F_r,A_m (three dimensionless groups which are used most often for the study of momentom transfer in fluidized beds) and ρ_r.

predicted variable	parameter	R-square
f_d	R_e,F_r	0.806
f_d	R_e',F_r'	0.810
f_d	R_e',F_r	0.806
f_d	R_e,F_r,A_m	0.806
f_d	R_e',F_r',A_m	0.812
$\ln(f_d)$	$\ln(R_e)$, $\ln(F_r)$	0.666
$\ln(f_d)$	$\ln(R_e')$, $\ln(F_r')$	0.666
$\ln(f_d)$	$\ln(R_e')$, $\ln(F_r)$	0.666
$\ln(f_d)$	$\ln(R_e)$, $\ln(F_r)$, $\ln(A_m)$	0.762
$\ln(f_d)$	$\ln(R_e')$, $\ln(F_r')$, $\ln(A_m)$	0.783
τ_w	ρ_r	0.288
τ_w	ρ_r,R_e,F_r	0.335
τ_w	ρ_r,R_e',F_r'	0.307
τ_w	ρ_r,R_e,F_r,A_m	0.335
τ_w	ρ_r,R_e',F_r',A_m	0.348
$\ln(\tau_w)$	$\ln(\rho_r)$	0.331
$\ln(\tau_w)$	$\ln(\rho_r)$, $\ln(F_r)$	0.384
$\ln(\tau_w)$	$\ln(R_e)$, $\ln(F_r)$	0.029

Table 22. Correlation coefficients for friction factors versus different dimensionless groups

Correlational coefficients for: f_d and τ_w

	f_d	$\ln(f_d)$	τ_w	$\ln(\tau_w)$
ρ_r	0.376	0.439	0.537	0.554
ε_s	-0.195	-0.212	0.155	0.179
d_p	0.354	0.267	-0.102	-0.148
d_j	0.625	0.744	0.000	-0.112
A_r	-0.559	-0.659	0.167	0.250
u	0.429	0.298	0.032	0.025
u_{mf}	0.427	0.351	0.139	0.188
R_e	0.849	0.741	0.089	-0.020
F_r	0.775	0.885	0.222	0.098
A_m	0.326	0.320	0.010	-0.005
ρ_r	0.376	0.439	0.537	0.554
R_e	0.852	0.747	0.092	-0.019
F_r	0.886	0.760	0.078	-0.013
$\ln(R_e)$	0.769	0.757	-0.036	-0.145
$\ln(F_r)$	0.885	0.775	0.222	0.098
$\ln(A_m)$	0.245	0.228	-0.015	-0.057
$\ln(\rho_r)$	0.353	0.417	0.516	0.575

Note: all variables are defined previously.

R_e = Reynold number.
F_r = Froude number.
A_m = Archimede number

ρ_r = density ratio
$R_e' = R_e \times (1 - A_r)$
$F_r' = F_r \times (1 - A_r)$

explanations. Table 22 on page 178 gives R-square values for all of the possible correlations examined by the SAS programs.

The following correlation equation for f_d gives an R-square value of 0.806 (i.e., a correlation coefficient, R = 0.898)

$$f_d = 471.54 + 111.05 \times Re + 0.1572 \times Fr \qquad [4.14]$$

where Fr = Froude number for the particle-fluid system, defined as --

$$Fr = (\frac{u_o^2}{gD})(\frac{\rho_p - \rho_f}{\rho_f})$$

Re = Reynolds number for particle near the distributor --

$$R_e = \frac{\rho_f d_p u_o}{\mu_f}$$

ρ_f = density of the fluid, Kg/m^3

μ_f = viscosity of the fluid, Kg/m s

g = gravitational constant, 9.8 for S.I. units.

Figure 55 on page 181 and Figure 58 on page 184 show plots of predicted f_d values versus experimental data for all particles: Master Beads, glass beads, and sands. The correlation equations predict most of the values within a fair range. Checking the physical meaning of the dimensionless groups will give us a better understanding of the Equation 4.14:

1. The Froude number, Fr, is an indicator of momentum transfer between gas jets and fluidized particles (see Filla et al. 1983). Therefore, the last term in Equation 4.14 can roughly represent the pressure loss recovered in the jets (i.e. the P_r term included in f_d)

2. The first two terms roughly represent the value of f_b, the bouncing force per unit area of the distributor. Note that the Reynolds number appearing in Equation 4.14 is based on the

velocity of the gas stream passing the distributor. This implies that the bouncing force is highly determined by the turbulence introduced by jet streams near the gas distributor.

The prediction of τ_w has involved difficulty: the correlation coefficients between τ_w and all experimental variables other than ρ_s are less than 0.2. However, a correlation having R-square of 0.331 (R=0.575) has also been obtained from the SAS programs--

$$\tau_W = 6.49 \times 10^{-5} \rho_r^{1.286} \qquad [4.15]$$

where

$\rho_r = (\rho_p - \rho_f) / \rho_f$ = density ratio.

Figure 59 on page 185 shows a plot of the number of data points versus the percentage error of the predicted τ_w. A standardized normal distribution curve which shows a standard deviation of 40.9% is also plotted for the comparison. The unsatisfactory correlation provided by Equation 4.15 can be explained as follows: the shear stress between the rig wall and fluidizing particles, τ_w, can be highly affected by the size of the rig. Since we used a fluidized bed of only one size in obtaining all of the pressure ratio data, we may not have sufficient data to enable us to find a generalized correlation.

Appendix A gives an example demonstrating an advantage of multi-staged shallow fluidized bed in comparison with a single deep bed. The simulation program shows that pressure drop across a fluidized-bed system can be reduced by about 43% by dividing a single deep bed (with static bed height of 2000-mm) into forty staged shallow beds.

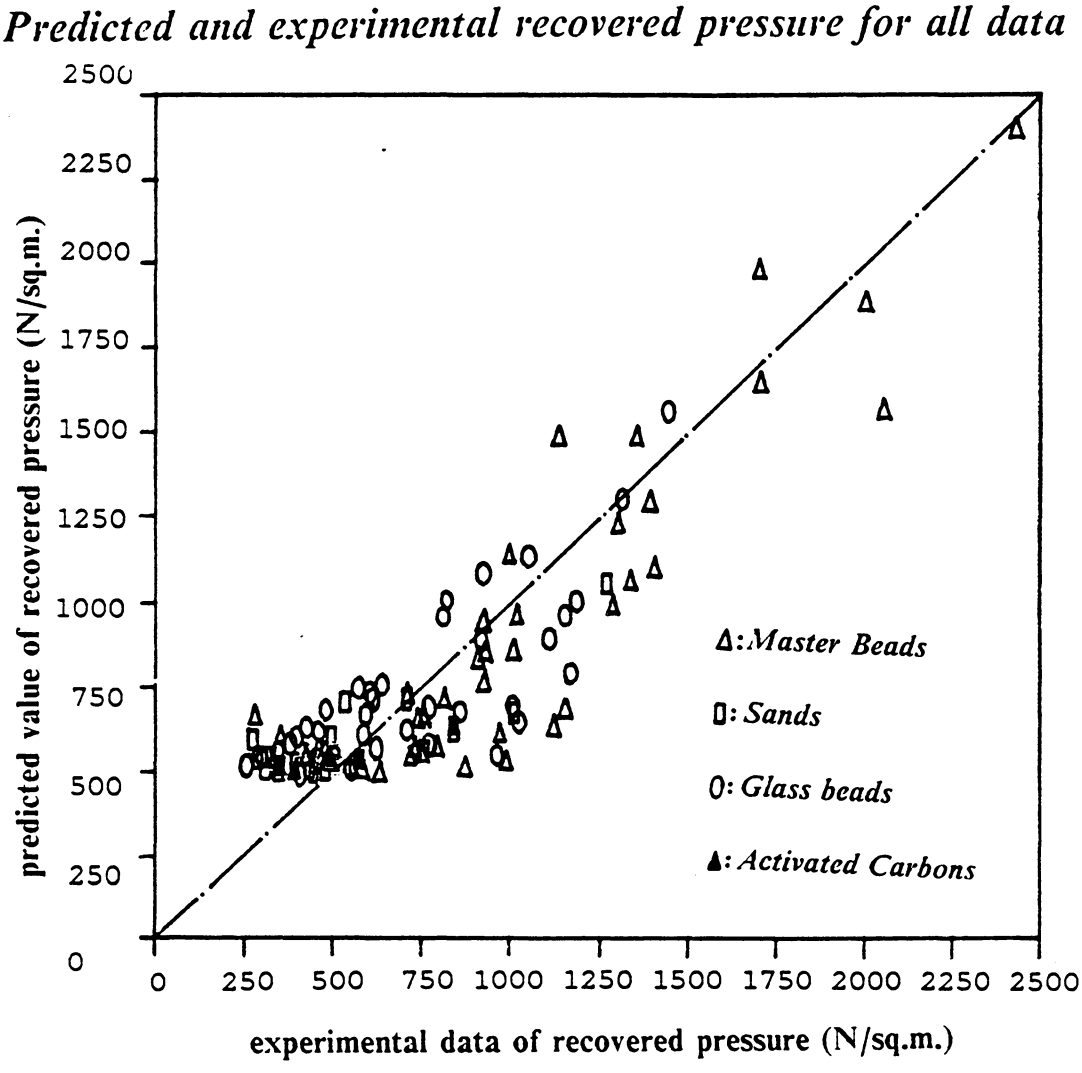

Figure 55. Predicted recovered pressure versus experimental data for all particles

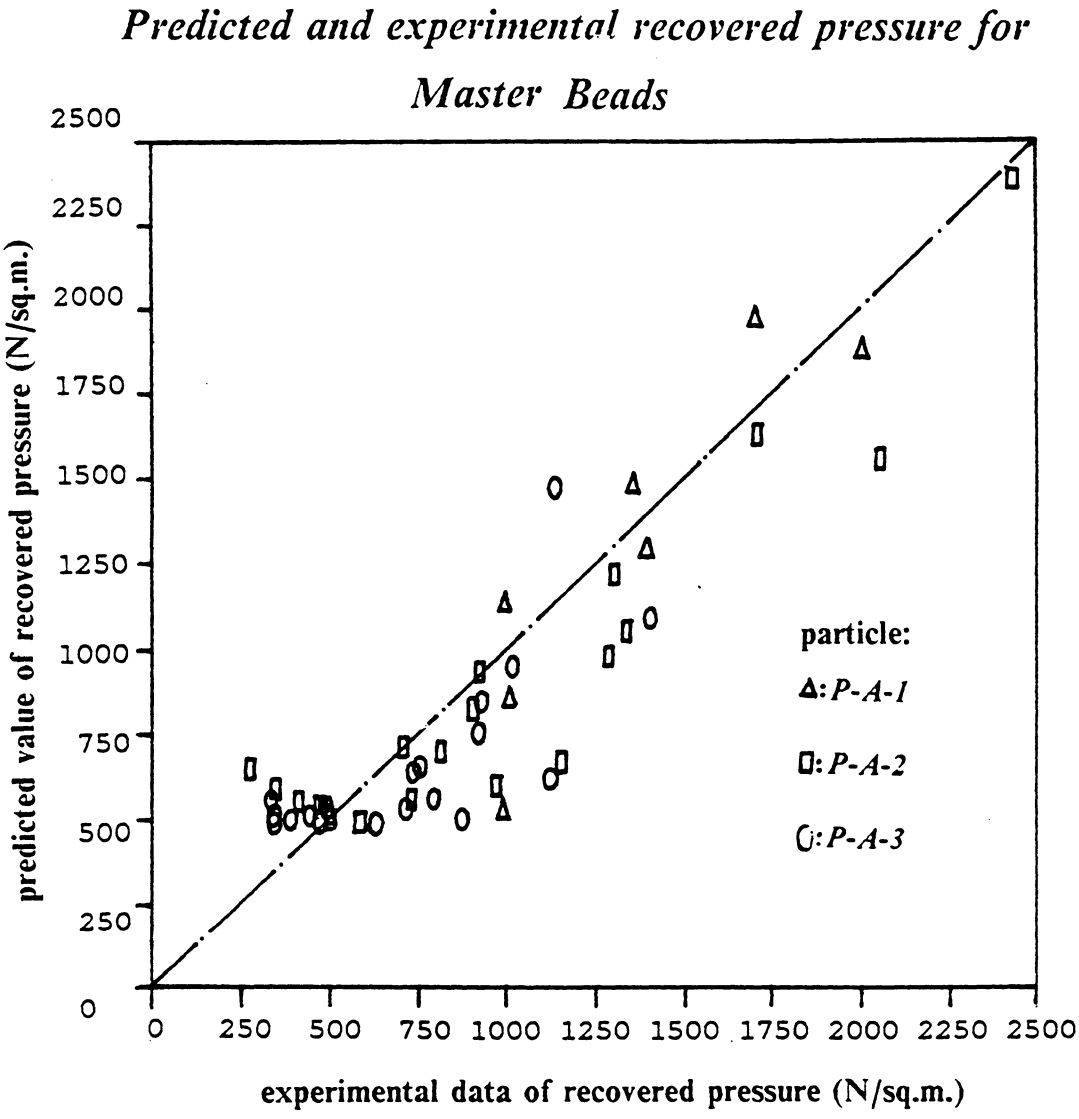

Figure 56. Predicted recovered pressure versus experimental data for Master Beads

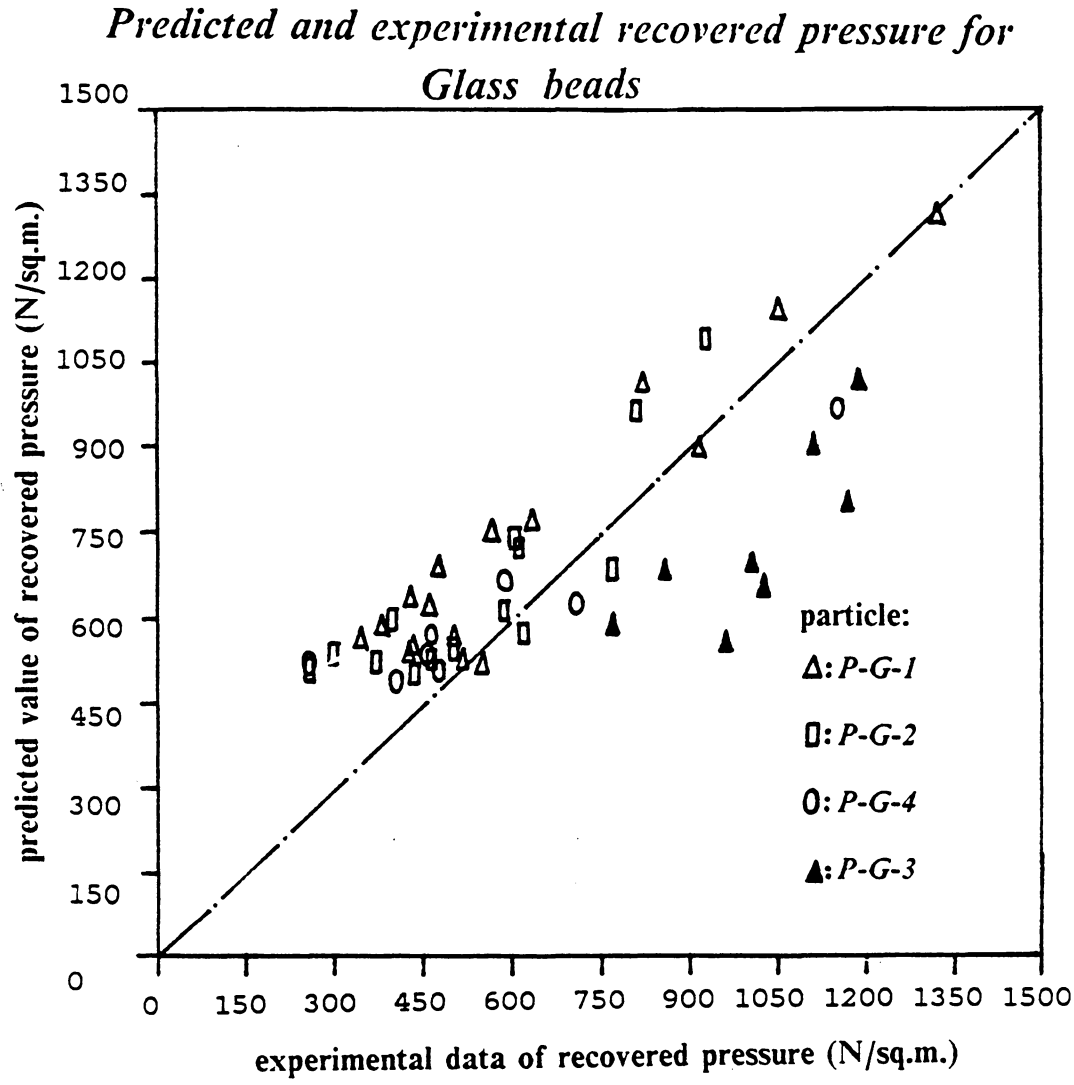

Figure 57. Predicted recovered pressure versus experimental data for glass beads

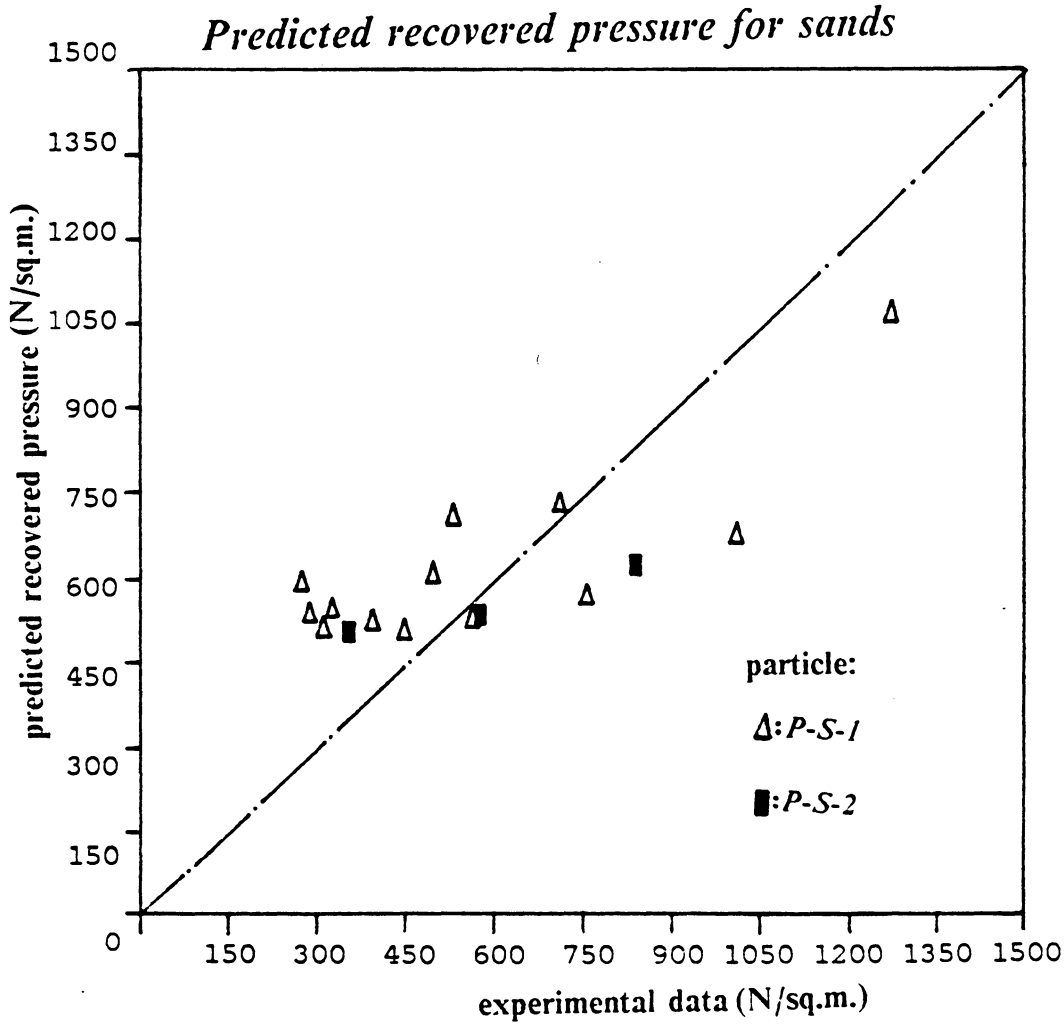

Figure 58. Predicted recovered pressure versus experimental data for sands

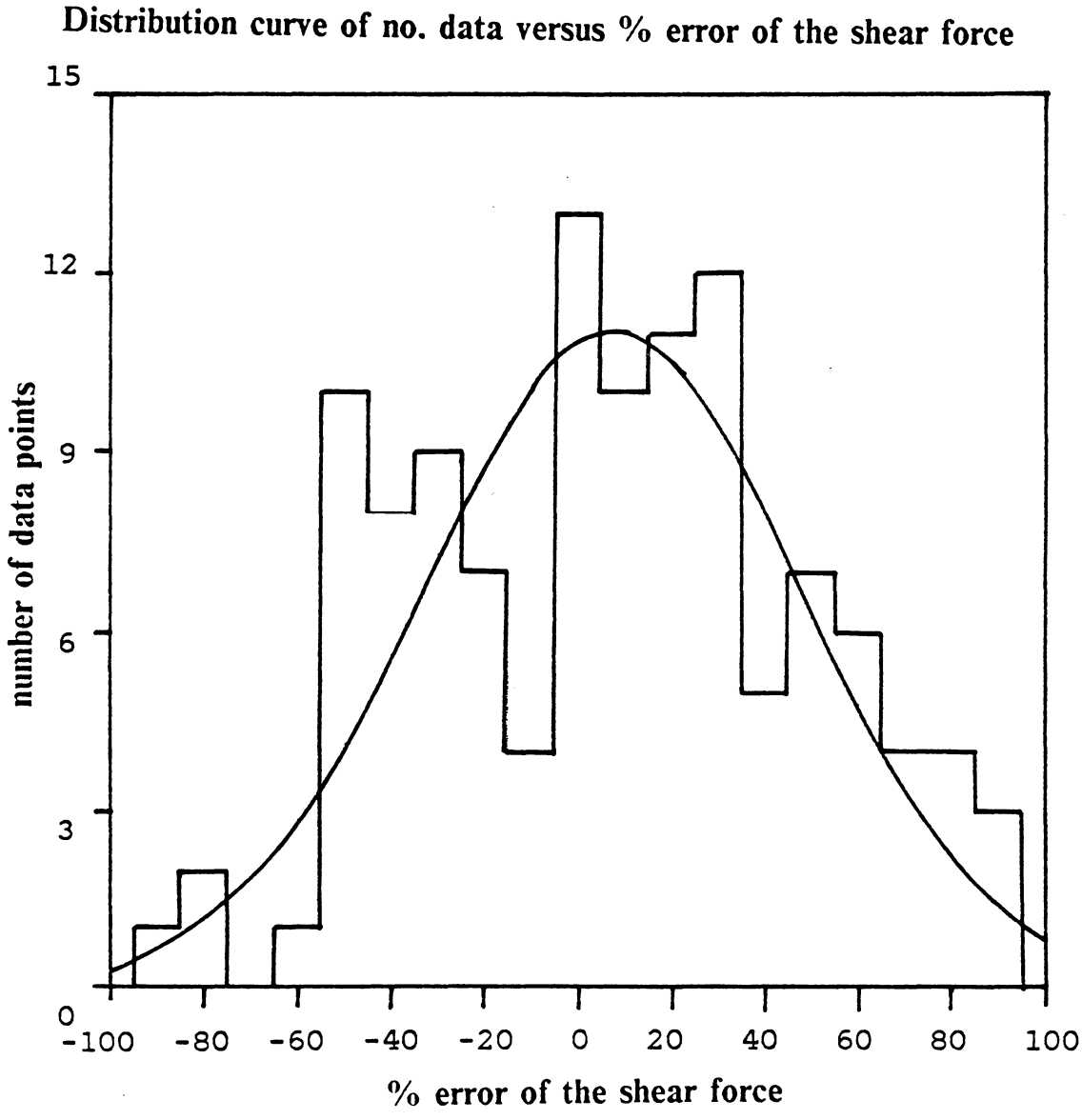

Figure 59. Number of data points versus the percentage error of the predicted wall friction.

CHAPTER 5 PRESSURE DISTRIBUTION IN SHALLOW FLUIDIZED BEDS

5.1 Fundamentals for the pressure distribution in shallow fluidized beds

Out of all of the measurable properties of fluidized beds, pressure distribution probably is the easiest to obtain. Almost any simple manometer can be modified to measure the pressure at a desired location inside a fluidized bed. Pressure distribution data can provide us valuable information about hydrodynamic features of fluidized beds:

1. For the bottom section of the bed, the pressure head in gas streams passing through orifices in the distributor will lower the measured pressure data. This can provide us a way to roughly estimate the jet penetration depth.

2. At any specific point, the pressure reading will indicate the force that all of the particles above that point exerts upon the part of the bed beneath the given point. Therefore, the variation of pressure reading with elevation reflects the change in this force of interaction between elements of the bed.

3. Toward the top of a fluidized bed, the pressure gradient will decrease as the point density of particles decreases. This gives us a chance to determine the bed surface and evaluate the bed expansion ratio.

5.2 Experimental method and conditions

The same experimental apparatus for measurement of pressure drops across fluidized beds have been employed for determining pressure distribution. Five different kinds of particles (P-A-1,P-A-2,P-A-3,P-S-1, and P-C-1) in conjunction of four distributors (D-1,2,3,4) have been used for this study. Gas velocity has been varied from 0.5 to 2.5 m/s with 0.5 m/s increment (unless particle entrainment places a practical limit on the velocity). In each set of experiment, the amount of particles has been increased stepwise: 10, 20, 40, 100, 300, 500, 100, and 1500 grams.

5.3 General features of pressure distribution curves in shallow fluidized beds

From general hydrodynamic theory, the pressure distribution curve for a homogeneous fluidized bed should ideally resemble the development of hydrostatic head in a true fluid; that is, the distribution "curve" should exhibit a straight line connecting a maximum pressure at the bottom (which reflects the total weight of the material divided by the cross-sectional area) and zero pressure at the surface. This is the "ideal" line e-f in Figure 60 on page 190. However, Figure 60 on page 190 shows an actual and typical pressure distribution curve, measured in a shallow fluidized bed with 300 grams (16.3-mm static bed height) of 335-μm Master Beads (particle P-A-3) fluidized at a superficial gas velocity of 1.5 m/s passing a 3.6% open-area perforated plate (distributor D-2).

The pressure distribution curve can be generally divided into three sections:

1. In accordance with the type of gas distributor used, the bottom section of a fluidized bed will give a pressure distribution either like curve a-b or like line e-b in Figure 60 on page 190. For a bed with a jet-producing distributor (e.g., perforated plates such as D-1,2 and 3), the pressure measured at the bottom will deviate from the straight line model of hydrostatics [i.e. the deviation of point (a) from point (e) in Figure 60 on page 190]. The magnitude of the deviation (segment a-e) and its persistence [height of the point (b)] will increase as gas velocity increases or as open area of the distributor decreases. According to the previous discussion on the pressure drop across the shallow fluidized beds, this deviation can be explained by the contribution of the pressure head produced by the high-velocity gas streams passing through the orifices on the distributor. Therefore, the deviation of the pressure drop from "ideal" near the bottom of the bed can provide an indicator of jet penetration; see a later discussion on this point. For a fluidized

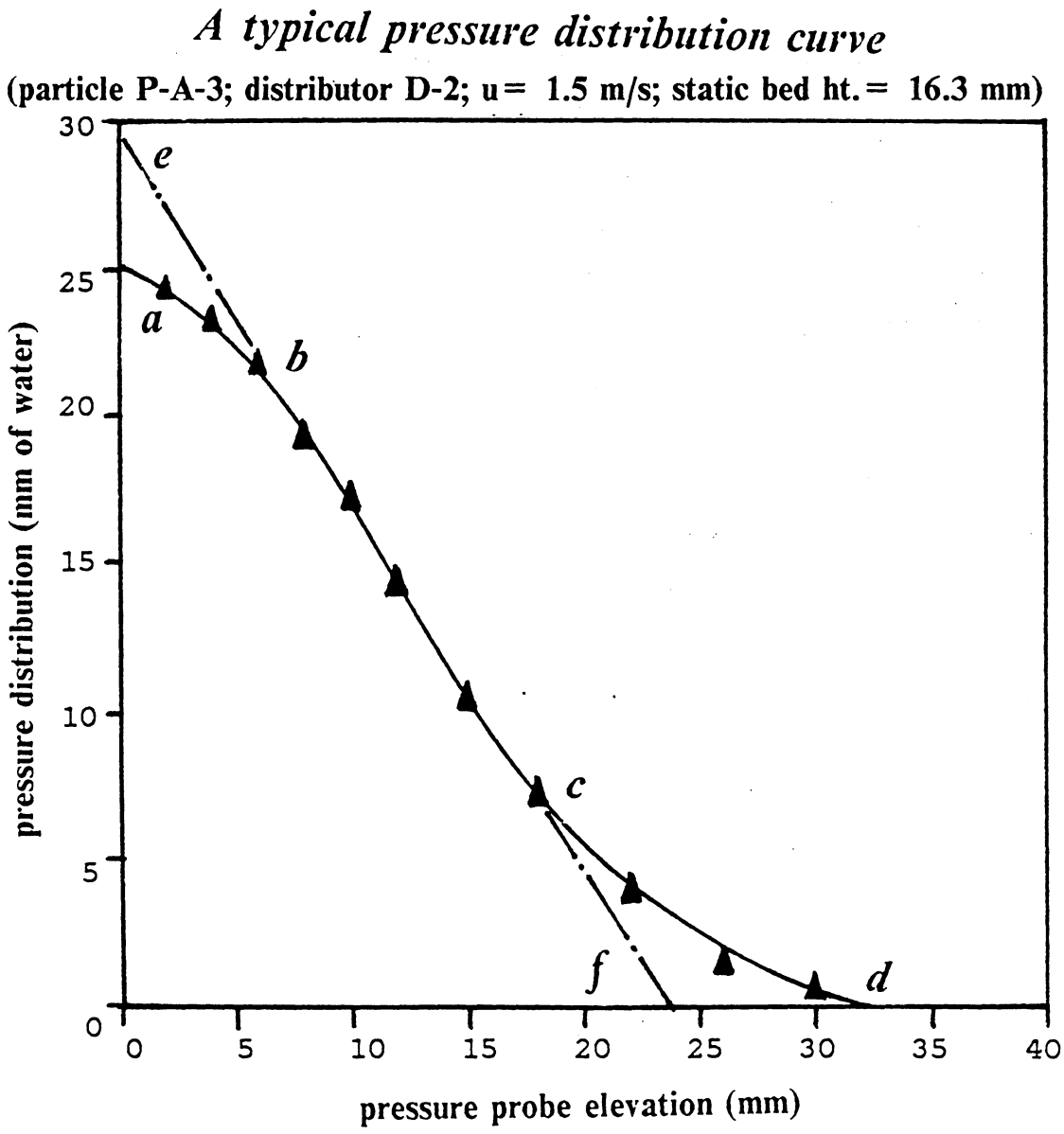

Figure 60. A typical pressure distribution curve.

bed having a laminated-plate distributor, the pressure deviation at the bottom of the bed almost disappears. This circumstance provides further evidence that the pressure deviation is associated with gas jets.

2. For all of our pressure distribution curves, we find a straight-line segment in the middle portion of the curve (like the line b-c in Figure 60 on page 190). Even though the position and magnitude of those segments may vary, a linear regression analysis for all of the 131 curves (with static bed height $>$ 25 mm) shows that a linear expression reproduces the pressure distribution data at an astonishing high correlation factor of 0.9993 (R-square = 0.9985, with a deviation of 0.0017). This suggests that a fluidized bed will have homogeneous pressure-related properties in the middle section.

3. It has been found that the upper section of most pressure distribution curves displays an exponential decay. This can be easily explained by the fact that the pressure probe will encounter a diminishing number of flying particles as the probe moves upward from the bed surface. However, a quantitative description must be established for one to utilize the pressure distribution curves at the upper section. This will be discussed later in this chapter.

5.4 Pressure distribution for all types of shallow fluidized beds

Pressure distribution curves for different types of shallow fluidized beds are shown in Figure 61 on page 193 to Figure 65 on page 197. It should be noted that for three of the nine types (for types E, G and I), a portion of the particle weight rests on the gas distributor. This prevents us from correlating pressure distribution data, since we have no means for evaluating the force exerted by particles resting on the distributor. Descriptions of pressure distribution curves for other types of shallow fluidized beds can be summarized as follows:

1. **Type A bed** (Figure 61 on page 193): The curve follows the description of the typical curve given in the previous section. The exponential decay in pressure can extend to high elevations above the bed surface. This can be explained as arising from vigorous traffic of particles into the free-board far above the bed. The particle density curve extends to a higher elevation when the pressure probe moves from the center to the edge of the fluidized bed. This provides further emphasis upon the importance of the bed wall in determining the hydrodynamic character in the upper section of a type A bed.

2. **Type B bed** (Figure 62 on page 194): The extension of the exponential section of the pressure distribution curve does not persist to such high elevations above the bed as for type A beds. However, the height of the upper section of a type B bed can be comparable to the height of the rest of the bed. This demonstrates the significance of cloud and spray zones in a shallow fluidized bed. Unfortunately, we have not been able to discover a clearly identifiable point of separation between cloud and spray zones.

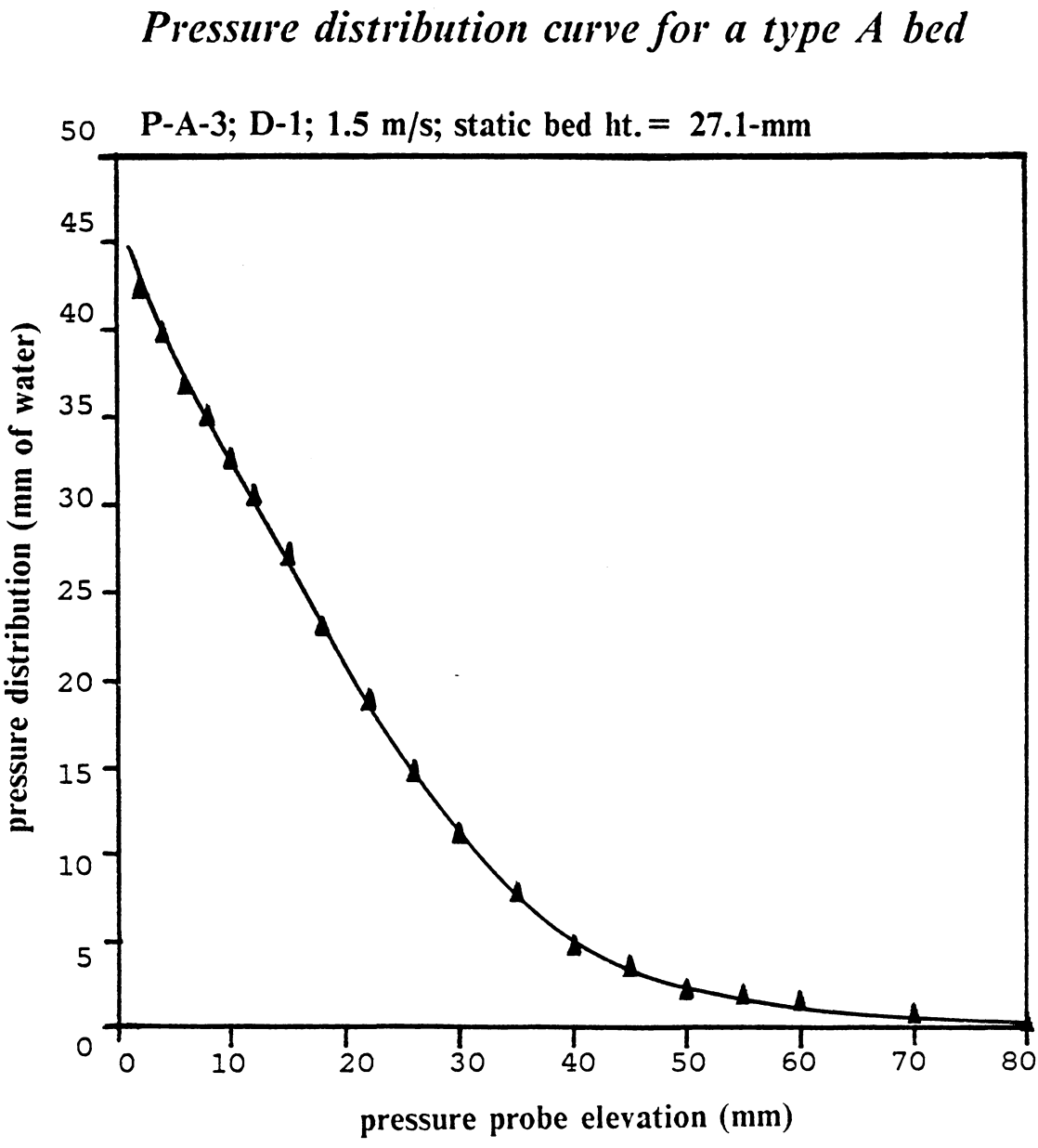

Figure 61. Pressure distribution curve for a type A bed: (particle P-A-3; distributor D-1; H_s = 27.1-mm; u = 1.5 m/s)

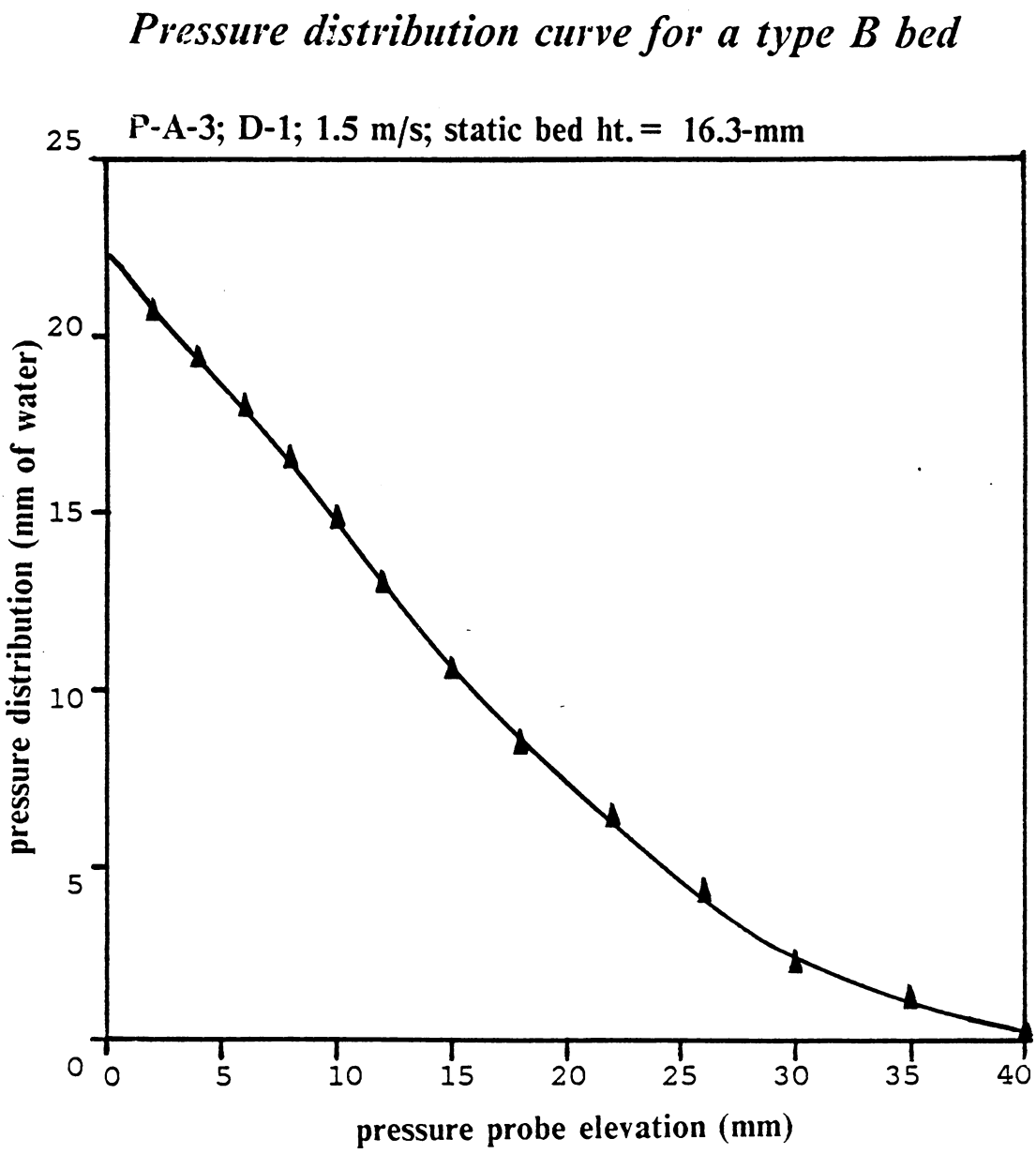

Figure 62. Pressure distribution curve for a type B bed: (particle P-A-3; distributor D-1; H_s = 16.3-mm; u = 1.5 m/s)

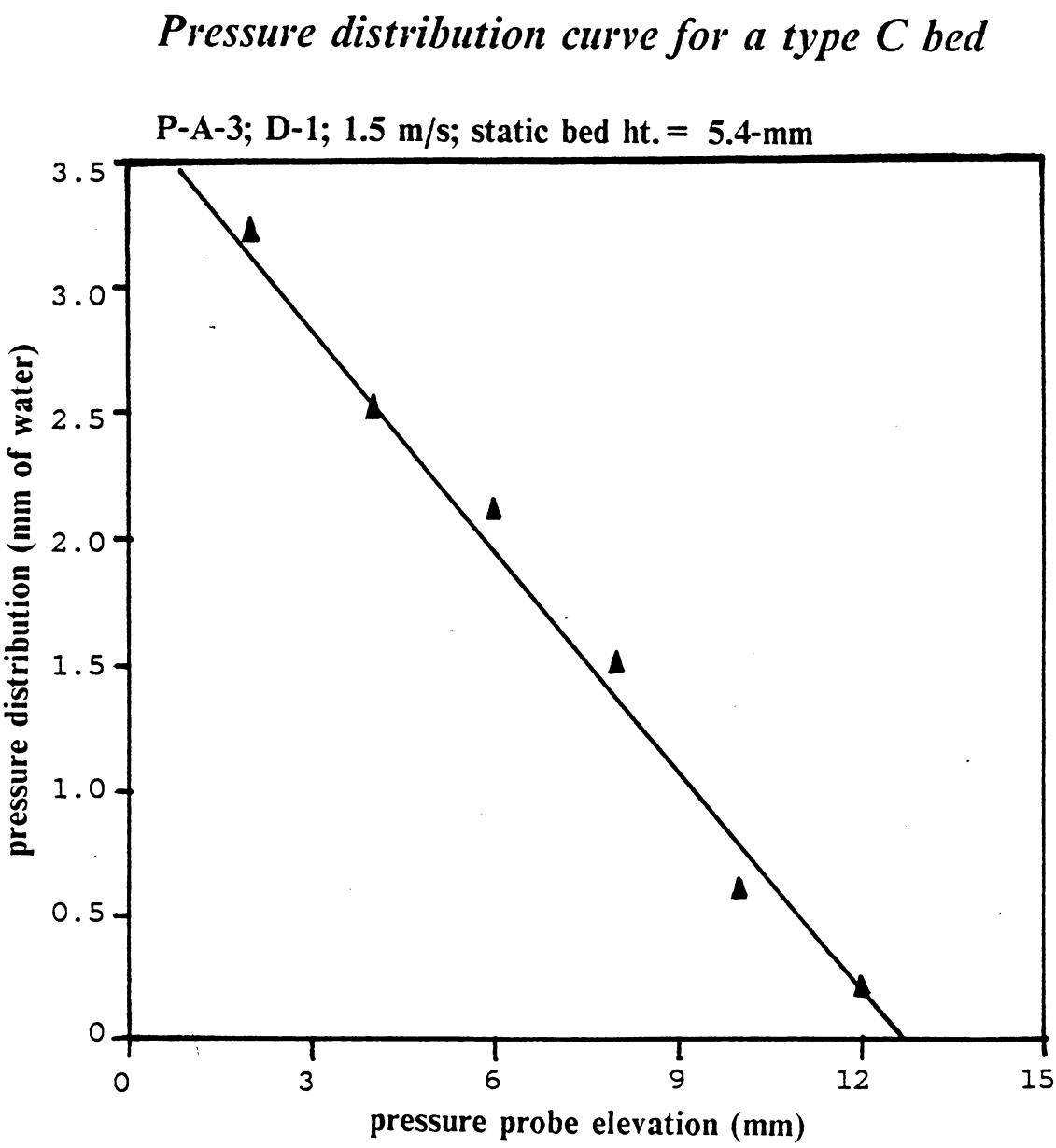

Figure 63. Pressure distribution curve for a type C bed: (particle P-A-3; distributor D-1; H_s = 5.4-mm; u = 1.5 m/s)

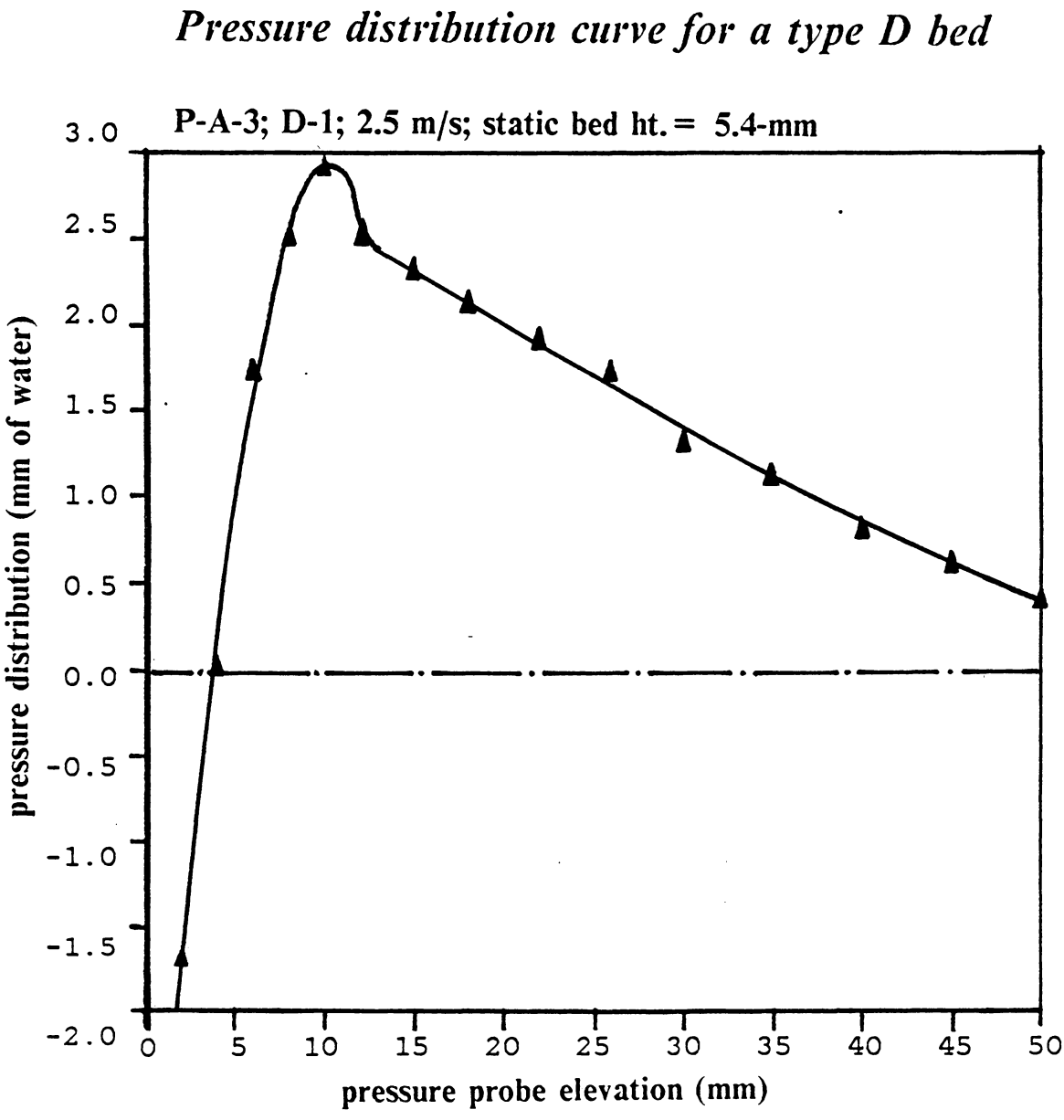

Figure 64. Pressure distribution curve for a type D bed: (particle P-A-3; distributor D-1; H_s = 5.4-mm; u = 2.5 m/s)

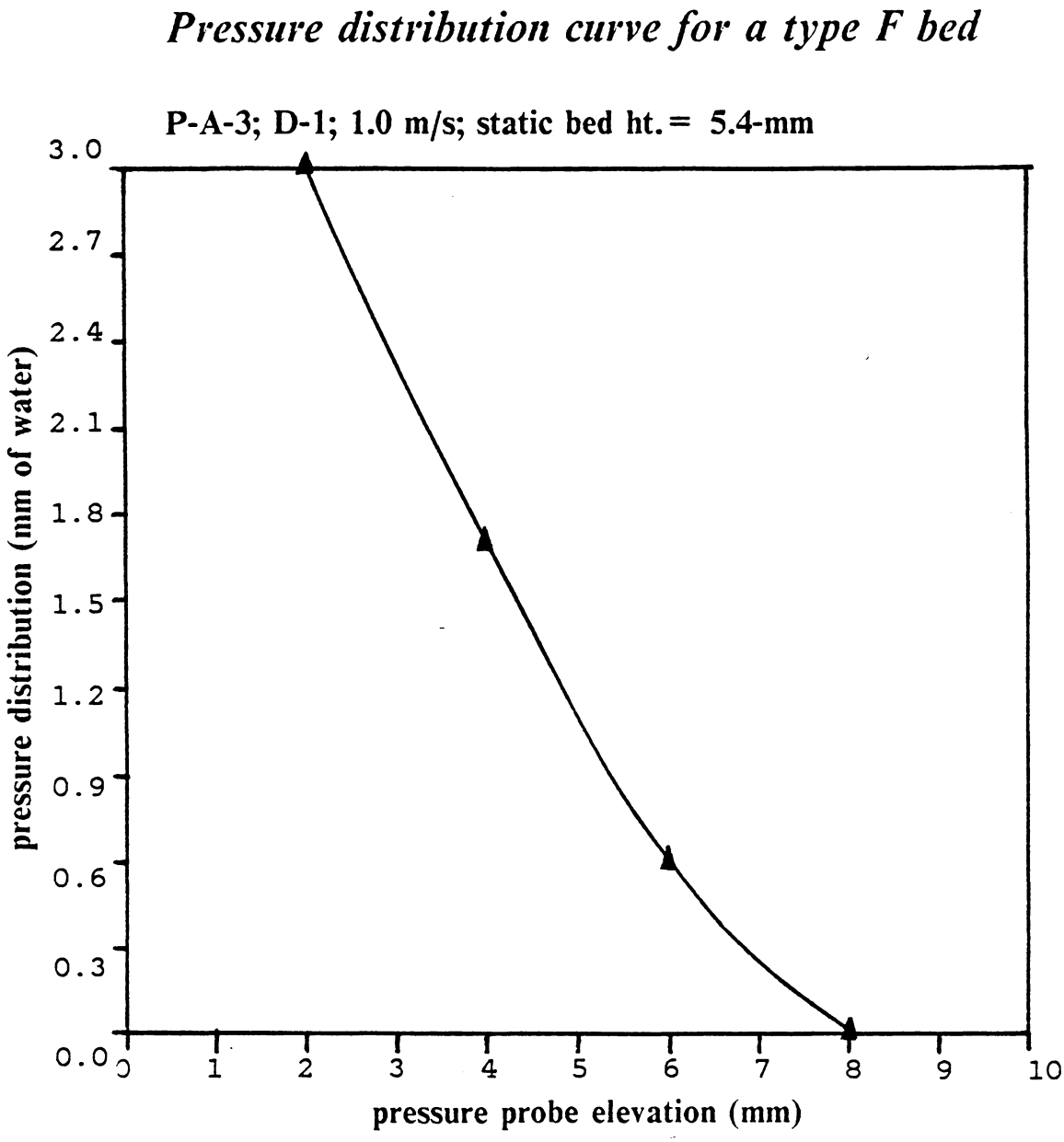

Figure 65. Pressure distribution curve for a type F bed: (particle P-A-3; distributor D-1; H_s = 5.4-mm; u = 1.0 m/s)

Pressure distribution curve for a type G bed

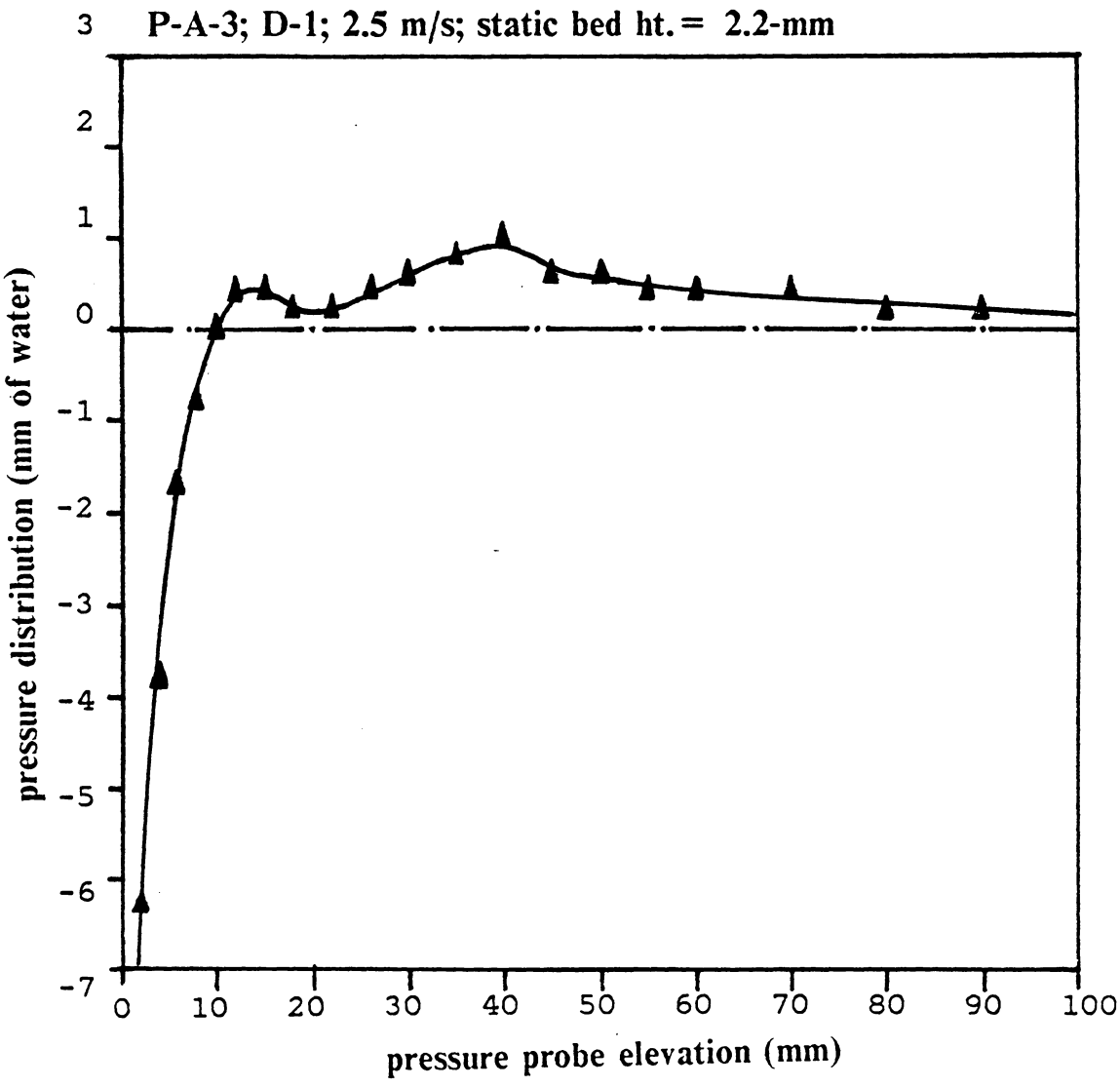

Figure 66. Pressure distribution curve for a type G bed: (particle P-A-3; distributor D-1; H_s = 2.2-mm; u = 2.5 m/s)

3. **Type C bed** (Figure 63 on page 195): The most distinguishing feature of the pressure distribution curve of a type C bed is its trivial exponential decay section in comparison with this section for type A and B beds. This can be easily explained by the fact that the dimples on the surface of a type C bed extends for less than 10 mm in most of our experiments. Figure 67 on page 200 combines the pressure distribution curves of the previous three figures for beds of type A, B, and C respectively. It can be observed that the exponentially decaying segment of the curves is distinctly characteristic for each of these types of beds.

4. **Type D bed** (Figure 64 on page 196): A bed of type D will demonstrate a totally different pressure distribution curve from other types of beds. As shown in Figure 64 on page 196, the lower portion of the curve confirms the existence of pressure recovery from the jet streams by showing a negative value near the bottom of the bed. The upper portion of the curve (right after the maximum pressure) exhibits a linear decrease instead of exponential decay. This confirms our observation about the homogeneity of type D beds.

5. **Type F bed** : Figure 65 on page 197 shows two important features of type F beds--

   a. There are no surface fluctuations; i.e., there is no exponential decay.

   b. Influence of the jets near the bottom is less important in a type F bed than in other types of shallow beds.

6. **Type G bed** (Figure 66 on page 198): The lower portion of the curve is similar to that for a type D bed, with further negative values. The pressure data for the upper portion vary within a small range of only 1 mm of water; this reflects the swirling of the dilute region.

Pressure distribution curves for type A, B and C beds

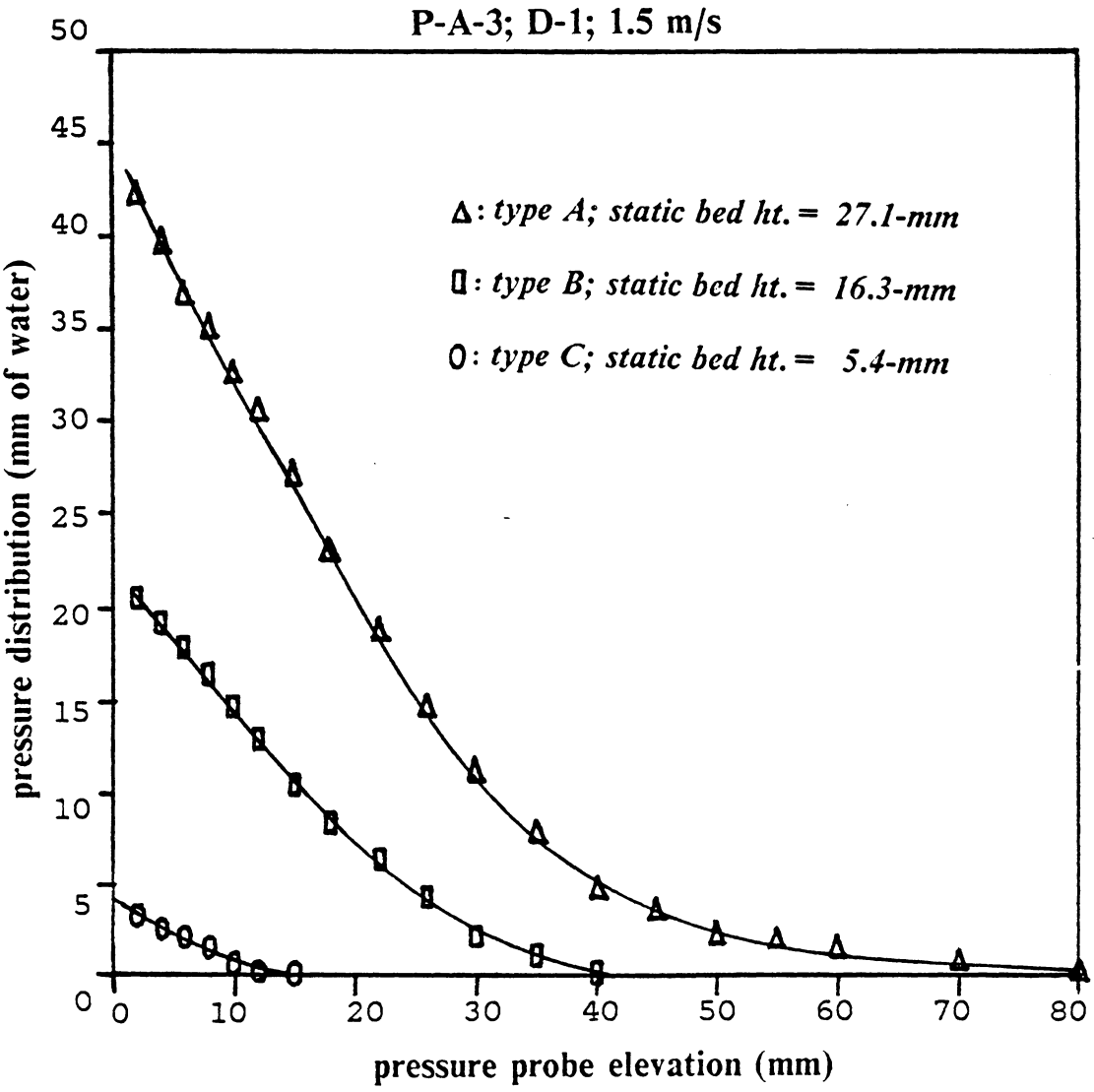

Figure 67. **Pressure distribution curve for type A, B and C beds:** (particle P-A-3; distributor D-1; H_s varies; u = 1.5 m/s)

5.5 *Variables affecting the pressure distribution curves*

All of the variables influencing hydrodynamic features of fluidized beds can affect the pressure distribution also. However, that some of them are more influential than others, the following discussion will demonstrate.

5.5.1 Effect of the amount of particles

When discussing the types of shallow fluidized beds, we stated that changing the amount of particles would shift the shallow fluidized bed from one type to the other. Even though all of the types have been described in the previous section, it is still worthwhile to emphasize the importance of pressure distribution as a response to the total particle weight.

In most of our experimental conditions, the collection of pressure distribution data has been extended to deep beds. Figure 68 on page 202 shows the pressure distribution curves for beds at static bed heights of 16.3, 27.1, 54.2 and 81.3 mm, respectively. (Notice that all of these beds are type A except the one with 16.3-mm height, which falls in type B.) It can be seen that the shape of the uppermost portions of the curves become similar as the static bed height increases. This can be illustrated more clearly by Figure 69 on page 203, in which each of the pressure distribution curve has been "normalized"; i.e., pressures are expressed as the percentage of a maximum pressure reading.

The curves become more similar as the inventory of particles increases. This can be explained by the fact that the fluctuation of the bed surface cannot extend to an infinite range. After the fluctuation reaches a certain magnitude, further increase in the particle inventory will simply cause the middle region to expand.

Pressure distribution curves for beds having different amounts of particles

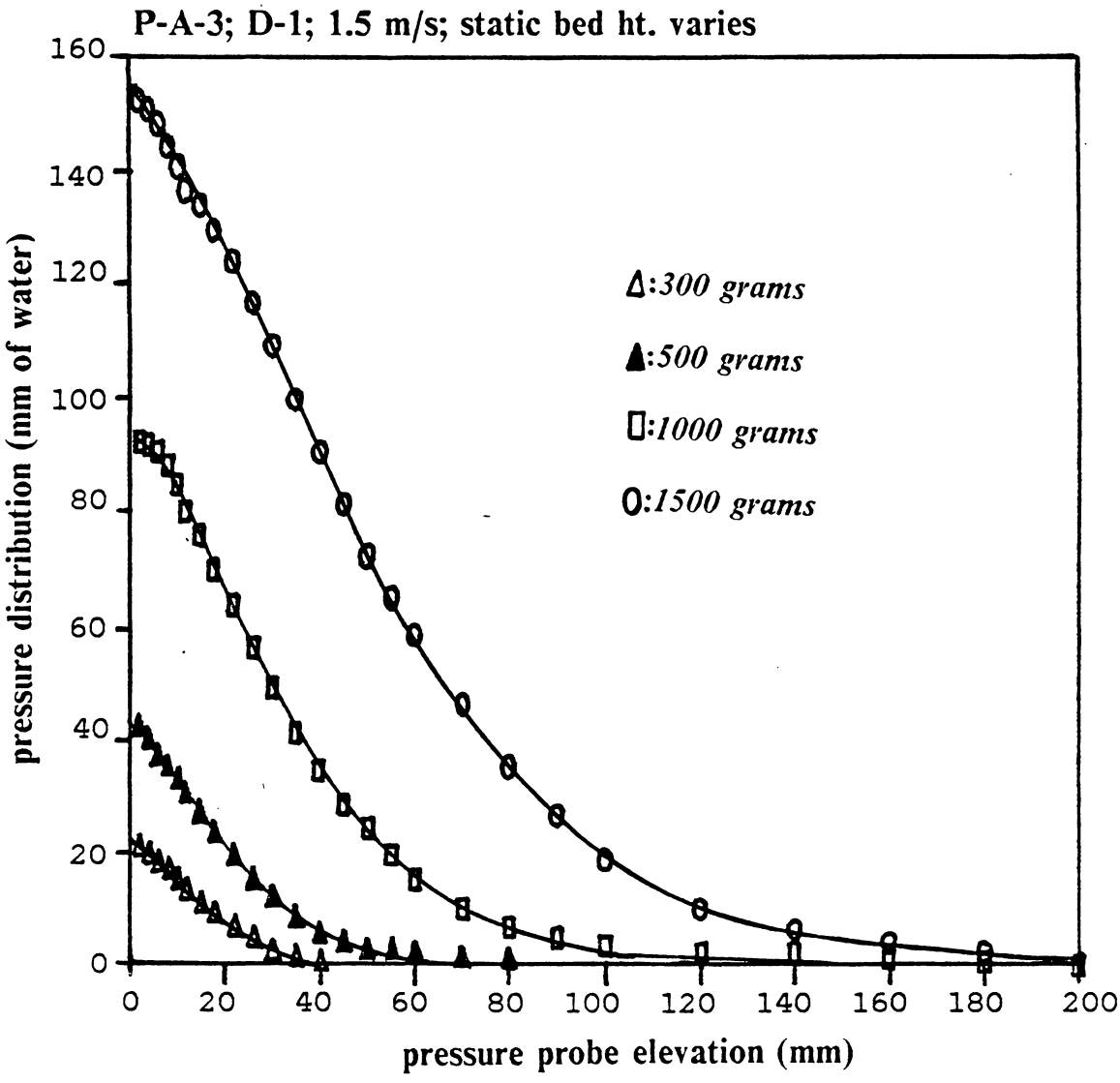

Figure 68. Pressure distribution curves for different amounts of particles:figdesc(particle P-A-3; distributor D-1; H_s = 16.1, 27.1, 54.2, 81.3-mm; u = 1.5 m/s)

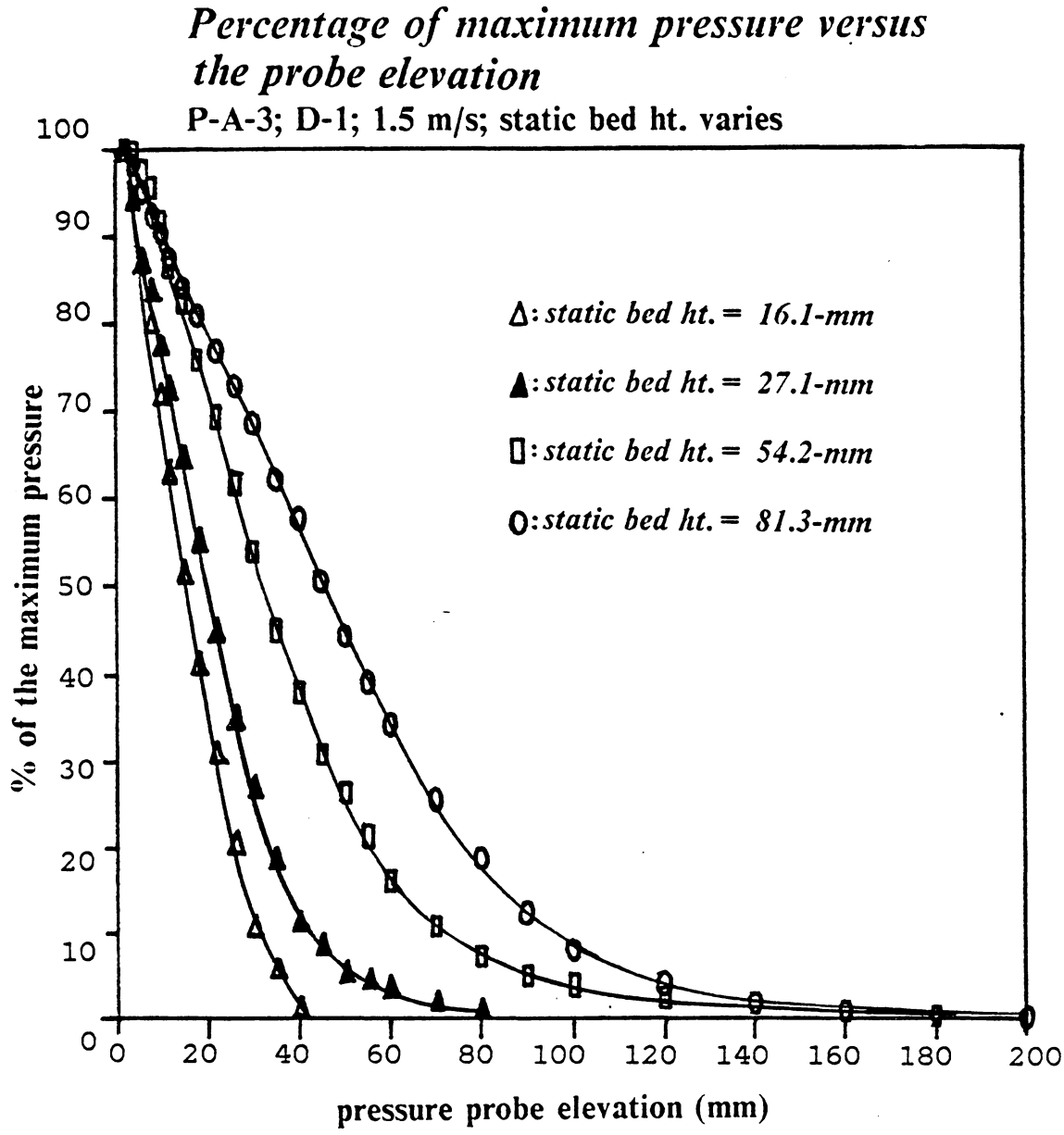

Figure 69. **Percentage of maximum pressure versus probe elevation for different static bed heights:**figdesc(particle P-A-3; distributor D-1; H_s = 16.1, 27.1, 54.2, 81.3-mm; u = 1.5 m/s)

5.5.2 Effect of gas velocity

From the earlier discussions on the general behaviour of the pressure distribution curves, we can draw the following conclusion on the effect of the gas velocity on the pressure distribution curve:

1. The pressure head transformed from jet streams will increase as the superficial gas velocity increases.

2. The fluctuation (or the tendency for exponential decay) of pressure distribution is also increased at higher gas velocity.

However, the importance of the gas velocity diminishes as the total weight of particles increases. This can be illustrated by Figure 70 on page 205 to Figure 72 on page 207. In Figure 70 on page 205, there is only a very small amount of particles (static bed height = 5.4 mm) in the bed. The dissimilarities among the curves can be easily seen by comparing the smoothed lines.

After the static bed height reaches a medium range of 16.3 mm (see Figure 71 on page 206), variations lessen so rapidly that the only curve far different from the others is the one having a highest gas velocity. It can be seen on Figure 72 on page 207 that the gas velocity does not significantly change the shape of the pressure distribution curve insignificant extension after the bed height reach a "deep" range (in this case, static bed height = 81.3-mm).

Pressure distribution curves for beds having a small amount of particles

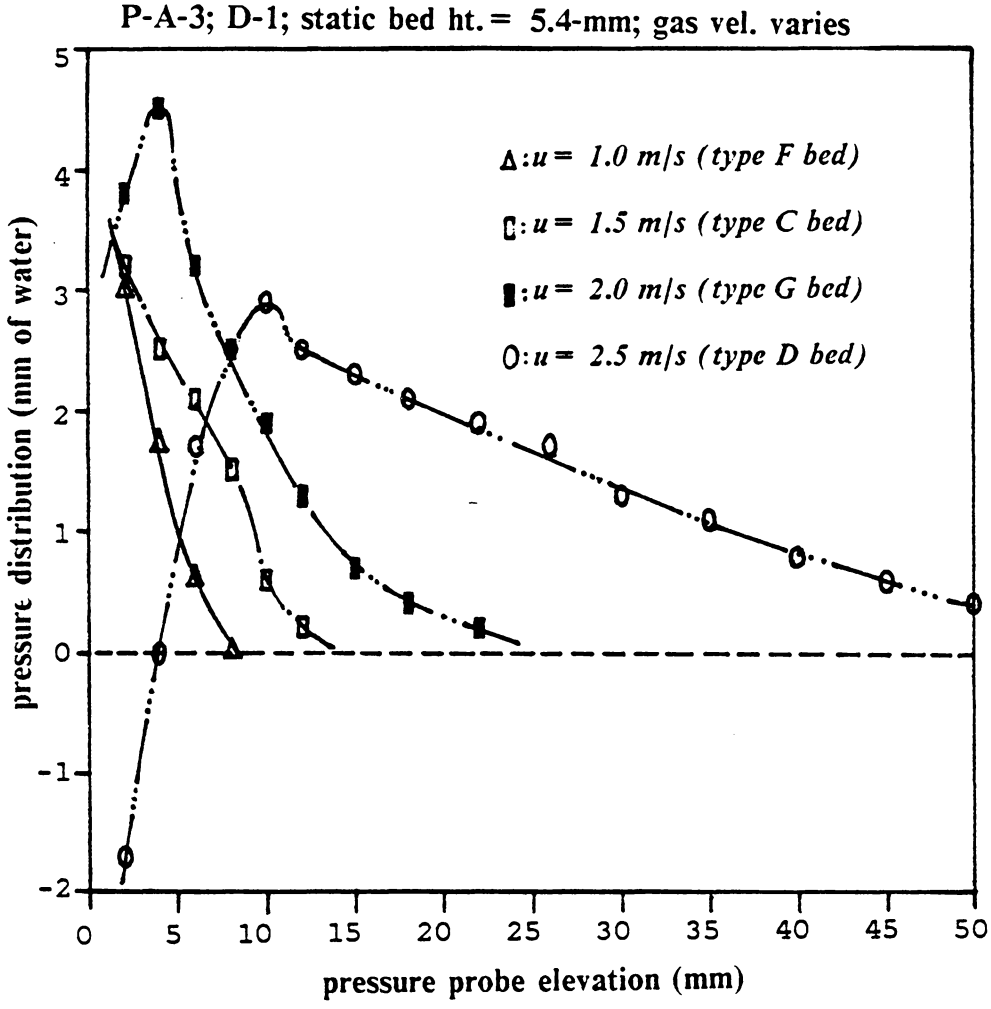

Figure 70. **Pressure distribution curves for beds having a small amount of particles:** (particle P-A-3; distributor D-1; H_s 5.4-mm; u = 1.0, 1.5, 2.0, 2.5 m/s)

Pressure distribution curves for beds having a medium amount of particles

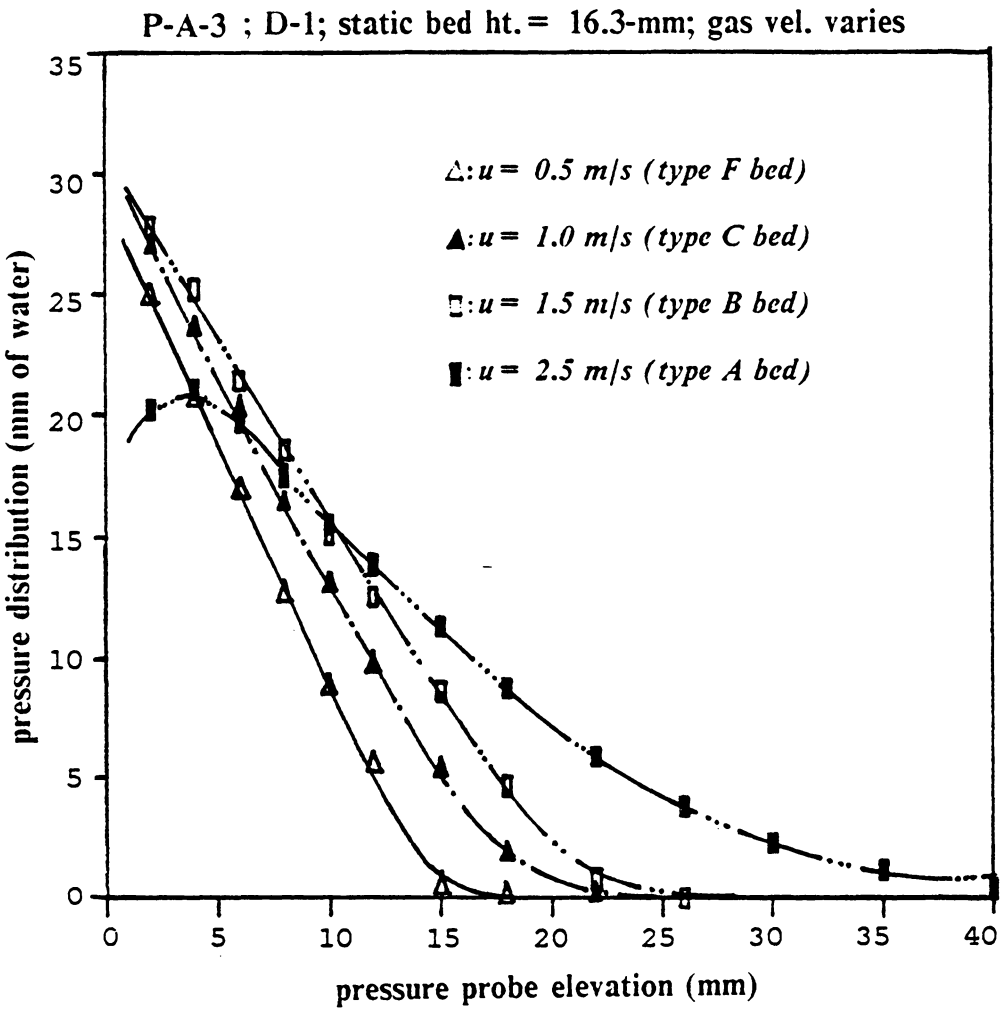

Figure 71. Pressure distribution curves for beds having a medium amount of particles: (particle P-A-3; distributor D-1; H_s 16.3-mm; u = 0.5, 1.0, 1.5, 2.0 m/s)

Pressure distribution curves for beds having a large amount of particles

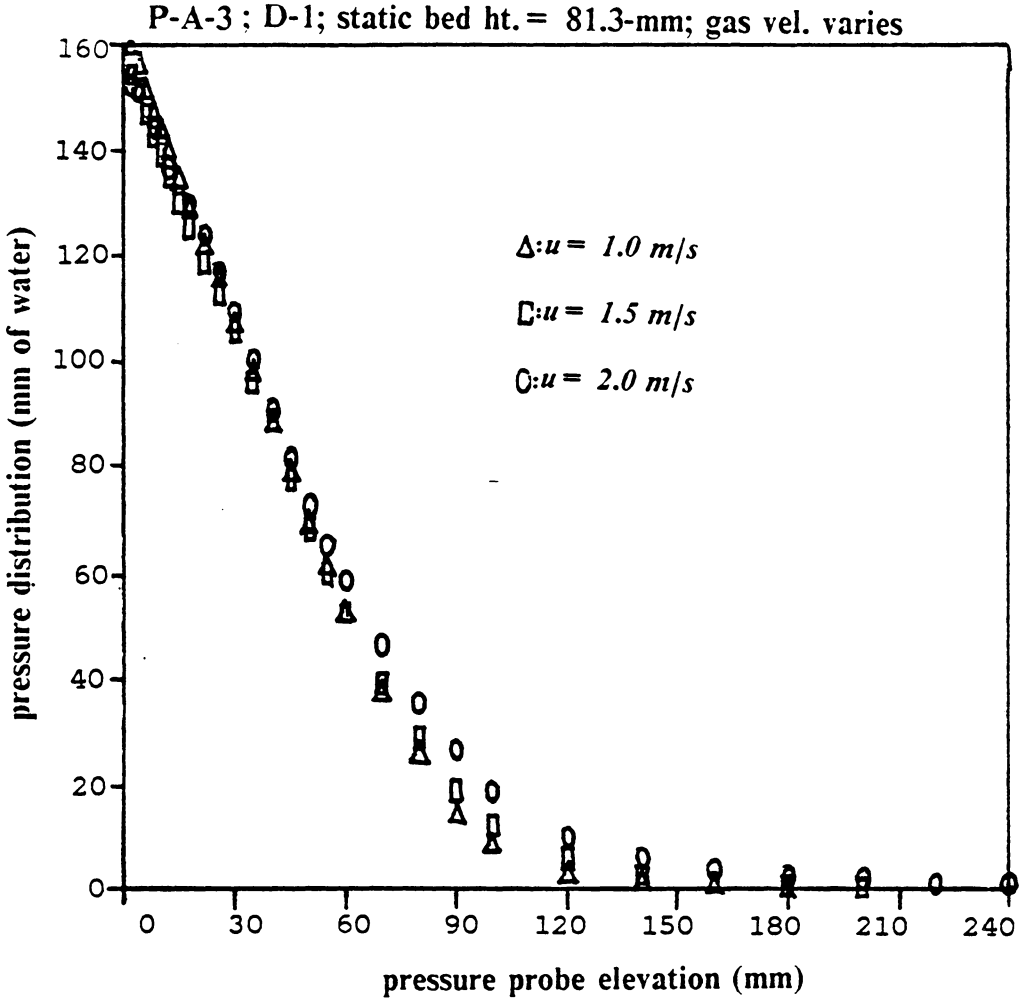

Figure 72. **Pressure distribution curves for beds having a large amount of particles:** (particle P-A-3; distributor D-1; H_s 81.3-mm; u = 1.0, 1.5 2.0 m/s)

5.5.3 Effect of particle size

In most of hydrodynamic studies of fluidized beds, it is usually difficult to single out the effect of particle size from other system variables. A feature of shallow beds is that the use of particles of different sizes will sometimes cause the bed to fall into different "types" even though other variables are carefully controlled. Figure 73 on page 209 shows the the pressure distribution curves for three different sizes of Master Beads. We can see that:

1. In the jet-affected region (bottom of the bed), the zone of pressure recovery will extend higher for the bed having smaller particles.

2. The range of fluctuating bed surface expands as the particle size decreases.

3. In the middle section of the bed, the pressure distribution curves are much the same regardless of particle sizes.

5.5.4 Effect of particle density

Like particle size, particle density is rarely discussed separately from other particle properties. However, there are three different kinds of particles having the same particle size (630 μm in diameter) in our study. Figure 74 on page 210 shows the pressure distribution curves for these three particles: Master Beads, sands, and activated carbons, respectively. For convenience of comparison, all curves are for type A beds with normalized percentage of maximum pressure data on the y-axis.

It can be seen that the recovered pressure head at the bottom as well as the fluctuation at the top increase when particle the density decreases. We can also see that the slopes for the middle section of the curves decrease with decreasing particle density. Figure 75 on page

Pressure distribution curves for beds having different sized particles

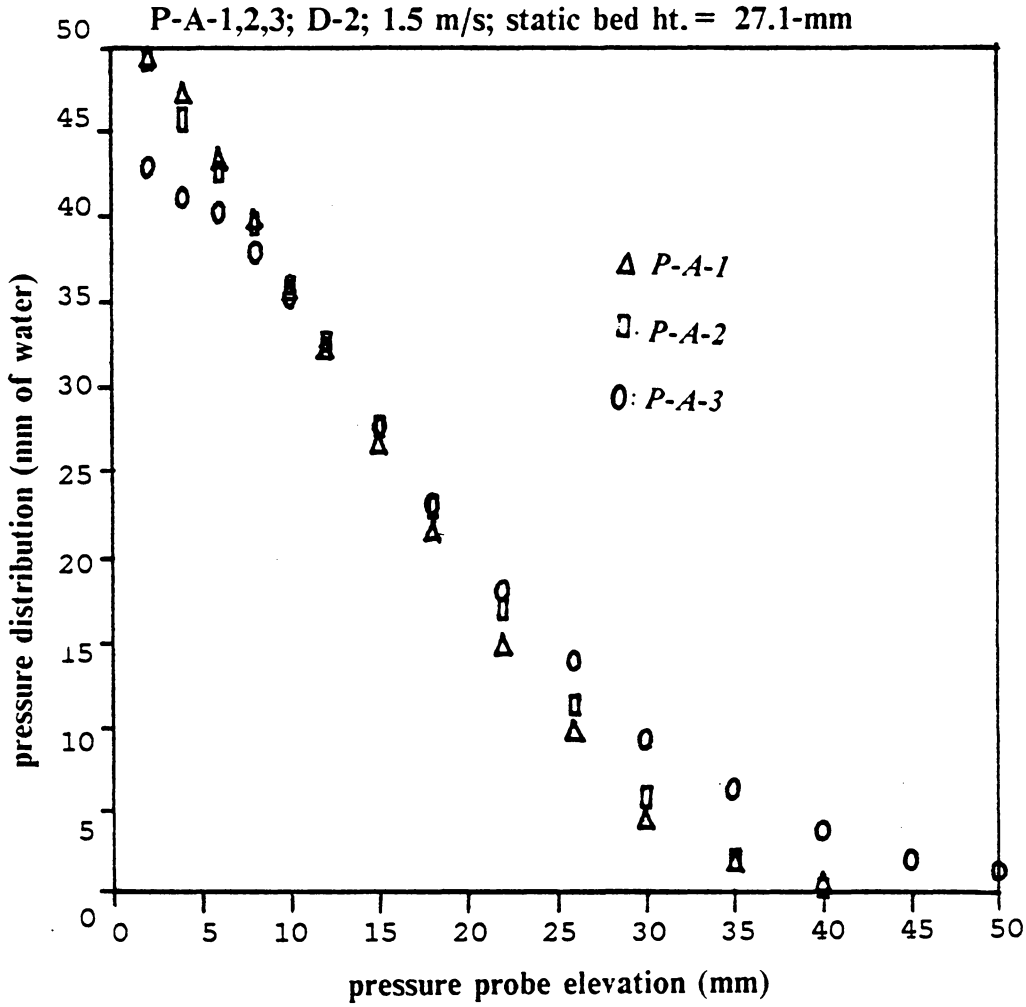

Figure 73. Pressure distribution curves for beds having different sized particles: (particle P-A-1, P-A-2, P-A-3; distributor D-2; H_s = 27.1 mm; u = 1.5 m/s)

Pressure distribution curves for beds having different kinds of particles

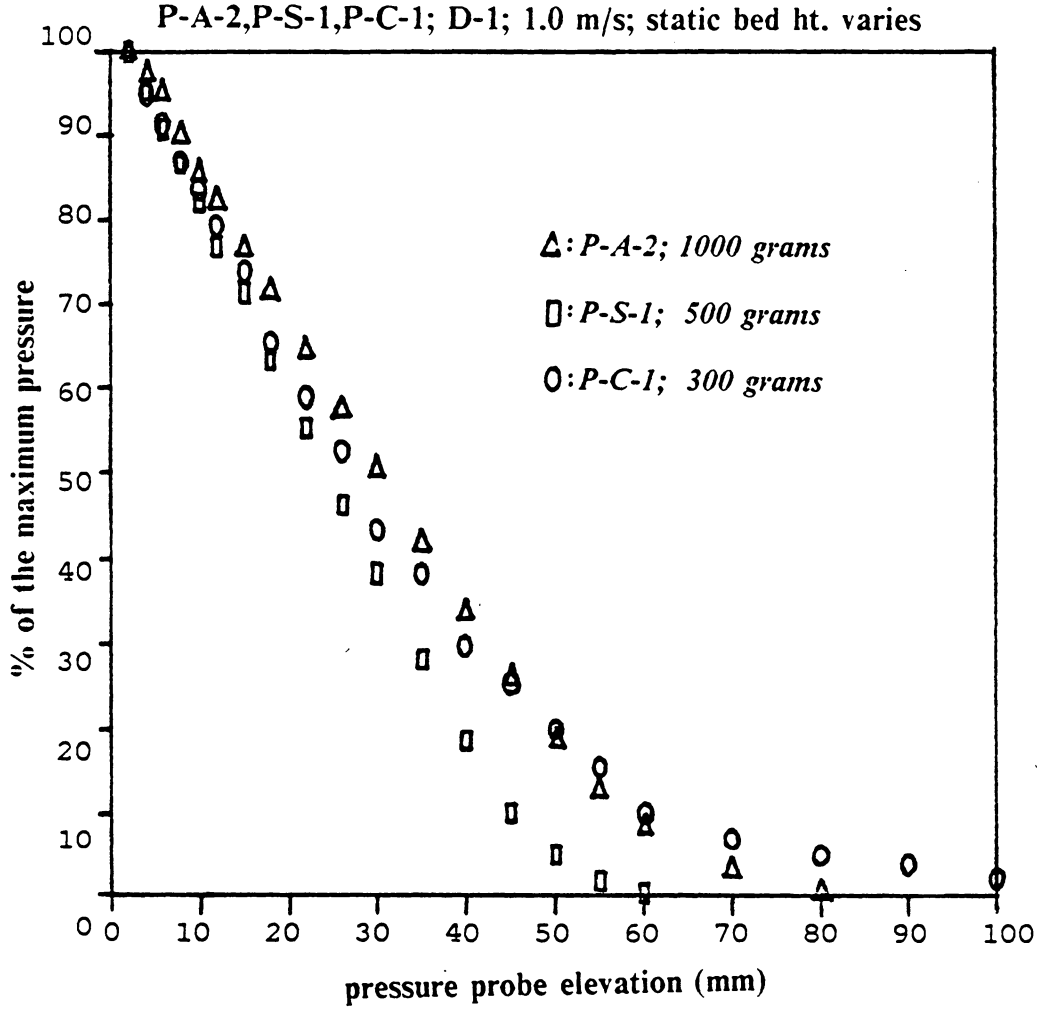

Figure 74. **Pressure distribution curves for beds having different kinds of particles:** (particle P-A-2, P-S-1, P-C-1; distributor D-1; H_s = 35.9, 54.2, 68.9-mm; u = 1.0 m/s)

212 shows the pressure distribution curves for the activated carbon at several inventories of particles. It can be seen that the surface fluctuation is significant even for a relatively shallow bed. This is probably due to the lightness of particles. (The apparent specific gravity for the activated carbon is 0.96).

5.5.5 Effect of distributor

As mentioned earlier, the most important effect for the gas distribution on the pressure distribution curve is the recovered pressure head near the bottom of the beds. Figure 76 on page 213 and Figure 77 on page 214 demonstrate this effect for different gas distributors.

It can be seen that the recovered pressure head can be as high as 24 mm of water for a bed having a perforated distributor (D-3). We can also observe that the upper portion of the pressure distribution curve is almost independent of the type of gas distributor used. The estimation of the jet-affected region will be discussed later in this chapter.

Pressure distribution curves for beds having activated carbons

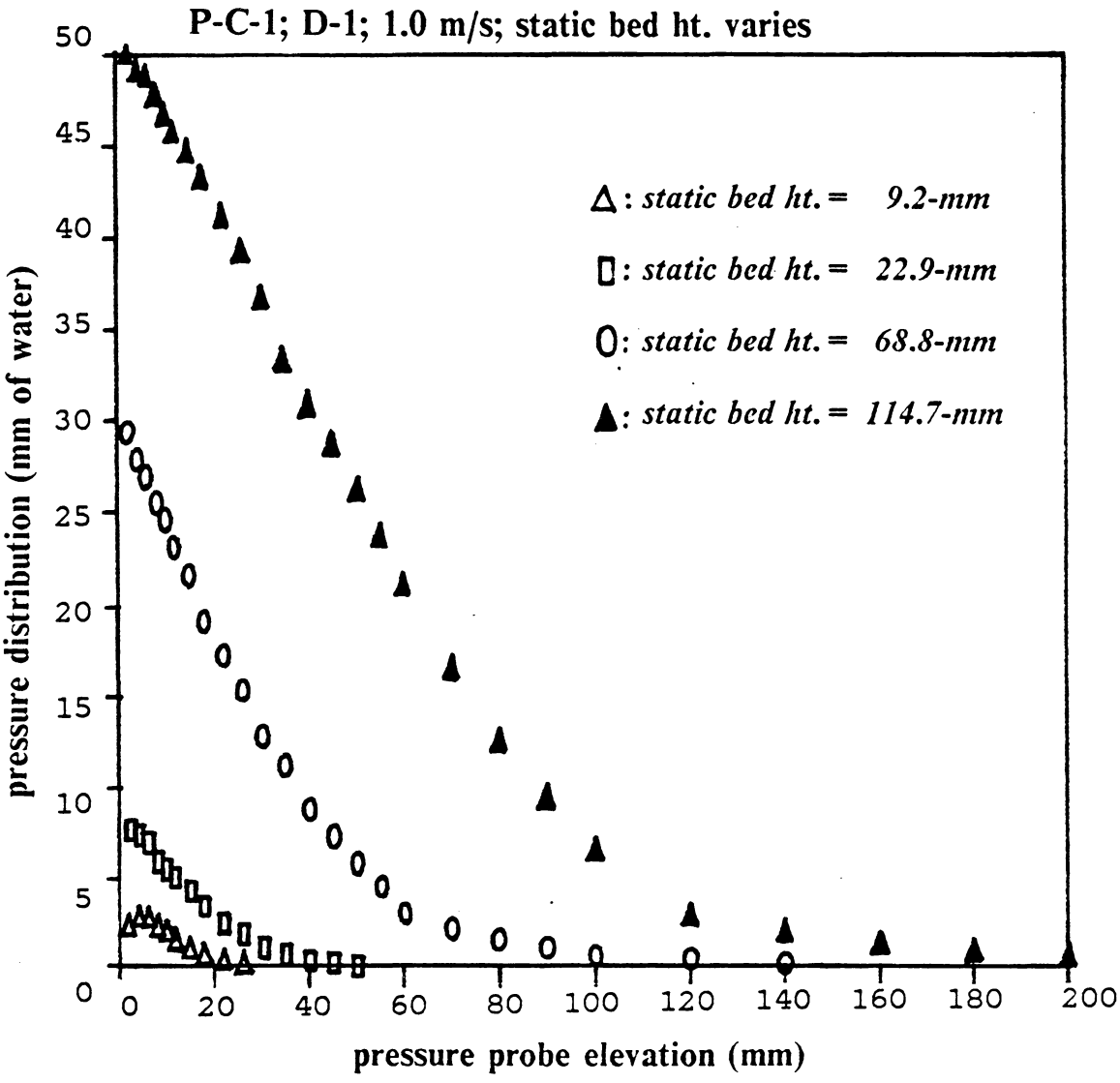

Figure 75. Pressure distribution curves for beds of activated carbon: (particle P-C-1; distributor D-1; H_s = 9.2, 22.9, 68.8, 114.7-mm; u = 1.0 m/s)

Pressure distribution curves for beds having perforated distributors

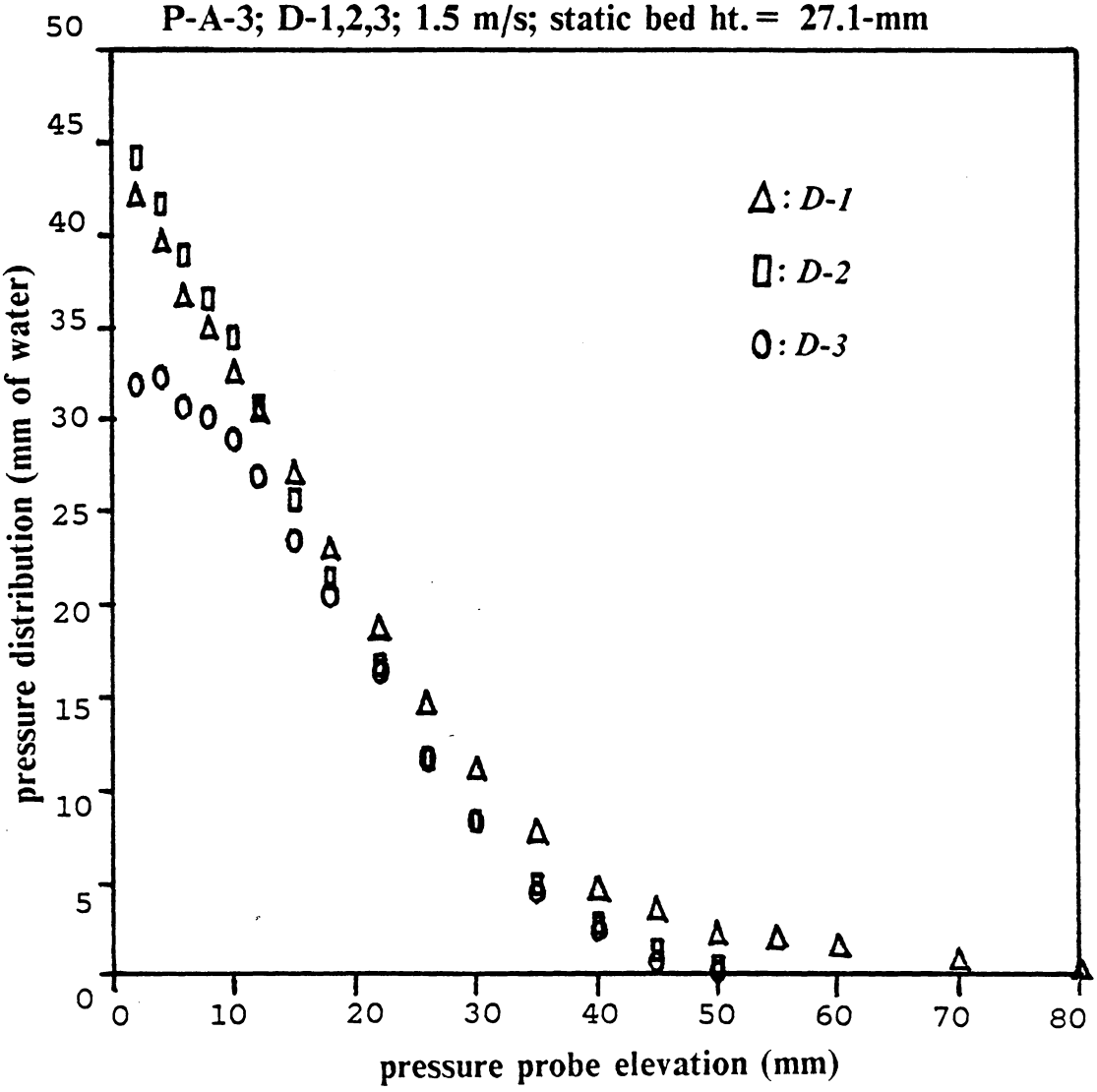

Figure 76. Pressure distribution curves for beds with perforated distributors: (particle P-A-3; distributor D-1, D-2, D-3; H_s = 27.1-mm; u = 1.5 m/s)

Pressure distribution curves for beds having different types of distributors

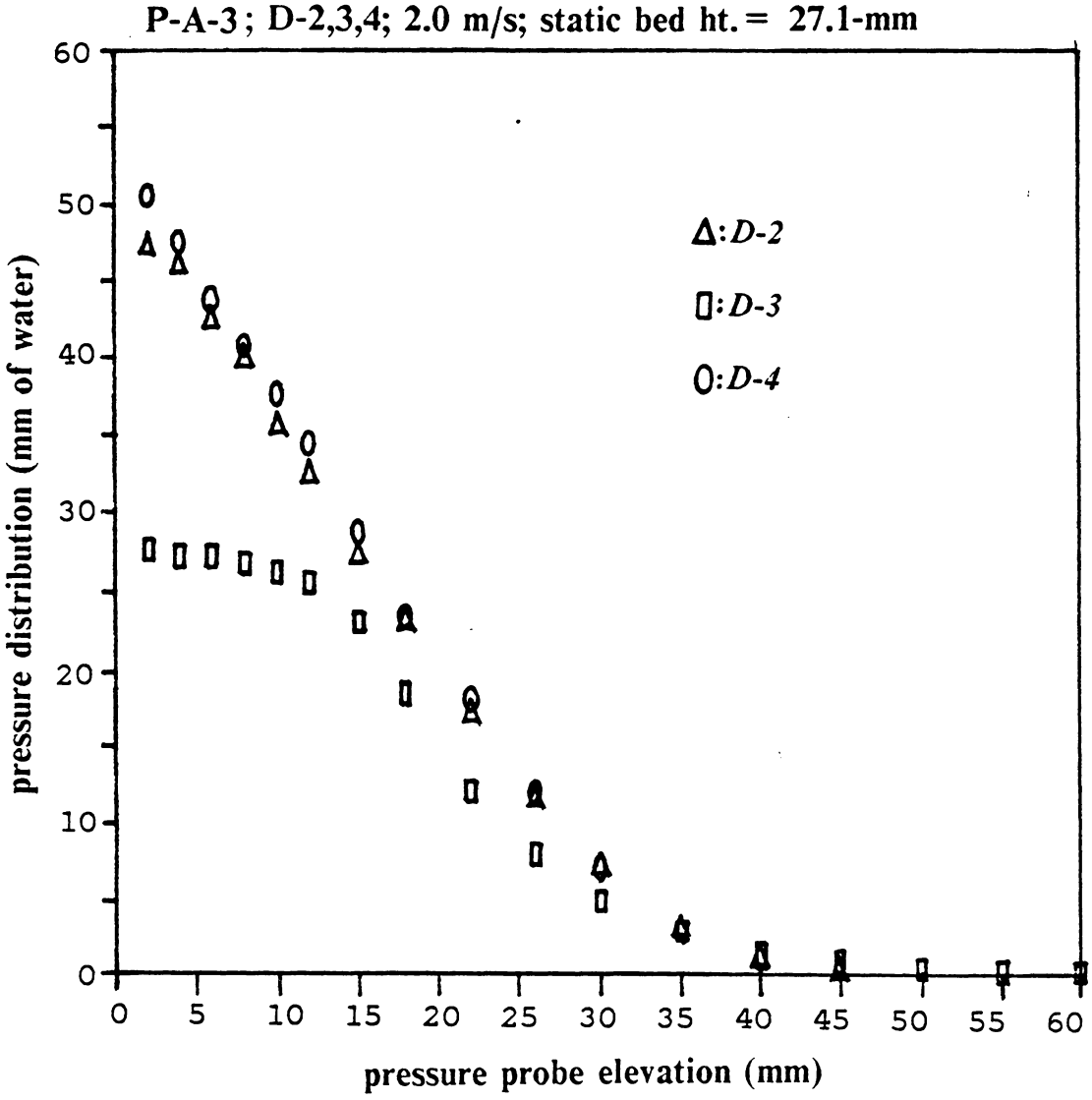

Figure 77. Pressure distribution curves for beds with different types of distributors: (particle P-A-3; distributor D-2, D-3, D-4; H_s = 27.1-mm; u = 2.0 m/s)

5.6 Estimating bed expansion from pressure distribution curves

For fluidized beds operated in any of the regimes of aggregative fluidization, the bed "surface" is always fluctuating by virtue of eruption of bubbles or by the disturbance of turbulent streams. Most of the correlations used to estimate bed expansion are based on the assumption that the bed expands homogeneously and hence are not applicable for predicting the bed expansion of an aggregatively fluidized bed. A new procedure/technique is proposed here for estimating the bed expansion ratio by using pressure distribution curves.

Figure 78 on page 216 shows diagrams of three important hydrodynamic variables (i.e. the pressure distribution, the particle volume-fraction, and the particle fluctuation ratio-- see the next chapter) versus the bed height for 0.5 Kg of particle P-A-2 (630 μm Master Beads) fluidized in a bed having distributor D-1 and operating under 1.5 m/s. Some observations can be summarized as follows:

1. The bed height at which the particle volume-fraction has the maximum value (point J on Figure 78 on page 216) is very close to the point for the particle fluctuation ratio to hit the minimum value (point I on Figure 78 on page 216). (See the next chapter for a discussion of particle volume-fraction and the fluctuation ratio.)

2. Point E on Figure 78 on page 216 indicates the bed height where the pressure distribution starts to deviate from a straight line. Above this specific height, the fluctuation ratio increases sharply while the particle volume-fraction drops very fast. Therefore, the bed level D can be taken as the lowest value for the fluctuation of the bed surface.

3. The pressure distribution curve reaches zero while particle volume-fraction has the value of about 0.05. This shows one of the shortcomings of the pressure distribution curves:

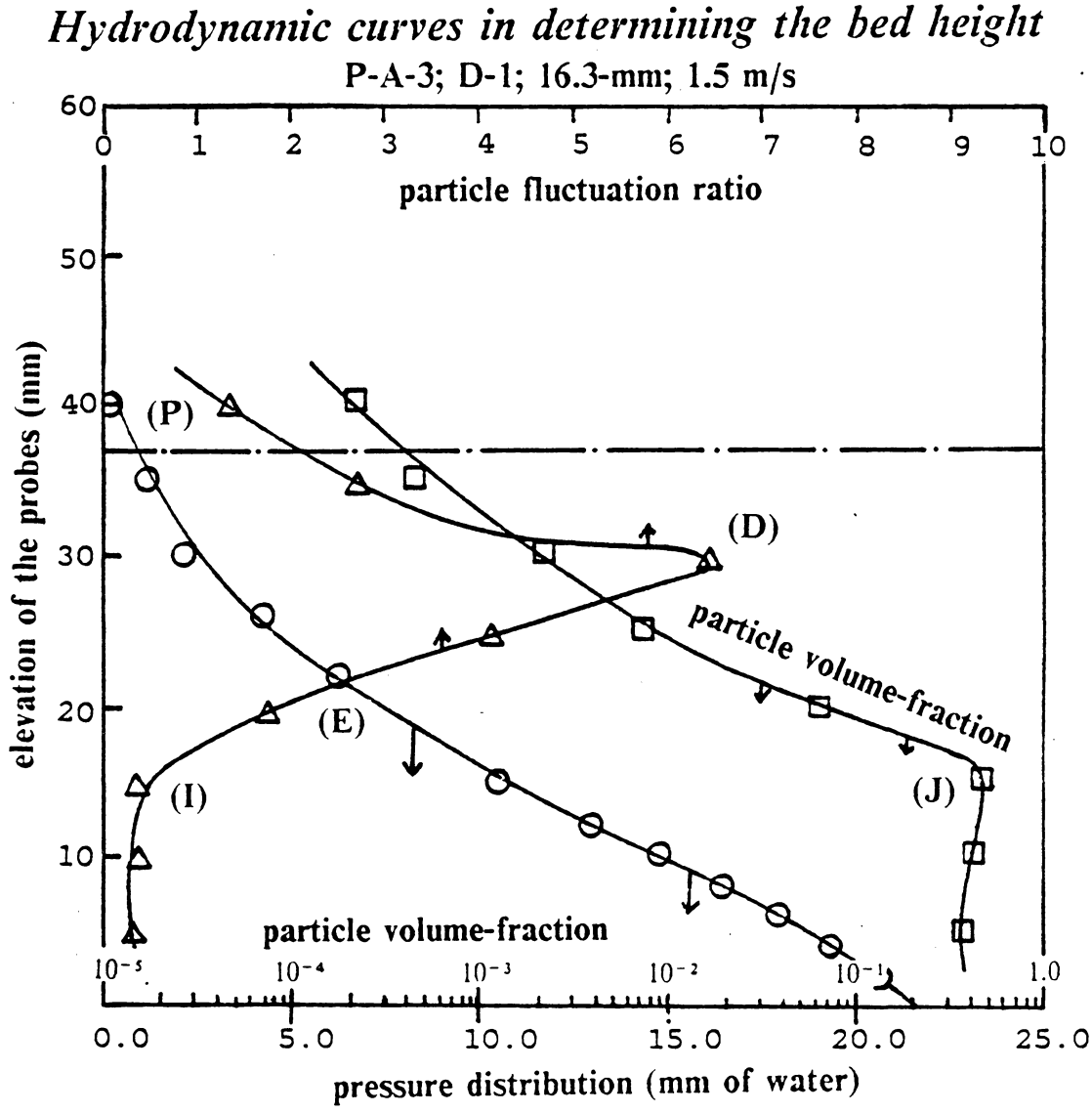

Figure 78. Three hydrodynamic curves for determining bed height

they are not capable of defining bed characteristics for the ultimate upper reach of the bed -- that is to say, the free-board region.

4. The bed height at which the bed pressure decreases to about 2% of the maximum pressure (point P on Figure 78 on page 216) can be taken as the average bed height. In most of the fluidizing conditions that we have studied, this height can also be taken as that for which the particle fluctuation ratio reaches to 1. (This indicates a vigorous mixing between particles and voids.)

Table 23 on page 218 lists the bed expansion ratio for different particles and velocities. The ratio has been calculated by defining the bed height as the point where the pressure falls to 2% of its maximum. Notice that:

$$\text{bed expansion ratio} = \frac{\text{fluidizing bed height}}{\text{static bed height}} \qquad [5.1]$$

Table 24 on page 219 compares the bed expansion ratio for different gas distributors in experiments fluidizing particle P-A-2 with a static bed height of 54.1 mm. It can be seen that the bed expansion ratio is almost independent of the distributor design (!!!). Table 25 on page 220 compares bed expansion ratios for different static bed heights for distributor D-1 and particle P-A-2. We conclude that the bed expansion ratio will not vary much with increase in static bed height. Therefore, our way of identifying fluidized-bed height by using the pressure distribution curves should give us a reasonably consistent result.

We may compare our methods for estimating bed expansion ratio with literature predictions if we remember that correlations for estimating the bed porosity provide a way to evaluate the fluidized expansion ratio. One of the most commonly used correlations is that proposed by Staub and Canada (1978) --

$$\frac{u}{\varepsilon_f} = \frac{(1 - \varepsilon_s)}{\varepsilon_s} \times u_{mf} + C_o u$$

Table 23. Bed expansion ratios for different particles and gas velocities

Bed expansion ratios for different particles

(the average data taken from all distributor for $H_s \cong 50$ mm)

Particle	Gas velocity (m/s) 0.5	1.0	1.5	2.0	2.5
P-A-1	-----	1.09	1.34	1.56	1.78
P-A-2	1.07	1.36	1.67	1.93	2.53
P-A-3	1.46	1.81	2.35	2.84	-----
P-S-1	1.19	1.48	1.85	-----	-----
P-S-2	1.34	1.64	2.05	-----	-----
P-C-1	1.17	1.56	-----	-----	-----
P-G-1	-----	1.21	1.45	1.70	1.97
P-G-2	-----	1.31	1.52	1.80	-----
P-G-3	-----	1.40	1.60	1.84	-----
P-G-4	1.32	1.76	2.16	-----	-----

Table 24. Bed expansion ratios for beds having different distributors

Bed expansion ratios for different distributors

(particle P-A-2; static bed height = 54.1 mm)

Distributor	Gas velocity (m/s) 0.5	1.0	1.5	2.0	2.5
D-1	1.07	1.36	1.63	1.90	2.34
D-2	-----	1.29	1.66	1.92	-----
D-3	-----	1.35	1.63	1.94	-----
D-4	-----	1.37	1.72	1.99	2.38
D-6	-----	1.40	1.66	1.92	2.31
D-7	-----	1.38	1.70	1.92	2.28
average	1.07	1.36	1.67	1.93	2.33

Table 25. **Bed expansion ratios for beds having different static bed heights**

Bed expansion ratios for different static bed heights

(distributor D-1 and particle P-A-2.)

Static bed height (mm)	Gas velocity 0.5	1.0	1.5	2.0	2.5
16.3	-----	1.29	1.48	1.82	2.45
27.1	1.04	1.28	1.52	1.82	2.37
54.2	1.07	1.36	1.63	1.93	2.34
81.3	1.08	1.35	1.58	1.85	-----
Ave.	1.06	1.32	1.55	1.86	2.39

Table 26. Experimental Bed expansion ratios and values calculated from equations 5.3 and 5.4

Comparison of the experimental and correlational bed expansion ratio

d_p (μm)	ρ_s (kg/m^3)	ε	u (m/s)	u_{mf} (m/s)	H_r ($expt.$)	H_r^{**}	error (%)
1260	3680	0.38	1.50	0.90	1.34	1.41	5.2
1260	3680	0.38	2.00	0.90	1.56	1.55	0.9
1260	3680	0.38	2.50	0.90	1.78	1.68	5.5
630	3680	0.38	1.00	0.42	1.36	1.41	4.0
630	3680	0.38	1.50	0.42	1.67	1.62	3.0
630	3680	0.38	2.00	0.42	1.93	1.83	5.3
630	3680	0.38	2.50	0.42	2.33	2.03	12.7
335	3680	0.38	0.50	0.15	1.46	1.42	2.6
335	3680	0.38	1.00	0.15	1.81	1.85	1.9
335	3680	0.38	1.50	0.15	2.35	2.30	3.5
335	3680	0.38	2.00	0.15	2.84	2.69	5.3
630	2870	0.44	1.00	0.34	1.48	1.51	2.1
630	2870	0.44	1.50	0.34	1.85	1.77	4.5
359	2840	0.48	0.50	0.13	1.34	1.59	18.4
359	2840	0.48	1.00	0.13	1.64	2.17	32.5
359	2840	0.48	1.50	0.13	2.05	2.76	34.6
630	960	0.40	1.00	0.13	1.56	1.38	11.6
842	2500	0.38	1.50	0.45	1.45	1.46	0.3
842	2500	0.38	2.00	0.45	1.70	1.61	5.5
842	2500	0.38	2.50	0.45	1.97	1.76	10.8
705	2500	0.38	1.00	0.36	1.31	1.35	2.8
705	2500	0.38	1.50	0.36	1.52	1.52	0.0
705	2500	0.38	2.00	0.36	1.80	1.69	5.9
484	4490	0.39	1.00	0.33	1.40	1.59	13.4
484	4490	0.39	1.50	0.33	1.60	1.88	17.6
484	4490	0.39	2.00	0.38	1.84	2.02	9.8
353	2500	0.39	0.50	0.11	1.32	1.42	7.5
353	2500	0.39	1.00	0.11	1.76	1.84	4.4
353	2500	0.39	1.50	0.11	2.16	2.26	4.5

* average error = 8.0 %

** $H_r = 1.0 + 3.70 \times 10^{-6} \times \rho_r \times \sqrt{d_p} \times (u/u_{mf}) \times [\varepsilon/(1-\varepsilon)]$

This can be rearranged to read:

$$H_r = \frac{H_f}{H_s} = \frac{1 - \varepsilon_s}{1 - \varepsilon_f} = \frac{(1 - \varepsilon_s) + C_o\varepsilon_s(u/u_{mf})}{1 + \frac{\varepsilon_s}{1 - \varepsilon_s}\frac{u}{u_{mf}}(C_o - 1)} \qquad [5.2]$$

where

ε_s = static bed porosity, dimensionless.

ε_f = fluidizing bed porosity, dimensionless.

u = superficial gas velocity, $\frac{m}{s}$.

C_o = a constant (about 1.05).

u_{mf} = minimum fluidization velocity, $\frac{m}{s}$.

H_s = static bed height, *m*.

H_f = fluidizing bed height, *m*.

H_r = bed expansion ratio = $(\frac{H_f}{H_s})$, dimensionless.

By exploring different values of $\frac{u}{u_{mf}}$, it has been found that Equation 5.2 can be approximated by --

$$H_r = 1.0 + K_o \times \frac{\varepsilon_s}{1 - \varepsilon_s} \times \frac{u}{u_{mf}} \qquad [5.3]$$

where

$K_o \cong 0.38$

for $2.0 < \frac{u}{u_{mf}} < 15.0$; $\varepsilon_s \cong 0.4$

We have used equation 5.3 to calculate bed expansion ratio H_r under fluidizing conditions listed in Table 23 on page 218. However, equation 5.3 always underestimates the values. As indicated earlier, a reason for the failure of equation 5.3 may be that it should be applied only to the particulate fluidization.

Based on the assumption that the K_o value in equation 5.3 should be a variable determined by the fluidized-bed properties instead of a constant, we have tested a number of pos-

sible models and correlations. With use of the Generalized Linear Regression Method in the SAS program at Virginia Tech, we have found the following correlation that we propose for evaluating K_o value--

$$K_o = 3.7 \times 10^{-6} \times \rho_r \times \sqrt{d_p} \qquad [5.4]$$

where

ρ_r = density ratio of the bed = $(\rho_s - \rho_f)/\rho_f$.

ρ_s = density of the particle, Kg/ m^3.

ρ_f = gas density, Kg/ m^3.

d_p = particle diameter, μm.

Table 26 on page 221 compares bed expansion ratios calculated from equations 5.3 and 5.4 with experimental values. Equations 5.3 and 5.4 predict the bed expansion ratio closely (having a average error of 8%). The SAS program also shows the R^2 to have a value of 0.76. This implies that the correlation coefficient between the calculated and experimental values is 0.87 (the value of R).

5.7 Jet penetration depth

5.7.1 Correlations for predicting jet penetration depth

The jet phenomenon is of fundamental importance to the performance of fluidized-bed reactors. In the simplest fluidized bed, the fluidizing gas passes through the distributor holes in the form of jets; and it is important to know how far the jets penetrate into the bed. If a high-velocity jet impinges on vessel internals, such as immersed heat-transfer tubes, its sandblasting effect is likely to be erosive, with possibilities for disastrous consequences. For beds in which chemical reactions are taking place, much of the conversion may occur in the jet region near the distributor plate, especially when a reaction is fast. There are even some special techniques for separation heavy/large particles from light/small particles by utilizing the non-uniformity the velocity field near single or multiple jets.

Although a number of experimental correlations have been published for estimating jet penetration depth in a fluidized bed, there is little agreement on the values predicted by the published correlations. Perhaps the most popular correlation is that proposed by Yang and Keairns (1978). Their correlation can be written --

$$\frac{L_j}{d_o} = B_o \left(\frac{\rho_f}{\rho_s - \rho_f} \frac{u_o^2}{g\, d_o}\right)^{B_1} \qquad [5.5]$$

where

$\frac{L_j}{d_o}$ = the jet penetration depth ratio.

L_j = the jet penetration depth (in mm).

d_o = the diameter of the orifice on the gas distributor (in mm).

u_o = the gas velocity passing through the orifice (in m/s).

B_0, B_1 = two constants to be evaluated.

Notice that the dimensionless group in the brackets can be seen as a two-phase Froude number (see Wallis, 1969).

Filla and Massimilla (1983) analyzed the criterion for bubble detachment based on a balance between the jet momentum flow-rate and the momentum in the wake of bubbles. They have found that the two-phase Froude number should be a key factor to be included in an equation to correlate jet penetration depth. This observation provides some theoretical basis to Yang and Keairns' equation. In comparison with other correlations for jet penetration (see Chapter 2), Yang and Keairns' equation also has the beauty of simplicity, a feature always appreciated by a design engineer.

Although Yang and Keairns have demonstrated that their correlation fits most of the experimental data within ± 40% limit, their correlation still has a serious shortcoming. Particle size -- a variable always of importance in determining the behavior of a fluidized bed -- is not included in their equation. It should be noticed that the range of particle size in each of the data sets used by Yang and Keairns is always small. Not knowing whether the Froude number can reflect some of the characteristics related to particle size in a fluidized bed, Yang and Keairns ignore the particle size as an independent variable in the correlation.

By checking all possible dimensionless groups, Blake et al. (1982) modified Yang and Keairns' expression to obtain the following equation --

$$\frac{L_j}{d_o} = B_o \left(\frac{\rho_f}{\rho_s}\right)^{B_1} \left(\frac{u_o^2}{g\, d_o}\right)^{B_2} \left(\frac{u_o\, d_p\, \rho_f}{\mu_f}\right)^{B_3} \qquad [5.6]$$

Combining with the fluid properties (density, velocity and viscosity), particle size had been added to the correlational equation in the form of a Reynolds number.

Blake et al. had shown that approximately 5% of the data points they cited lied outside the ± 40% band of their correlational curve. In light of the fact that more than 10% of the data fell outside the ± 40% band when Yang and Keairns' equation was used, Blake et al.'s correlation could be regarded as an improvement.

It should be mentioned that the undetermined constants (B_0, B_1, B_2, and B_3) correlation has increased from two to four. This could be regarded as a disadvantage. However, having Filla and Massimilla's analysis in mind, we can combine the density ratio and Froude number to form a two-phase Froude number and still maintaining a reasonable agreement with the physical analysis. This will decrease the number of undetermined constants by one and should not hurt the data fit too much.

By studying the mechanism of the jet development mentioned by Merry (1975), it can be appreciated that the pitch distance between two jets will affect jet growth, especially when two jets are close. Therefore, a dimensionless group $(P_t - d_o)/P_t$ can be introduced into the correlational equation to distinguish between single and multiple jets. The correlational equation for jet penetration can then be modified further to the following form --

$$\frac{L_j}{d_o} = B_o \left(\frac{\rho_f}{\rho_s - \rho_f} \frac{u_o^2}{g\, d_o}\right)^{B_1} \left(\frac{\rho_f d_p u_o}{\mu_f}\right)^{B_2} \left(\frac{P_t - d_o}{P_t}\right)^{B_3} \qquad [5.7]$$

where

P_t = the pitch distance between two orifices on the distributor (in mm).

Notice that the pitch distance P_t for a fluidized bed with a single jet can be taken as ∞. This will cause the value of $(P_t - d_o)/P_t$ to be 1, and make equation 5.7 to become a general correlation for jet penetration of either single or multiple jets.

5.7.2 Experimental conditions and results of the estimation of jet penetration depth

Figure 79 on page 228 shows a set of typical pressure distribution curves for particle P-A-2 (the 630-μm Master Beads) having a total bed weight between 100 to 1500 grams in the 101.6-mm I.D. column with gas distributor D-1. (Note: 1-mm static bed height = 18.45 grams of Master Beads). Since the curves for total weight of particles greater than 500 grams follow

the pattern of curve a-b-c-d in Figure 60 on page 190, one can use the position of point (c) to estimate the jet penetration depth at different experimental conditions. In many situations, the straight-line segments on the curves with a static bed height less than 50 mm can be easily. It is therefore recommended that jet penetration depths be estimated from pressure distribution curves for static bed heights greater than 50 mm. The point at which the pressure distribution curve deviates from a straight line [point (c) in Figure 60 on page 190] is not easy to be specified exactly under some conditions (especially, at low gas velocities). However, the possible range of this initial point of deviation can be estimated easily as shown on Figure 79 on page 228.

Table 27 on page 229 lists the jet penetration depths estimated from pressure distribution curves for particles P-A-1,P-A-2,P-A-3,P-S-1 and P-C-1 in fluidized beds having the three perforated distributors. The data predicted from the three most popular correlations (i.e., Blake et al.; Wen et al.; and Yang and Keairns) are also listed for comparison.

5.7.3 Comparison of correlations with experimental data

Figure 80 on page 230 to Figure 82 on page 232 show the predicted $\frac{L_j}{d_o}$ values versus experimental $\frac{L_j}{d_o}$ data reported in the literature and from this work. Predicted values are shown for equations 5.5, 5.6 and 5.7 respectively. Table 28 on page 233 lists the symbols for all of the data points given in those figures. Statistical information on the quality of the curve fitting in conjunction with all of the constant values (B_o to B_3) are listed in Table 29 on page 234. Notice that different correlational constants have been proposed for beds with single and multiple jets.

By checking the "constants" (B_o, B_1, B_2 and B_3) for all of the equations in Table 29 on page 234, we can find that there are some differences between the jet penetration depths for the bed with single jet and for the bed with a multiple-orifice gas distributor (hence, producing multiple jets). Blake et al.'s correlation gives a negative B_1 value in the case of a single jet.

Evaluation of the jet penetration depth using the pressure distribution curves

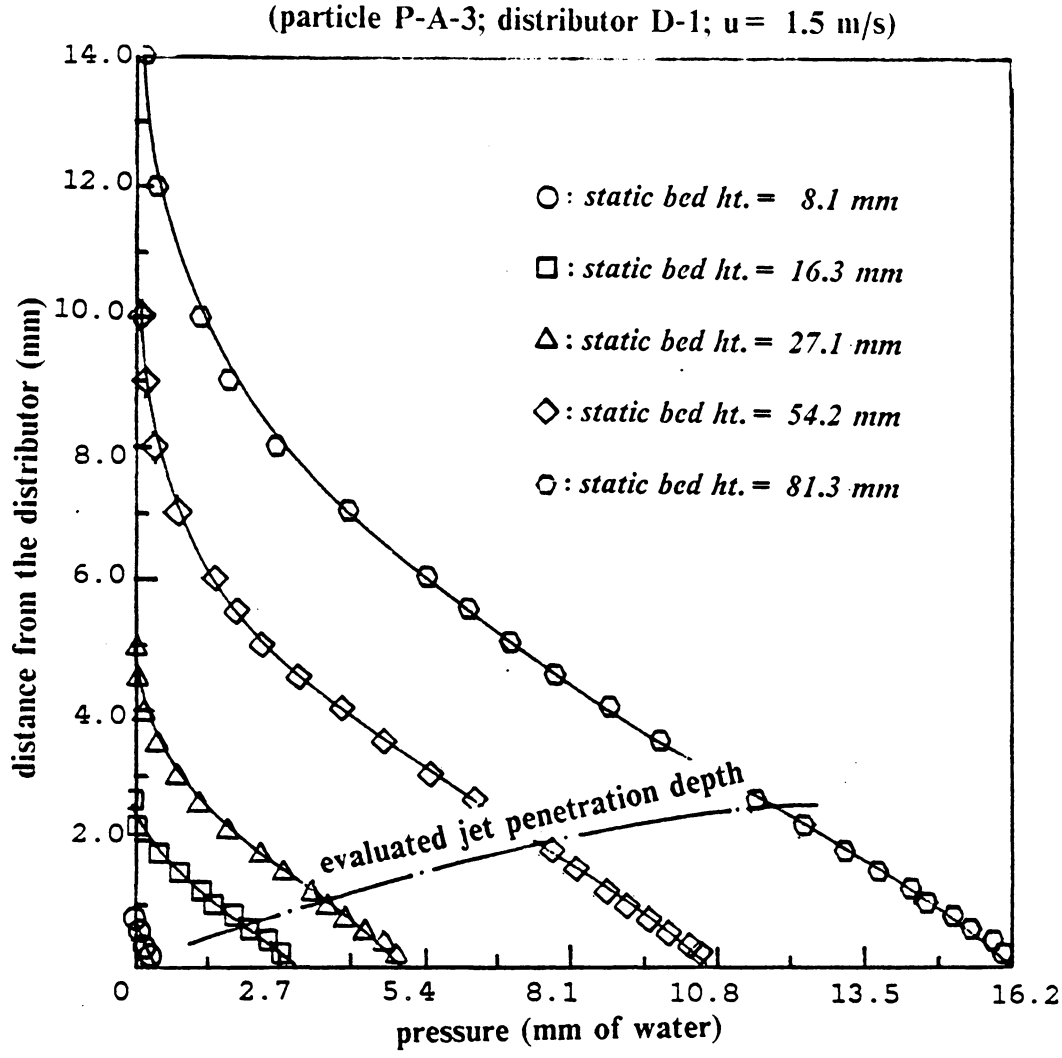

Figure 79. A set of pressure distribution curves for estimating jet penetration

Table 27. Jet penetration depth estimated from pressure distribution curves

Jet penetration depths got from pressure distribution curves

Distr.	Particle	u(m/s)	L_j	L_j^1	L_j^2	L_j^3
D-1	P-A-2	0.5	17	09	12	18
D-1	P-A-2	1.0	21	11	16	23
D-1	P-A-2	1.5	26	13	19	27
D-1	P-A-2	2.0	31	15	22	30
D-1	P-A-3	1.0	22	11	15	23
D-1	P-A-3	1.5	26	13	19	27
D-1	P-A-3	2.0	30	15	22	30
D-1	P-S-1	0.5	20	10	15	19
D-1	P-S-1	1.0	26	13	20	24
D-1	P-C-1	0.5	22	15	47	23
D-1	P-C-1	1.0	28	21	62	30
D-2	P-A-1	1.0	22	14	16	28
D-2	P-A-1	1.5	26	16	19	32
D-2	P-A-1	2.0	30	18	22	36
D-2	P-A-1	2.5	33	20	24	39
D-2	P-A-2	1.0	24	14	19	28
D-2	P-A-2	1.5	30	16	23	32
D-2	P-A-2	2.0	35	18	26	36
D-2	P-A-3	0.5	23	10	15	21
D-2	P-A-3	1.0	28	14	22	28
D-2	P-A-3	1.5	30	16	26	32
D-2	P-A-3	2.0	34	18	30	36
D-2	P-S-1	0.5	22	12	18	22
D-2	P-S-1	1.0	27	15	25	29
D-2	P-C-1	0.5	25	19	56	27
D-2	P-C-1	1.0	30	26	75	35
D-3	P-A-1	1.0	26	21	24	47
D-3	P-A-1	1.5	30	25	28	55
D-3	P-A-1	2.0	32	28	32	61
D-3	P-A-2	0.5	24	16	21	36
D-3	P-A-2	1.0	28	21	28	47
D-3	P-A-2	1.5	32	25	33	55
D-3	P-A-3	0.5	27	16	24	35
D-3	P-A-3	1.0	30	21	32	47
D-3	P-A-3	1.5	35	25	38	55
D-3	P-S-1	0.5	26	18	27	38
D-3	P-S-1	1.0	35	24	36	49
D-3	P-C-1	0.5	32	30	82	47
D-3	P-C-1	1.0	38	40	100	61

1. data predicted from the correlation proposed by Blake et. al.
2. data predicted from the correlation proposed by Wen et. al.
3. data predicted from the correlation proposed by Yang and Kearns

Predicted and experimental jet penetration ratios for data from literature using the correlation of Yang & Keairns

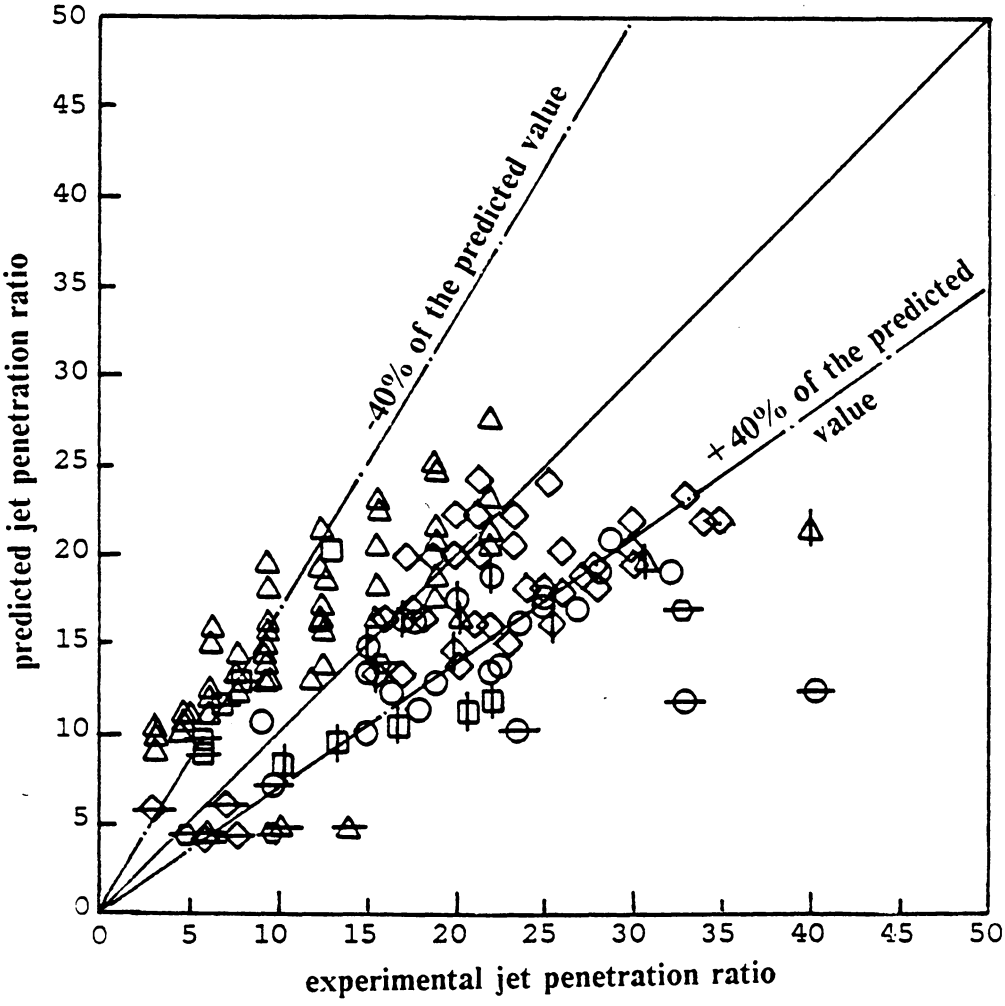

(see Table 28 for labels)

Figure 80. Experimental jet penetration ratio versus prediction by Yang and Keairns correlation

Predicted and experimental jet penetration ratios for data from literature by using the correlation of Blake et al.

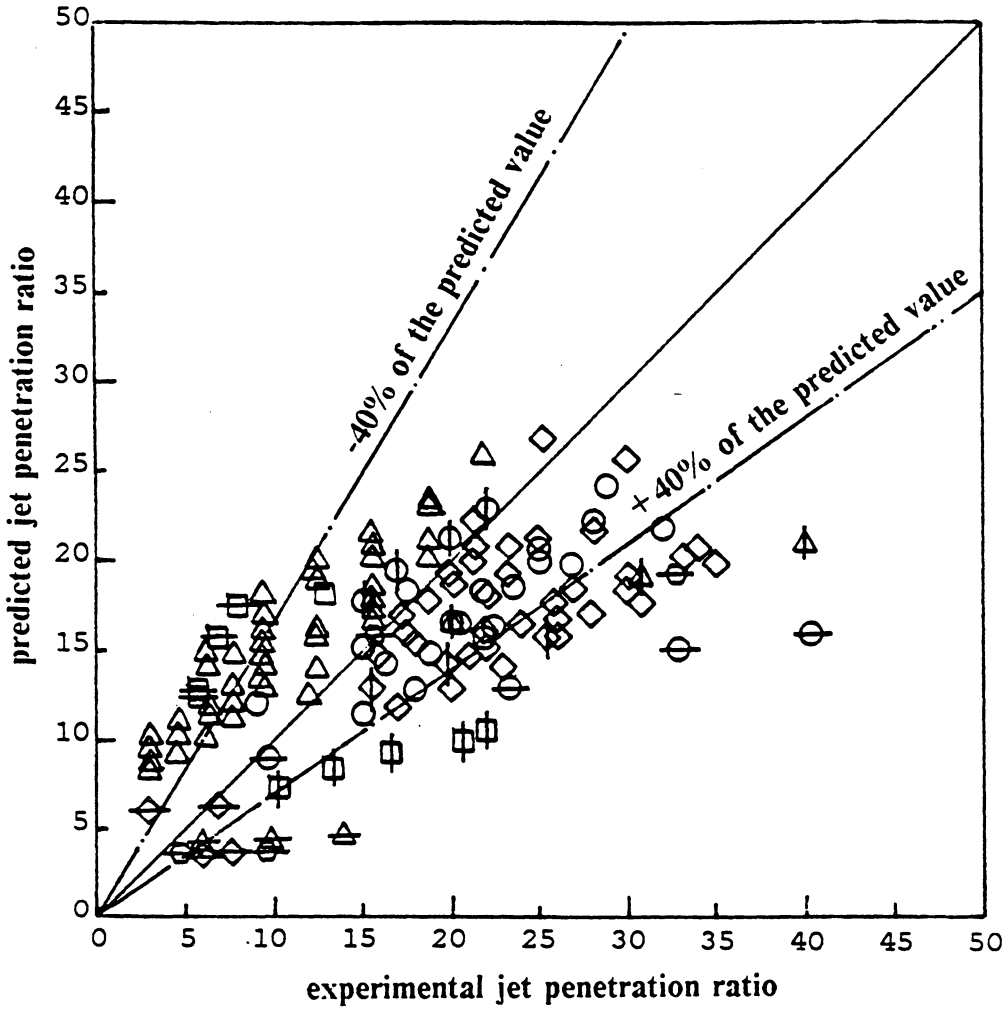

(see Table 28 for labels)

Figure 81. Experimental jet penetration ratio versus prediction by the correlation of Blakes et. al.

Predicted and experimental jet penetration ratios for data from literature by using the correlation of this study

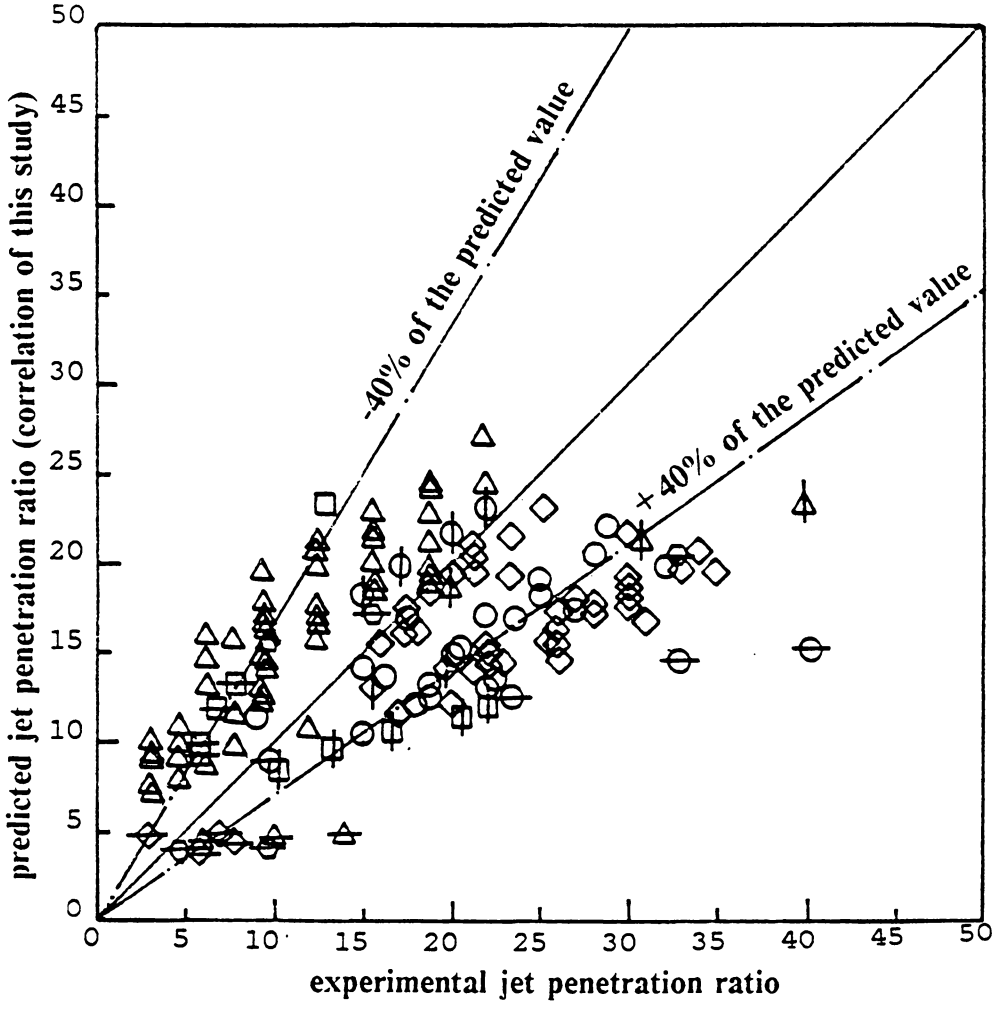

(see Table 28 for labels)

Figure 82. Experimental jet penetration ratio versus prediction from the correlation of this study

Table 28. Symbols for all data in the figures comparing correlations for jet penetration

Symbols for the data collected for the jet penetration study

1. Basov, et. al. (1969)	
2. Ghadiri, et. al. (1980)	
3. Wen, et. al. (1982)	
4. this study	
5. Behie, et. al. (1971)	
6. Galdaspow, et. al. (1983)	
7. Ishida, et. al. (1982)	
8. Kececioglu, et. al. (1984)	
9. Markhevka, et. al. (1971)	
10. Merry (1975)	
11. Shakhova (1968)	
12. Yang and Keairns (1970)	
13. Zenz (1968)	

Table 29. Constants for the three correlations for jet penetration

Constants in three different correlations for the jet penetration

Correlation Equation	data catagory	B_0	B_1	B_2	B_3	R^2
Yang and Keairns	all	8.46	0.137	-----	-----	0.361
	single jet	11.6	0.128	-----	-----	0.526
	multiple jet	4.70	0.24	-----	-----	0.476
Blake, et. al.	all	24.62	0.303	0.167	-.062	0.391
	single jet	8.27	-.108	0.144	-.101	0.716
	multiple jet	53.70	0.614	0.343	-.176	0.587
this work	all	16.00	0.167	-.079	0.721	0.387
	single jet	28.80	0.152	-.122	-----	0.579
	multiple	23.00	0.512	-.398	-2.93	0.684

Note:

1.the comparison is based on the $\ln(L_j/d_o)$ values.
2.the number of data : tatal --159; signle jet --34; multiple jets -- 125.
3.R^2 = the coefficient of determination.

This means that the jet penetration depth increases as the particle density increases -- a contradiction to both the common sense and momentum-transfer theory (see Filla and Massimilla, 1983). Therefore, we conclude that the correlational Equation 5.7 predicts the jet penetration depth best from considerations of simplicity, fitness, and good physical sense.

For fluidized beds having multiple jets, the values for B_0 to B_3 in equation 5.7 are determined by the fluidized bed characteristics -- i.e. B values are not universal constants for all fluidized beds. Table 30 on page 236 lists the B values from a regression analysis based on equation 5.7 for the data from Basov et al. (1969), Wen et al. (1982), and the present study. Notice that the number of data points in those three set of experiments are 22, 64 and 39, respectively -- the sample sizes are believed to be sufficiently large from a statistical point of view. Figure 83 on page 237 plots values of predicted $\frac{L_j}{d_o}$ versus experimental $\frac{L_j}{d_o}$ for these three data sets, based on equation 5.7 and the corresponding B values. There has been a reasonably good improvement on the prediction that most of experimental values now fall into the $\pm$ 20% range of the prediction curve.

Figure 84 on page 238 plots values of predicted $\frac{L_j}{d_o}$ versus experimental $\frac{L_j}{d_o}$ values for the data in this study by using one general set of B values listed in Table 30 on page 236, based upon all of the data from three different distributors. One can see that almost all of the data are within the $\pm$ 20% range of predicted values. Figure 85 on page 239 plots values of predicted $\frac{L_j}{d_o}$ versus experimental $\frac{L_j}{d_o}$ by using one set of B values ($B_3 = 0$) for each family of data collected from the same gas distributor. There is not much improvement from Figure 84 on page 238 to Figure 85 on page 239. Therefore, the dimensionless group $(P_t - d_o)/P_t$ can determine the role of the gas distributor in predicting the jet penetration.

Table 30. Constants of three sets of data for predicting jet penetration

Constants for the correlation of jet penetration from three sets of data

based on the equation proposed by this study

Souce of data	number of data	constants			
		B_0	$B_{1\|}$	B_2	B_3
Basov et. al. (1969)	22	34.5	0.51	-0.66	-0.55
Wen et. al. (1982)	64	9.49	0.373	-0.205	-0.708
this study	39	8.23	0.218	-3.09	-3.09

Predicted and experimental jet penetrations for data from three different sources with different B values

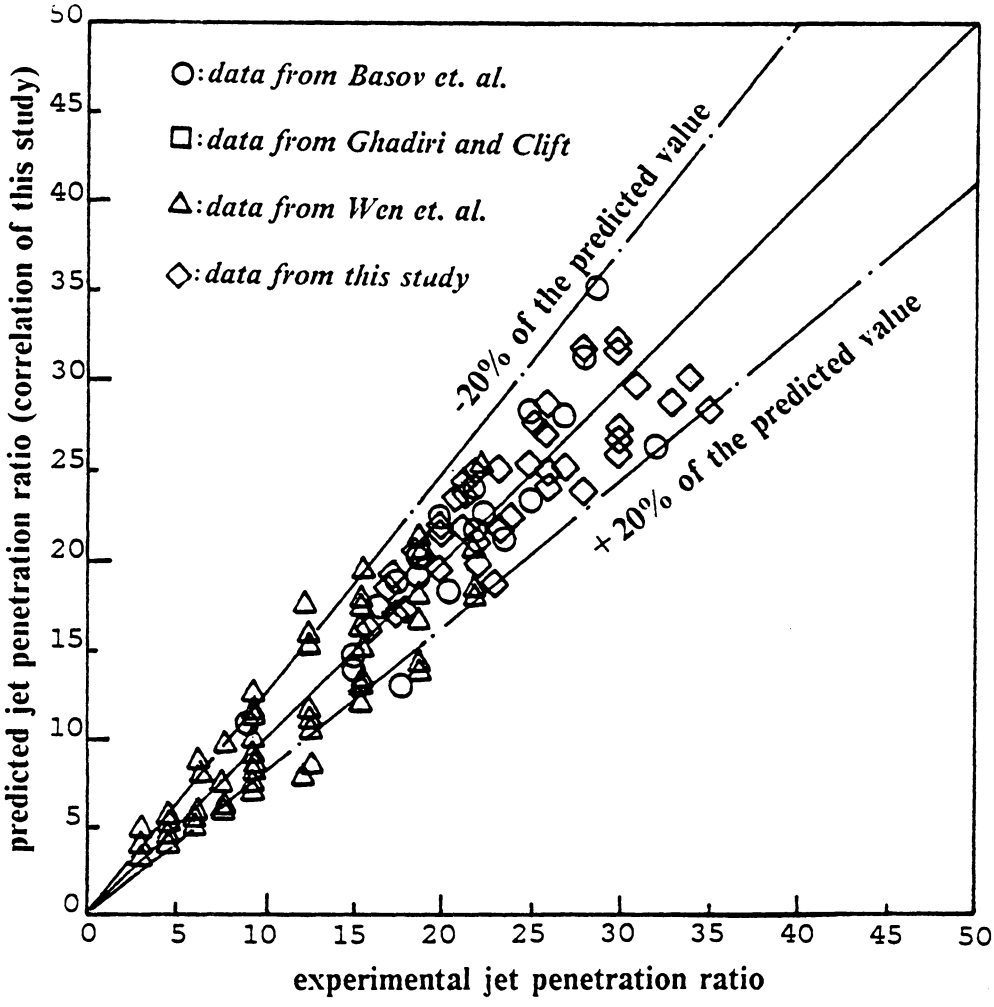

Figure 83. Predicted and experimental jet penetrations for three sets of data

Predicted and experimental jet penetration ratios for data from this study with a set of B values for all distributors

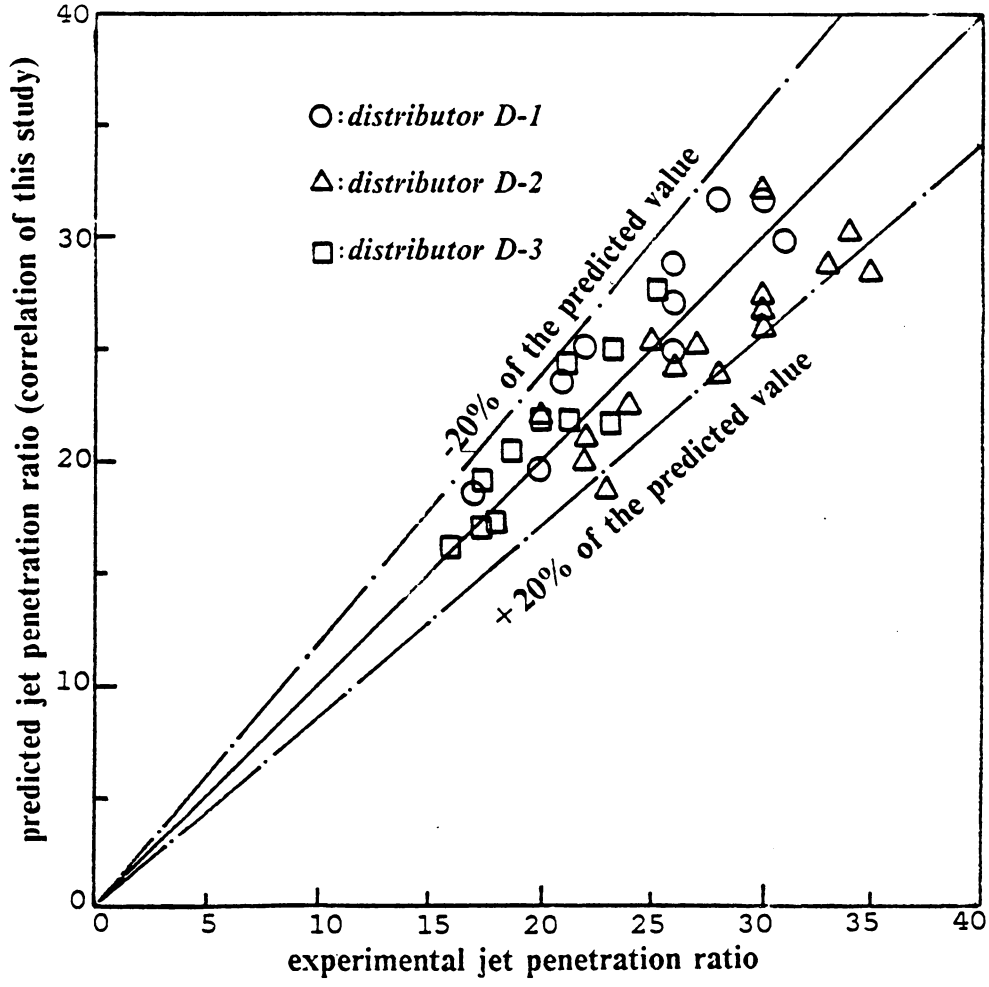

Figure 84. Predicted and experimental jet penetrations

Predicted and experimental jet penetration ratios for data from this study with a set of B values for each distributors

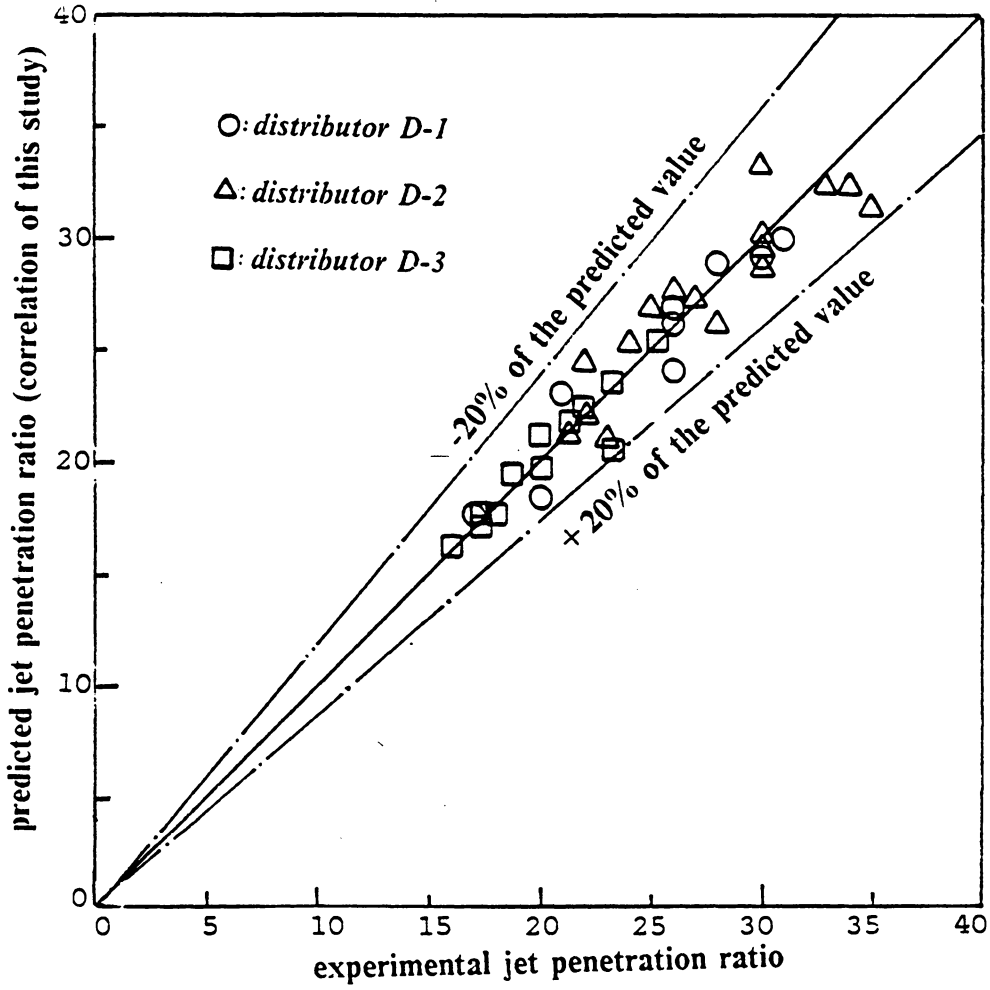

Figure 85. Predicted and experimental jet penetrations for the same distributor

5.7.4 Conclusions for predicting jet penetration with use of pressure distribution curve

1. Jet penetration depth is dependent on the amount of particles in the fluidized bed, especially when the static bed height is less than 50 mm.

2. B values in most of the correlational equations are not unique, but depend on characteristics of the fluidized bed.

3. Correlational equation 5.7, developed in this work, appears to give the best currently available prediction of jet penetration depth.

4. Jet penetration mechanism for multiple jets is significantly different from that for single jet.

5. The dimensionless group $(P_t - d_o)/P_t$ can well represent the role of the design of a gas distributor in determining the jet penetration depth.

CHAPTER 6 PARTICLE VOLUME-FRACTION IN SHALLOW FLUIDIZED BEDS

6.1 The light probe

A light probe modified from the Dutta and Wen's (1969) original design has been developed for measuring particle volume-fraction in our fluidized beds. Two calibration procedures, which are in good accord, have been used to find a mathematical relationship between the particle volume-fraction and output voltage from the light probe. The first calibration method utilizes a theoretical particle volume-fraction distribution derived from particle properties and optical theory. The second method uses the light probe in conjunction with a vibro-fluidized-bed system and takes advantage of the ability of vibrofluidization to provide a homogeneous bed of particles of a known porosity. The mathematical correlation between the particle volume-fraction and output voltage from the probe has provided us with a powerful tool to study the local particle distribution and fluctuation in fluidized beds.

6.1.1 Original idea of the light probe

In fluidization studies, the particle volume-fraction (or voidage) has always been an important variable to be examined in order to find out the crucial hydrodynamic parameters such as bubble size, bubble velocity, solid mixing, and jet penetration. Many experimental techniques have been proposed in the literature for the qualitative study of the voidage in fluidized beds. Usually, those techniques involve the application of electronic devices such as light probe, capacitance probe, tracer detector, pressure sensor, and radioscope.

However, none of the experimental technique mentioned above has been utilized for the quantitative study of the particle volume-fraction in fluidized beds. This becomes understandable by reviewing the basic principles of gas-solid fluidization and considering the non-homogeneous character of a fluidizing system. In other words, most of those experimental techniques cannot be referred to as a specified homogeneous voidage for purpose of their calibration.

Among all of the voidage measurement devices, the light probe has been chosen in this study due to its simplicity (less electronic components), low cost (less than $20, if the read-out device is not counted), and readiness for quantitative calibration.

6.1.2 Design and calibration of light probe

Design of the light probe

Figure 86 on page 244 to Figure 88 on page 246 show the complete light probe assembly, its details of construction, and the electronic circuit, respectively. The light probe is modified from the original design of Dutta and Wen (1969). In Figure 87 on page 245, a tiny light-emitting diode (XC880-A Inferred LED) acts as the light source. The sensing element is a

photo transistor (TIL81 IR Transistor) of about 3 mm diameter and 8 mm in length. Our use of infrared light and of a relatively sensitive transistor is an improvement over Dutta and Wen's design, permitting us to work in a lighted room and eliminating need for an amplifier. The LED and the photo transistor are encased in an aluminum tube and separated from each other by a distance of 9.53 mm. Rectangular slots of 9.53 mm by 5.08 mm are cut near one end of the tube for face-to-face positioning of the LED and the photo transistor and also to allow undisturbed movement of solid particles between LED and transistor. Two Pyrex glass sheets are placed in the slots to cover and protect the LED and the photo transistor, while two black plastic sheets are attached to the other two walls of the hole to eliminate possible refraction of light by aluminum. These arrangements make available (free) space between the LED and the transistor about 230 mm^3 (4.13 mm by 7.30 mm by 7.62 mm).

Figure 88 on page 246 shows the electronic circuit for the light probe assembly while Table 31 on page 247 lists specifications of all elements. Detailed descriptions on the characteristics of the elements can be found in the manufacturers' manuals.

The computer interfacing system

An IBM Personal Computer in conjunction with an interfacing system have been used for recording and managing output from the light probe system. A Data Translation's DT2801 interfacing board has been plugged into one of the system expansion slots in the IBM Personal Computer backplate. The DT2801 is a high-performance analog and digital input/output board that can be programmed from the IBM PC's interpreted or compiled BASIC language to perform the Analog-to-Digital or Digital-to-Analog conversions without any further hardware connection.

The analog signal from the optical probe system can be transferred into digital data via a 12-bit A/D converter on the DT2801 board. For our probe system, with its maximum output of 10.5 volts, a 12-bit conversion implies that the resolution can be as good as 2.5 mV. The

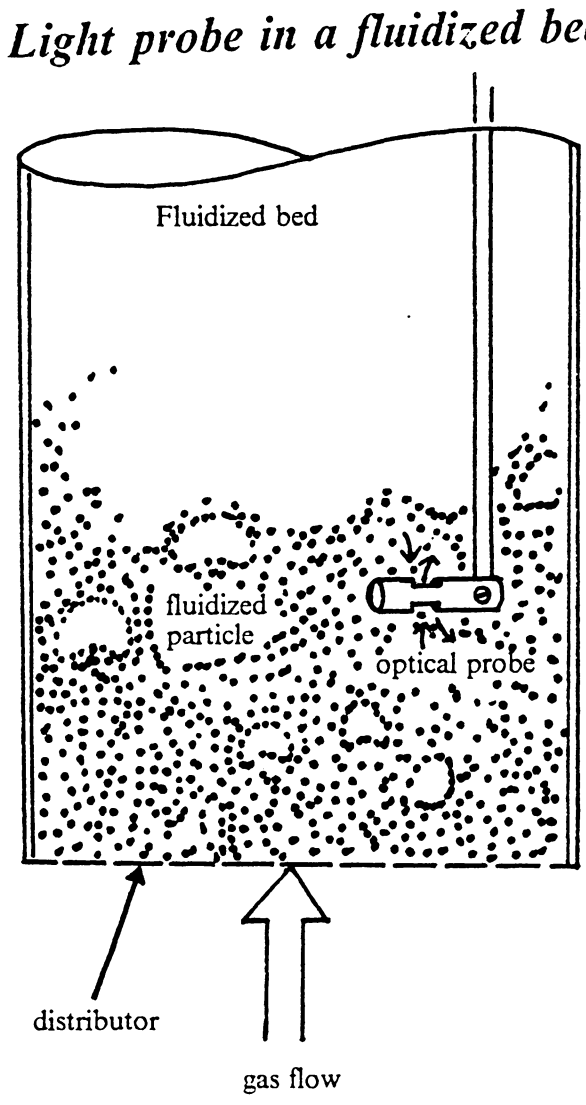

Figure 86. The light probe arrangement

Detailed construction of the light probe (top view)

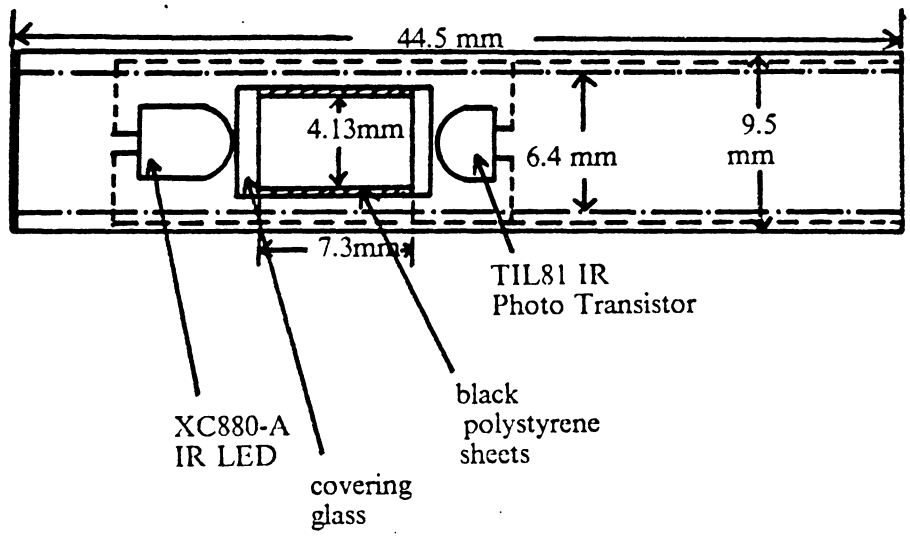

Figure 87. Detail of the construction of the light probe: (top view)

Electronic circuit of the light probe

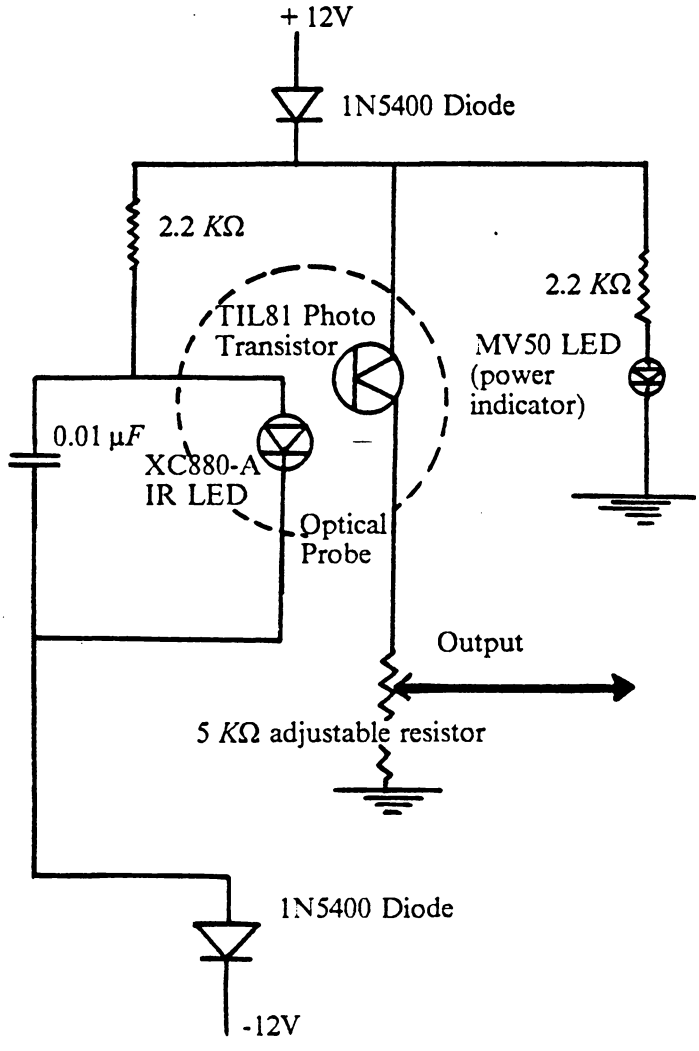

Figure 88. Electronic circuit for the light probe

Table 31. Elements and functions of the light probe

Elements and functions of light probe

Element	Function	Comments
1N5400 Diodes	keep the electric current in one direction	eliminate the damage caused by wrong connection
2.2 $K\Omega$ Resistances	adjust the voltage and current for LEDs	
0.01 μF Capacitor	eliminate the peak current	protect the IR LED
XC880-A IR LED	give light source for the photo transistor	near visible emission wave length = 915 nm.
TIL81 IR Photo Transistor	change the light signal into voltage	the shield effect of particles will make the output voltage up and down
5 K Ω Resistance	adjusted to amplify the output voltage	the output voltage can be adjusted from 0 to 10.5 Volts

built-in A/D converter has a 13.7 kHz throughput when a machine level (assembler) language program is activated. However, a compiled BASIC program can provide an approximately 10-kHz conversion, which is fast enough for this experiment. [By using the DMA (Direct Memory Address) technique, the data acquisition rate can be 30 kHz for the BASIC program.]

A Data Translation's DT707 screw-terminal panel has been used for convenience in making connections between light probe system and DT2801 interfacing board. Since we use only one of the 16 single-ended channels provided by the DT2801 board, all of channels not used are connected to the ground through 10 $k\Omega$ resistors in order to eliminate any noise from cross-talk. Figure 89 on page 249 shows details of the interface system between the light probe assembly and the IBM PC.

A computer program using the Advanced BASIC under IBM PC's DOS Version 2.1 has been written for securing and interpreting data. Figure 90 on page 250 gives the flow diagram for the computer program for obtaining output from the light probe via the computer interface system.

Appendix B lists the BASIC program for control and conversion of output data from the light probe through the DT2801 board. The most important tasks in specifying the constants in the computer programming are choice of a number of data points to be accumulated and selection of a sampling rate. In our studies, fluctuations in most of our shallow fluidized beds have a frequency in the magnitude of 10-20 Hz. This is comparable to the frequencies of fluctuation in somewhat deeper beds reported by Fan et al (1984). A sampling period of at least about 2 seconds (covering 20-40 cycles) is needed to record a complete story of particle fluctuation from a statistical point of view. Primarily by a trial-and-error effort, we have found that the slowest sampling rate must be 600 Hz in order to follow details of particle fluctuations completely. This implies that the number of data points to be accumulated must be at least 1000 (a value afforded by collecting data for 2 seconds at 600 Hz) to fulfill our requirements for collecting fluctuation data. Figure 91 on page 251 shows fluctuations of particle volume-fractions at a 600-Hz sampling rate.

The Interface between the light probe and IBM PC

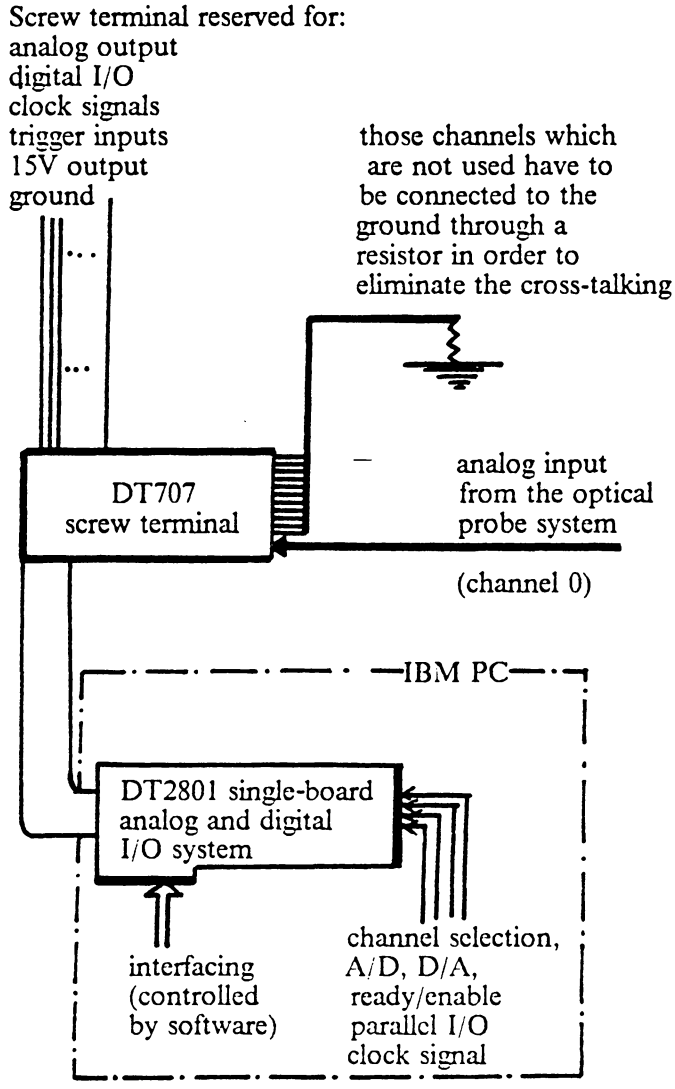

Figure 89. Interface system between light probe and IBM PC

Flow diagram for obtaining output from the light probe

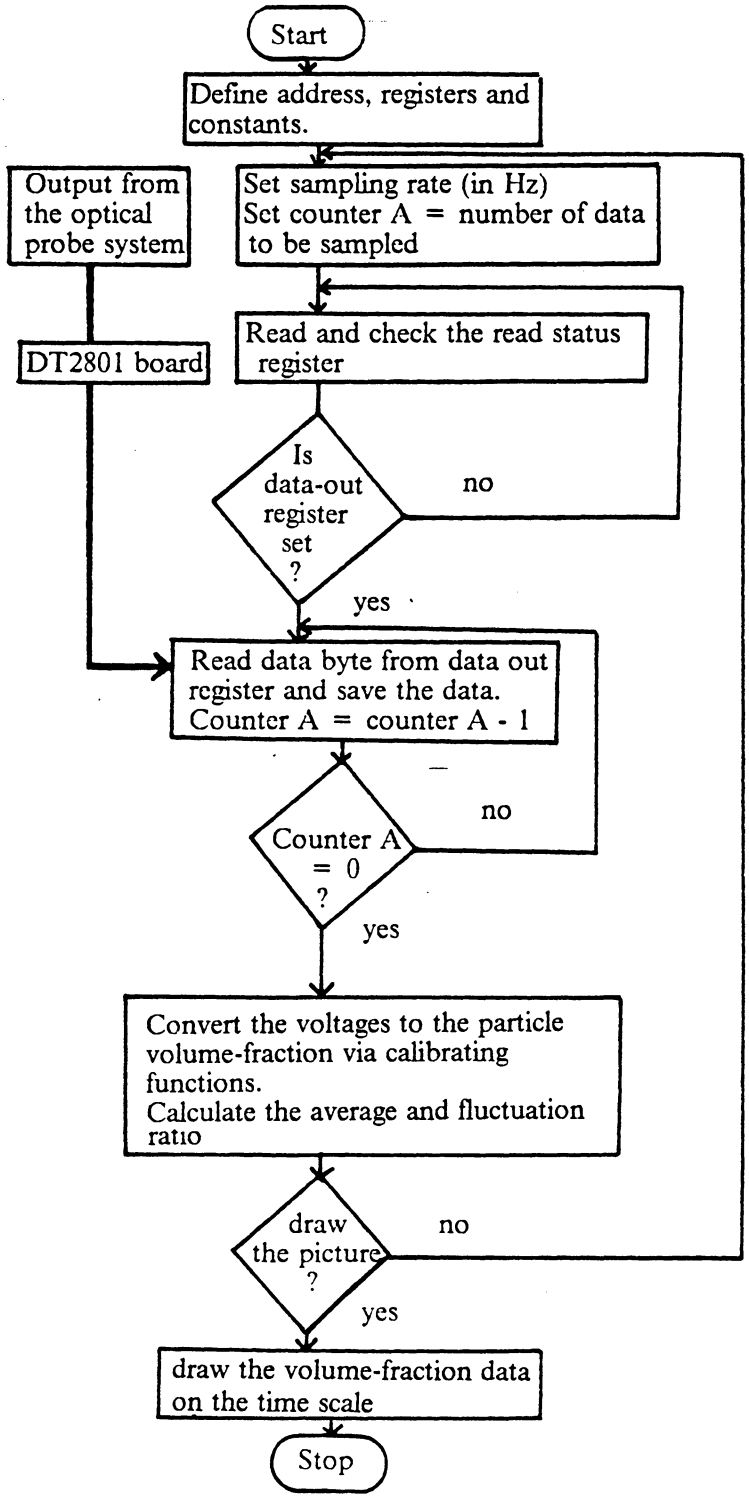

Figure 90. Flow diagram for obtaining output from light probe via IBM PC

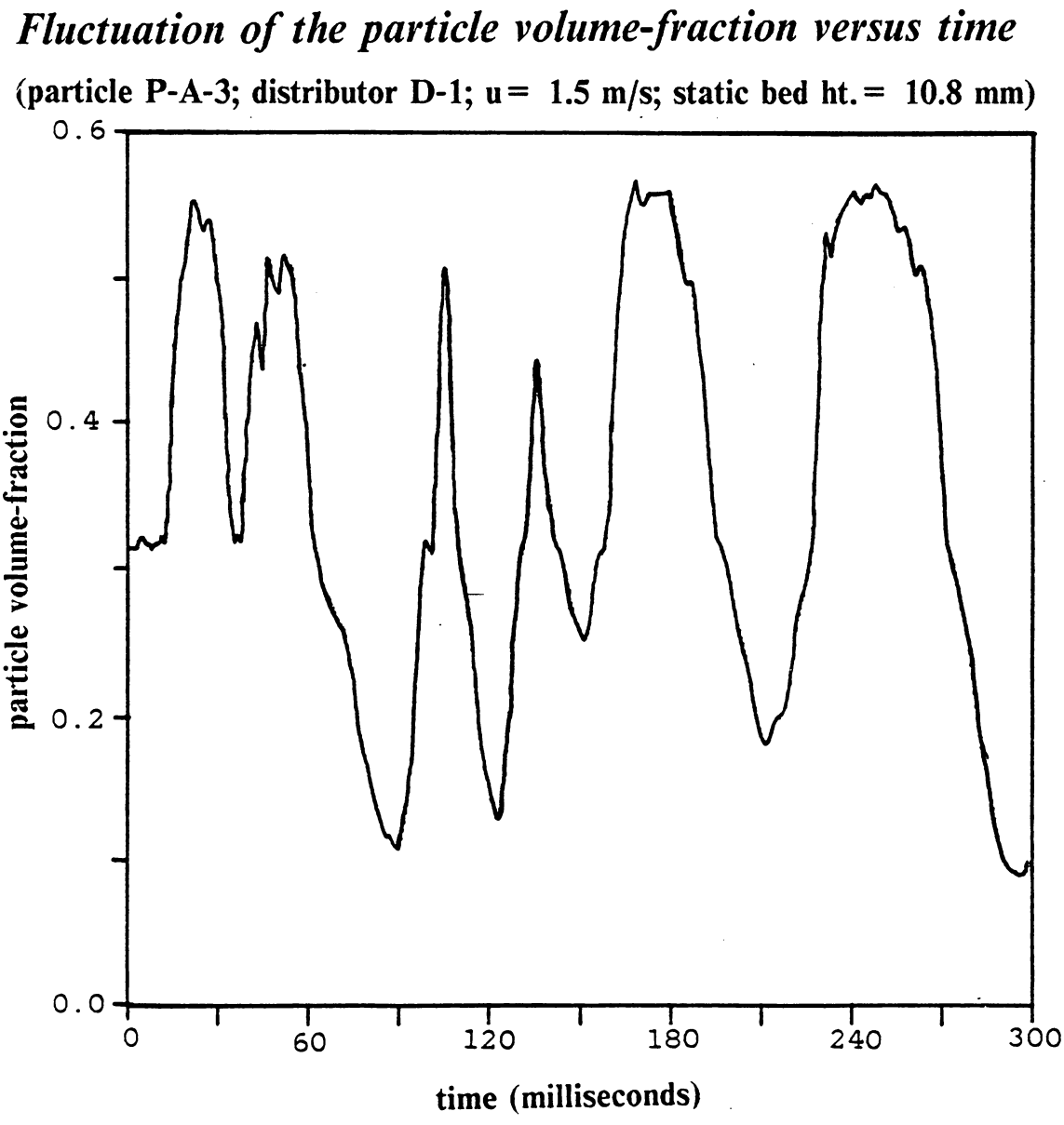

Figure 91. Fluctuation of particle volume-fraction versus time: for 10.8 mm of 335-micron Master Beads in the 101.6-mm I.D. bed having distributor D-1 and gas velocity = 1.5 m/s

Calibration of light probe

In published reports of the application of light probes for observing phenomena in fluidized beds, no quantitative descriptions have been furnished on the relationship between voidage and output signal of the probe. In many reports, light probes have been used to identify the existence of a jet or the passage of a gas bubble, and quantitative values of bed densities were not of much interest.

We required a correlation function between output voltage and bed voidage. We have used two techniques for calibrating our light probe. It should be kept in mind, however, that the calibrations we have succeeded in obtaining are affected not only by the particle properties (shape, size, and color) but also by the characteristics of the electronic assembly.

Calibration of light probe using optical theory and particle volume-fraction

A primary theoretical calibration curve can be obtained from the following assumptions:

1. Light beams are parallel between the LED and photo transistor.

2. There is no deflection and diffusion of the light.

3. Output voltage is linearly proportional to the intensity of the light passing through voids among particles.

The particle volume-fraction can be expressed by the following primary form (for the detailed derivation, see Appendix C):

$$d_V = 1 - \varepsilon = \frac{2}{3} \times [1 - (0.1 \times V)^{n_p}] \qquad [6.1]$$

A fluidized bed having 335-μm Master Beads has been used to check the calibrating equation 6.1. The bed is 101.6-mm in diameter with a perforated distributor (D-1) having an open area percentage of 5.63%. The superficial gas velocity is kept at 2.0 m/s, while the total weight of particles in the bed is increased from 10 to 250 grams. The output voltage from the light probe is recorded at different probe elevations. Due to the fluctuating character of the output voltage, 1800 data points are recorded to calculate the average voltage for each probe elevation. Having the voltage data, the primary theoretical bed-density distribution can be calculated using equation 6.1. After integrating this primary theoretical bed-density distribution curve from bottom to the top of the fluidized bed, we can calculate the "theoretical total particle weight", which will then be compared with the actual value to check the validity of equation 6.1.

It has been found that the calculated weight of particles based on Equation 6.1 is in agreement with the actual value only for very dilute beds. For a denser fluidized bed, equation 6.1 always underestimates the particle density. Therefore, it is desirable to modify the correlational equation to a more realistic form. A simple modification will be multiplying the right-hand side of equation 6.1 by a polynomial function

$$d_v = g(V)\ \frac{2}{3}\left[1 - (0.1\ V)^{n_p}\right] \qquad [6.2]$$

where g(V) is a polynomial function in V, the voltag output. For the simplicity of the modification, g(V) is assumed to have a quadratic form, that is

$$g(V) = a + b \times V + c \times V^2 \qquad [6.3]$$

A computer program has been written to minimize the difference between the actual weights of particles in the bed and the values derived by integrating light-probe data obtained throughout the bed, with voidages calculated from equations 6.2 and 6.3. The method of Hook and Jeeves (see Bazaraa and Shetty, 1979) is used to find optimal values of a, b and c. Appendix D gives a listing of the FORTRAN program. It was found that the data set of (3.4, 0.45,

0.011) gave a minimum disagreement between theoretical and actual total weights of 335-μm Master Beads for our light-probe system.

It has also been observed that equation 6.3 underestimates the volume-fraction for a dilute fluidized bed. Therefore, the best correlational equation can be expressed as

$$d_v = g(V)\ \frac{2}{3}[1 - (0.1\ V)^{n_p}] \qquad [6.4]$$

$g(V) = 1$ for $V < 6.305$

$g(V) = 3.4 + 0.45\ V + 0.011\ V^2$ for $V > 0.6305$

Notice that the function g(V) is equal to 1 when V=6.305. This makes the voltage value of 6.305 for the output voltage to be the "natural" dividing point for the data of dilute and dense phases.

Figure 92 on page 255 gives calibrating curves for particle volume-fraction versus output voltage of the optical probe, based on equations 6.1 and 6.4. It can be seen that equation 6.4 eliminates the problem of underestimation and extends the applicable range of the equation to a particle volume-fraction of about 0.35. Actual total weights of particles versus weights calculating from particle density distribution on the basis of equation 6.4 are represented on Figure 93 on page 256. It can be seen that the error is confined in a range of ± 4 %. This gives us confidence that equation 6.4 is valid.

Calibration of optical probe with use of a vibrofluidized-bed system

From vibrofluidization theory, a confined space containing a certain amount of particles can be vibrated to achieve a situation where all of the particles are homogeneously mixed and distributed. Having a vibro-bed system conveniently available in the Novel Fluid-Particle Research Laboratory of the Chemical Engineering Department at Virginia Tech., it has been possible for us to use it for a direct calibration of our optical probe.

Calibration curve of the light probe from the optical theories

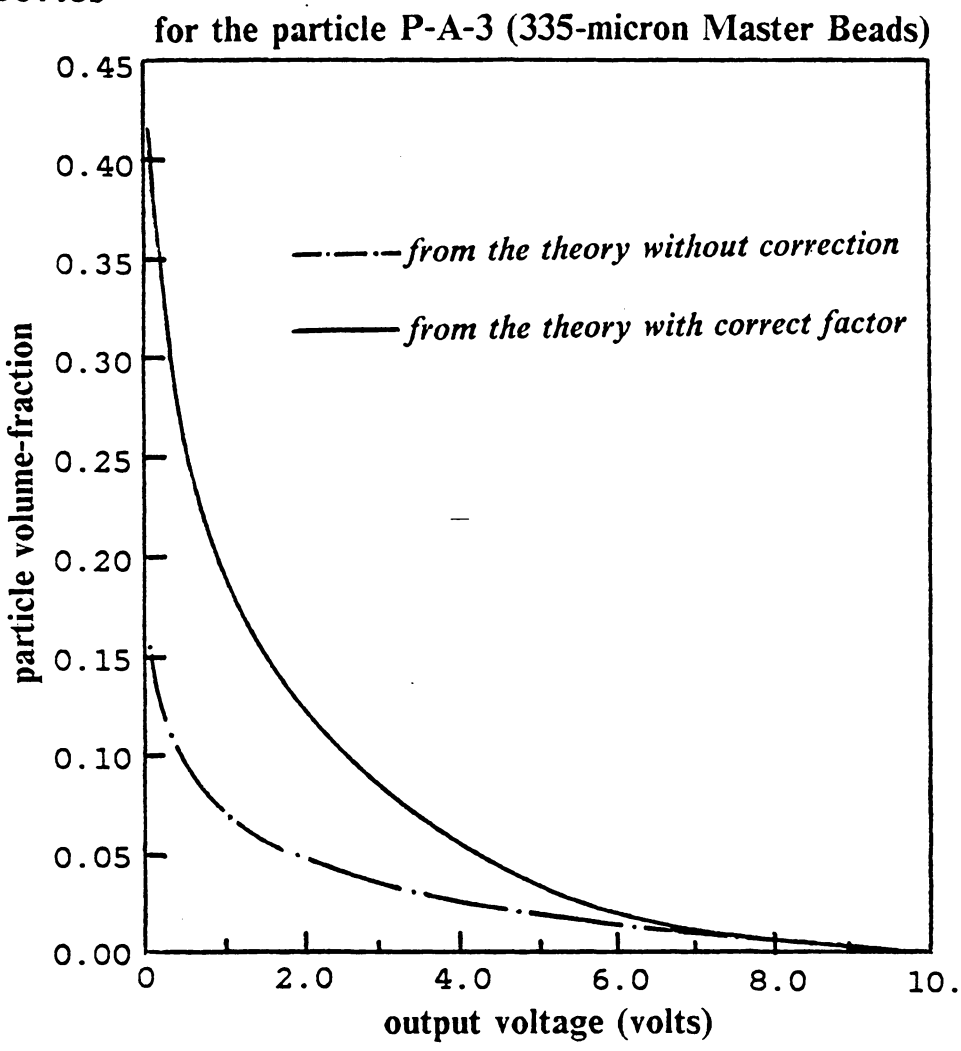

Figure 92. Calibration curve of light probe from optical theory: Particle volume-fraction versus output voltage for 335-micron Master Beads.)

Comparison of the actual and calculated particle weight for the optical theories

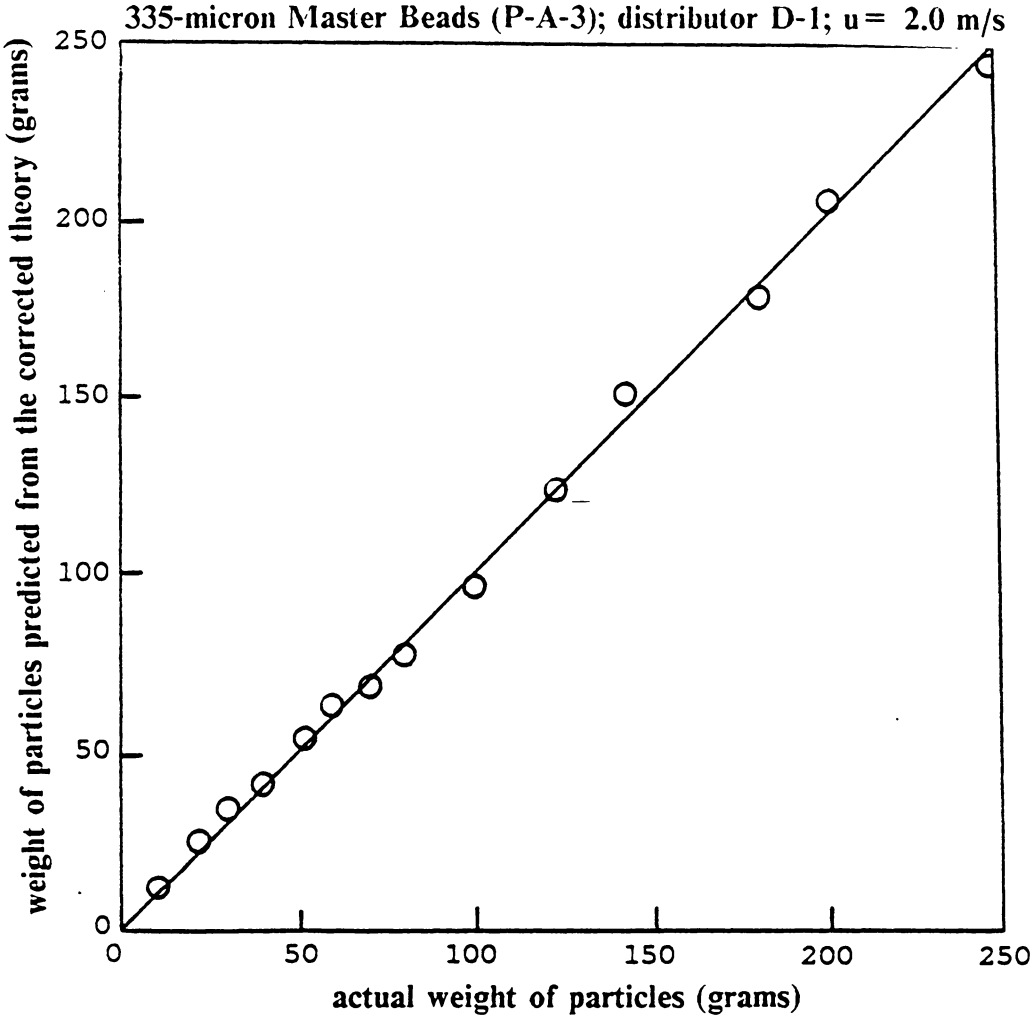

Figure 93. Comparison of actual and calculated particle weight from optical theory: (for 335-micron Master Beads.)

Before performing the calibration, a confined space having the same dimensions as the opening between the LED and photo transistor (4.13 mm by 7.33 mm by 7.62 mm) was built for checking the homogeneity of the vibrofluidized particles. The confined space is made of transparent plastic sheets for the convince of observations. Different amounts of particles are put into the space, while the whole testing element is fixed onto a vibrating table vibrator. All reachable frequencies and accelerating forces have been tried to make sure that particles can be homogeneously distributed inside the space.

A strobe light has been adjusted to synchronize with the frequency of the vibrator. This provides us a way to observe the homogeneity of particles inside the confined cube. Normally, the particle density distribution is dependent on the amplitude and frequency of vibrator. Figure 94 on page 258 shows the particle density distributions on the amplitude-frequency plane. However, it has to be kept in mind that the optimal amplitude and frequency to make the particle homogeneous depends on the properties of particles and may also depend upon the material used to confine the space.

It was found that the frequency has to be in the range of 20 - 28 Hz. and vibrational acceleration must exceed 3.5 times gravity for Master Beads to be homogeneously distributed in the confined space. The relationship between the particle density and total weight of particles in that space can be expressed by the following equation

$$W_p = V_p \times \rho_s \times d_v \qquad [6.5]$$

where

W_p = the weight of particles inside the confined space, kg.

V_p = the volume of the confined space, m^3.

ρ_s = density of the particles, $\frac{kg}{m^3}$.

d_v = volume-fraction of the particle inside the space, dimensionless.

The following procedures have been followed for direct calibration of the optical probe by using the vibrofluidized bed:

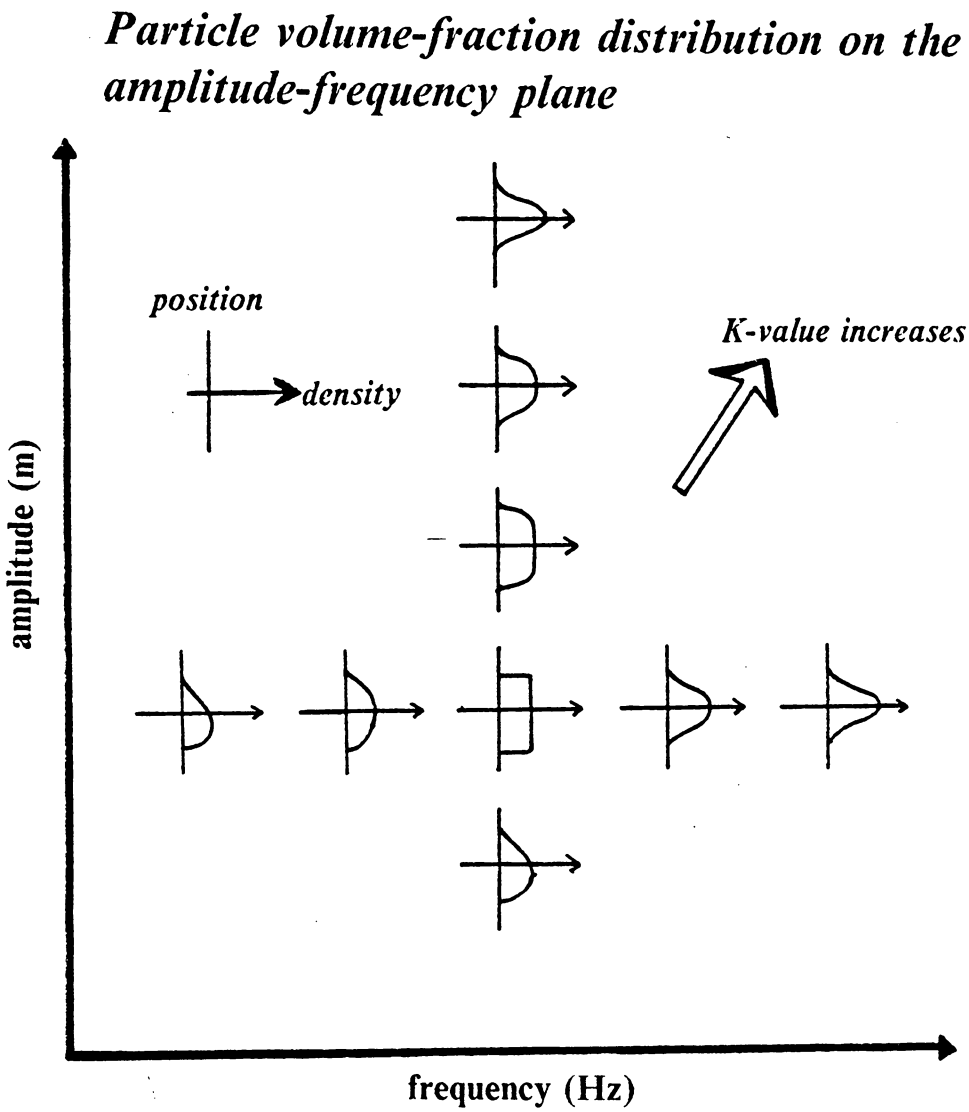

Figure 94. Particle volume-fraction distribution on the amplitude-frequency plane: (for particles confined in a small cube)

1. Putting a desired amount of particles (given d_v) into the space of the optical probe and into the reference transparent confined cube.

2. Confining the space of the optical probe by two pieces of black plastic (the same material used for the reference cube).

3. Fixing the optical probe and the reference cube on the vibrating table.

4. Adjusting the vibrationalquency and acceleration of the vibro-bed to make sure that particles in the reference cube are distributed homogeneously. A strobe light is useful in judging whether the particle distribution is homogeneous. Since the rig for study of vibro-beds is arranged so that the acceleration relative to gravity (K) can be read directly from the oscilloscope via a transducer, the acceleration (K) value is followed instead of amplitude. Notice that these two variables are interdependent:

5. Recording the average output voltage from light probe and the specified d_v value.

In the vibro-fluidizing system, the K value can be calculated by --

$$K = \frac{(x_0 \times \omega^2)}{g}$$

where

x_0 = the maximum displacement, *m*.

ω = the angular velocity of the vibration, *s*.

g = the gravitational force.

Figure 95 on page 260 shows calibrating curves for the three kinds of Master Beads with average particle diameters of 335, 630, and 1260 μm respectively. An interesting fact worth mentioning here is that the calibrating curves for Master Beads can be simplified to the following mathematical form for most of the range of output voltages--

Calibration curves for Master Beads using the vibro-bed system

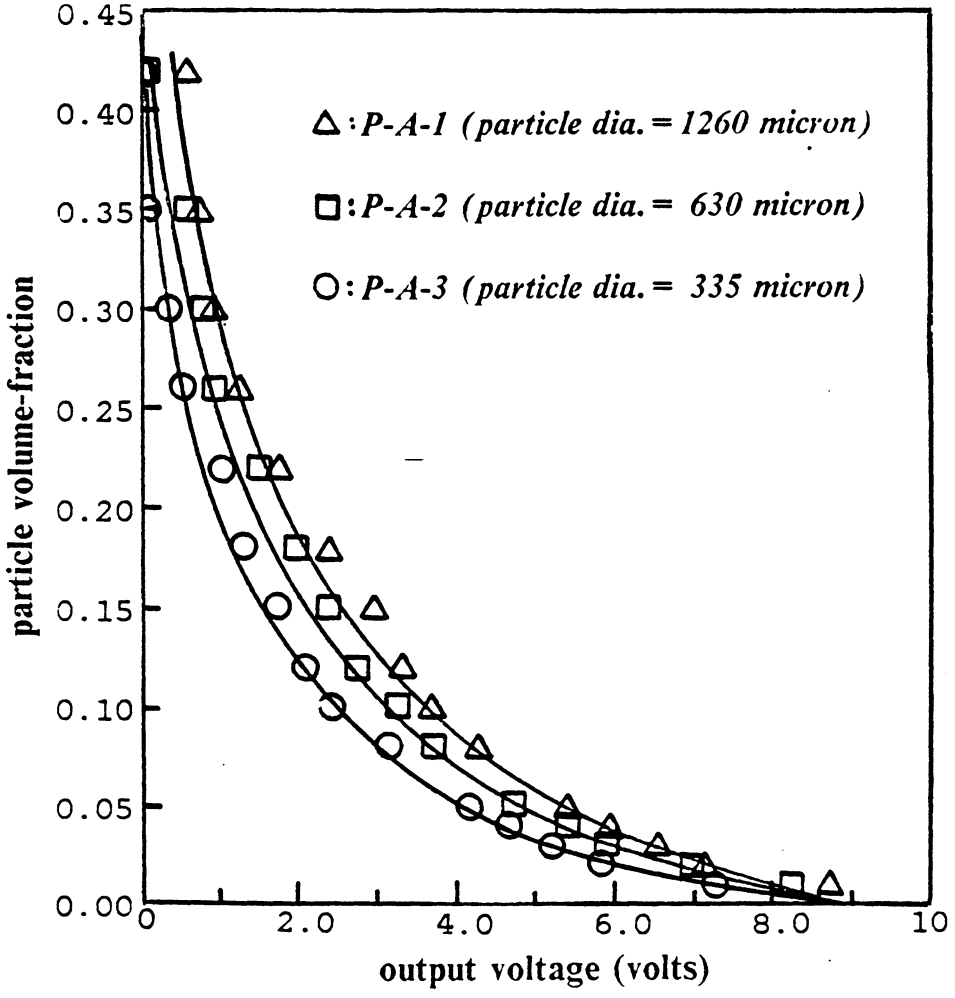

Figure 95. Calibration curves for Master Beads using the vibro-bed system

$$d_v = A \times e^{B\,V} \qquad [6.6]$$

where A and B are two constants determined by characteristics of particles. Figure 96 on page 262 shows that the experimental data are in good agreement with the predictions by Equation 6.6.

Comparison of the two calibration techniques

Comparisons of our two techniques for calibrating the light probe are given in Table 32 on page 263. Although the vibrofluidization technique is easier to apply and affords a more direct calibration, both techniques are recommended to provide assurance that all of the experimental procedures are correct and under control. Figure 97 on page 264 shows calibrating curves from both techniques for 335-$\mu\overline{m}$ Master Beads. The disagreement between the two techniques is always less than 4 %, and so one may adopt either technique with little error if the other is not available.

It is also worth noticing that the calibration of light probe using the particle-density distribution curves highly depends on the validity of the assumption used in calculations from the optical theory. For non-black particles, those assumptions may no longer be valid even if the modified correlation equation like Equation 6.4 can be applied. Figure 98 on page 265 shows the calibration curve for 630-μm sand particles (non-spherical, non-black) in comparison with Master Beads having the same particle size by utilizing the vibor-bed technique.

Application of light probe and discussion of data

Figure 99 on page 266 to Figure 101 on page 268 show measured particle volume-fraction curves versus elevation of the light probe for different experimental situations. The exper-

Comparison of proposed calibrational equation with data from the vibro-bed system

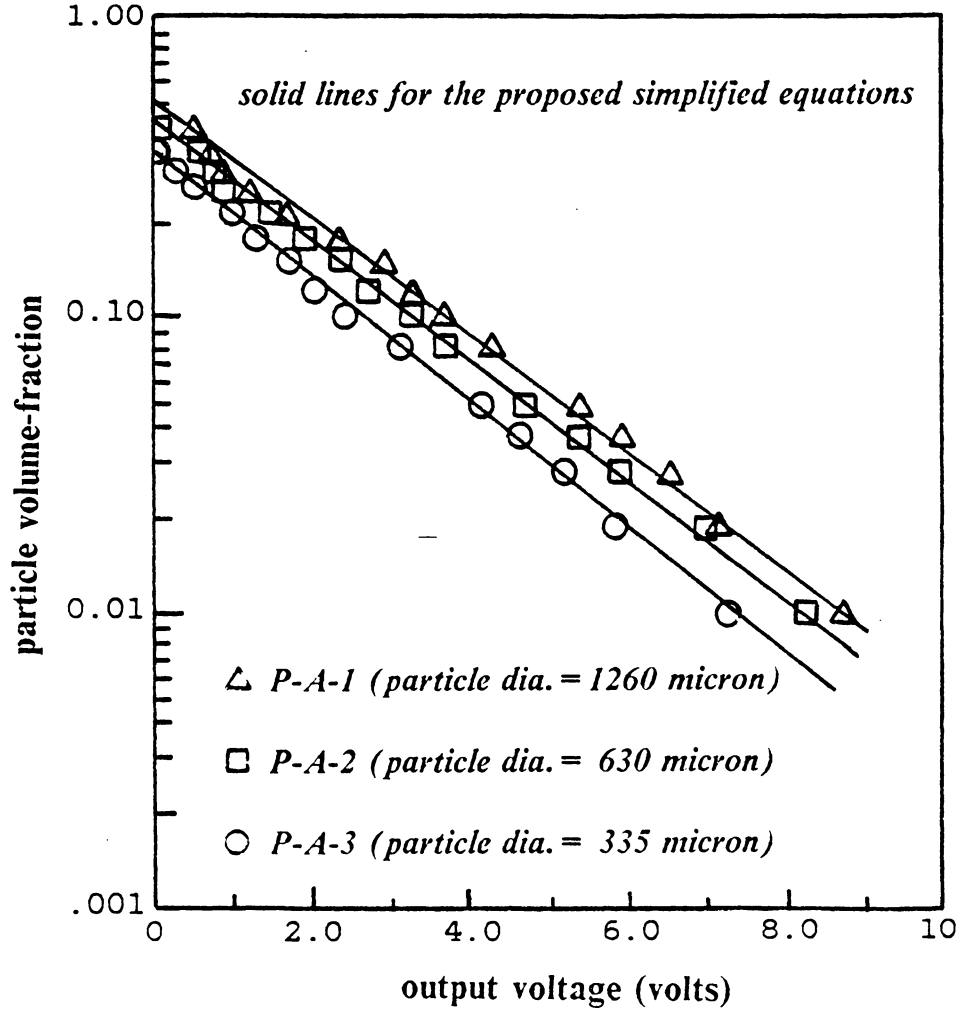

Figure 96. Comparison of proposed calibrational equation with the data from vibro-bed system

Table 32. Comparison of two techniques for calibrating the light probe

Comparison of the two calibration techniques for the light probe

comparison	techniques	
	particle distr.	vibro-bed
direct calibration	no	yes
extra set-up	no	yes
mathematics and computer work	yes	no
required properties of particles	black, spherical are preferred	any particle
calibration for large low-density particle	has to use high gas velocity	difficult(*)
error	can be controlled to about 5%	smaller

* This implies that only few particles have to be weighted and placed in the confined space. From a statistical point of view, less than 30 particles will give a bias on the average properties of particles.

Comparison of the two calibration techniques for the light probe

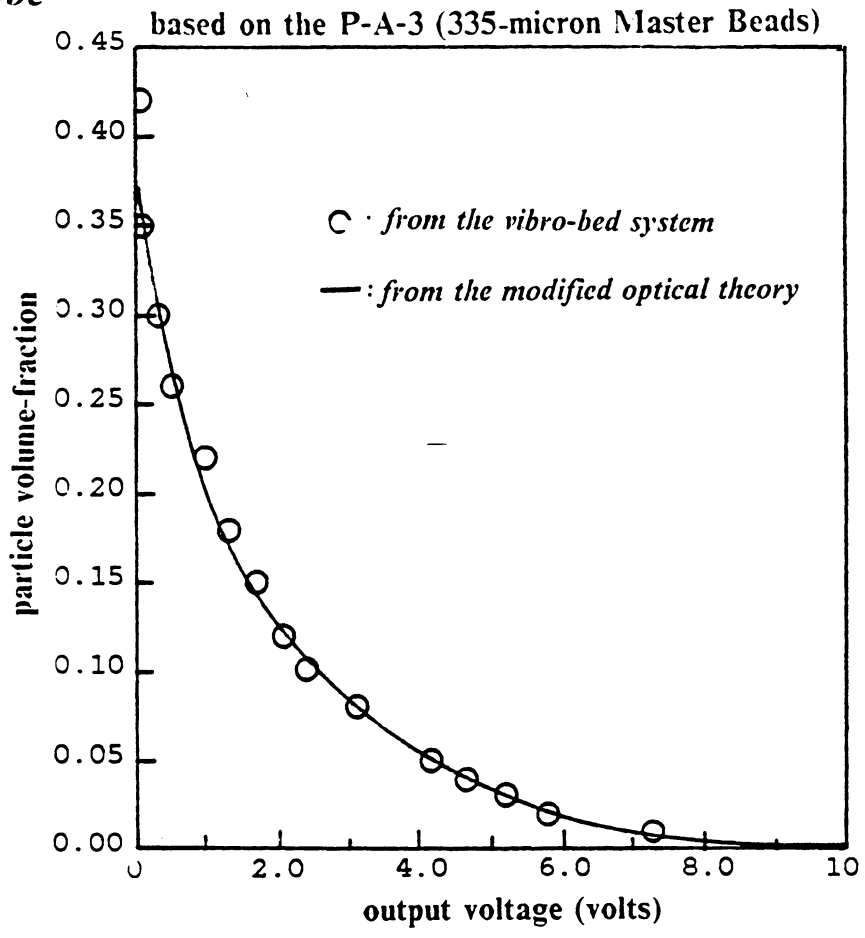

Figure 97. Comparison of two techniques for calibrating the light probe

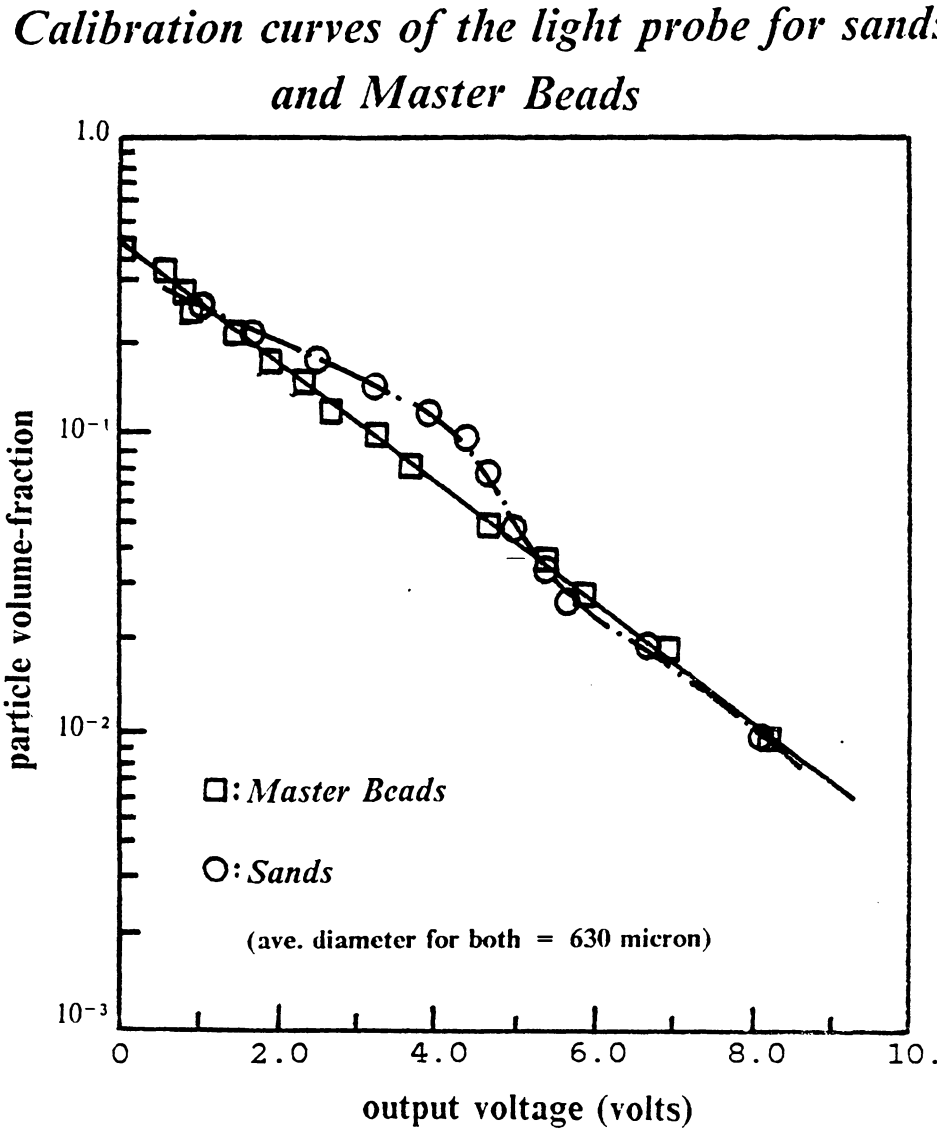

Figure 98. Comparison of calibration curves for Master Beads and sands: (for the same particle size --630 micron, using the vibro-bed system)

Particle volume-fraction distribution curves for beds having different static bed heights

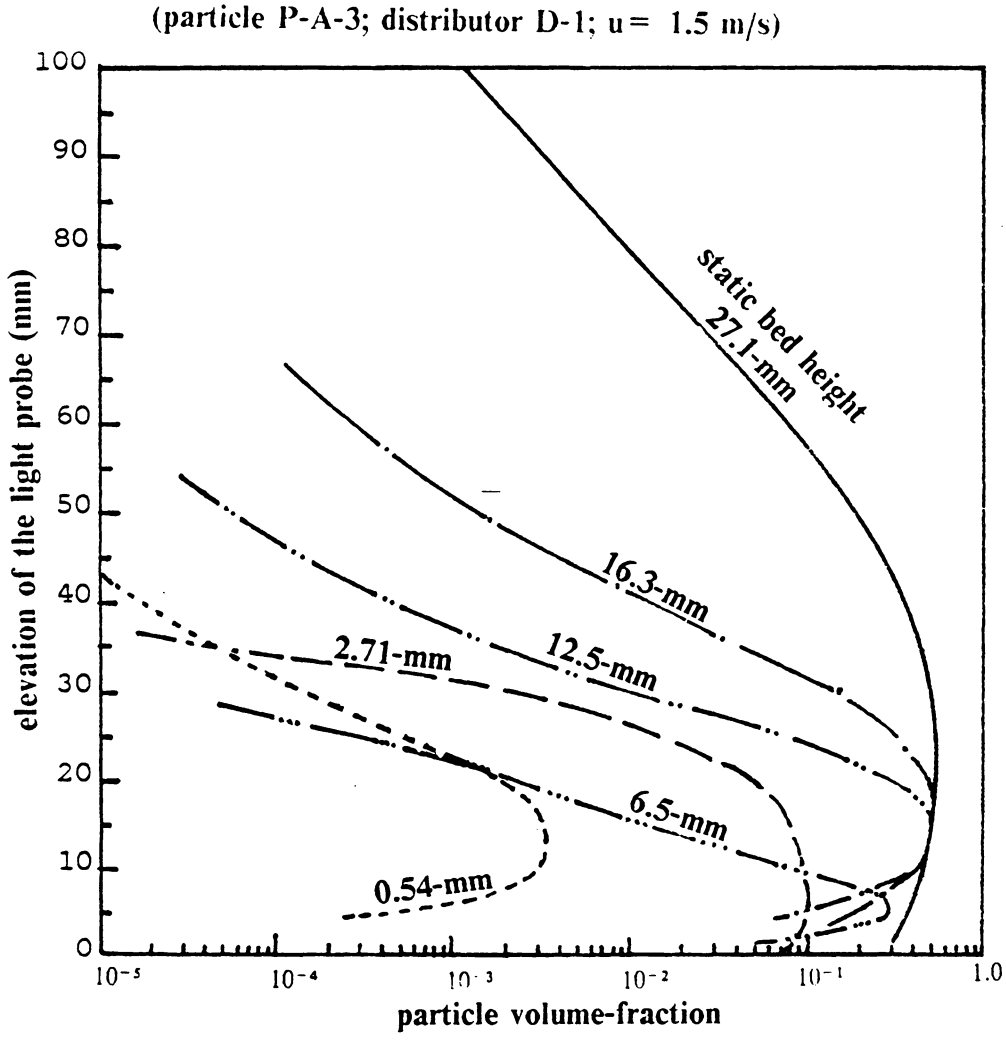

Figure 99. Typical particle volume-fraction versus probe elevation with different amounts of particle: (particle P-A-3; distributor D-1; gas velocity = 1.5 m/s)

Typical particle volume-fraction distributions for beds with different distributors

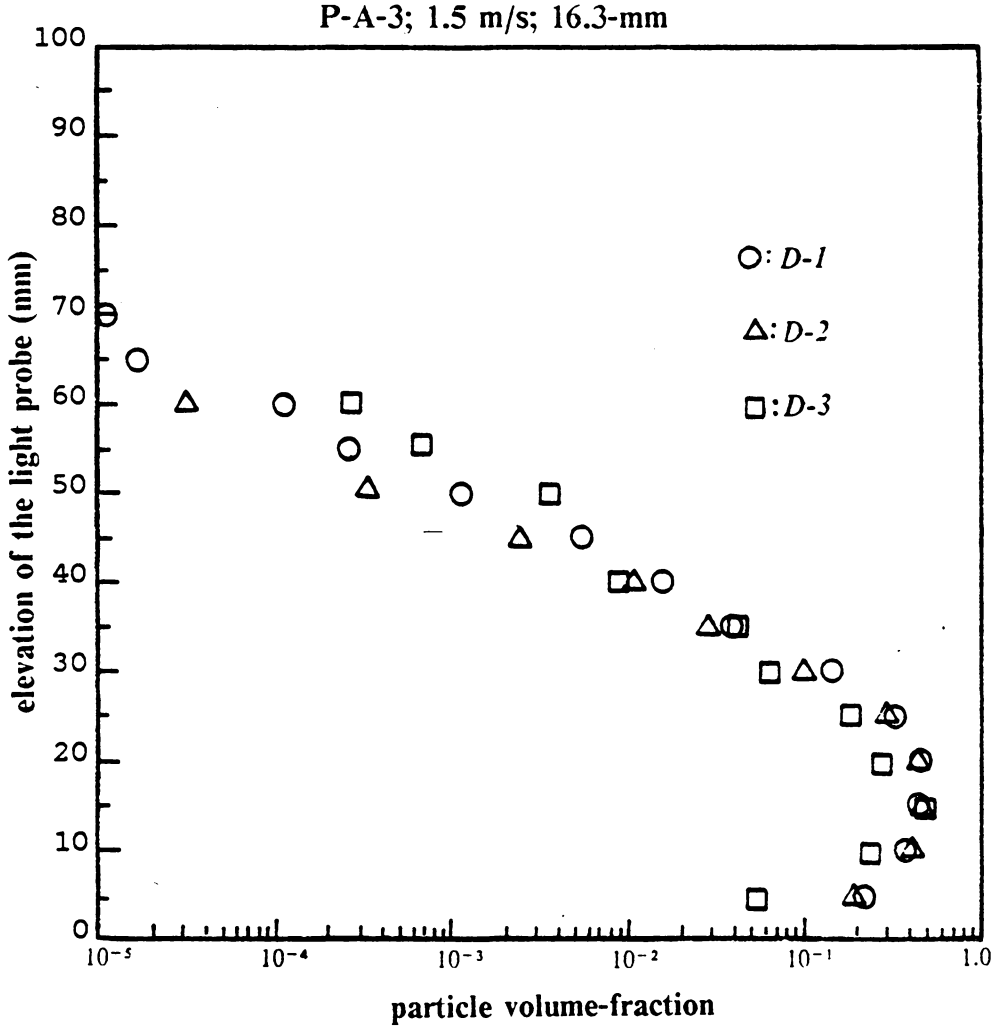

Figure 100. Typical particle volume-fraction versus probe elevation with different distributors: (particle P-A-3; H_s = 16.3-mm.; gas velocity = 1.5 m/s)

Typical particle volume-fraction distribution curves for different Master Beads

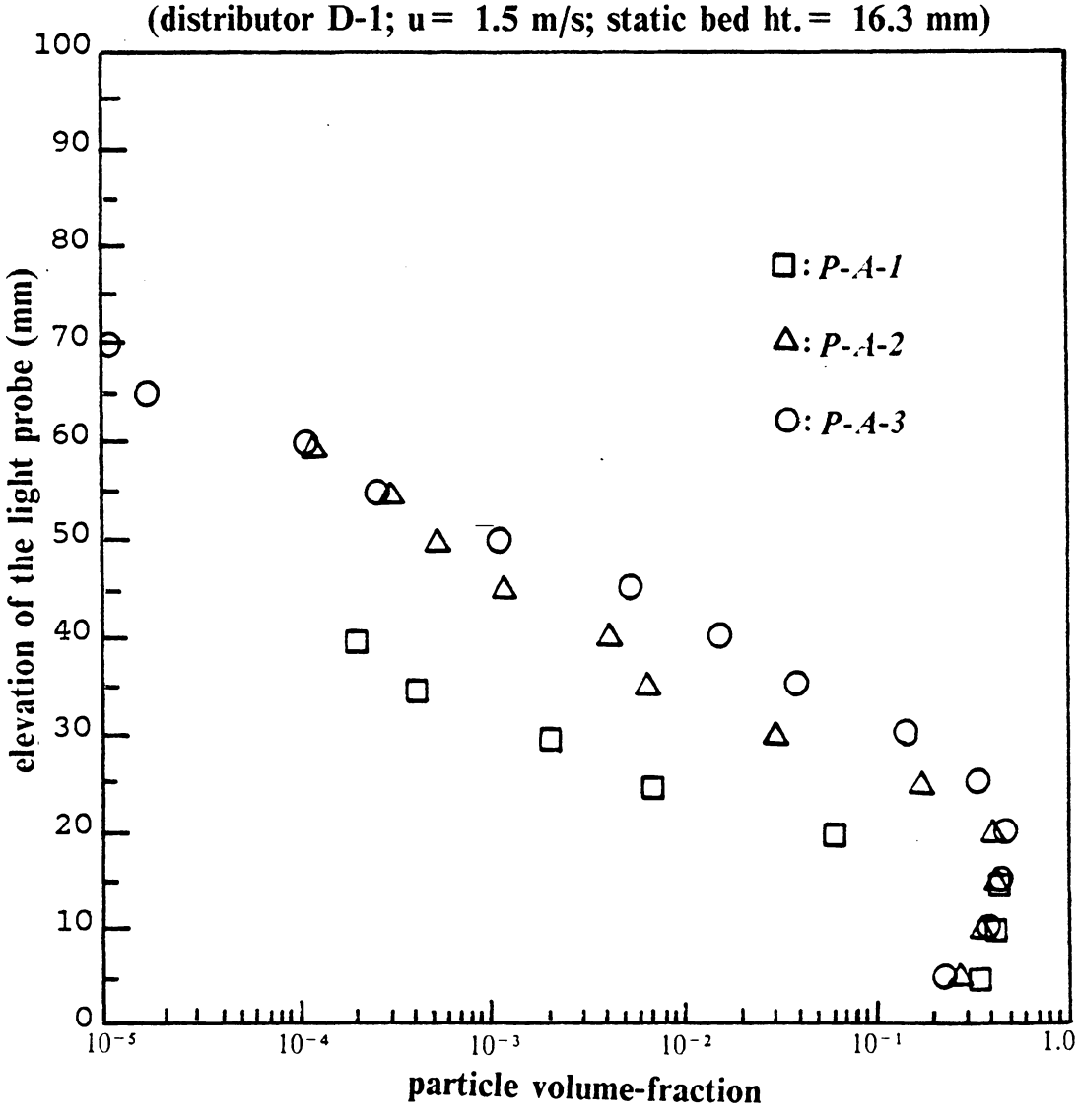

Figure 101. **Typical particle volume-fraction versus probe elevation for Master Beads of different sizes:** (distributor D-1; H_s = 16.3-mm.; gas velocity = 1.5 m/s)

iments are carried out in a fluidized rig of 101.6-mm diameter and operated at relative "shallow" conditions.

Figure 99 on page 266 gives the particle volume-fraction distribution curves for different static bed heights. It can be seen that fluidized particles are flying high when there only a very small amount of particles are present. The bed surface is "compressed" as the particle inventory increases, until the densest part of the bed achieves a "stabilized value" (with a particle fraction of about 0.47 on Figure 99 on page 266) Thereafter, extra particles added to the bed increase the bed height.

The effects of gas distributor and particle size on the particle volume-fraction distribution curves can be observed from Figure 100 on page 267 and Figure 101 on page 268. It is not a surprise to find that the distributor with small open area affords vigorous agitation near the bottom of the fluidized bed, while large particles tend to "compress" the bed surface.

It is worth mentioning that each value for particle volume-fraction presented in these figures is actually an average of one thousand consecutively acquired bits of data. The standard deviation of these one thousand values can be utilized to indicate the degree of "fluctuation" of the bed at the measuring point. Therefore, we can define a fluctuation ratio as the standard deviation divided by the average particle volume-fraction. Figure 102 on page 270 gives the fluctuation ratio together with particle volume-fraction versus the probe elevation. It can be seen that the fluctuation ratio decreases from the bottom of the bed to a minimum value as elevation increases. The large value of the fluctuation ratio can be easily explained by the vigorous solid movement near the free-board region.

Example of the particle volume-fraction and its fluctuation ratio curves

(particle P-A-3; distributor D-1; u = 1.5 m/s; static bed ht. = 12.5 mm)

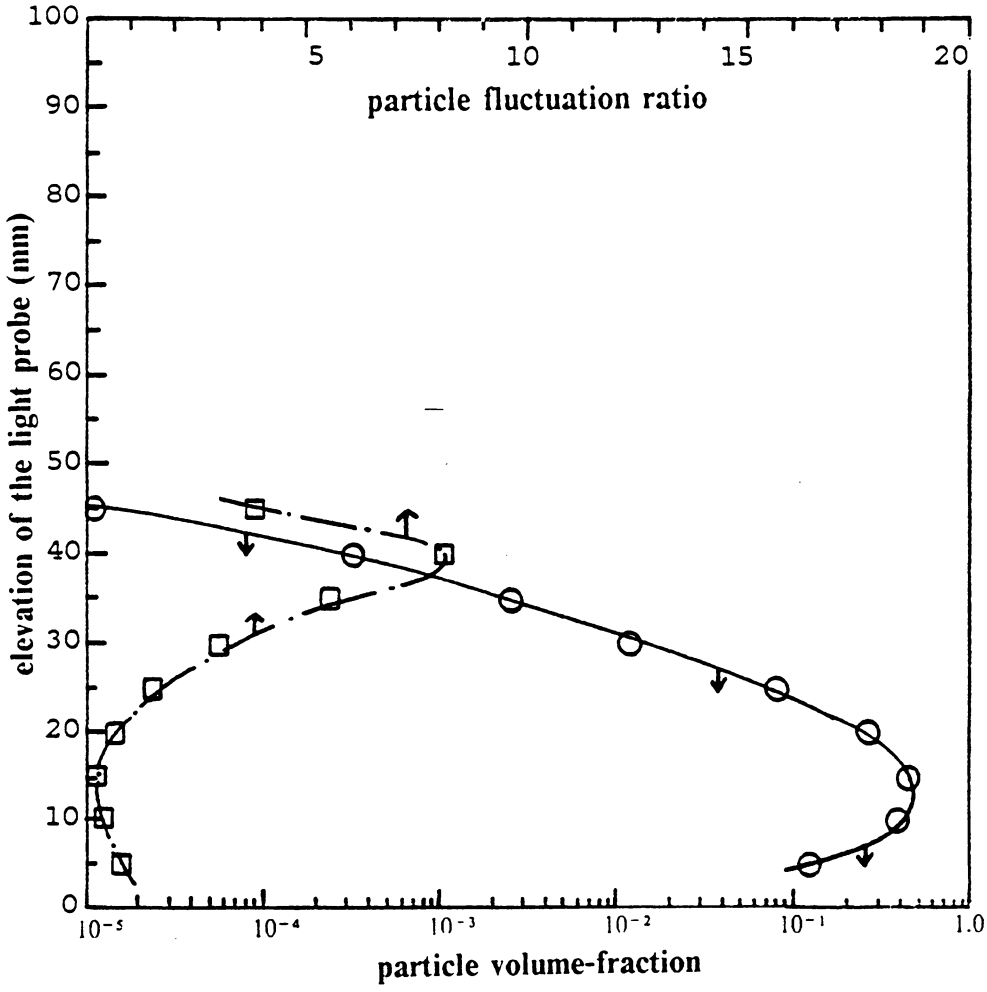

Figure 102. Sample curves of fluctuation ratio and particle volume-fraction: (distributor D-1; H_s = 16.3-mm.; gas velocity = 1.5 m/s; particle P-A-3)

6.2 Particle volume-fraction data from the light probe

The calibrated light probe has been used to study particle volume-fraction distributions in shallow beds. However, there are some limitations for the measurement, as mentioned in the previous section. Three Master Beads, of different sizes, are fluidized in the 101.6-mm I.D. bed with different gas distributors. The light probe records the data in the fluidized bed with a 5-mm increment on the probe elevation for each set of static bed height and gas velocity. Since the particle fluctuation is always vigorous due to the existence of bubbles and other factors, one thousand data points are collected at 600 Hz for each probe position. The BASIC program used to record the output from light probe will convert the voltage signals into the required particle volume-fractions. The average and standard deviation of those one thousand values are also calculated and stored "instantaneously".

Examining all of the particle volume-fractions, we have found that the standard deviation of the particle volume-fraction data (at fixed probe elevation) can be treated as an indicator of the solid mixing/fluctuation inside a shallow fluidized bed. However, a new terminology --particle fluctuation ratio, R_p, --is defined for the convenience of the work that follows.

$$\text{particle fluctuation ratio} = \frac{\text{standard deviation of particle volume-fraction data}}{\text{average of particle volume-fraction data}}$$

Notice that both each value of standard deviation as well as each value of a particle volume-fraction has been calculated from one thousand observations.

Figure 102 on page 270 shows a typical plot for the particle volume-fraction and particle fluctuation-ratio distributions versus the elevation of light probe. Note that the axis for the particle volume-fraction distribution is arranged in a log-scale. This is due to the extraordinarily large variation in particle volume-fraction in most of the shallow fluidized beds.

More than three hundreds plots similar to Figure 102 on page 270 have been drawn to permit examination of features of the particle volume-fraction distribution curves. We have

found that these plots provide valuable information on the hydrodynamic properties of shallow fluidized beds. This will be discussed in the following sections.

Figure 99 on page 266 gives particle volume-fraction data versus the light probe elevation for several static bed heights. The curves can be regarded as typical models of shallow beds with varying amounts of particles. Some features can be described as follows:

1. Bed height (roughly defined as the highest point the particles can reach in significant numbers) first drops as the amount of particle increases and then increases after passing through a minimum.

2. Particle volume-fraction distribution curves decrease sharply near the top of the fluidized beds. Converting the log-scale of x-axis into normal values, one can see that most curves decay exponentially.

3. At the bottom section of the curves on Figure 99 on page 266, the particle volume-fraction curves decrease as the light probe approaches the bottom (gas distributor). This can be easily explained by the existence of gas jets right above the distributor. In fact, this section of diminishing particle volume-fraction had been taken as the jet penetration depth in the literature (e.g. Wen et al. 1982).

4. Examining the middle portions of all curves on Figure 99 on page 266, one can see that the maximum values of the particle volume-fraction data have an upper limit of about 0.45. As the static bed height increases, the maximum value of the particle volume-fraction curves increase before reaching the ceiling. Adding particles into the bed after the static bed height reaches 12.5-mm will only increase the bed surface instead of affecting the particle volume-fraction in the middle section of the fluidized bed.

6.3 Particle volume-fraction curves for shallow beds of different types

Figure 103 on page 274 to Figure 109 on page 280 show particle volume-fraction distribution and particle fluctuation-ratio curves for shallow fluidized beds of types A, B, C, D, F, G, and H, respectively. Note that the figures for types E and I beds are not presented, because dead regions exist in these two types of beds. It can be seen that the particle fluctuation-ratio curves provide some extra information in addition of the shapes of the particle volume-fraction distribution curves in categorizing the types of beds.

Figure 110 on page 281 summarizes in simplified form the particle volume-fraction profiles for various types of shallow fluidized beds. From a comparison of the figures, one can conclude that:

1. Type A bed -- The particle volume-fraction falls away more gradually at the top than for the other types. The width of the peak near the top of the particle fluctuation ratio curve is relatively large in comparison with curves for other types.

2. Type B bed -- The particle volume-fraction falls away faster than for type A, and so the zone of declining volume-fraction is narrower. Thus, the free-board region (cloud and spray zones) is smaller for a type B bed (see Chapter 3). Comparing the particle fluctuation-ratio data, we can also observe that the peak near the top of the curve becomes narrower as the bed moves from type A to type B.

3. Type C bed -- As mentioned earlier, the free-board section of a type C bed extends to only a few centimenters. The particle volume-fraction distribution curve near the top of the bed also reflects the narrow range in which particle volume-fraction declines sharply.

Particle volume-fraction and its fluctuation ratio curves for type A bed

(particle P-A-2; distributor D-2; u = 2.0 m/s; static bed ht. = 27.1 mm)

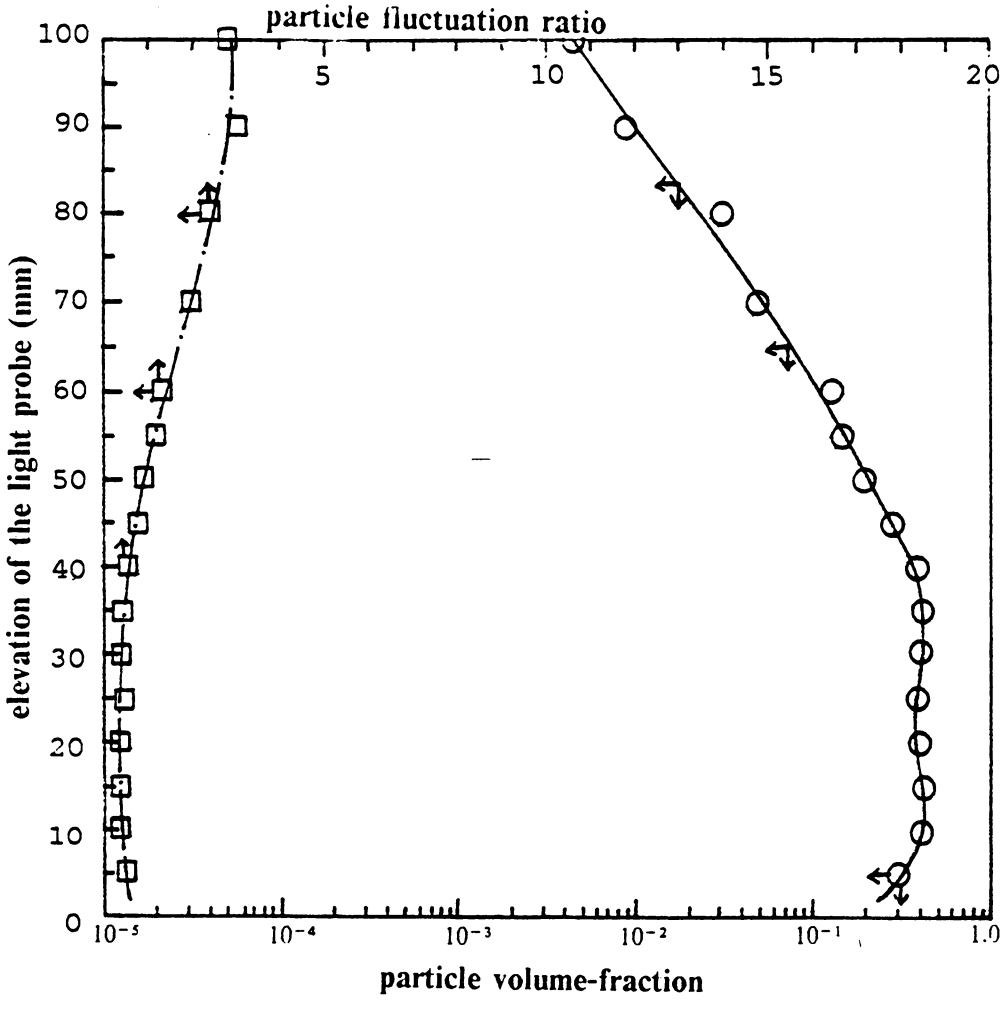

Figure 103. Particle volume-fraction and fluctuation curves for a type A bed

Particle volume-fraction and its fluctuation ratio curves for type B bed

(particle P-A-2; distributor D-2; u = 1.0 m/s; static bed ht. = 27.1 mm)

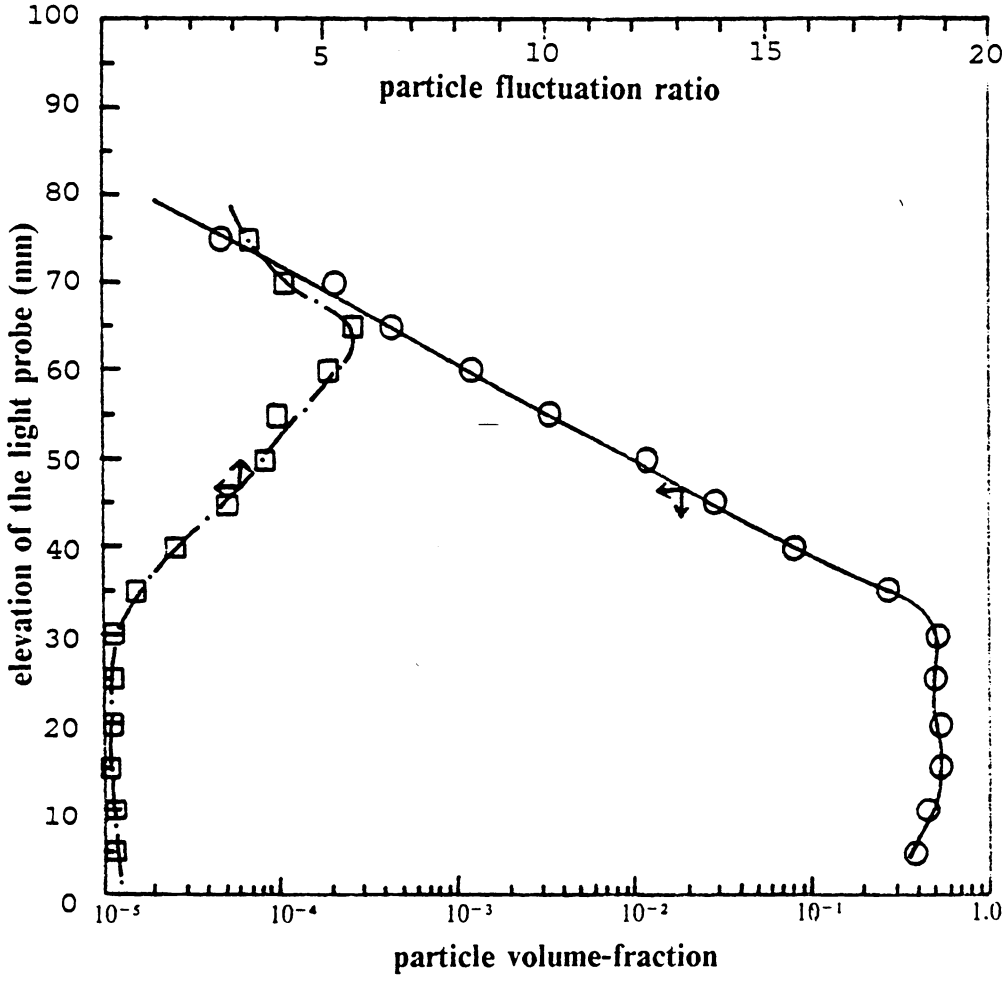

Figure 104. Particle vloume-fraction and fluctuation curves for a type B bed

Particle volume-fraction and its fluctuation ratio curves for type C bed

(particle P-A-2; distributor D-2; u = 1.5 m/s; static bed ht. = 9.2 mm)

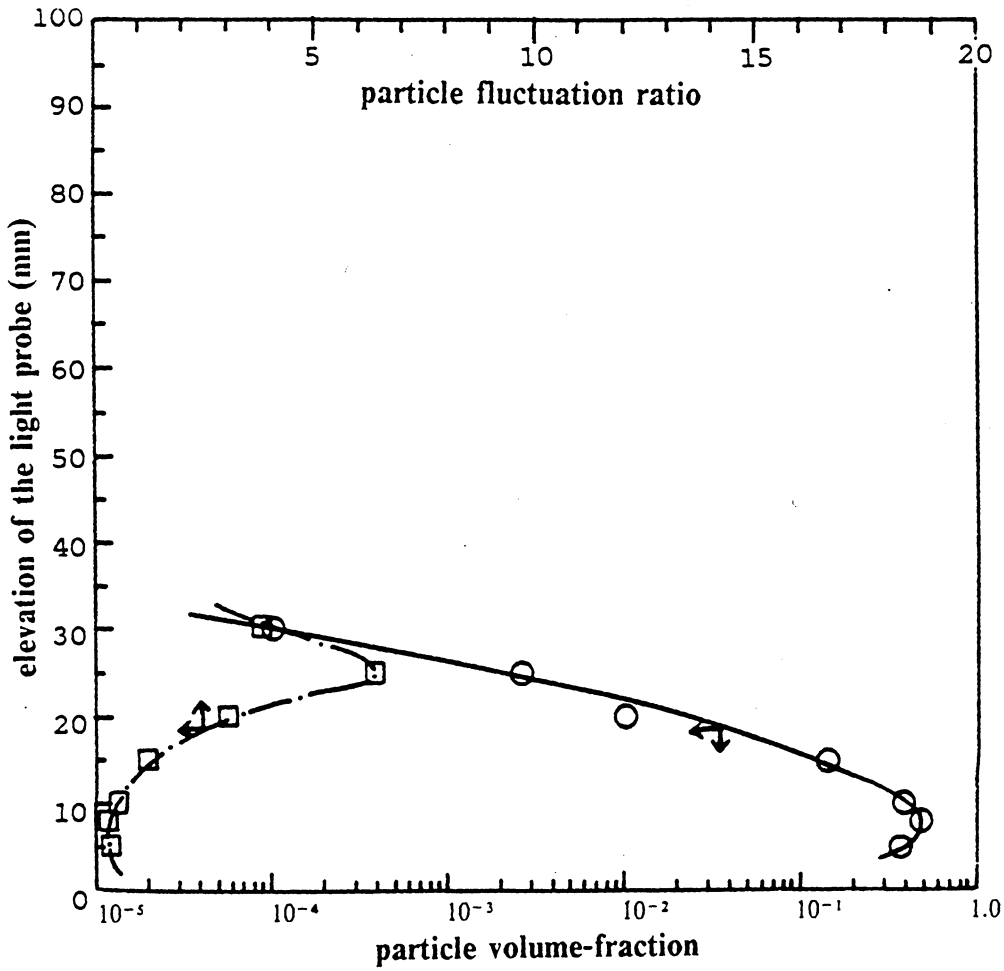

Figure 105. Particle vloume-fraction and fluctuation curves for a type C bed

Particle volume-fraction and its fluctuation ratio curves for type D bed

(particle P-A-3; distributor D-3; u = 1.5 m/s; static bed ht. = 6.5 mm)

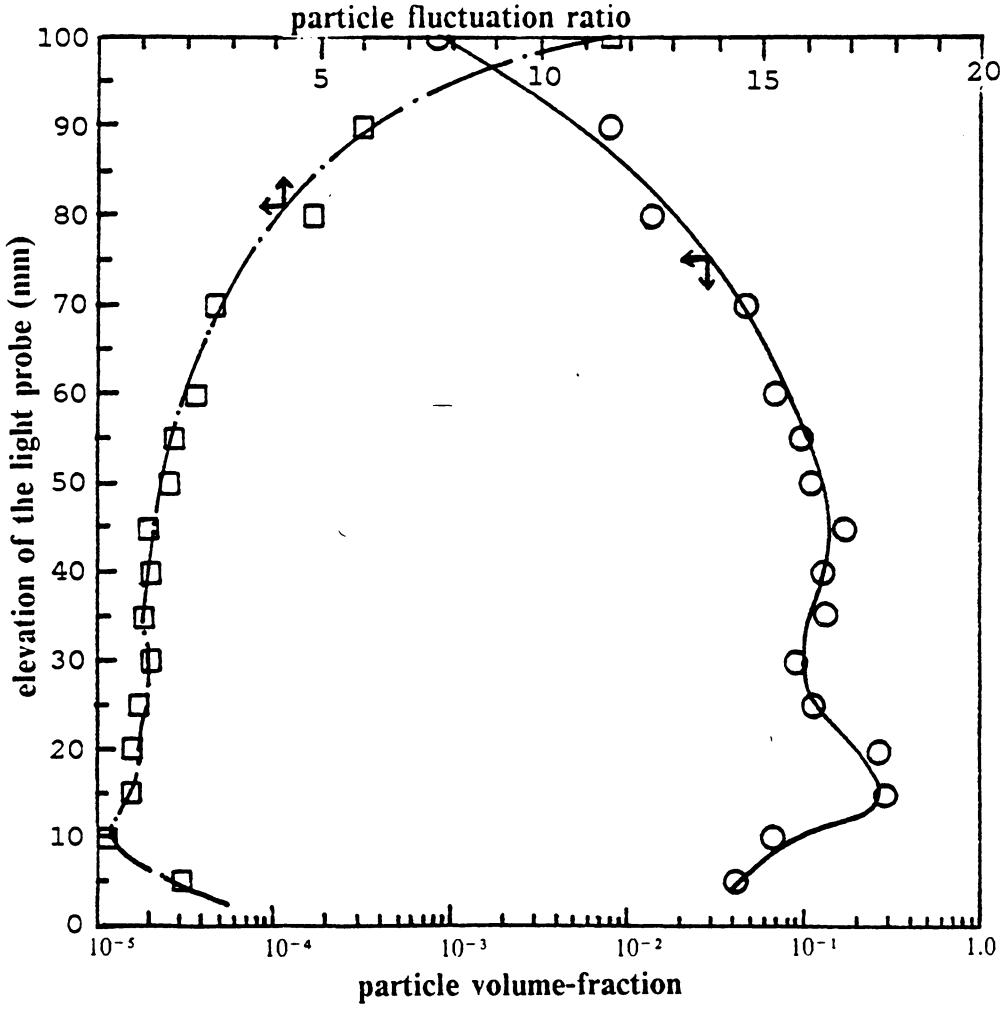

Figure 106. Particle vloume-fraction and fluctuation curves for a type D bed

Particle volume-fraction and its fluctuation ratio curves for type F bed

(particle P-A-2; distributor D-2; u = 1.5 m/s; static bed ht. = 6.5 mm)

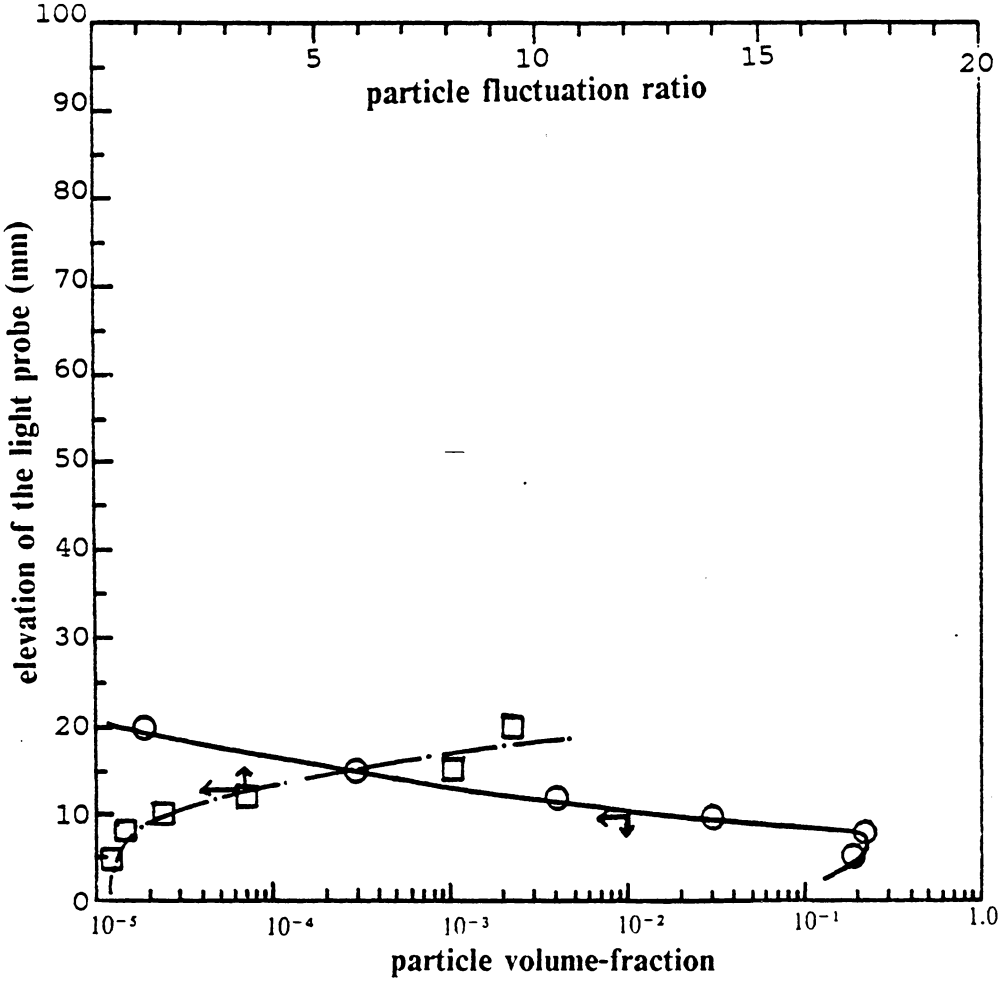

Figure 107. Particle vloume-fraction and fluctuation curves for a type F bed

Particle volume-fraction and its fluctuation ratio curves for type G bed

(particle P-A-2; distributor D-2; u = 2.0 m/s; static bed ht. = 1.6 mm)

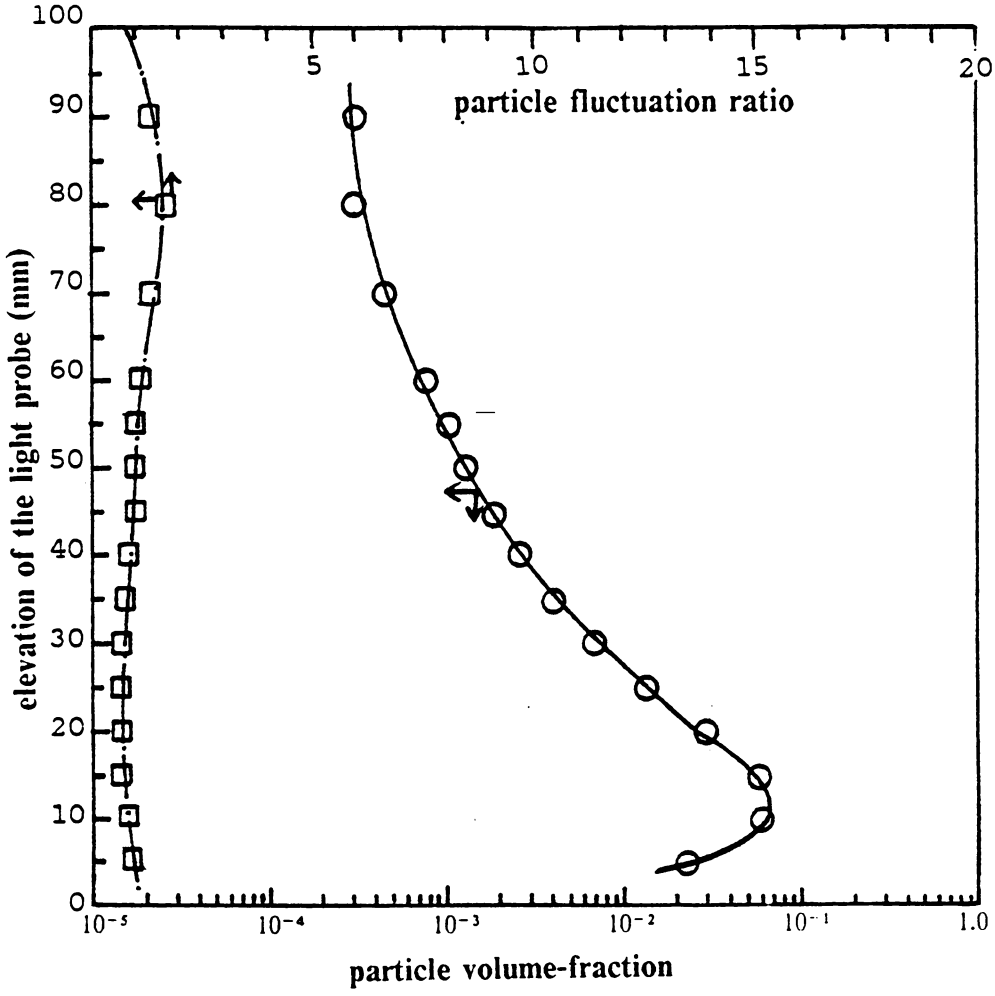

Figure 108. Particle vloume-fraction and fluctuation curves for a type G bed

Particle volume-fraction and its fluctuation ratio curves for type H bed

(particle P-A-2; distributor D-2; u = 1.5 m/s; static bed ht. = 1.6 mm)

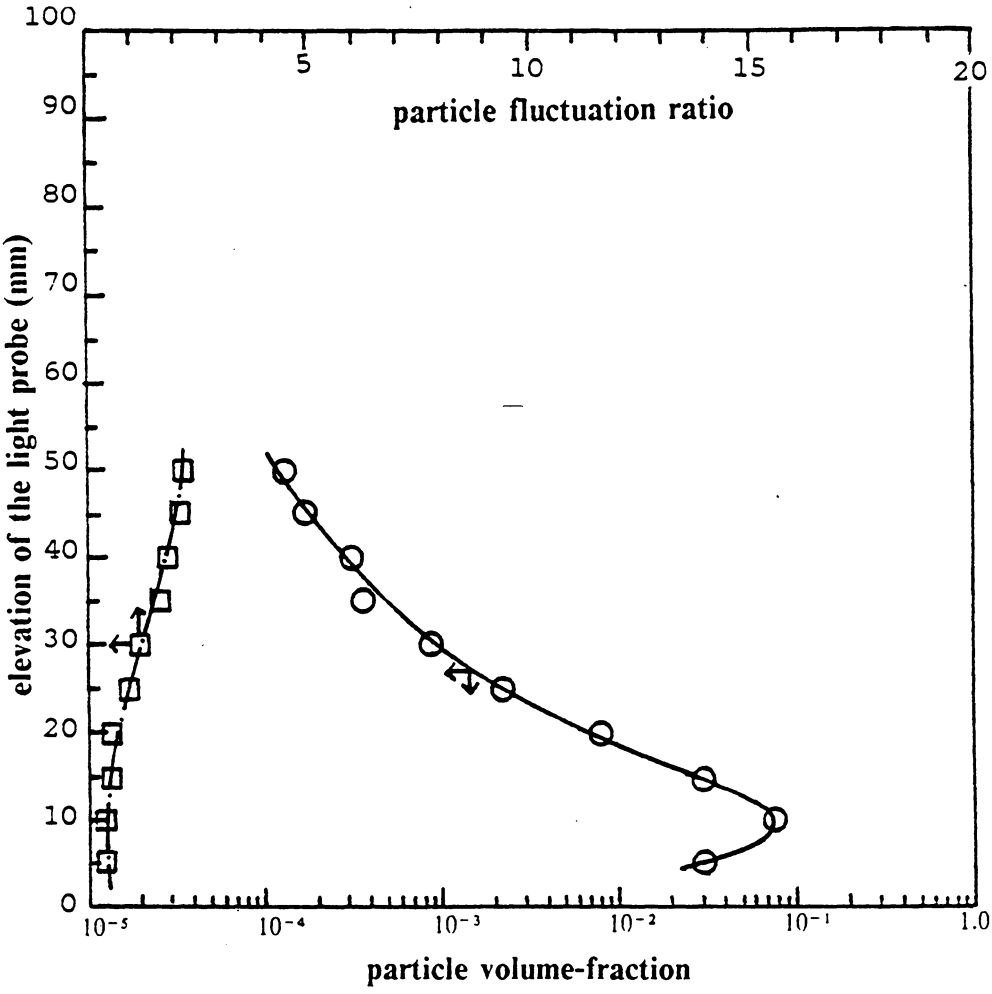

Figure 109. Particle vloume-fraction and fluctuation curves for a type H bed

Particle volume-fraction and particle fluctuation-ratio curves fore different types of shallow beds

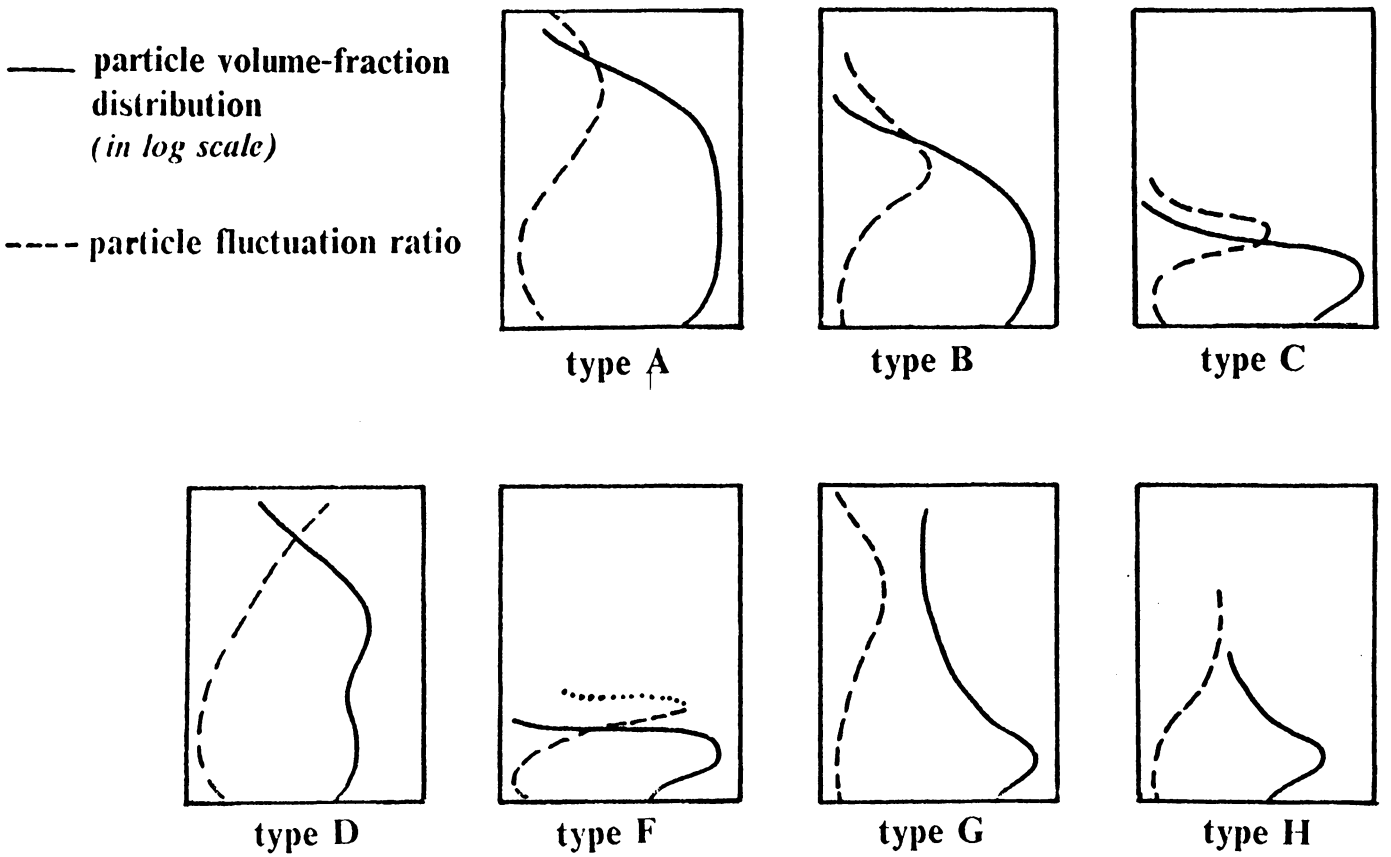

Figure 110. Particle vloume-fraction and fluctuation curves for different types of bed

As we might expect from the comparison of the "peak" near the top of particle fluctuation-ratio curves for the previous two types of beds, the width of this peak shrinks even further in a type C bed.

4. Type D bed -- The particle volume-fraction distribution curve for a type D bed shows the broadness of the section with relative homogeneity and the slackness of the decay of the particle volume-fraction as the light probe moves toward top of the bed. Non-existence of the "peak" for the upper portion of the particle fluctuation-ratio curve can also be taken as a specific feature.

5. Type F bed -- In most of type F beds of this study, the particle volume-fraction decreases from 0.1 - 0.3 to zero as the light probe moves only over a span of 10 mm. This puts further emphasis on the conclusion that the sharpness of surface is the prime feature for a type F bed. However, an increase in the particle fluctuation ratio as the probe moves toward the surface indicates that solid mixing is still occurring near the top.

6. Type G bed -- The particle volume-fraction distribution curve for a type G bed is quite similar to that for type D, except that the shape of the curve is much smoother. This can be appreciated by reference to the fact that a type G bed displays a more homogeneous appearance in comparison with the swirling character of a type D bed. This can be further confirmed by noting the relatively small values (between 0.5 and 2.0) seen in data for particle fluctuation ratio.

7. Type H bed -- The type H bed has a particle volume-fraction distribution resembling the curve for type G, but both particle volume-fraction and fluctuation-ratio curves are compressed, extending across a lower elevation.

Although the particle fluctuation ratio can be taken as an indicator of solid mixing in a shallow fluidized bed, it should be noticed that particle fluctuation ratios are always high

(above 1 and sometimes over 10) in the upper section (free-board region) in fluidized beds of almost all types. This can be understood by observing that particles in dilute regions of all of the beds tend to cluster in packets under most circumstances (except for the type G bed). These particle clusters usually have a relatively high density, and hence they escalate the particle volume-fraction reading when they pass the light probe, producing momentarily a high reading even if such passages are relatively rare.

As described in the previous section, the middle portions of beds of type A, B and C (in some cases, of type F also) will have an upper limiting particle volume-fraction of less than 0.5. However, the actual value of this upper ceiling is dependent upon fluidization variables such as particle properties, distributor design, and fluidizing velocity. Comparing particle volume-fraction curves of this chapter with the pressure distribution curves given in Chapter 5, we would draw attention to the fact that the middle sections of our shallow beds are relative "homogeneous" and "stable". This can easily seen from the relatively small values for particle fluctuation-ratio data in the mid-elevations of our beds. The physical appearance of these mid-elevations reflects a slowly-agitated, dense region perturbed by the passing of gas bubbles.

Light probe data show two features for the bottom sections of most of our shallow beds:

1. Particle volume-fraction decreases as the light probe moves toward the gas distributor.

2. Particle fluctuation-ratio increases when the measured point approaches the distributor.

This is due to the existence of intense jets and/or bubbles right above the gas distributor. Those bubbles and jets can promote solid mixing. In the next section, we discuss the estimation of jet penetration using data from the bottom section of shallow fluidized beds.

6.4 Jet penetration heights obtained from particle volume-fraction curves

As mentioned in earlier chapters, many proposed ways have been suggested for measuring jet penetration depths. However, three of the most common mentioned and convenient experimental techniques for measuring the jet penetration depth are --

1. High-speed movie camera in conjunction with a 2-dimensional fluidized bed (Yang and Keairns, 1979; Hirsan, et al, 1980; Blake et al., 1982)

2. Radioscope or optical probe (via measurement of particle volume-fraction distributions) (Wen et. al., 1982)

3. Pressure measurement (as mentioned in the last chapter, pressure distribution curves can provide us with jet penetration data)

Table 33 on page 285 compares these three techniques. Wen et al. (1982) suggested that jet penetration heights could be defined as the distance from the gas distributor to the point at which an optical probe senses the smallest fraction of void time (in other words, the point at which the bed starts becoming dense). After acquiring particle volume-fraction distribtion curves by means of our light-probe system, we can do a similar analysis. As shown on the Figure 110 on page 281, the jet penetration height might be defined as the bed height at which the particle volume-fraction hits a maximum and/or the particle fluctuation ratio hits a minimum.

Table 34 on page 288 lists jet penetration heights obtained from particle volume-fraction curves. Jet penetration heights obtained from pressure distribution curves are also listed for

Table 33. Comparison of the techniques of measuring jet penetration depths

Techniques for measuring the jet penetration

Exptal. techniques	camera and 2-D bed	radioscope or optical probe	pressure distr.
cost	high	high for radio. low for probe	low
complexity	complex	easy measurement	simple
error	due to the wall effect	due to the disturbance of the probe	due to the non-ideal of curves

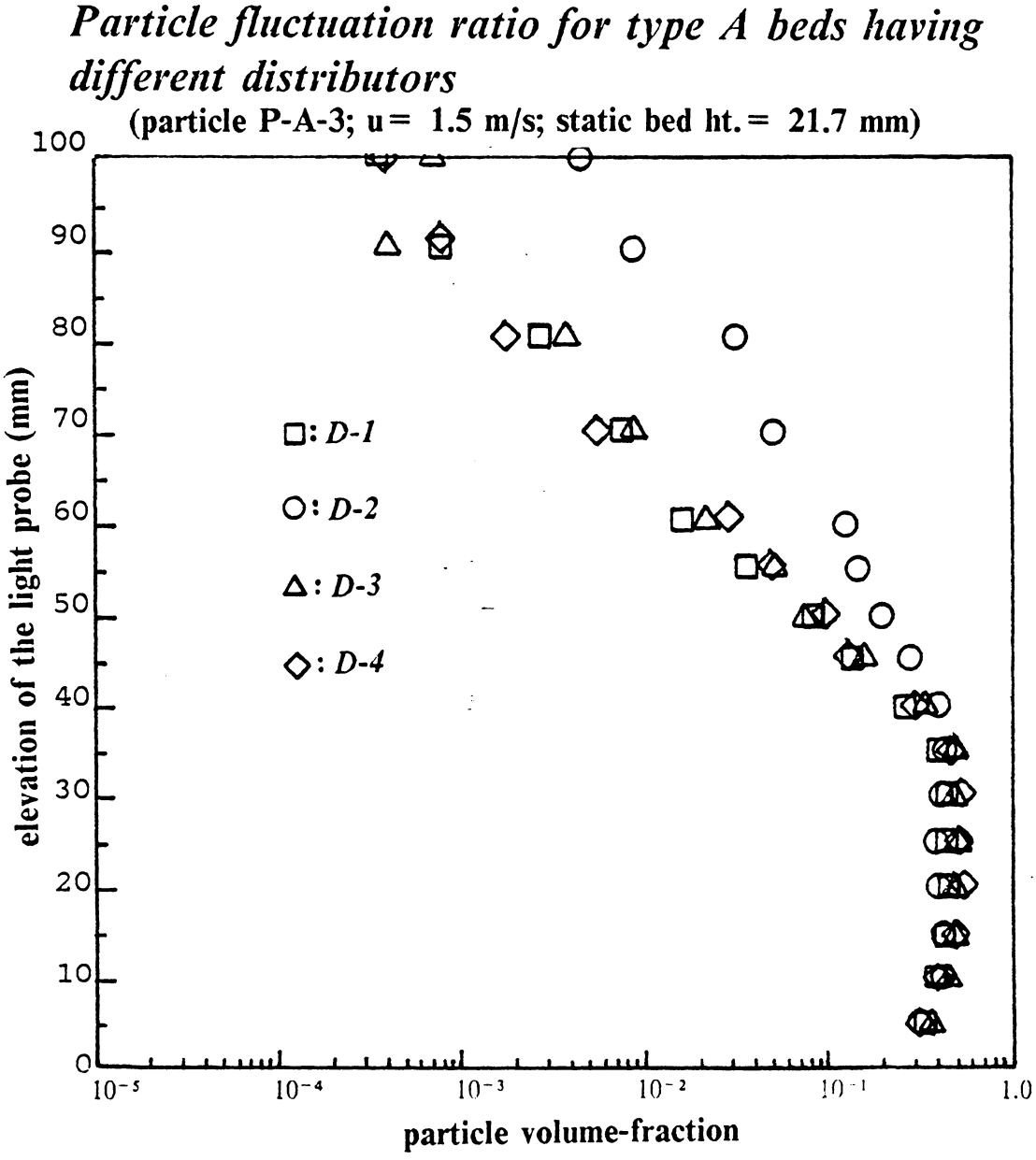

Figure 111. Particle volume-fraction curves for beds having different distributors

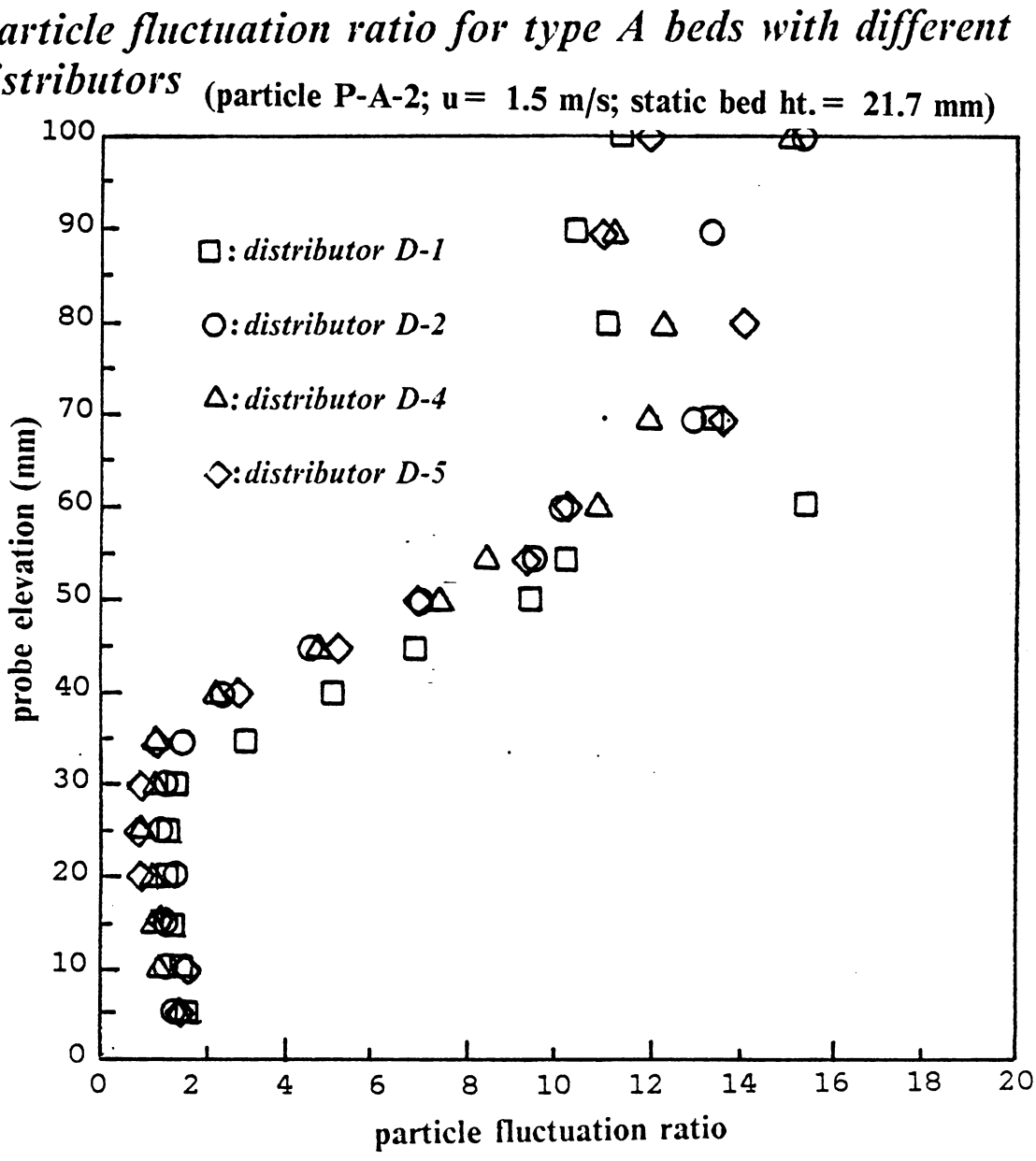

Figure 112. Particle fluctuation curves for beds having different distributors

Table 34. Jet penetrations evaluated from volume-fraction and from pressure-distribution data

Jet penetration evaluated from particle volume-fraction and from pressure-distribution data

Distributor	particle	U (m/s)	L_j^1	L_j^2	L_j^2/L_j^1
D-1	P-A-1	0.50	14	--	----
D-1	P-A-1	1.00	20	22	1.10
D-1	P-A-1	1.50	23	26	1.13
D-1	P-A-1	2.00	27	30	1.11
D-1	P-A-2	1.00	17	21	1.24
D-1	P-A-2	1.50	22	26	1.18
D-1	P-A-2	2.00	25	31	1.24
D-1	P-A-3	1.50	15	--	----
D-1	P-A-3	2.00	22	--	----
D-2	P-A-1	0.50	15	23	1.53
D-2	P-A-1	1.00	21	28	1.33
D-2	P-A-1	1.50	25	30	1.20
D-2	P-A-1	2.00	28	34	1.21
D-2	P-A-2	1.00	16	24	1.50
D-2	P-A-2	1.50	23	30	1.30
D-2	P-A-2	2.00	27	35	1.30
D-2	P-A-3	1.50	20	26	1.30
D-2	P-A-3	2.00	24	30	1.25
D-3	P-A-1	0.50	20	27	1.35
D-3	P-A-1	1.00	25	30	1.20
D-3	P-A-1	1.50	30	35	1.17
D-3	P-A-2	1.00	20	28	1.40
D-3	P-A-2	1.50	25	32	1.28
D-3	P-A-1	1.00	14	26	1.86

1. L_j^1 --jet height from particle volume-fraction data.
2. L_j^2 --jet height from pressure-distribution data.
3. L_j^2/L_j^1 has an average of 1.29 with a standard deviation of 0.17.

comparison. It is seen that pressure-distribution curves give values for jet penetration about 30% higher than values obtained from particle volume-fraction measurements.

Since the measurement of particle volume-fraction is more precise than a record of pressure distribution, jet penetrations from light-probe data are more convincing. However, there are still not enough data for sufficient different situations for us to feel motivated to change the correlations in the previous chapter.

6.5 *Effect of gas distributor on particle volume-fraction*

Reviewing all of the particle volume-fraction curves for shallow fluidized beds with different distributors (perforated plates: D-1,2,3; laminated plates: D-4,5), we found that the design of gas distributors could affect the particle volume-fractions in two aspects:

1. Fixing all other fluidizing conditions (particle, gas velocity, static bed height, ...), a change of gas distributor can shift the fluidized bed from one type to another. As mentioned earlier in this chapter, beds of different types demonstrate distinguishable particle volume-fraction and fluctuation ratio curves.

2. In the bottom section of shallow beds, jets and bubbles disperse particles and reduce the particle volume-fraction. Therefore, a jet-producing (perforated) distributor makes particle volume-fraction lean and fluctuation ratio high for a region right above it.

Once the fluidized bed falls into a certain type, the particle volume-fraction distribution curves follow the patterns we have described rather than reflecting an effect from a gas distributor. Figure 111 on page 286 and Figure 112 on page 287 show the particle volume-fraction distribution and particle fluctuation-ratio curves for a type A bed with different gas distributors. The bed had been filled with 27.1 mm (static bed height) of particle P-A-2 (630-mu m Master Beads) and fluidized by a superficial gas velocity of 1.5 m/s. It can be seen that the curves reveal no significant distributor effect.

6.6 Conclusions of the particle volume-fraction study

(1).The light probe in conjunction with an IBM PC interfacing system provides us with a satisfactory measurement of particle volume-fraction distribution in shallow fluidized beds. However, the accuracy and reliability of the calibration techniques of the light probe is limited to Master Beads at this stage. Further improvement for the light probe (both hardware and calibration theory) is needed for study of other particles.

(2).The particle volume-fraction and particle fluctuation-ratio data can provide valuable information on the hydrodynamics of shallow fluidized beds, including:

1. quantitative distinctions for different types of shallow beds

2. relative magnitude of solid mixing

3. bed surface and bed height (also see the previous chapter)

4. jet penetration depth and effects of gas bubbles

(3).Fluctuation of particle motion inside a shallow fluidized bed is always vigorous and patternless, especially for the free-board section. It has been found that the variation among data from different runs using the light probe can be as high as 30-40%, even though the number of data points exceeds one thousand. As mentioned earlier, this is probably due to the fact that particles appear as packets in most lean phases of shallow beds.

(4).After a test, it has been found that the traditional mechanical recorder can give misleading results for acquiring data output from a light probe. This is mainly due to the fast fluctuating character of system and the slow response of most traditional recorder. As mentioned in the

discussion of the IBM PC interfacing system, the recording system requires 1.67 milliseconds (a sampling rate of 600 Hz) in order to track the microscopic variations in particle volume-fraction. Unfortunately, many publications of data from light probes have used a mechanical recorder, probably with response times less than 0.1 seconds. Therefore, one should note both sampling rate and recorder response time when reviewing the literature based upon use of a light probe.

CHAPTER 7 HEAT TRANSFER IN SHALLOW FLUIDIZED BEDS

7.1 System for measuring heat-transfer coefficient

7.1.1 Design of heat probe

Two methods have commonly been used to measure bed-to-surface heat-transfer coefficients in fluidized beds:

1. A coaxial cartridge heater is placed within a copper tube having insulated ends. Thermocouple beads in grooves cut into the surface of the tube are used to read the surface temperature.

2. Heating strips are glued onto an insulating rod, with thermocouples placed underneath to monitor surface temperature.

However, both of these methods have disadvantages (see Huang, 1983). Usually, grooves on the copper tube affects the temperature distribution pattern on the probe surface and change the particle movement pattern around it. Heating strips have low thermal capacities and therefore permit large fluctuations in temperature, especially when the fluidized bed is "sluggish" and does not afford rapid and homogeneous mixing of particles.

A new heat probe has been designed to overcome the drawbacks of the two methods. A theoretical analysis of the conduction process in the probe with varying local heat-transfer coefficients has been performed to ensure validity of data obtained from the new heat probe (Liu and Squires, 1985).

The design of the probe is shown scehmatically in Figure 113 on page 295. Within the probe, there is nichrome heating coil wound on an aluminum annulus. Coil and supporting annulus are coated with fifteen layers of a special paint that is thermally conducting but electrically insulating. The painted coil is inserted into a hollow copper tube with wall thickness of 3.1 mm. An epoxy of high thermal conductivity is applied uniformly upon the paint to ensure that no air gap can appear between the coil and copper tube. The copper tube is drilled from a 80-mm rod of 12.7 mm diameter. Surface temperatures are measured at several points using copper-constantion (T-type) thermocouples. T-type thermocouples are chosen because they display a large variation of output voltage with measured temperatures in the range of interest (below 200°C). As shown in Figure 113 on page 295, the thermocouples pass radially inward from the surface of the copper tube, traverse the nichrome coil and supporting annulus, and emerge from the center of the aluminum annulus. Thermocouple beads are placed in tiny depressions on the surface of the copper tube and are soldered in place with silver-solder. The soldered spot is sanded down to provide a smooth heat-transfer surface.

Several considerations must be taken into account in designing supports for the heat probe:

1. The supports must be mechanically strong.

2. The supports must be thermally insulated from the heat probe and fluid bed.

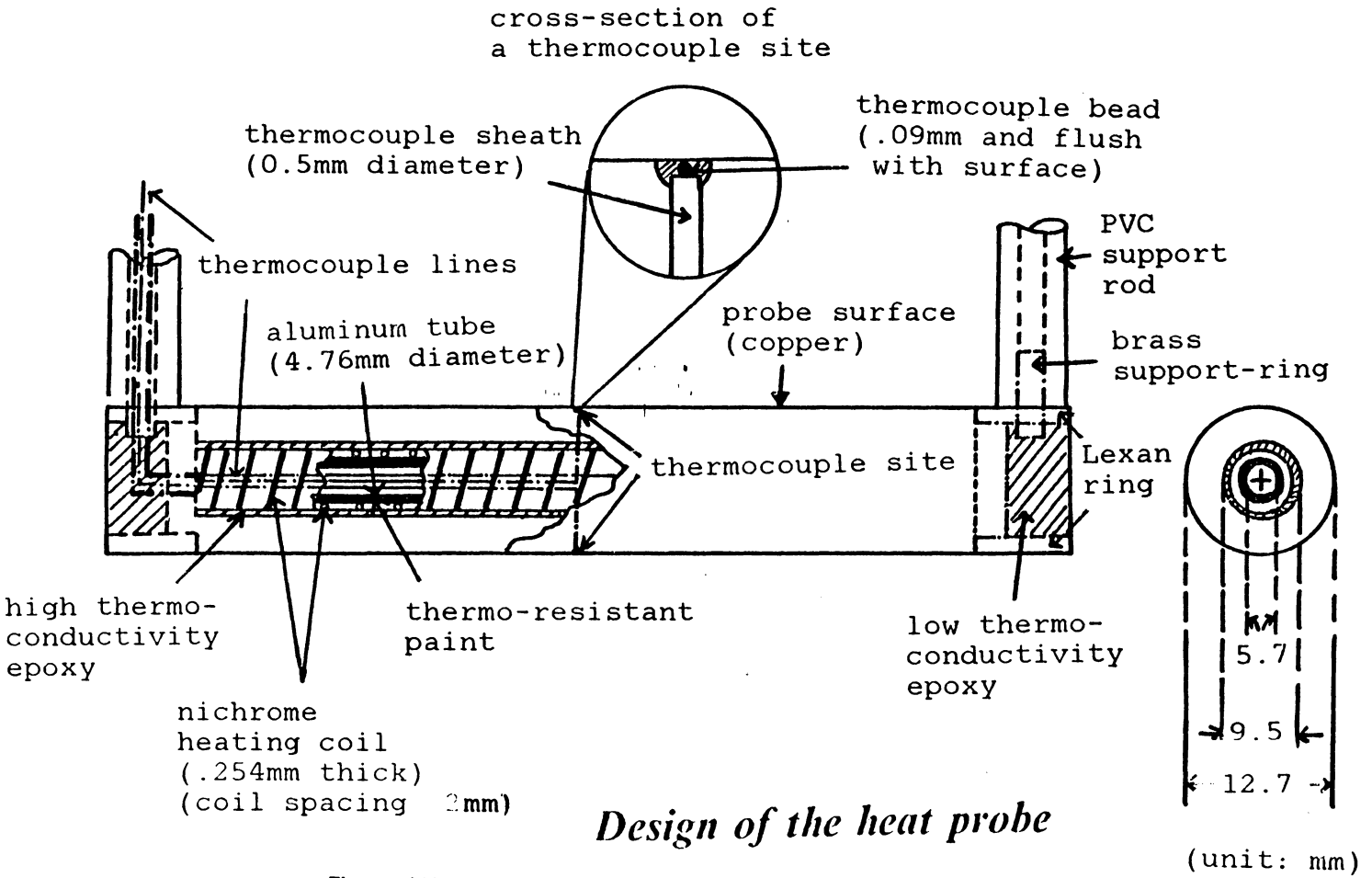

Figure 113. Design of heat probe

3. Effects of the supports on particle movement should be minimized.

The probe is supported by two cylindrical PVC rods of 6.35-mm outside diameter. Two 5-mm Lexan "insulating" rings are used to connect the heat probe and the support rods with help of two tiny brass "supporting rings". All of the electric wires and thermocouples pass through the Lexan ring and one of the support rods. An epoxy of low thermal conductivity is placed into the space inside the Lexan ring for mechanical reinforcement of the supports.

7.1.2 Obtaining heat-transfer data

At the top of the heat-probe supports, a panel is installed to hold connectors at the ends of thermocouple and power lines leading from the probe. The use of these connectors enable us to disconnect and move the heat-probe system freely.

A DC (direct-current) power-supply system with an upper limit of 30-Volts (at 3 Amperes) is constructed to match the requirements of the heat probe. A digitized multimeter and a 0.1-Ω power resistor are connected on the power lines to monitor the power output of the heat probe. (See later in this chapter for the calculation of power consumption.)

A temperature read-out system consists of three elements: control box, DORC 404 thermocouple read-out device, and an IBM PC with DT2801 data-acquisition board. The system is shown in Figure 114 on page 297. The control box serves mainly as the channel selector of the thermocouples. It can connect with up to sixteen thermocouples with help of a 16-channel multiplexer. The channel selection can be made either by four on-board switches or by sending a signal from the IBM PC. Four channels connect with thermocouples on the heat probe, and two additional channels monitor the temperature in the fluidized bed.

A selected signal passes to the DORC 404 thermocouple read-out device to display temperature in '°C' (to an accuracy of ± 2°C). The temperature reading can also be automatically recorded on the IBM PC through the DT2801 data-acquisition board. It is worth mentioning

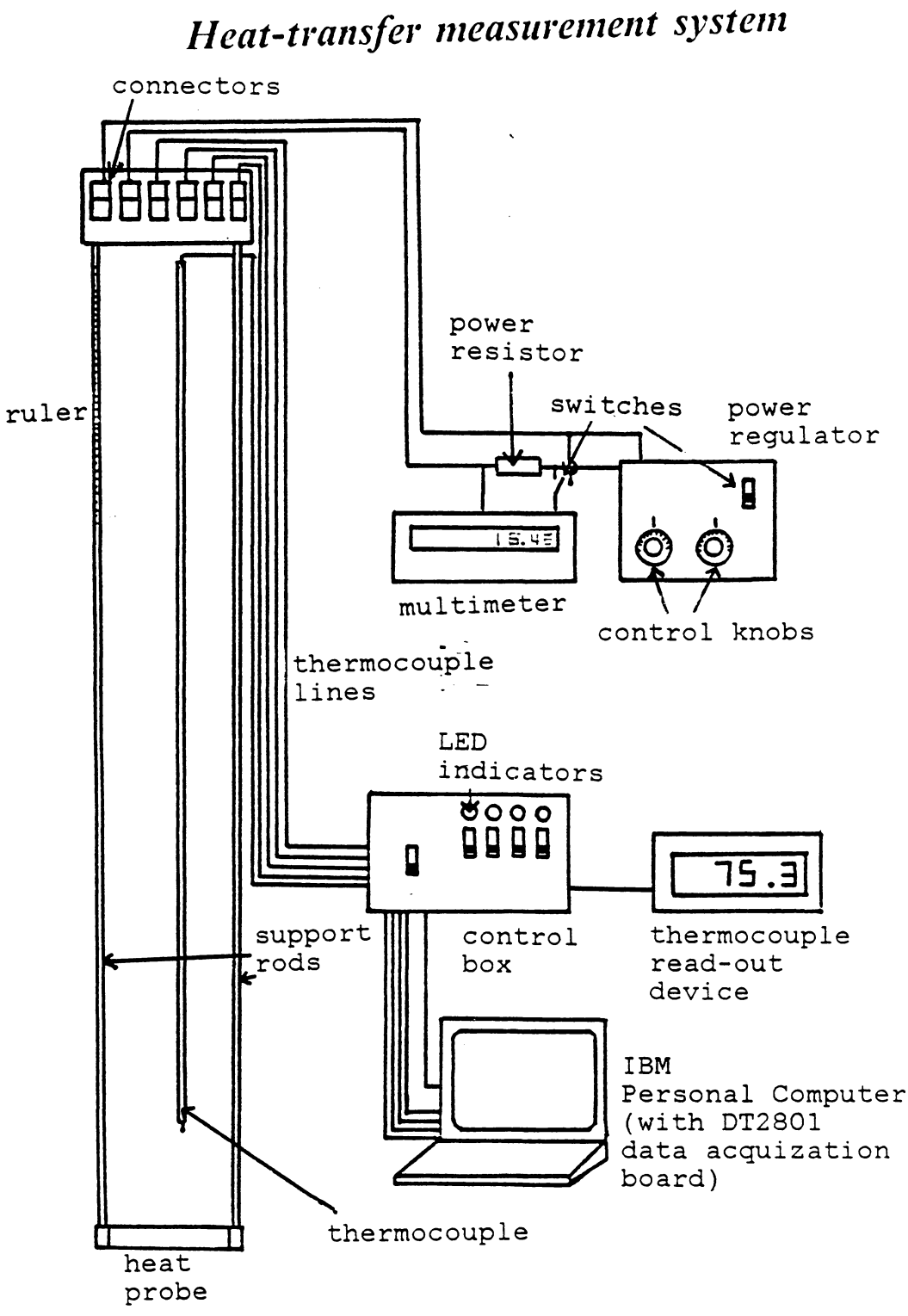

Figure 114. The temperature read-out system for the heat probe

that all of the connections for the temperature read-out system are made using copper-constantion wires to ensure no distortion of output voltage from thermocouples.

7.1.3 Calculation of heat-transfer coefficient

The basic equation to calculate an overall heat-transfer coefficient is --

$$h_c = \frac{Q}{A_p \times \Delta T} \qquad [7.1]$$

where

Q = power supplied to the probe (W)

A_p = surface area of the probe (m^2)

ΔT = average temperature difference between the bed and the probe surface.

The probe is 80.0 mm in length and of 12.7-mm outside diameter (therefore, A_p = 3192 mm^2). Four thermocouples have been mounted on the surface of the heat probe. Figure 115 on page 299 shows the placement of the four thermocouples. By assuming a linear temperature distribution, the average temperature on the probe surface can be calculated as--

$$T_{ave} = \frac{(T_1 + T_3 + T_a + T_b)}{4}$$

where

$T_a = \alpha \times T_1$

$T_b = \alpha \times T_3$

$$\alpha = \frac{(1.216 \times T_0 - 0.216 \times T_2)}{(2.262 \times T_2 - 1.216 \times T_0)}$$

Positions of the thermocouples on the heat probe

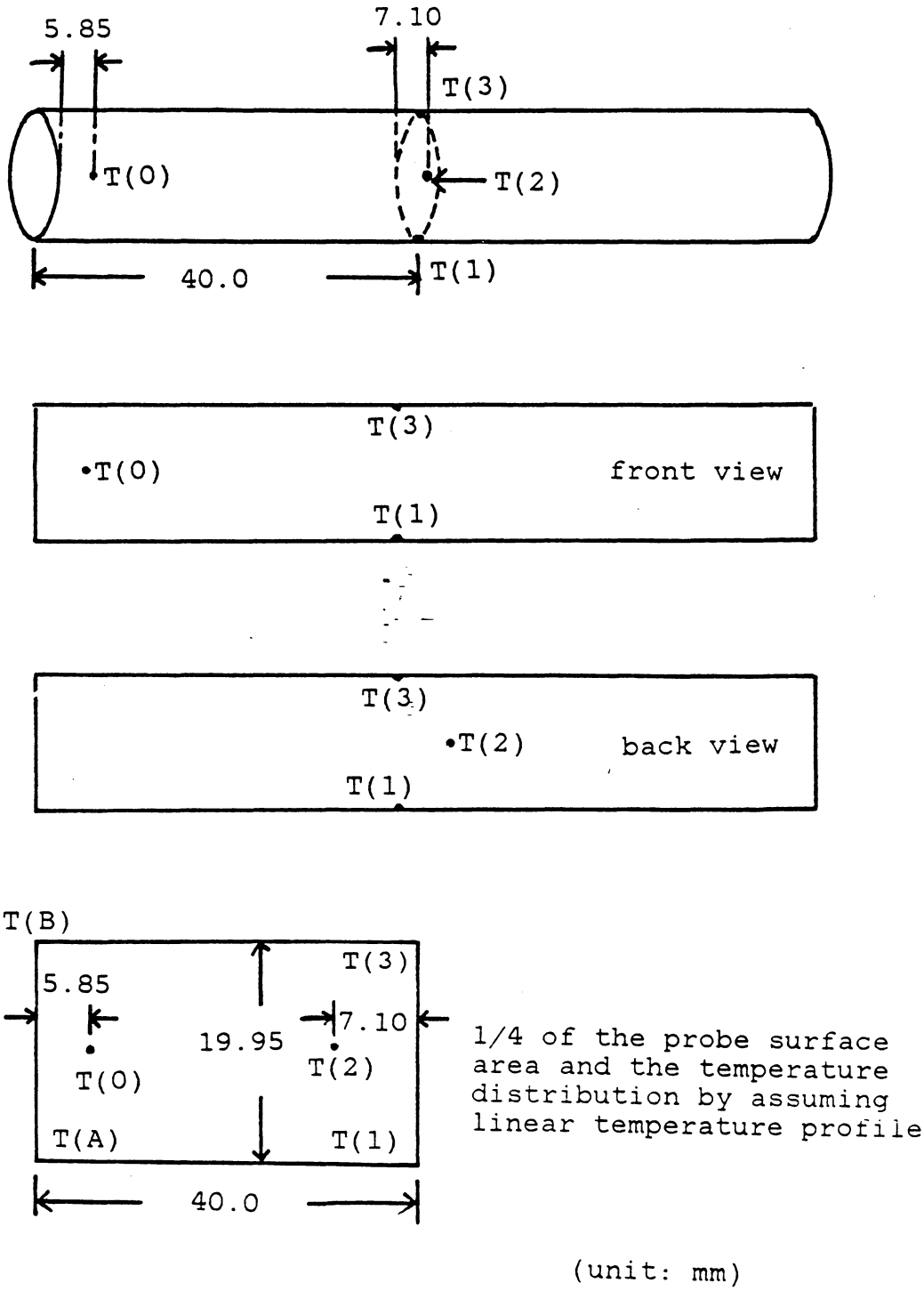

Figure 115. Position of the thermocouples on the heat probe

T_0, T_1, T_2, T_3 are from the reading of the thermocouples shown in Figure 115 on page 299

Under most experimental conditions, the largest temperature difference among $T_0 \ldots T_3$ has been smaller than 3° C. Considering the high thermal conductivity of the copper tube, we see that our assumption of linear temperature profiles between the selectual thermocouples could produce an error in the average temperature on the order of 1° C. The ΔT in this study has been maintained between 40 and 50 K, and so uncertainties arising from the design of our temperature measurement system should introduce an error on the order of 2% of our reported overall heat-transfer coefficients.

The bed temperature was measured with a movable temperature probe consisting of a thermocouple on the tip of a steel rod.

At room temperature, the maximum difference observed among the readings of all of our thermocouples was less than 0.2° C..

A specially-designed power supply with DC output up to 30 Volts was used as the power source for the heat probe, and the voltage drop across the probe was measured by a multimeter. A power resistor of 0.1 Ω was connected in series with the heating element so that the current passing though the system could be calculated by--

$$I = \frac{V_2}{R_2}$$

where

I = the current passing the system (amp).

V_2 = the voltage drop across the power resistor (volts)

R_2 = the resistance of the power resistor (0.1 Ω)

The power consumption by the heating element was calculated from $Q = I \times V_1$, where V_1 is the voltage drop across the heating element. Appendix E gives an error analysis of the heat lost at the two ends of the heat probe. This heat loss introduces an error that is always less

than 1%. If all possible errors are taken into account, our heat-probe system should provide an accuracy of ± 2%.

7.1.4 Heat transfer in an empty column

Figure 116 on page 302 shows heat-transfer coefficients versus probe height in a empty 101.6-mm I.D. column, fitted with gas distributor D-1, and operating at superficial gas velocities of 0.5 and 1.0 m/s. The heat-transfer coefficient is relatively high for the region directly above the gas distributor. This is easily understood to result from the high degree of turbulence created by air jets immediately above the gas distributor. The turbulent-flow theory also predicts the sharply decreasing heat-transfer-coefficient data as the probe elevates. At most experimental conditions, the heat-transfer coefficient reaches steady-state when the probe elevation exceeds 250 mm.

Douglas and Churchill proposed a correlation to calculate the Nusselt Number a horizontal cylindrical tube and an air stream inside a column --

$$Nu_t = (0.46\, R_e^{0.5} + 0.00128\, R_e)\,(1 + \frac{d_t}{D_b}) \qquad [7.2]$$

where

Nu_t = the tube Nusselt Number = $h_c d_t / k_g$

R_e = the tube Reynolds Number = $d_t\, u\, \rho_g / \mu_g$

h_c = heat-transfer coefficient (W/m^2 K)

d_t = diameter of the heat-transfer probe (mm)

k_g = thermal conductivity of the air (W/m K)

D_b = diameter of the fluidized bed (m)

ρ_g = density of the air (Kg/m^3)

μ_g = viscosity of the air (Kg/m s)

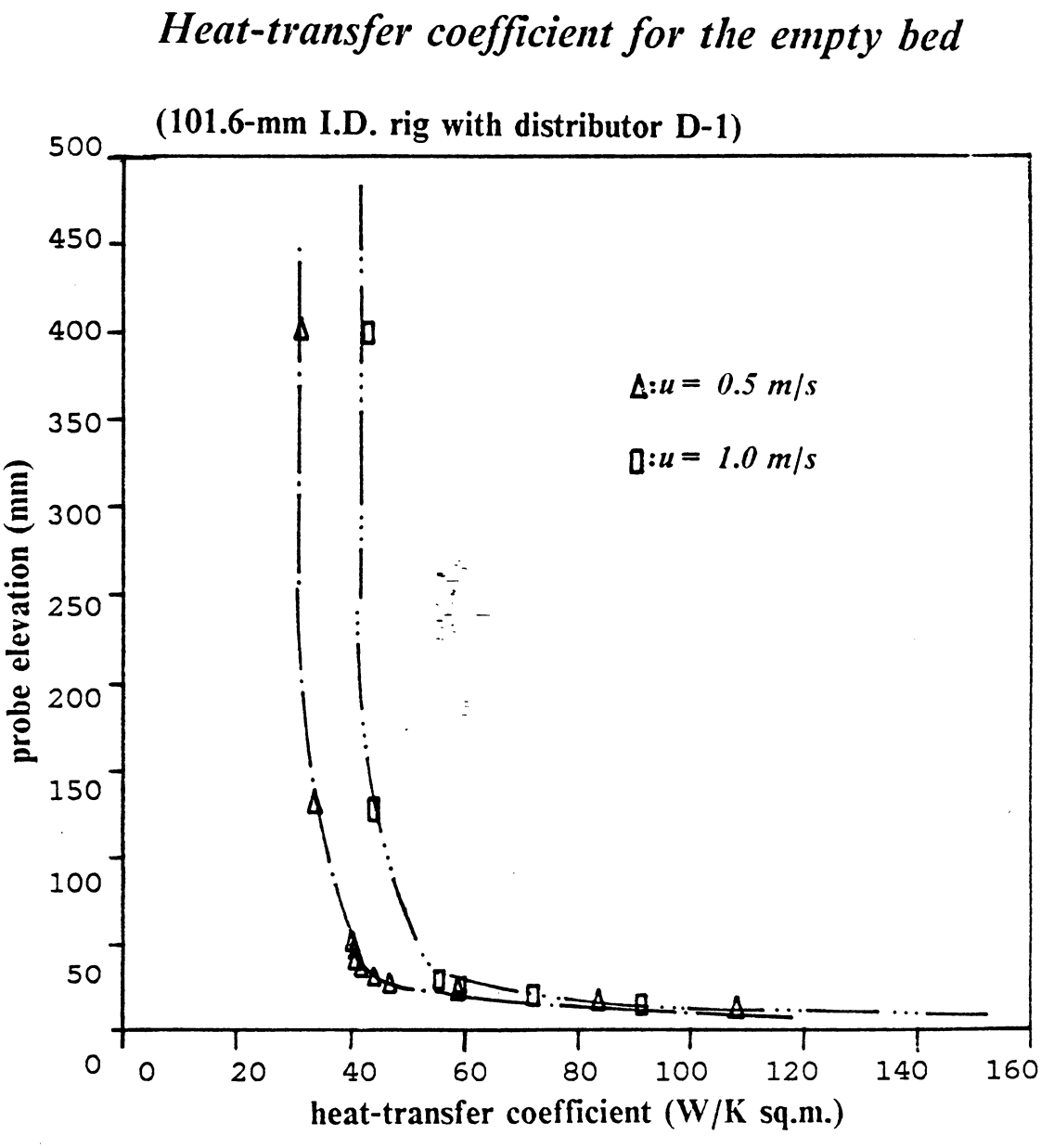

Figure 116. Heat-transfer coefficient versus probe height in empty bed: (gas distributor D-1; the perforated plate having 5.6% open area)

Table 35. Comparison of experimental and predicted Nusselt numbers in an empty bed

Comparison of experimental and predicted Nusselt Numbers in an empty bed

gas velocity (m/s)	$N_u(a)$ (from Eq. 8.1)	$N_u(b)$ (experimental)	$N_u(a)/N_u(b)$
0.5	10.6	15.2	.658
1.0	15.3	20.8	.736
1.5	18.0	25.9	.695
2.0	22.3	30.8	.724
2.5	25.3	34.7	.729
3.0	28.0	38.1	.735
		average = .713	

measured in a empty column with distributor D-1 (open area = 5.6%); tube elevation = 60mm.

Table 35 on page 303 lists Nusselt Numbers predicted from Equation 7.2 and those calculated from the experimental data for the 400-mm tube elevation. Equation 7.2 predicts a heat-transfer coefficient (or Nusselt Number) of about 70% of the experimental value.

7.1.5 Stability of the heat-transfer coefficient

At most experimental conditions, we have controlled the surface temperature of the heat probe at around 75°C to ensure consistency of the measurements. A preliminary test had been used to check the dependency of heat-transfer coefficient upon probe temperature. Table 36 on page 305 lists heat-transfer coefficients and probe temperatures for a fluidized bed having an 81.3-mm static bed height of 1260-μm Master Beads (P-A-1). When the average surface temperature was varied from 69.4°C to 81.1°C, the heat-transfer coefficient displayed an average variation of only 0.27%. Therefore, we can conclude that the heat-transfer coefficient is very stable as long as the probe temperature is confined between 70°C *and* 80°C.

Table 36. Stability of heat-transfer coefficient with variation in probe surface temperatures

Heat-transfer coefficient in the homogeneous region for different static bed heights

(distributor D-1; particle P-A-1,2,3)

Particle	H_s	u= 0.5	1.0	1.5	2.0	2.5	3.0
P-A-1	21.7	----	----	260	261	260	258
P-A-1	27.1	----	----	265	264	263	259
P-A-2	16.3	----	----	278	284	288	----
P-A-2	21.7	----	(275)	280	284	284	----
P-A-2	27.1	----	280	282	284	283	----
P-A-3	16.3	----	----	311	340	337	----
P-A-3	21.7	(282)	(320)	335	340	335	----
P-A-3	27.1	298	331	340	336	337	----

Notes:

1. Units: W/ m^2 K
2. The values in the parentheses are difficult to be specified exactly from the heat-transfer coefficient versus paobe elevation curves.
3. For particle P-A-1 (1260-μm Master Beads), the average of h_o = 260; standard deviation = 2.5 (0.96%)
4. For particle P-A-2 (630-μm Master Beads), the average of h_o = 283; standard deviation = 2.8 (0.99%)
5. For particle P-A-1 (335-μm Master Beads), the average of h_o = 338; standard deviation = 2.2 (0.65%)

7.2 Heat-transfer data for Group B particles

Table 9 on page 97 and Table 10 on page 99 list specifications for distributors and particles used in our study of heat transfer in shallow fluid beds of Group B particles. There are too many variables to be studied in all combinations: with 10 types of particles, 9 distributors, 5 gas velocities, and 10 probe positions, we would have 4,500 combinations. At least 20 minutes are needed for temperatures of bed and probe surface to reach steady state, and so at least 1500 hours would be needed to study all of the combinations. In general, 630-μm Master Beads (P-A-2) have been used to check effects of the gas distributor on the heat-transfer coefficient, while distributor D-1 (open area percentage= 5.6%) has been chosen to study particle-size effects. In most of our experiments, static bed heights have been selected between 16 and 30 mm. Although some shallower beds have been studied, we have found that placing a heat-transfer tube in a shallow fluidized bed having a static bed height less than 10 mm appears infeasible from an economic standpoint.

Based upon our observations of the hydrodynamic behavior of shallow fluidized bed, reported in previous chapters, we can infer that only three types of shallow beds (types A, B and C) may practicably be specified for heat-transfer uses. Although their features may vary, each of these bed types display three regions:

1. Homogeneous region -- This region lies at middle elevations of the shallow fluidized bed. Particles are distributed relatively homogeneously. The region can be identified from hydrodynamic data of types described in previous chapters. Usually, in the homogeneous region:

   a. The pressure distribution curve is linear.

   b. The particle volume-fraction distribution curve attains and remains close to a maximum value.

c. The particle fluctuation ratio is relative low (less than 1 or 2).

Notice that these features suggest homogeneity and stability of particle movement and mixing.

2. Jet region -- This is the region right above the perforated distributor plate, and it may not be evident in beds fluidized with laminated distributors. According our previous observations, the solid-mixing pattern is highly dominated by the behavior of gas jets. Therefore, we may expect the jets also to affect the heat-transfer coefficient to some degree.

3. Free-board region -- Above the homogeneous region is the so-called "free-board region," in which the particle density decreases with increasing elevation. The height of this region will increase as the shallow fluidized bed moves from type C through type B to type A, as a result of increasing either the amount of particles or the superficial gas velocity (see Chapter 3). Even though the time-averaged particle volume-fraction may be small in this region, the high degree of mixing and fluctuation in particle volume-fraction can be expected to keep the heat-transfer coefficient reasonably high in many cases.

The following three sections describe features of our heat-transfer data in the three regions.

7.2.1 Heat transfer in homogeneous region

Figure 117 on page 308 to Figure 119 on page 310 show heat-transfer coefficients for a 21.7 mm static bed height of 630-μm Master Beads in beds fitted with various distributors. Figure 117 on page 308, Figure 120 on page 311, and Figure 121 on page 312 give heat-transfer coefficients for beds of Master Beads of various sizes at a fixed static bed height (21.7-mm). The presence of the homogeneous region is evident: it can be easily identified

Heat-transfer coefficient in a bed having particle P-A-2 and distributor D-1

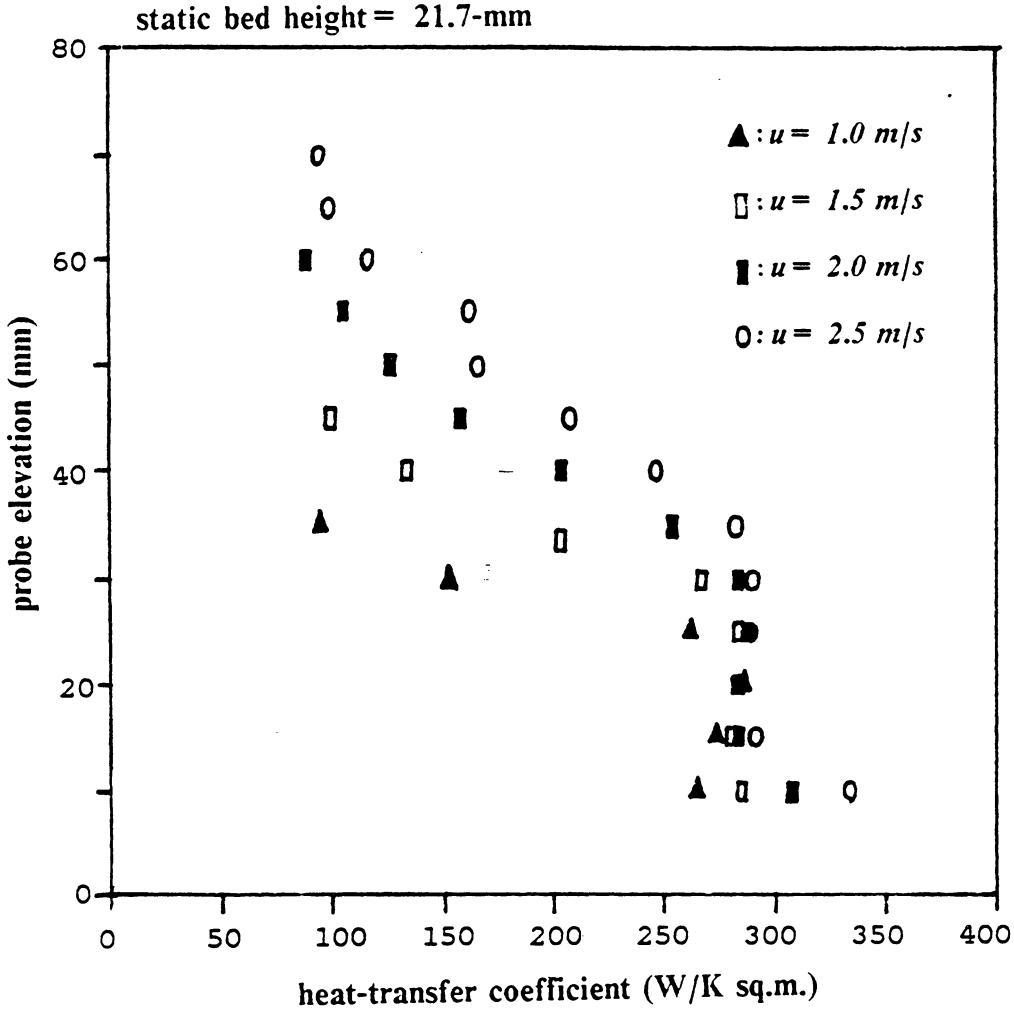

Figure 117. Heat-transfer coefficients for particle P-A-2 with distributor D-1

Heat-transfer coefficient in a bed having particle P-A-2 and distributor D-4

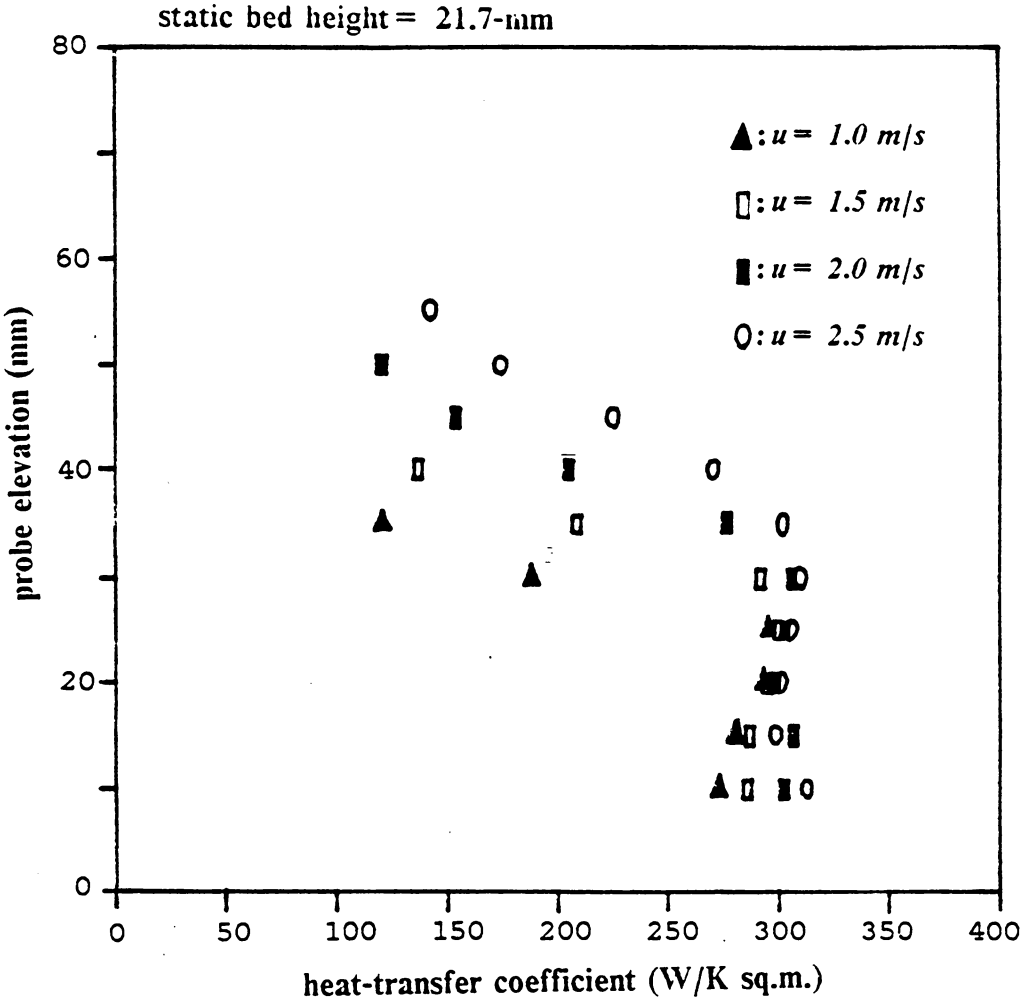

Figure 118. Heat-transfer coefficients for particle P-A-2 with distributor D-4

Heat-transfer coefficient in a bed having particle P-A-2 and distributor D-7

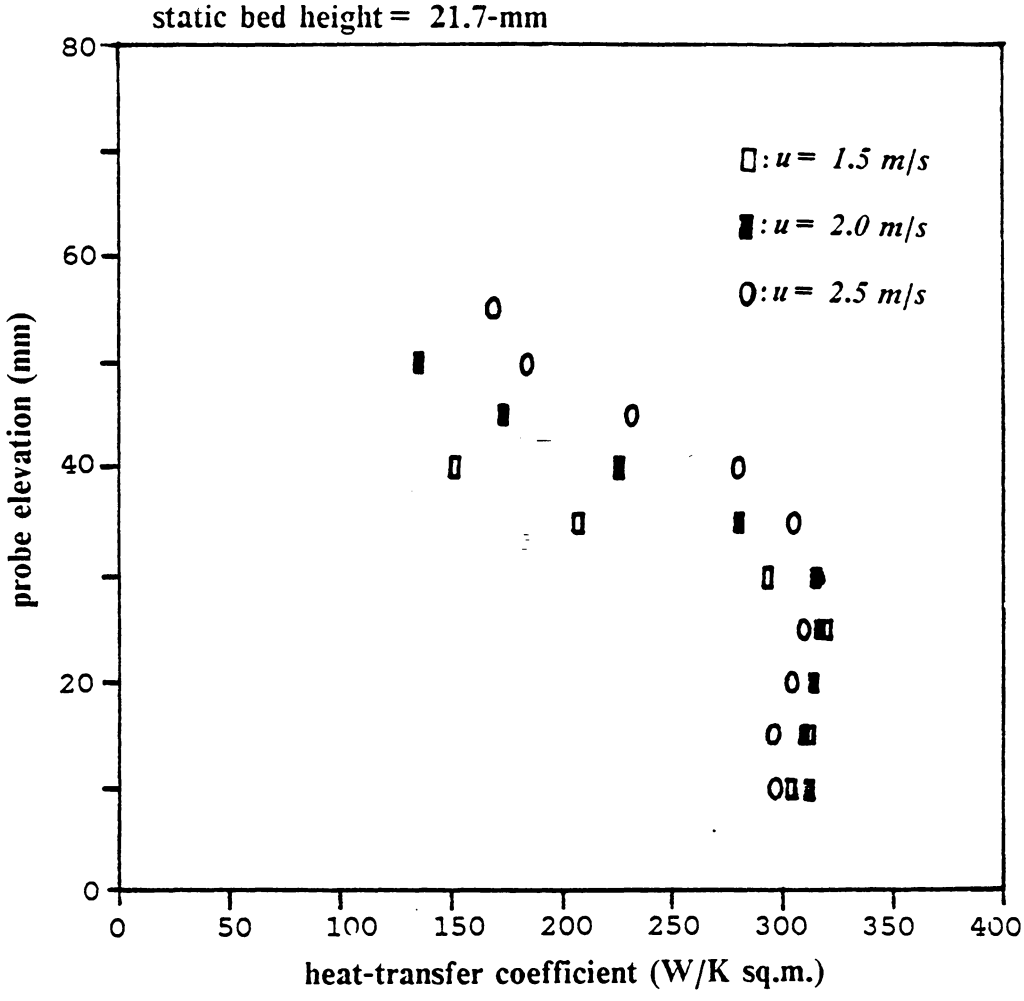

Figure 119. Heat-transfer coefficients for particle P-A-2 with distributor D-7

Heat-transfer coefficient in a bed having particle P-A-1 and distributor D-1

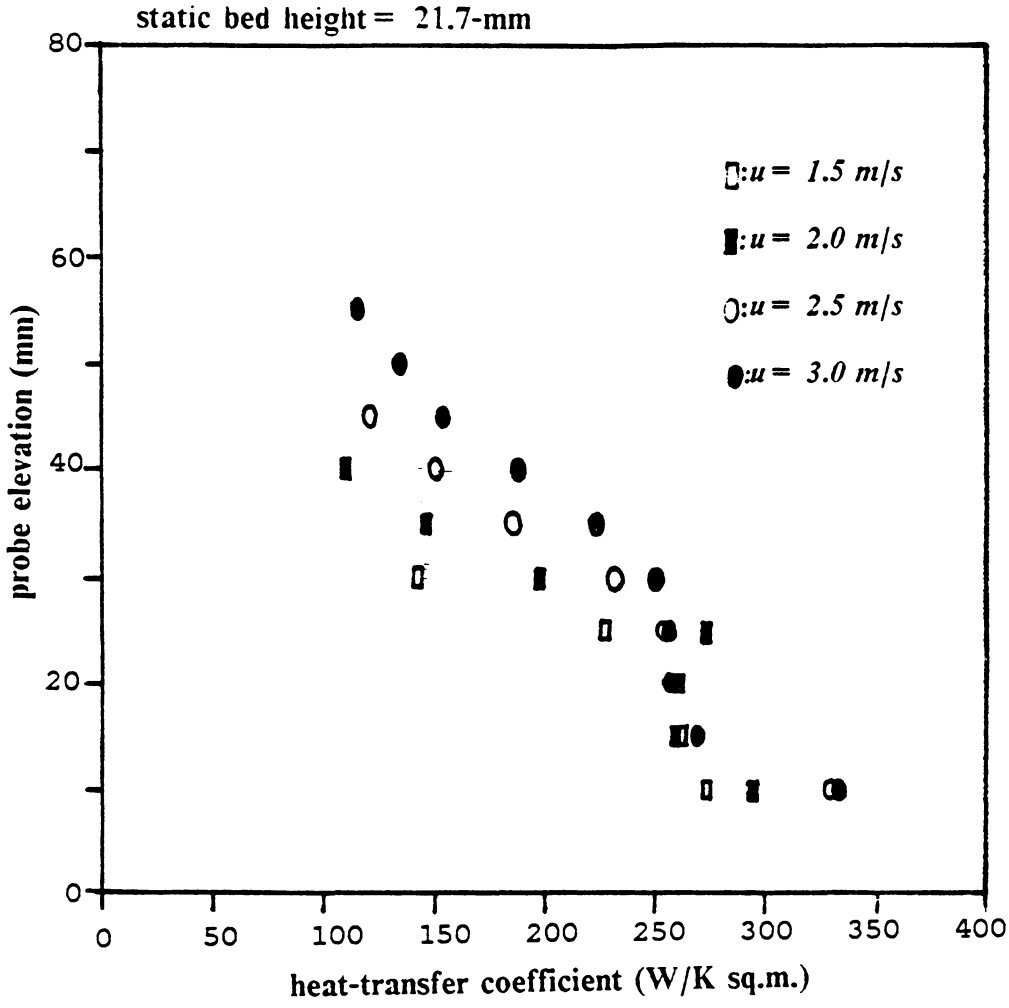

Figure 120. Heat-transfer coefficients for particle P-A-1 with distributor D-1

Heat-transfer coefficient in a bed having particle P-A-3 and distributor D-1

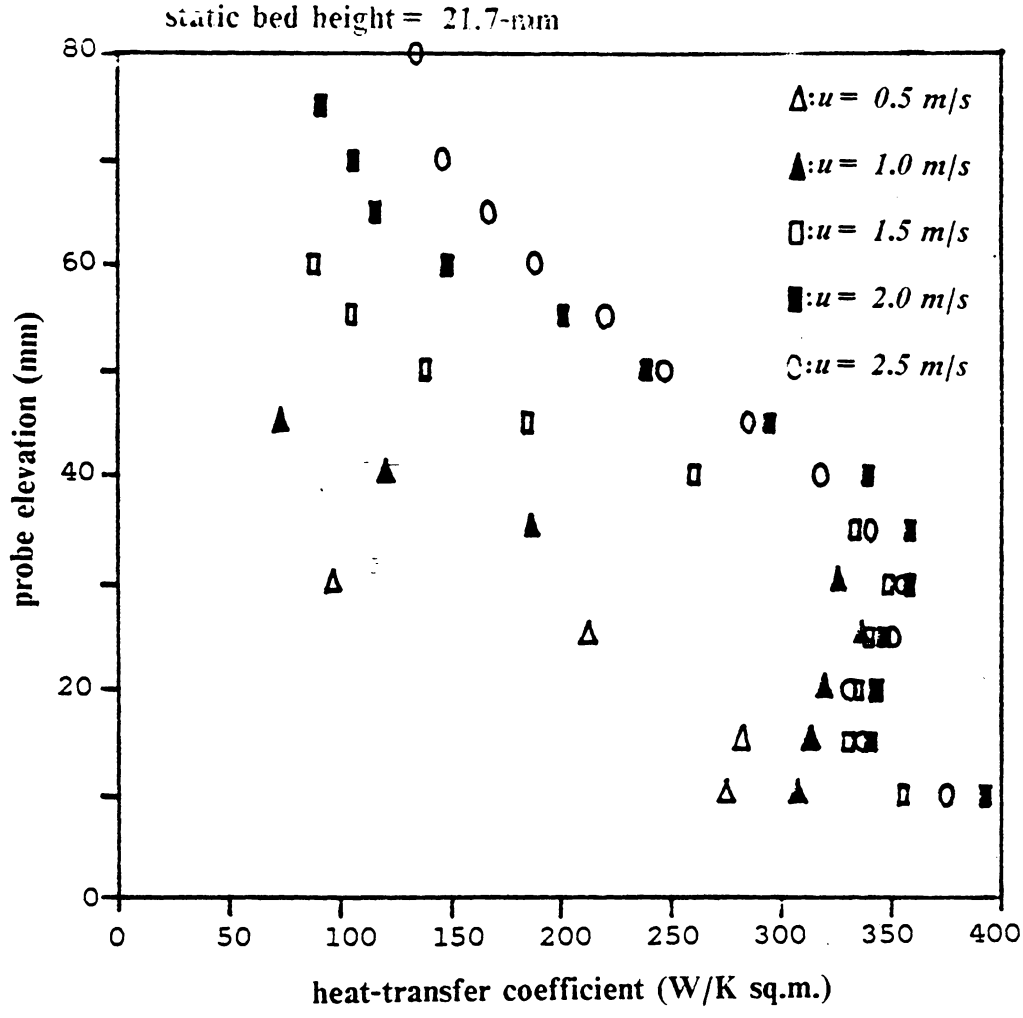

Figure 121. Heat-transfer coefficients for particle P-A-3 with distributor D-1

Table 37. Heat transfer coefficients in homogeneous region for different static bed heights

Heat-transfer coefficient in the homogeneous region for different static bed heights

(distributor D-1; particle P-A-1,2,3)

Particle	H_s	u= 0.5	1.0	1.5	2.0	2.5	3.0
P-A-1	21.7	----	----	260	261	260	258
P-A-1	27.1	----	----	265	264	263	259
P-A-2	16.3	----	----	278	284	288	----
P-A-2	21.7	----	(275)	280	284	284	----
P-A-2	27.1	----	280	282	284	283	----
P-A-3	16.3	----	----	311	340	337	----
P-A-3	21.7	(282)	(320)	335	340	335	----
P-A-3	27.1	298	331	340	336	337	----

Notes:

1. Units: W/ m^2 K
2. The values in the parentheses are difficult to be specified exactly from the curves of heat-transfer coefficient versus probe elevation.
3. For particle P-A-1 (1260-μm Master Beads), the average of h_o = 260; standard deviation = 2.5 (0.96%)
4. For particle P-A-2 (630-μm Master Beads), the average of h_o = 283; standard deviation = 2.8 (0.99%)
5. For particle P-A-1 (335-μm Master Beads), the average of h_o = 338; standard deviation = 2.2 (0.65%)

from plots of heat-transfer coefficient versus probe elevation. Table 37 on page 313 to Table 39 on page 319 give heat-transfer coefficients in the homogeneous region for varying static bed height, type of particle, and gas distributor, respectively. Some observations can be summarized as follows:

1. **The heat-transfer coefficient in the homogeneous region (h_o) does not vary much with change in superficial gas velocity**

   For beds operated at a superficial gas velocity smaller than about three times the minimum fluidizing velocity, u_{mf}, heat-transfer coefficients in the homogeneous region can be smaller than values observed at higher gas velocities. This can be easily attributed to the sluggishness of fluidization at such low fluidizing gas velocities. (Usually, this sort of bed falls near the boundary between type E and other types in the phase diagram.) Therefore, we may expect heat-transfer coefficient data for very low gas velocities to demonstrate different patterns from data obtained from high-velocity beds.

   Models for heat transfer in fluidized beds relate heat transfer to the residence time of packets (mixture of solid and gas) near a heat-transfer surface and to the voidage of the bed. When the air velocity is increased, the residence time of the packets at the heat-transfer surface decreases, and this decrease tends to produce an increase in the heat-transfer coefficient. At the same time, the voidage of the bed increases, and this tends to cause a decrease in heat-transfer coefficient due to lower frequency of the contact between the surface and packets. Hence, the two effects tend to cancel each other.

2. **h_o is independent of static bed height**

   Table 37 on page 313 shows heat-transfer coefficient data in the homogeneous region at various static bed heights (H_s) for three sizes of Master Beads. By noting the variations of the h_o with respect to gas velocity and static bed height, one observes that the average variation in the h_o values is within a very small range of less than 1%. Notice that H_s has to be greater than 15 mm to ensure the identification of an homogeneous re-

gion in the fluidized beds of Master Beads. In a shallower bed, the jet region and cloud region merge together and make the homogeneous region indiscernible.

3. **h_o does vary with particle characteristics**

Figure 122 on page 316 shows h_o values versus the average particle diameter for all particles studied, while Table 38 on page 317 lists all of the data. Two general conclusions can be drawn --

a. h_o increases as the particle size decreases.

b. h_o increases as the particle density increases.

These h_o values might logically be compared with literature data for deep beds, and perhaps a mathematical correlation can be proposed (see the next section).

4. **h_o increases as the open area percentage (A_r) of the gas distributor decreases. However, h_o becomes independent of the open area ratio for A_r greater than 6%.**

Table 39 on page 319 lists h_o data for different gas distributors, while Figure 123 on page 318 shows the relationship between h_o and the open area ratio. For the perforated plates, h_o decreases as A_r increases from 2.1 to 5.6%. This might be associated with solid-mixing effects produced by gas jets. However, the fact that h_o for laminated plates shows the same tendency suggests that turbulence in the lower portion of the bed can always affect h_o in the homogeneous region. (If the laminated plates produce "jets," these are "weaker" -- i.e., smaller and more numerous -- than jets above a perforated plate.)

In comparison with data for beds having large open-area distributors, h_o values are especially small at open area ratios between 4.2 and 5.6%. We do not have an explanation for this effect, and further study is in order, to substantiate the data and to develop explanations. However, all of the data on Figure 123 on page 318 (or in the last column

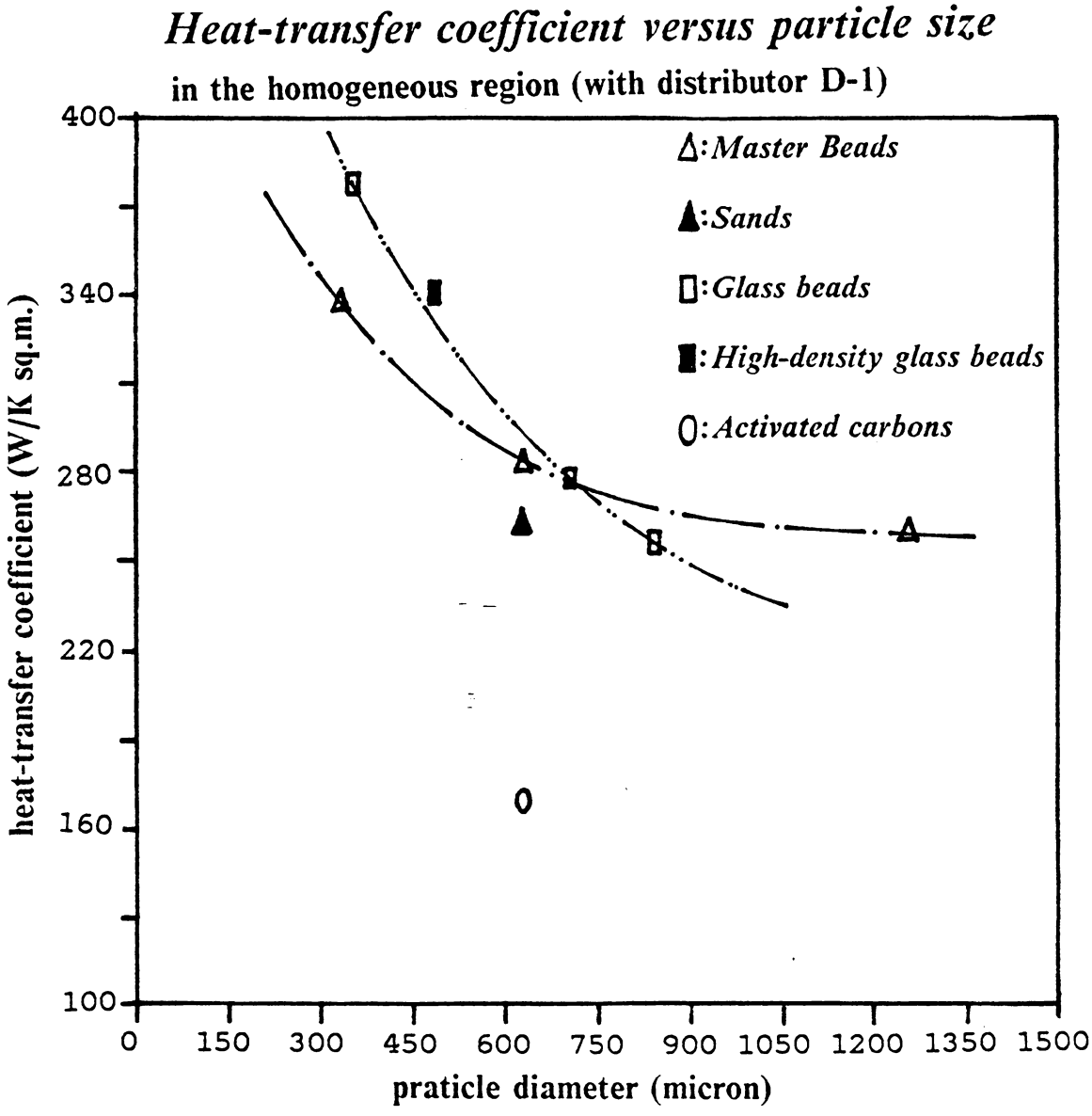

Figure 122. **Heat-transfer coefficients in homogeneous region versus particle diameter:** (Particle: Master Beads; Distributor D-1)

Table 38. Heat-transfer coefficients in homogeneous region for different particles

Heat-transfer coefficient in the homogeneous region for different particles

(distributor D-1; static bed height = 21.3-24.2 mm)

		gas velocity (m/s)						
H_s	Paritcle	0.5	1.0	1.5	2.0	2.5	3.0	ave.
21.7	P-A-1	----	----	260	261	260	258	260
21.7	P-A-2	----	(275)	280	284	284	----	283
21.7	P-A-3	(282)	(320)	335	340	335	----	337
23.0	P-S-1	-----	256	268	----	----	----	262
21.3	P-C-1	160	180	----	----	----	----	170
23.7	P-G-1	----	250	257	262	----	----	256
23.9	P-G-2	----	273	281	281	----	----	278
22.5	P-G-3	----	327	343	353	----	----	341
24.2	P-G-4	(345)	368	387	----	----	----	378

Notes:

(1). Units: W/ m^2 K.

(2).Values in the parentheses are difficult to be specified exactly from the curves of heat-transfer coefficient versus probe elevation.

Heat-transfer coefficient versus open area ratio of distributors

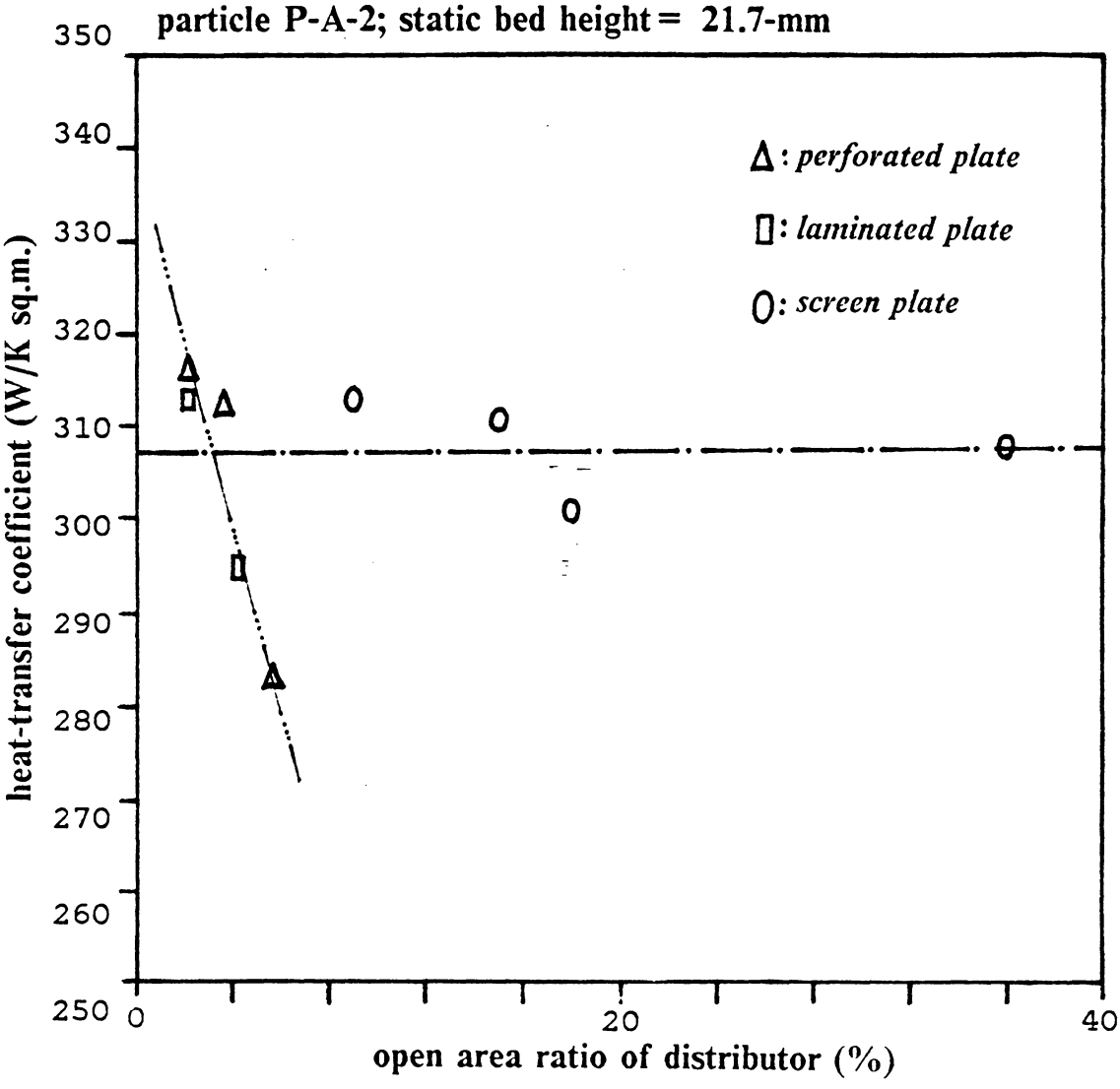

Figure 123. **Heat-transfer coefficients in the homogeneous region versus open area ratio of distributors:** (particle P-A-2; static bed height = 21.7 mm)

Table 39. Heat-transfer coefficients in the homogeneous region for different distributors

Heat-transfer coefficient in the homogeneous region for different distributors

(particle: P-A-2; static bed height = 21.7 mm)

Distributor	A_r	u = 1.0	1.5	2.0	2.5	Ave.
D-1	5.6%	(275)	280	284	284	283
D-2	3.6%	299	310	310	315	312
D-3	2.1%	270	316	----	----	316
D-4	4.2%	280	287	297	301	295
D-5	2.1%	283	315	310	----	313
D-6	9.0%	(300)	312	316	310	313
D-7	15.%	----	314	314	305	311
D-8	18.%	----	294	306	302	301
D-9	36.%	----	315	310	300	308

Notes:

(1). Units: W/ m^2 K.

(2).Values in the parentheses are difficult to be specified exactly from the curves of heat-transfer coefficient versus probe elevation.

(3).Average values are taken for velocity = 1.5, 2.0 and 2.5 m/s. (Because h_o values for u = 1.0 m/s are not compatiable with others.)

of Table 39 on page 319) display an overall average of 306 W/m^2 K and a standard deviation of only 10.8 W/m^2 °K (i.e., about 3.5% deviation).

5. **For A_r greater than 9% (all of the screen distributors), the heat-transfer coefficient is independent of the gas distributor**

   Figure 124 to Figure 126 on page 322 shows heat-transfer coefficient versus probe position for shallow fluidized beds using all of the four screen distributors at gas velocities of 1.5, 2.0, 2.5 m/s, respectively. For a fixed probe position, variations in the heat-transfer coefficient are always less than 50 W/m^2 K. In most cases, the variation falls between 20 and 30 W/m^2 K. Notice also that no correlation appears to exist, on the basis of small variations in heat-transfer coefficient, up or down, between this variable and the open area ratio of screen distributors.

7.2.2 Heat-transfer data in jet region

Table 40 on page 325 shows percentage increase in the heat transfer coefficients at probe elevation of 10 mm in a comparison with coefficients observed in the homogeneous regions of shallow fluidized beds above a number of distributors. Each bed contains 630-μm Master Beads (P-A-2) at a static bed height of 21.7 mm. Figure 127 on page 324 demonstrates the percentage increase of the heat-transfer coefficients versus the superficial gas velocity for three of the perforated distributors. Two observations can be made --

1. The percentage increase in the heat-transfer coefficient of the jet region increases sharply with increase in gas velocity.

2. For gas distributors D-2 (A_r = 3.6%) and D-3 (A_r = 2.1%), the curves for the percentage increase of the heat-transfer coefficients in the jet region are relatively close to each

Heat-transfer coefficient for beds having screen distributors

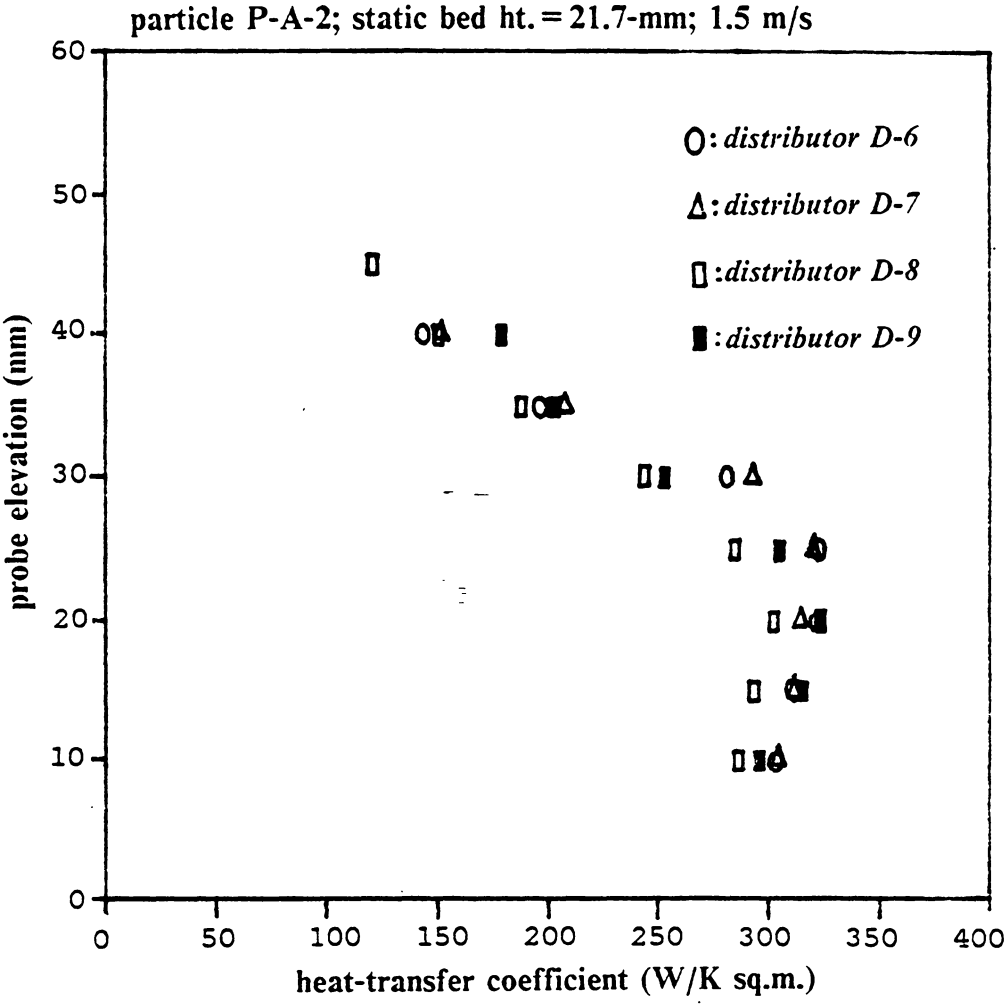

Figure 124. **Heat-transfer coefficient data for beds with screen distributors at u= 1.5 m/s:** (Particle P-A-2; static bed height = 21.7 mm.)

Heat-transfer coefficient for beds having screen distributors

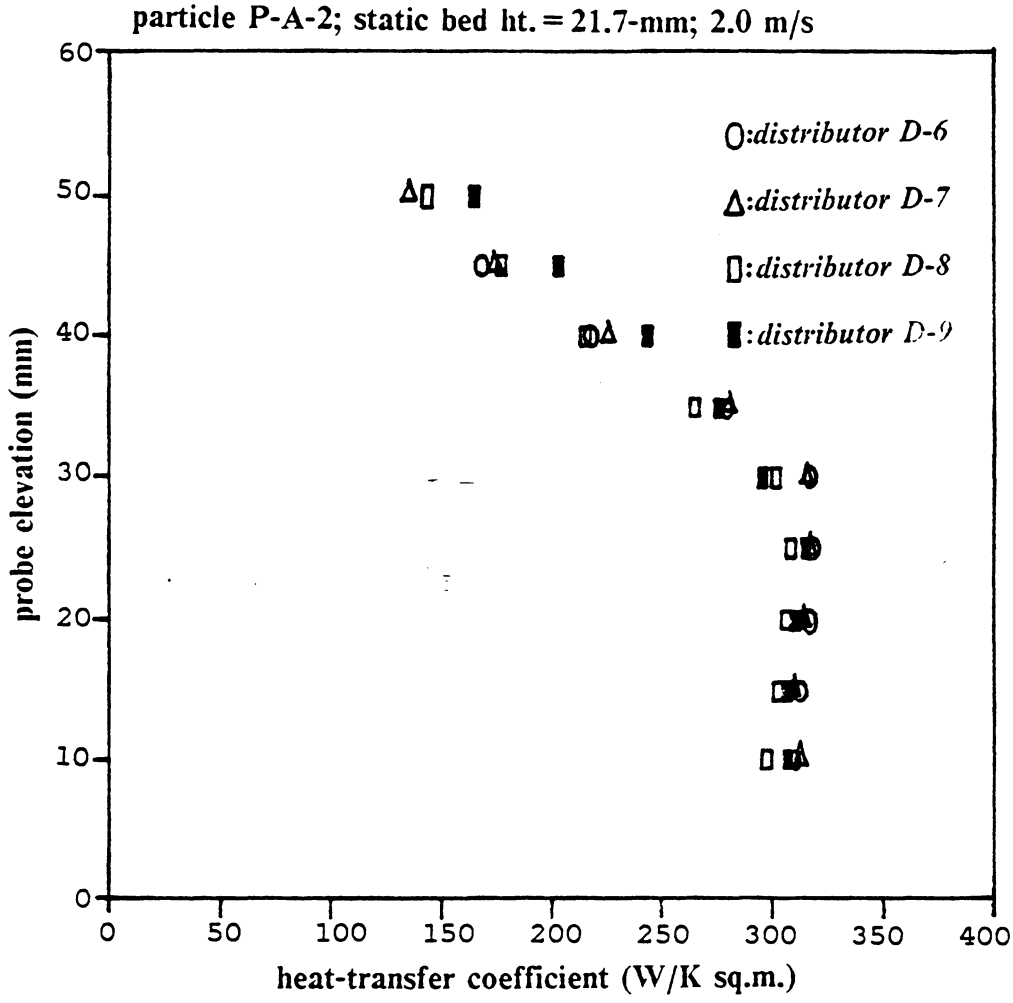

Figure 125. **Heat-transfer coefficient data for beds with screen distributors at u= 2.0 m/s:** (Particle P-A-2; static bed height = 21.7 mm.)

Heat-transfer coefficient for beds having screen distributors

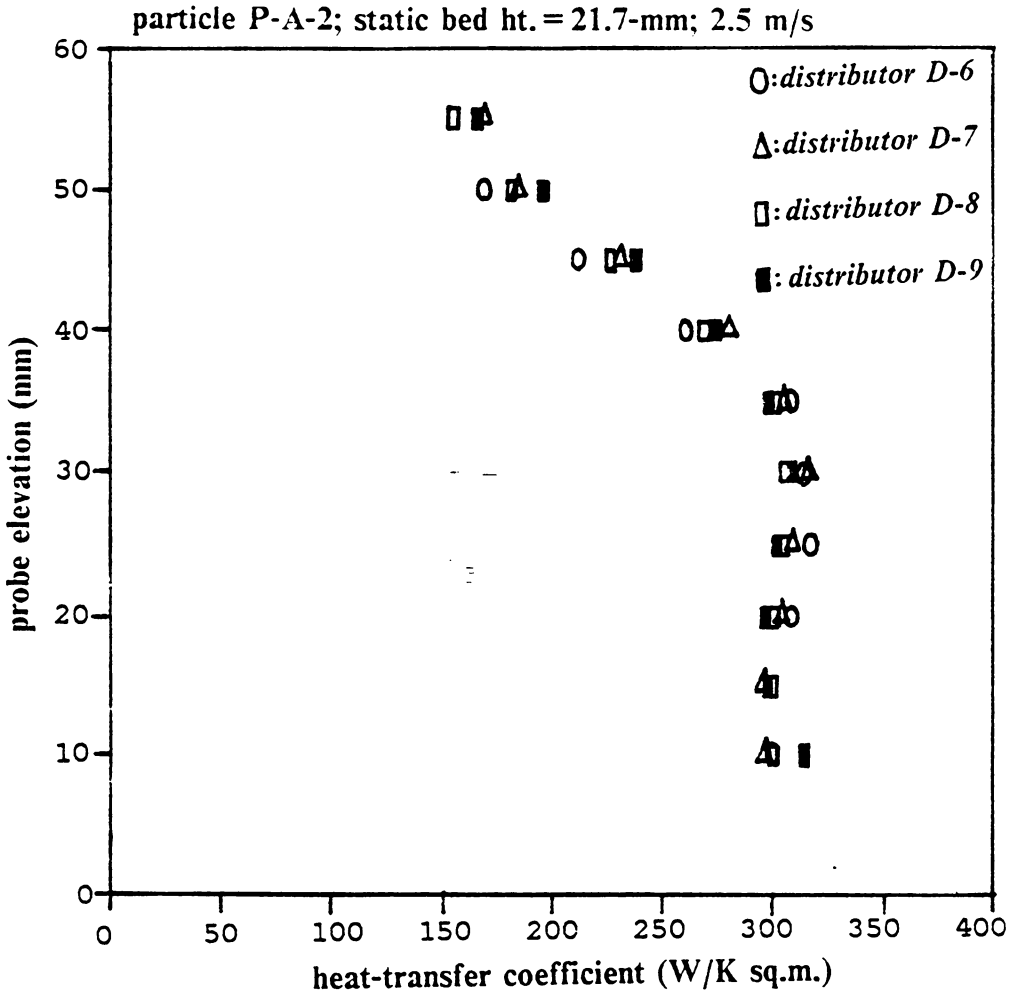

Figure 126. Heat-transfer coefficient data for beds with screen distributors at u= 2.5 m/s: (Particle P-A-2; static bed height = 21.7 mm.)

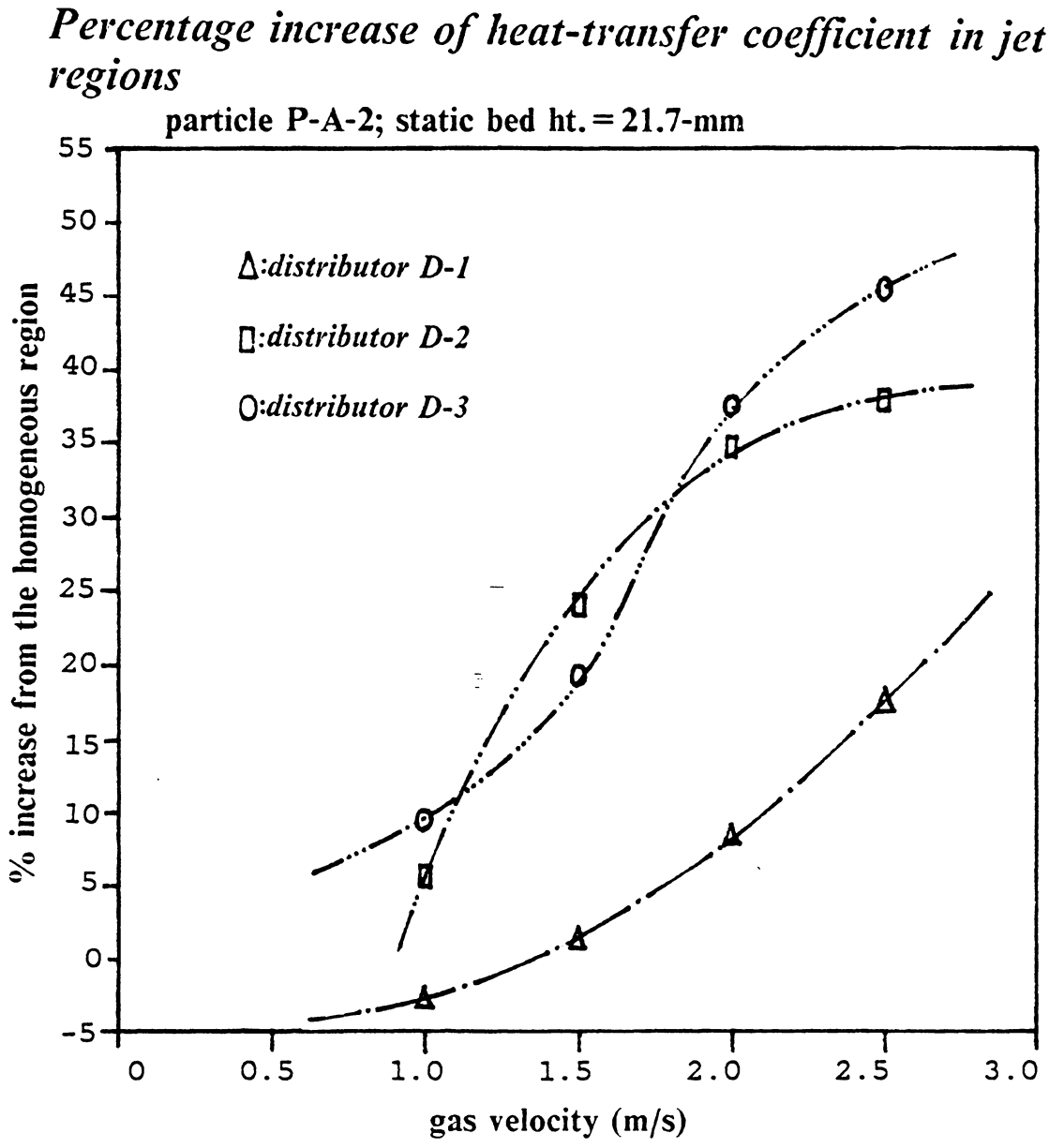

Figure 127. **Percentage increase in heat transfer in jet-affected region:** (w.r.t. the values obtained in the homogeneous region; distributor D-1,D-2,D-3; static bed ht. = 21.7 mm; particle P-A-2)

Table 40. Percentage increase in heat-transfer coefficient in jet region

Percentage of the increase of heat-transfer coefficient at the jet-affected region

from the probe position = 10 mm with respect to that in the homogeneous region (particle P-A-2; static bed ht. = 21.7 mm).

Distributor	u = (m/s) 1.0	1.5	2.0	2.5
D-1	-2.9	1.4	8.5	17.6
D-2	5.7	24.2	34.8	38.1
D-3	9.6	19.6	37.7(*)	45.6(*)
D-4	-2.5	-0.3	5.5	4.0
D-5	5.65	9.2	26.1	----
D-6	-3.3	-2.6	-1.9	-3.2
D-7	-----	-3.2	-0.6	-2.6
D-8	-----	-2.7	-2.9	-0.7
D-9	-----	-6.7	-1.3	5.0

* h_o is taken as 316 W/ $m^2°K$.

other. (Absolute values of the heat-transfer coefficients in the jet region are also very close for those two cases.)

It can also be seen that the percentage increase of heat-transfer coefficients in the "jet" region increases from 5.7 to 26.1 % as the gas velocity increases from 1.0 to 2.0 m/s for a shallow fluidized bed having gas distributor D-5 (a laminated plate having A_r =2.1%). In comparison with data for distributor D-4 (another laminated plate) in Table 40 on page 325, it appears that a distributor of small open-area ratio must produce some degree of turbulence in a shallow fluidized bed even if "jets" may not exist.

Table 40 on page 325 also shows that the percentage "increase" in the heat-transfer coefficient is always negative for the shallow beds above screen distributors (A_r from 9 to 36%). This might be explained by suggesting that the lower portions of these beds either display poor solid-mixing or or low particle density.

Theoretically, the circulation of particles is relatively intense and the frequency of pulsations is relatively high in the jet region due to the high-velocity gas streams that emerge from orifices in the distributor. When the gas velocity is increased, the residence time of packets must decrease considerably. Therefore, the combination of these two effects (vigorous circulation of particles and high frequency of the pulsation) could overcome effects due to increase in porosity and cause the heat transfer to increase almost monotonically increasing with gas velocity.

However, when the frequency of contact between the immersed heat-transfer surface and fluidizing particles is increased, erosion will inevitably become more severe. This implies that use of the jet region for heat transfer can be impractical. In deep-bed systems, a designer can easily arrange to provide a large amount of heat-transfer surface outside the jet-affected region. However, if the designer elects to use a shallow fluidized bed, avoiding the jet region might reduce the available space for housing heat-transfer surface unduly. This is an argument in favor of having porous plate or screen distributors in shallow beds for heat-transfer applications.

Fortunately, we have not experienced erosion problems throughout our heat-transfer studies. Nevertheless, we recommend the following precautions if shallow fluidized beds are used for heat transfer:

1. Choose erosion-resistant materials for heat-transfer surfaces.

2. Study erosion mechanisms so that the minimum feasible elevation of surfaces immersed in the bed can be determined (see Behie et al., 1970).

3. Periodically inspect the heat-transfer surface, and replace it if necessary.

7.2.3 Heat-transfer data in the free-board/cloud region

Table 41 on page 328 refers to the maximum heat-transfer coefficients observed near the bed surface. The table lists percentage increases in these heat-transfer maximia with respect to the homogeneous region of a shallow fluidized bed of 630-μm Master Beads with a 21.7-mm static bed height. The table gives data for all of our gas distributors. Table 42 on page 329 lists the same type of information for different particles. Some observations can be summarized as follows --

1. The percentage increase of the maximum heat-transfer-coefficient in the free-board region is independent of the design of the gas distributor. Examination of the data in Table 41 on page 328 shows that the percentage increase for the 630-μm Master Beads (P-A-2) has an average value of 2.8% for all of the gas distributors.

2. The percentage increase in the maximum heat-transfer-coefficient in the free-board region increases as: (a) the particle density increases; and (b) the particle size decreases. This can be explained by suggesting that smaller and lighter particles are mixed more

Table 41. Percentage increase in heat-transfer coefficient in jet region for different distributors

Percentage increase of the heat-transfer coefficient at the free-board region for different types of distributors

the highest value in the free-board region with respect to the homogeneous region for different types of distributors (particle P-A-2; static bed ht. = 21.7 mm).

Distributor	u = (m/s) 1.0	1.5	2.0	2.5
D-1	4.0	1.1	0.	2.1
D-2	5.4	1.6	0.	1.0
D-3	1.5	0.	----	----
D-4	5.4	4.2	6.6	3.0
D-5	6.7	1.3	5.2	----
D-6	8.3	3.5	0.6	2.6
D-7	-----	1.9	1.0	3.6
D-8	-----	2.7	0.7	1.3
D-9	-----	2.5	1.6	3.0

Table 42. Percentage increase of heat-transfer coefficients in free-board region for different particles

Percentage increase of the heat-transfer coefficient at the free-board region for different types of particles

the highest value in the free-board region with respect to the homogeneous region for different types of particles (distributor D-1; static bed ht. = 21.3 to 24.1 mm).

Particle	u = (m/s) 0.5	1.0	1.5	2.0	2.5
P-A-1	----	----	0.	5.0	0.
P-A-2	----	4.0	1.0	0.	2.1
P-A-3	----	----	3.9	5.3	6.0
P-S-1	----	7.8	7.1	----	----
P-C-1	12.5	27.1	----	----	----
P-G-1	----	2.8	0.	0.	----
P-G-2	----	3.3	0.7	0.	----
P-G-3	----	6.1	2.6	2.0	----
P-G-4	----	13.5	9.3	----	----

vigorously by fluctuations in the bed surface and hence give higher heat-transfer coefficients in comparison with h_0 (the value from the homogeneous region).

7.3 Heat transfer date from shallow fluidized beds of different sizes

Four rectangular fluidized rigs have been used to examine the effect of bed size upon heat transfer. All of those rigs are 0.6096 meter (2 feet) in height with a fixed length of 101.6 mm while widths are 38.1, 63.5, 101.6 and 152.4 mm, respectively (see Chapter 3 for details).

By comparing all of the heat-transfer coefficients in those rectangular fluidized beds, we have ascertained that the size of bed over the range studied does not affect the heat transfer. Figure 128 on page 331 shows heat-transfer coefficient data for the four rectangular rigs together with data obtained from the 101.6-mm I.D. circular bed. The data in the figure are for:

(1) static bed height = 21.7-mm.

(2) particle P-A-3 (335-μm Master Beads)

(3) distributor D-4 (laminated plate with 4.2% open area ratio)

(4) gas velocity = 1.5 m/s

It can be seen that differences among those curves are insignificant from a statistical point of view.

In Chapter 3, we conclude that the size and shape of fluidized bed does not influence the phase diagram, except as a bed becomes very small. Now we can further expand our earlier conclusions by stating that hydrodynamic and heat-transfer characteristics are also independent of design and scale. However, effects of particle fluctuations do increase if the rig

Heat-transfer coefficient data for fluidized beds of different sizes

(particle P-A-3; distributor D-4; u = 1.5 m/s; static bed ht. = 21.7 mm)

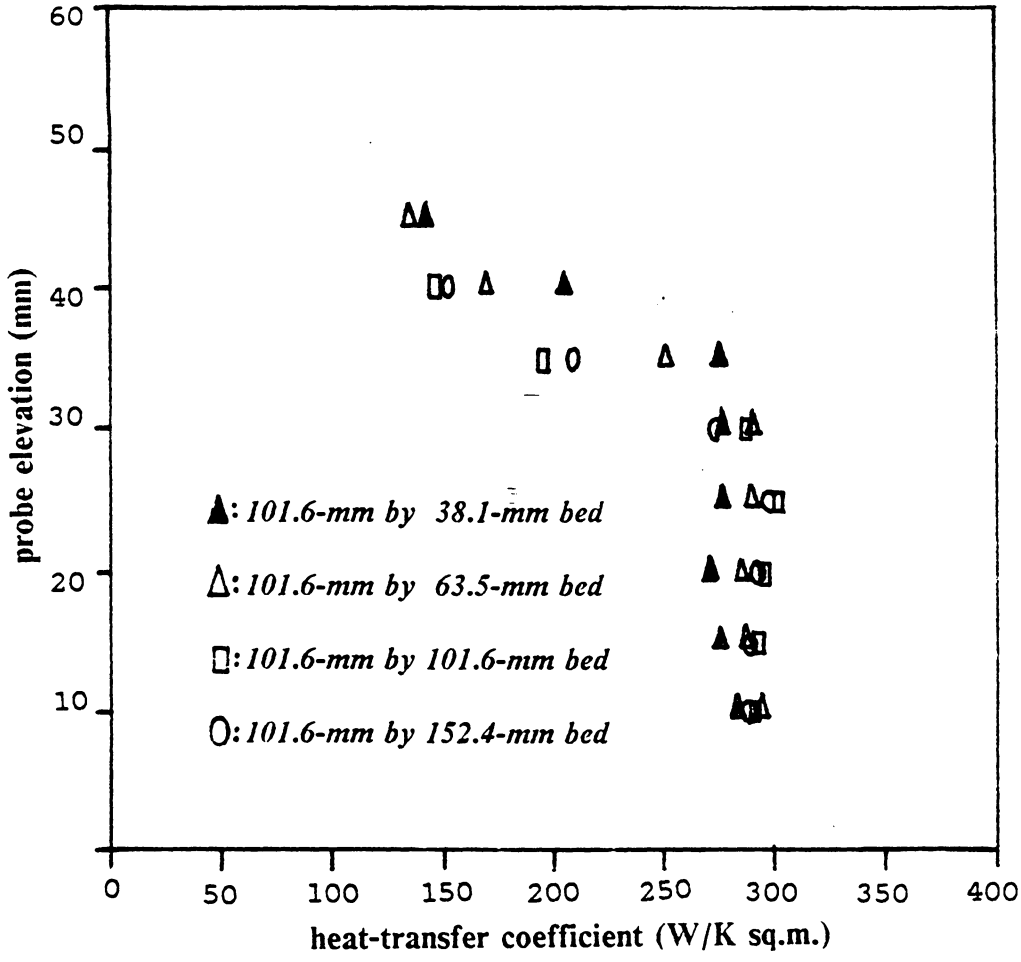

Figure 128. Heat-transfer coefficients data for fluidized beds of different sizes

is "too narrow" (in our case, the 38.1 by 101.6-mm rig). In this event, the rig wall can affect the behavior of a bed of type A (see Chapter 3).

In our experiments on heat transfer in rectangular rigs, we experienced static electricity problems for the narrowest (38.1-mm) rig when filled with the 335-μm Master Beads (P-A-3). We had not heard reports of static electricity problems for Group B particles in the literature, and we conclude that the phenomenon we observed may arise from the specific properties of our rig wall and Master Beads. We could see electrically-charged particles stick either to the wall or to each other to form cohesive packets. Existence of the packets decreases the chance for particles to reach the heat-transfer surface; the fluidization is sluggish; and heat-transfer coefficient is less.

Many fluidization researchers have used the humidified air as a fluidizing gas in attempts to eliminate problems arising from static electricity. Figure 129 on page 333 shows heat-transfer coefficient curves for the 38.1-mm by 101.6-mm rectangular bed when fluidized air with 10% and 100% relative humidity, respectively. From data in the homogeneous region (10-35 mm above the distributor), we see that the bed fluidized by the dry air, producing greater static electricity, gives a heat-transfer coefficient about 10% lower at the superficial gas velocity of 2.0 m/s. For the same bed at a gas velocity of 1.5 m/s, we have found the difference between dry and wet air to decrease to 5%. The difference diminishes with further decrease of superficial gas velocity or with increase in particle size (from 335-μm to 630-μm or 1260-μm Master Beads).

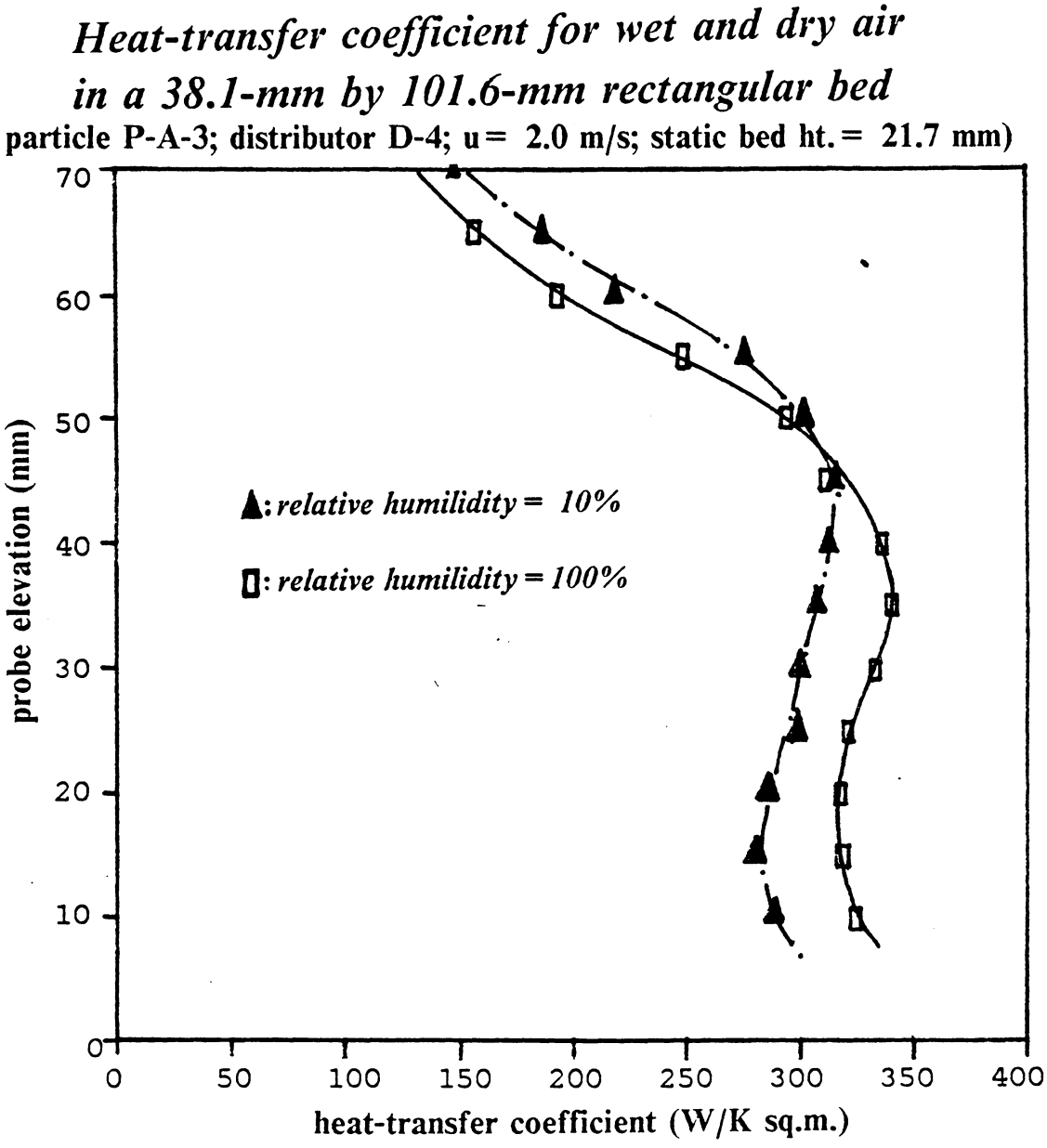

Figure 129. Comparison of heat-transfer coefficients for dry and wet fluidizing air

7.4 Correlation of heat-transfer coefficient in shallow beds

As mentioned earlier, the literature contains four correlations of heat-transfer coefficient in shallow fluidized beds. On examining those correlations, we find that eight different dimensionless groups are involved:

1. Reynolds number based on the heat-transfer tube diameter (Re_t) -- $\frac{d_t u \rho_f}{\mu_f}$.

2. Reynolds number based on the particle diameter (Re_p) -- $\frac{d_p u \rho_f}{\mu_f}$.

3. Archimides number for the particle-fluid system (A_{rm}) -- $\frac{u^2}{d_p^3 \rho_s^2 g}$.

4. Density ratio of the particle-fluid system -- $\frac{\rho_s}{\rho_f}$.

5. Prandtl number (Pr) -- 0.703 for air at 20°C, 1 atm.

6. Ratio of tube elevation to static bed height -- $\frac{H_t}{H_s}$.

7. Ratio of tube elevation to bed diameter -- $\frac{H_t}{D_b}$.

8. Bed porosity -- ε_f.

where

d_t = diameter of the heat probe, *m*.

d_p = diameter of the particle, *m*.

H_t = elevation of the heat probe, *m*.

H_s = static bed height, *m*.

ρ_s = density of the particles, $\frac{kg}{m^3}$.

ρ_f = density of the fluidizing medium, $\frac{kg}{m^3}$.

μ_f = viscosity of the fluidizing medium, $N\,s/m^2$.

After carefully examining all available correlations of heat-transfer coefficient in fluidized beds, Abu Bakar (1981) modified the equation proposed by Andeen and Glicksman (1976) to the form of --

$$Nu_t = 1135\,(1-\varepsilon)\,[\,Re_t\,(\frac{\rho_s}{\rho_g})\,(\frac{u^2}{d_p^3\,\rho_s^2\,g})]^{0.766}\,P_r^{0.3}\,(\frac{H_t}{H_s})^{0.145} \qquad [7.3]$$

Based upon our work, we can conclude that most of inconsistent results on heat transfer in shallow fluidized beds arise from two factors --

1. Contradictory data may be collected from different types of shallow fluidized beds even though experimental variables are similar. For example, one might be confused by the different heat-transfer patterns by fixing all experimental conditions except the static bed height and ignoring the fact that one's fluidized bed shifts about among the several "types."

2. Putting heat-transfer probe into different regions of a shallow fluidized bed can produce discrepant heat-transfer results. The tendency for the coefficient to increase in jet and free-board regions is difficult to describe in quantitative terms.

Therefore, only the homogeneous region of shallow fluidized beds is relatively free from characteristics specific to a particular experimental system. It is worth comparing data from this region with available correlations.

We have applied these correlations to all of the heat-transfer data that we have obtained in the homogeneous region of our shallow beds. We calculated the respective dimensionless groups from our data and converted them to logarithms. We then applied the Linear Regression Program under SAS package to determine the best coefficients. Almost all of the coefficients in the correlations must be modified to obtain a fit of our data. The correlations suggested by Vreedenburg (1958) and Ainshtein (1959) give poor fits: correlation coefficients

are 0.355 and 0.382 respectively. The equation suggested by Andeen and Glicksman (1976) and Abu Bakar (1981) gives a relatively high correlation coefficient of 0.796. (Since we are ignoring the effect of probe elevation in these tests of our data for the homogeneous region, the equations provided by these two sources are the same.)

Figure 130 on page 337 shows predictions of the three correlations for 335-μm Master Beads as a function of superficial gas velocity. None is very good. But by determining correlation coefficients for the experimental data with respect to all of the dimensionless groups, we are able to propose a new correlating equation --

$$Nu_t = \delta_0 (1 - \varepsilon) \left(\frac{u^2}{d_p^3 \rho_s^2 g}\right)^{\delta_1} (Re_t)^{\delta_2} (Re_p)^{\delta_3} P_r^{0.3} \qquad [7.4]$$

A regression program under SAS has been used to fit coefficients for the above equation. The data set (0.01134, 0.063, 1.60, -1.0) gives a correlation coefficient for the prediction of 0.964 (an indicator for a satisfactory correlation). Therefore, the new correlation equation can be stated as:

$$Nu_t = 0.01134 (1 - \varepsilon) \left(\frac{u^2}{d_p^3 \rho_s^2 g}\right)^{0.063} (Re_t)^{1.60} (Re_p)^{-1.0} P_r^{0.3} \qquad [7.5]$$

Figure 131 on page 338 shows plots predictions of Equation 7.5 versus experimental values. The solid line in Figure 130 on page 337 also represents the prediction of this equation for the 335-μm Master Beads at different gas velocities. Both figures give evidence of the quality of Equation 7.5. Since we have only twenty-five experimental data points, further studies are still required to justify the new proposed equation. However, the variety of the experimental conditions we have carried out (especially for the particle density and particle diameter) supports the value of the correlation, even though it must be regarded as preliminary. Another aspect of the shallow fluidized-bed heat-transfer research worth exploring would be correlations correlations for the jet-affected and free-board regions.

Comparison of different correlations for the heat-transfer coefficient of particle P-A-3

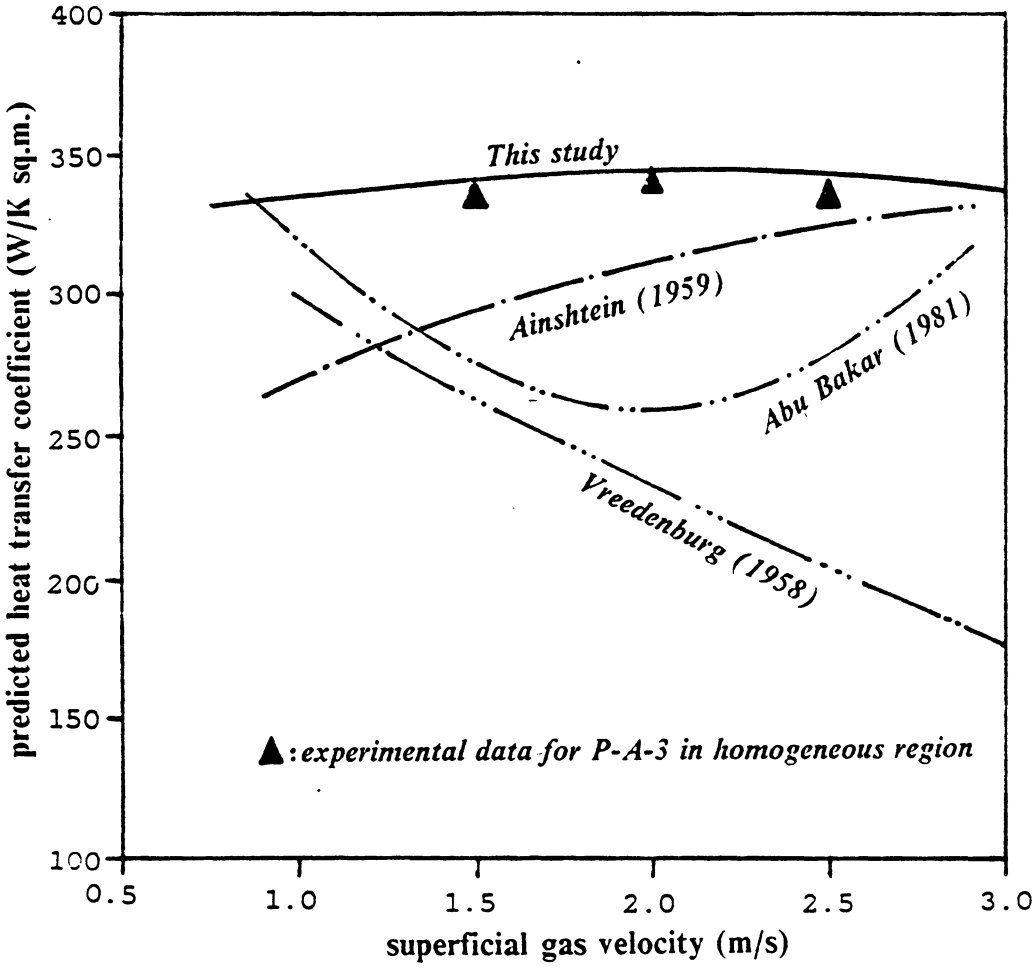

Figure 130. Comparison of correlations for heat-transfer coefficient

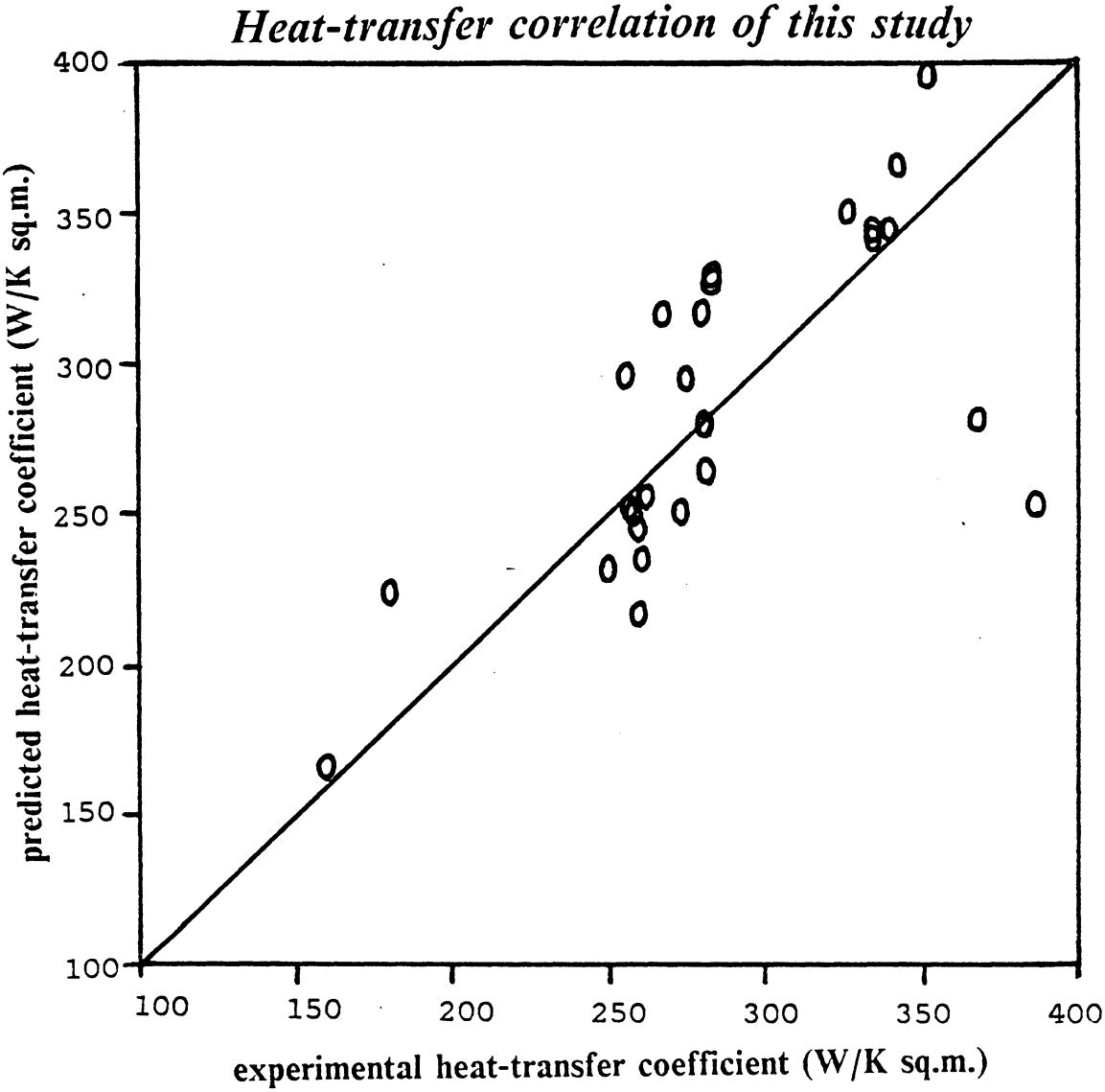

Figure 131. Comparison of the predicted and experimental heat-transfer data

7.5 Heat transfer of Group A particles in shallow fluidized beds

From a review of all of the literature on shallow fluidized-bed heat transfer, we are aware of only a single set of preliminary bed-to-surface heat-transfer data in the dissertation of Abu Bakar (1981) for a relatively fine powder, activated charcoal (average diameter = 165 μm and particle density = 900 Kg/m^3) displaying characteristics similar to Geldart's Group A solids. Abu Bakar's experiments were done with a perforated distributor of 0.64% open area ratio with orifices of 1.78-mm diameter. His fluidized bed had an inside diameter of 278 mm, and his heat probe was 277-mm long and 30-mm in outside diameter.

Abu Bakar's original data for activated charcoal particles are not sufficiently well presented in his thesis to allow one to evaluate the effects of key hydrodynamic regimes and certain independent variables in shallow bed heat-transfer with Group A solids. For example, superficial gas velocities used in Abu Bakar's experiments were not fixed to common values to permit an easy comparison of effects of other independent variables. An analysis and interpolation of Abu Bakar's data and our results for FCC powder has revealed some interesting and anomalous heat-transfer behavior.

Figure 132 on page 340 reproduces data on bed-to-surface heat-transfer coefficients in shallow fluidized beds from Abu Bakar's dissertation (1981). A notable feature shown by all data curves is that the heat-transfer coefficients drops sharply to small values at positions close to the distributor. Also included in the figure are two dashed lines labeled "jet region" and "jet-affected region" based on the jet penetration depths estimated by the correlation in Chapter 5. It can be seen that all estimated jet penetration depths are smaller than the heat-transfer tube elevations at which the heat-transfer coefficients are smallest. This result implies that the heat-transfer coefficients for fine activated-charcoal particles, a Group A solid, are actually not enhanced (increased) by the jet-penetration effect in both the jet region and

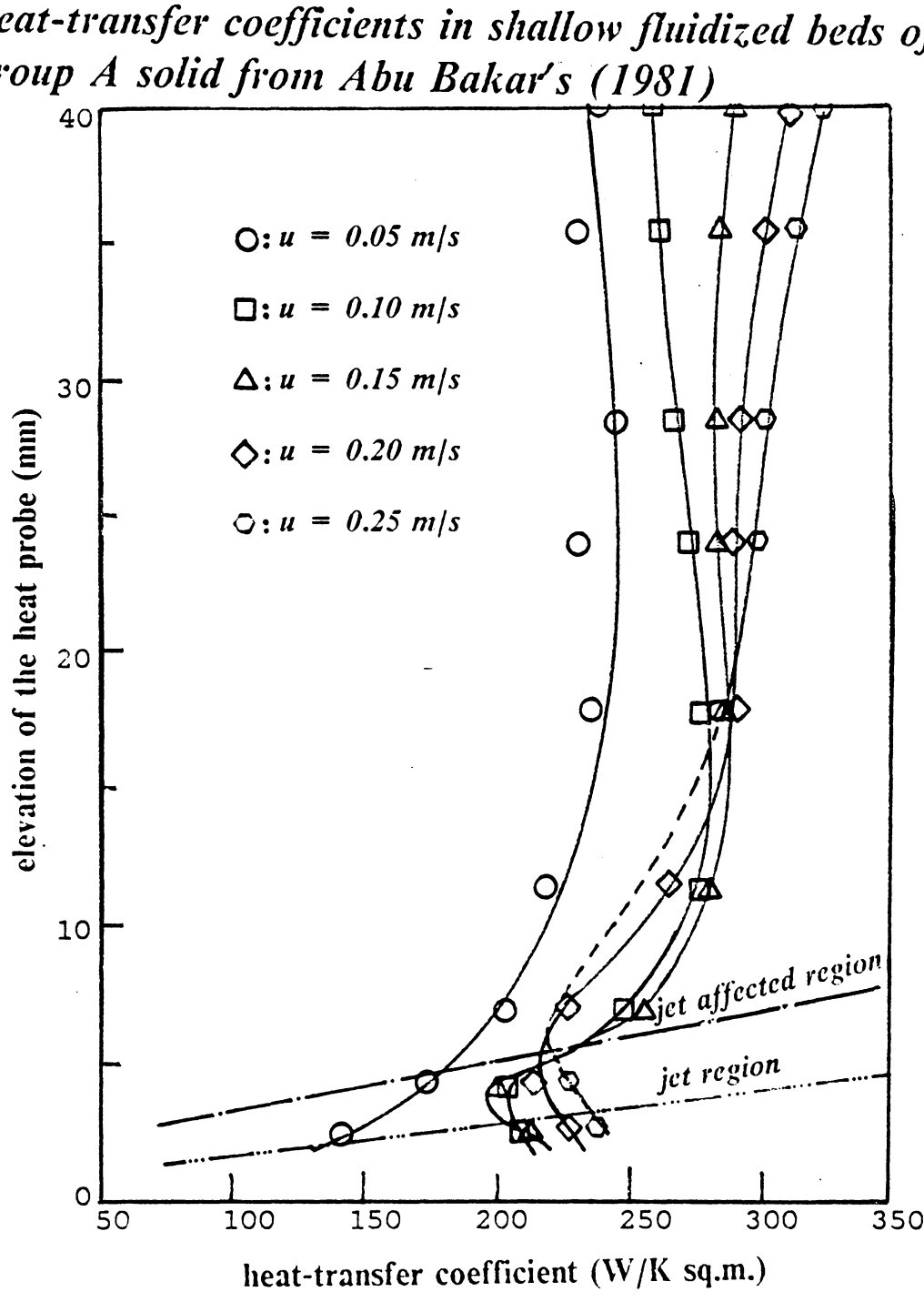

Figure 132. Heat-transfer data for a Group A powder from Abu Bakar's thesis

the jet-affected region. This is contrary to the enhanced bed-to-surface heat transfer in the jet region previously noted for relatively coarse solids, namely, Group B/D solids.

A preliminary study of heat-transfer for FCC (fluid cracking catalyst) powder revealed is serious static electricity problem for the study of this fine powder (the average particle diameter $\cong 71\,\mu m$). Since the building air we used to fluidize the particles had a relatively low humidity of about 10%, the static problem can be anticipated from a reading of existing literature. The static electricity phenomenon could be observed clearly by looking at the heat probe when it is elevated to the vicinity of bed surface. Usually, a layer of FCC powder will stick on the probe surface for a period of 1-2 seconds before the splash of the bed surface pulls it off. All fluidized bed heat-transfer theories suggest that existence of this powder layer will "insulate" the heat probe and therefore lower the heat-transfer coefficient between bed and probe surface. The static electricity problem can be further confirmed by the "sticky" behavior of the bed with FCC powder.

A humidifier was installed between the rotameter and windbox on the air supply line to increase the humidity of the fluidizing air. All of our experimental heat-transfer data for the FCC powder have been collected at a relative humidity of 100%.

Figure 133 on page 342 and Figure 134 on page 343 compare FCC heat-transfer data for wet and dry air (relative humidity, 100% and 10% respectively). Both figures represent the same fixed experimental conditions except for the superficial gas velocity. The data in Figure 133 on page 342 are for a superficial gas velocity of 0.1 m/s, while Figure 134 on page 343 is for a gas velocity of 0.2 m/s. Note that the minimum fluidizing velocity of FCC powder is about 0.02 m/s. In order to minimize the effect of static electricity produced by a high shear of particles near the gas distributor, a laminated distributor (D-4) has been used with FCC powder to suppress the vigorous solid mixing created by gas jets.

Some observations can be summarized from a comparison of the heat-transfer coefficients for FCC powder with wet and dry fluidizing air:

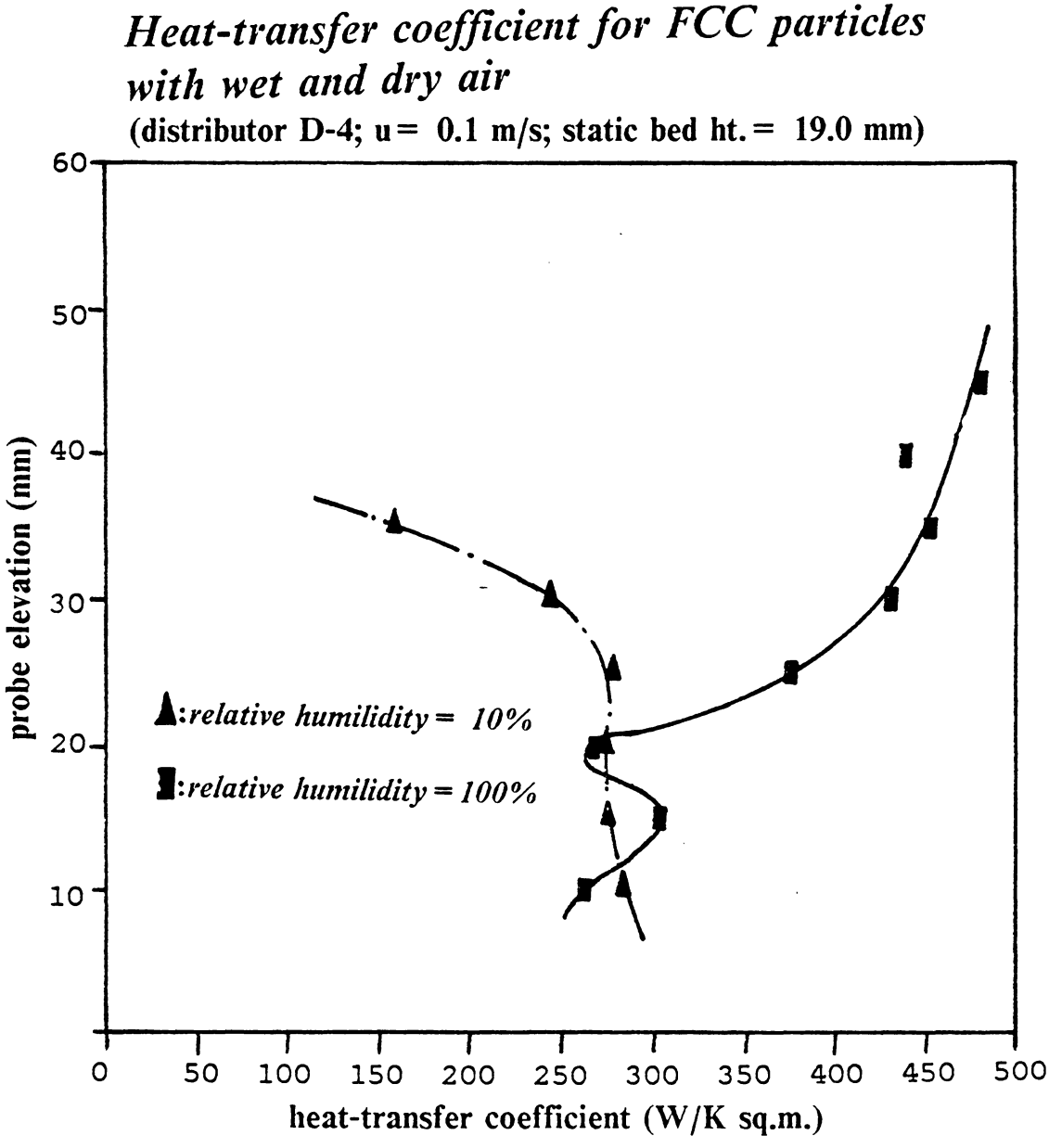

Figure 133. Heat-transfer data for FCC powder obtained with dry and wet air at u = 0.1 m/s

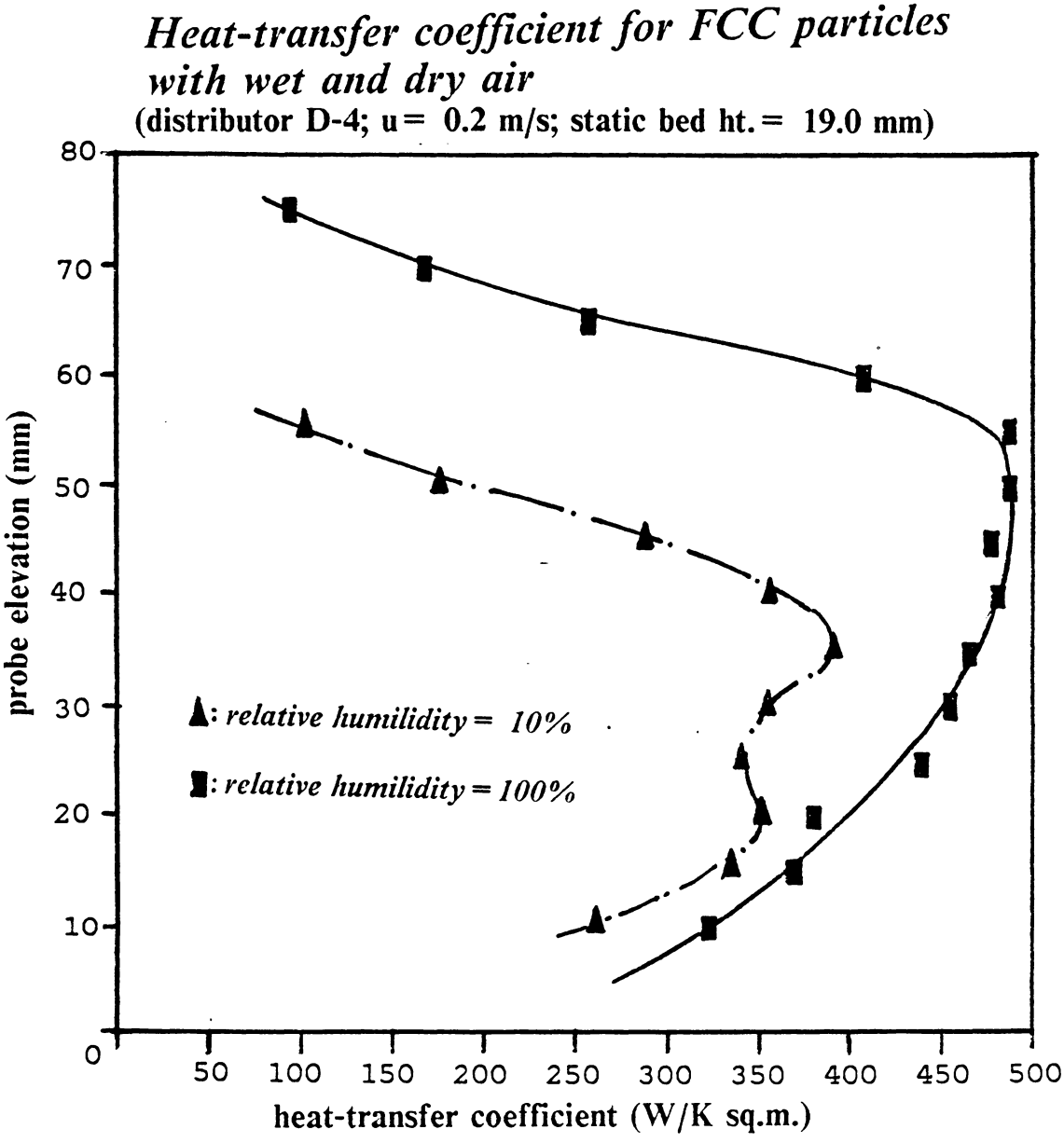

Figure 134. Heat-transfer data for FCC powder with dry and wet air at u = 0.2 m/s

1. The bed expansion for the bed with wet air is greater. Accordingly, a greater space is available for heat transfer. By eliminating the "stickiness" that results from static electricity, the FCC powder can be fluidized "more freely".

2. The bed with wet air affords better heat transfer. By increasing the relative humidity from 10% to 100%, we have raised the maximum heat-transfer coefficient by 35% (in Figure 133 on page 342) or even 60% (in Figure 134 on page 343). This effect can also be explained by the elimination of the static electricity problem and the improved fluidization behavior of the bed.

Figure 135 on page 345 shows the heat-transfer curves for FCC powder in a bed at 19.0-mm static bed height, fluidized by wet air (relative humidity = 100%) via a laminated distributor (D-4). Data are presented for four different superficial gas velocities: 0.1, 0.2, 0.25, and 0.3 m/s.

As many workers have reported, entrainment of particles from a fluidized bed of a Group A powder can become serious after the superficial gas velocity exceed 10 to 20 times the minimum fluidizing velocity. In our experiments, appreciable the entrainment appeared when the gas velocity reached 0.2 m/s. Rubber sheets of a 0.2-m width have been used to form a cone shape on top of the fluidized rig to serve as a temporary substitute for a cyclone. This has enabled us to increase the superficial gas velocity to 0.3 m/s without serious loss of powder. However, the amount of FCC powder carried out of the bed by the air stream still becomes a serious problem as the gas velocity is increased still further.

Data in Figure 135 on page 345 demonstrate some features of the heat-transfer coefficients for a Group A powder that are not commonly seen for Group B particles:

1. Like the data from Abu Bakar's (1981) (see Figure 130 on page 337), data from the bottom section of the bed display poor bed-to-surface heat transfer. In our previous discussion of heat transfer in the jet region for Group B particles, we have stated that two factors influence the heat-transfer mechanism in the jet region:

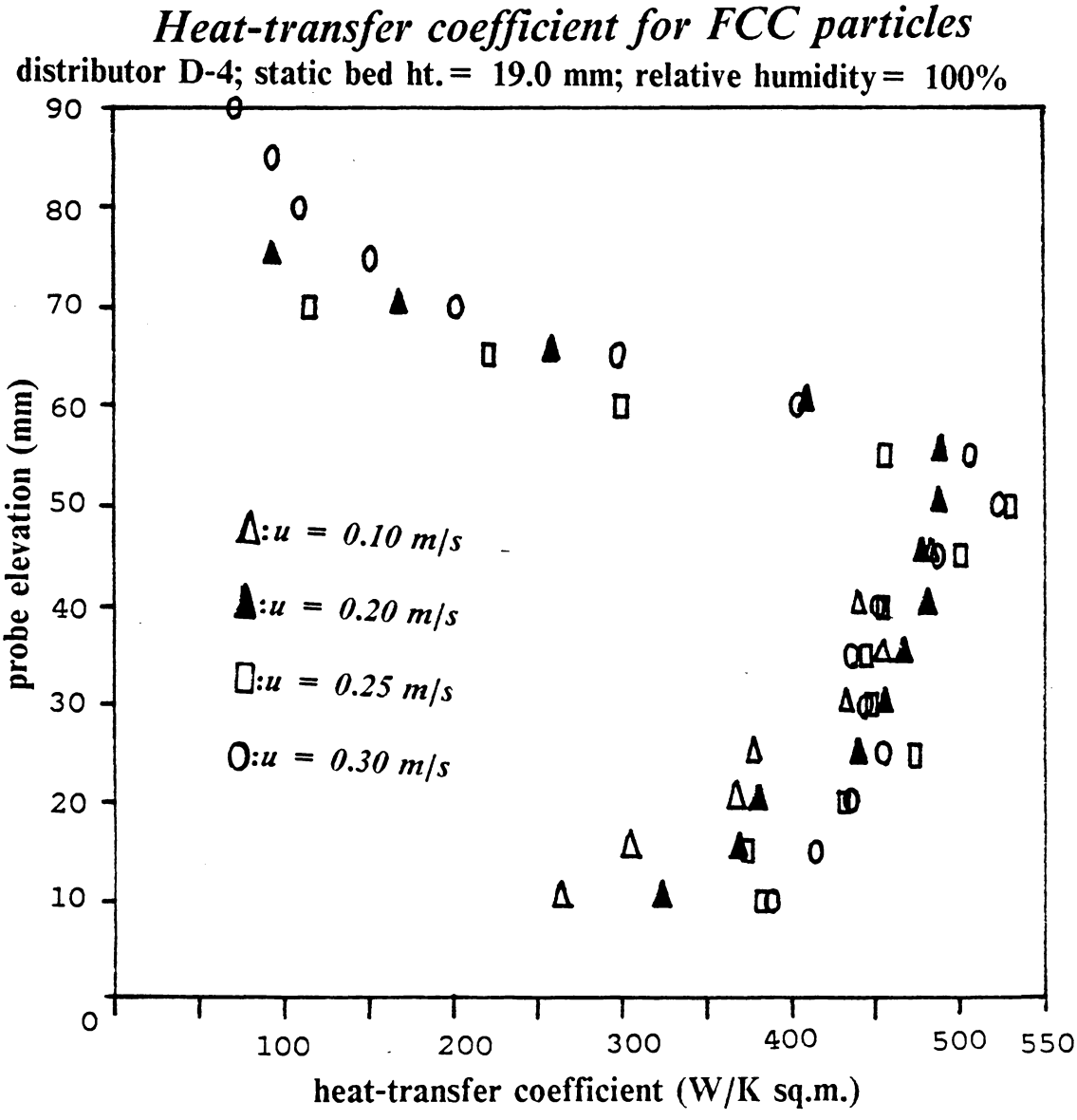

Figure 135. Heat-transfer data for FCC powder at several gas velocities

a. vigorous circulation of the particles and high frequency of the pulsation (a factor increasing the heat-transfer coefficient)

b. increase in porosity of the bed (a factor decreasing the heat-transfer coefficient)

For Group B particles, the gain from solid mixing (particle circulation and pulsation) overcomes effects from the increase of bed porosity, and hence the heat-transfer coefficient in the jet region is enhanced. However, the trend appears to go in an opposite direction for a Group A powder, according to the curves of Figure 135 on page 345.

2. Even though they might not be very smooth, the heat-transfer coefficient curves increase almost monotonically with increasing elevation of heat probe. Checking the solid movement in the free-board region, we can easily conclude that the splashing of particle "clusters" near the bed surface tends to increase heat-transfer coefficient dramatically for a Group A powder.

3. Comparing the heat-transfer data in the upper and bottom regions in shallow fluidized beds, we can propose a fundamental difference between the heat-transfer mechanisms for Group A and Group B particles. For Group B particles, the vigor of the solid mixing can be the most important factor in setting the heat-transfer coefficient. However, the role of the bed voidage and a tendency to cluster (and, in an experimental situation, static electricity) become the more important variables as the particle size and density decrease, so that the particle classification shifts from Geldart's Group B to Group A. A systematic research covering the full range between a particle type that is dominately Group B and a type that is dominately Group A could provide interesting information.

It is worth mentioning that heat-transfer coefficients for FCC powder can reach 500 $W/K\,m^2$. This must be compared with the 250 to 350 $W/K\,m^2$ that we have observed for Group B particles. This comparison is in accord with predictions from most theories and

correlations, which produce an increase in heat-transfer coefficient as the particle diameter decreases.

CHAPTER 8 SUMMARY AND RECOMMENDATIONS

Summary

1. Based upon their physical appearance, shallow fluidized beds have been categorized into nine different types. Regions in which the several types appear can be plotted on a "phase diagram" -- i.e., a plot of superficial gas velocity versus static bed height in which lines are drawn showing transitions among the various types. A minimum gas velocity and a minimum bed height have been identified for the appearance of a zone of "smooth" homogeneous fluidization.

2. A specially-designed manometer has allowed us to measure the pressure drop and pressure distribution in shallow fluidized beds with the elimination of pressure fluctuations caused by the bubbling.

3. Correlations for predicting the pressure drop across a shallow fluidized bed have been proposed. The pressure drop across a fluidized-bed system can be reduced dramatically by dividing a single deep bed into many multi-staged shallow fluidized beds.

4. Pressure distribution data have provided information about hydrodynamic features of fluidized beds, such as bed expansion ratio, jet penetration depth, and identification of different regions in shallow fluidized beds.

5. An equation for estimating the distance of penetration of both single and multiple jets has been proposed. It is a modification of correlations that appear in the literature.

6. A light probe has been developed for measuring particle volume-fraction "at a point" -- i.e., in a narrow region -- in a shallow fluidized bed. Two calibration procedures are in good accord. The light probe is a powerful tool to study the local particle distribution and fluctuations in shallow fluidized beds.

7. Particle volume-fraction and particle fluctuation-ratio data have provided information on the hydrodynamic behavior of shallow fluidized beds, including: (a) quantitative distinctions for different types of shallow fluidized beds; (b) relative magnitude of solid mixing; (c) bed surface and bed height; (d) jet penetration and effects of gas bubbles.

8. Based upon our observations of the hydrodynamic behavior of shallow fluidized beds, we can infer that only three types of shallow beds may practicably be specified for heat-transfer applications. Each of these bed types display three regions: a jet-affected region near the bottom; a free-board region near the top; and a homogeneous region sandwiched in between. Only heat-transfer coefficients in the homogeneous region behave in a sufficiently regular manner to become subjects for correlation with fluidization variables, such as particle and gas properties, static bed height, and gas velocity. A correlation of these heat-transfer coefficients has been presented. It is a modification of correlations from the literature.

9. For Group B particles, the vigor of solid mixing can be the most important factor in determining the heat-transfer coefficient. Bed voidage and static electricity effects can be-

come important in influencing heat transfer for smaller and/or lighter particles of Group A.

10. Hydrodynamic and heat-transfer characteristics are independent of design and scale of the fluidized bed as long as the bed is not "too narrow."

Recommendations for further work

1. Distinctions among the nine types of shallow fluidized beds depend upon visual observation at this stage of our research. However, a careful scrutiny of particle volume-fraction distribution data may provide better criteria for distinguishing among the nine types. With more reliable type-identification criteria and better theoretical description of the behavior of gas bubbles and voids, one might hope to to derive correlations for predicting the location of boundaries on the phase diagram.

2. We have calibrated our light probe only for Master Beads, which have relatively ideal properties: spherical shape and black in color. It would be desirable to extend our two calibration procedures to irregular and/or white or colored particles.

3. Since the measurement of volumetric particle density distribution is more precise than the record of pressure distribution, jet penetration values estimated from from light-probe data could be more convincing than data we are now able to provide. However, the size of the light probe might have to be reduced markedly to minimize its disturbance on the jets.

4. The correlation equation for heat-transfer coefficient that we propose in Chapter 7 is limited to the homogeneous region. Additional studies might make it possible for us to derive the correlation for the heat-transfer of both free-board and jet regions.

5. We have studied only one Group A powder (FCC particles, 71 μm). The work should be extended to other Group A solids, and it would be interesting to obtain data for a series of particles forming a bridge between one that is definitely Group B to a second, like FCC, that is definitely Group A. To permit additional studies of Group A solids, cyclones would have to be provided to retain powder entrained from a fluid bed, and filters would have to be provided beyond the cyclones to prevent residual powder from entering the laboratory.

Nomenclature

Symbol	Definition
A^*	a constant (see. Eq. 2.34), dimensionless.
A_b	cross-sectional area of a fluidized bed, m^2.
A_c	characteristic area of a particle ($= \pi d_p^2/4$), m^2 .
A_m	cross-area of manometer, m^2.
A_p	surface area of a particle, m^2.
A_p^*	maximum horizontal area of a particle, m^2.
A_s	area of heat-transfer surface, m^2.
A_t	surface area of heat-transfer tube, m^2.
a	acceleration of the fluid in a manometer, $\frac{m}{s^2}$.
B^*	a constant ($= \frac{u_f^*}{u_{mf}}$), dimensionless.
B_0	constant in the correlations for jet penetration, dimensionless.
B_1	constant in the correlations for jet penetration, dimensionless.
B_2	constant in the correlations for jet penetration, dimensionless.
B_3	constant in the correlations for jet penetration, dimensionless.
B_4	constant in the correlations for jet penetration, dimensionless.
C^*	a constant (see. Eq. 3.2), dimensionless.
C^{**}	a constant (see. Eq. 3.3), dimensionless.
C_b	correlation factor in Eq. 2.47, dimensionless.
C_D	drag coefficient, dimensionless.
C_e	heat capacity of the packet of emulsion, $\frac{J}{kg\,K}$.
C_g	heat capacity of the gas, $\frac{J}{kg\,K}$.
C_o	orifice coefficient, dimensionless.
C_o^*	a constant (see Eq. 4.13), dimensionless.

Symbol	Definition
C_s	heat capacity of the solids, $\frac{J}{kg\,K}$.
C_1	a constant (in Eq. 2.35), dimensionless.
C_2	a constant (in Eq. 2.35), dimensionless.
C_3	a constant (in Eq. 2.35), dimensionless.
D_b	diameter of the fluidized bed, m.
d_A	characteristic diameter of a particle, m.
d_o	orifice diameter, m.
d_p	particle average diameter of particles, m.
d_t	diameter of heat-transfer tube, m.
d_v	volume of the space confined in light probe, m^3.
Fr	Froude number ($= \frac{\rho_f}{\rho_s - \rho_f}\frac{u^2}{gD}$), dimensionless.
f_d	$(= P_r + f_b)$, $\frac{N}{m^2}$.
G	volumetric flow rate of the gas, $\frac{m^3}{s}$.
Ga	Galileo number, $= \frac{d_p^3 \rho_f (\rho_s - \rho_f)\, g}{\mu_f^2}$. dimensionless.
G_m	volumetric flow rate at the minimum fluidizing condition, $\frac{m^3}{s}$.
g	acceleration due to gravity, $9.8\frac{m}{s^2}$.
$g(V)$	a function defined in Eq. 6.3, dimensionless.
H	bed height, m
H_f	fluidized-bed height, m
H_r	bed expansion ratio $(= \frac{H_f}{H_s})$, dimensionless.
H_s	static bed height, m.
H_s^*	static bed height with respect to p^*, m.
$H_{s'}$	critical static bed height beneath which $u_c = 0$, m.
H_t	elevation of the heat-transfer tube, m.

Symbol	Definition
h_b	heat-transfer coefficient between bubbles and the surface, $\frac{W}{m^2K}$.
h_c	heat-transfer coefficient $\frac{W}{m^2K}$.
h_e	heat-transfer coefficient in emulsion phase, $\frac{W}{m^2K}$.
h_f	heat-transfer coefficient in fluidized-bed, $\frac{W}{m^2K}$.
h_i	local instantaneous heat-transfer coefficient, $\frac{W}{m^2K}$.
h_L	local time-averaged heat-transfer coefficient, $\frac{W}{m^2K}$.
I	current passing the heat probe, amp.
I_{ab}	intercept for the line separating type A and B beds in phase diagram, m.
I_{bc}	intercept for the line separating type B and C beds in phase diagram, m.
K	a constant (see Eq. 3.13), dimensionless.
K_A	a constant ($= \frac{u_t^*}{u_t}$), dimensionless.
K_o	a constant (see Eq. 5.3), dimensionless.
K_s	volumetric shape factor of a particle, dimensionless.
K_V	characteristic kinetic energy per unit volume ($= \rho_f u^2/2$), $\frac{kg}{m\,s}$.
k_e	thermal conductivity of the packet, $\frac{W}{m\,K}$.
k_e^o	thermal conductivity between packed bad and fluid, $\frac{W}{m\,K}$.
k_g	thermal conductivity of the gas, $\frac{W}{m\,K}$.
k_s	thermal conductivity of the solids, $\frac{W}{m\,K}$.
L	length of the heat transfer tube, m.
L_j	jet penetration depth, m.
L_m	loaded length of manometer, m.
l_e	thickness of the layer of emulsion, m.
m	number of particles, dimensionless.

Symbol	Definition
N	variable used for the calculation of Re_t (see Eq. 2.4), dimensionless.
N_D	Nusselt number based on particle diameter ($= h_f d_t / k_g$), dimensionless.
Nu_p	Nusselt number based on tube diameter ($= h_f d_t / k_g$), dimensionless.
Nu_t	variable in the Richardson-Zaki correlation (Eq. 2.5), dimensionless.
n	a positive number in two-phase theory (see Eq. 2.12), dimensionless.
n_p	a constant (see Appendix C), dimensionless.
P	pressure loss recovered (see Eq. 4.9), $\frac{N}{m^2}$.
Q	heat-transfer rate, W.
Q_b	volume of bubbles, m^3.
q_i	heat flow rate into the packet of emulsion, W.
R_h	wetted perimeter, m.
R_2	resistance of the power resistor, Ω.
S_{ab}	slope for the line separating type A and B beds in phase diagram, s.
S_{bc}	slope for the line separating type B and C beds in phase diagram, s.
T_b	bed temperature, C.
T_0	temperature of thermocouple label-0, C
T_1	temperature of thermocouple label-1, C
T_2	temperature of thermocouple label-2, C
t_c	dimensionless residence time (in Eq. 2.26), dimensionless.
t_e	contact time between heat-transfer surface and a packet of emulsion, s.
t_{fb}	fraction of the time heat-transfer surface covered by bubbles, dimensionless.
U_r	flow velocity in the r-direction around a bubble, $\frac{m}{s}$.
U_θ	flow velocity in the θ-direction around a bubble, $\frac{m}{s}$.
u	superficial gas velocity, $\frac{m}{s}$.

Symbol	Definition
u_A	characteristic velocity ($= u - u_{mf} + u_B$), $\frac{m}{s}$.
u_B	raising velocity of a bubble, $\frac{m}{s}$.
u_c	critical characteristic velocity (see Eq. 3.12), $\frac{m}{s}$.
u_f^*	minimum smoothly fluidizing velocity, $\frac{m}{s}$.
u_g	gas flow velocity, $\frac{m}{s}$.
u_{mb}	minimum bubbling velocity, $\frac{m}{s}$.
u_{mf}	minimum fluidizing velocity, $\frac{m}{s}$.
u_o	fluid velocity through the orifice, $\frac{m}{s}$.
u_p	velocity of the gas stream passing through the fluidized bed, $\frac{m}{s}$.
u_s	solid velocity, $\frac{m}{s}$.
u_{sl}	rising velocity of the slug, $\frac{m}{s}$.
u_t	terminal velocity of a particle, $\frac{m}{s}$.
u_t^*	terminal velocity of a particle in an assemblage, $\frac{m}{s}$.
V	voltage, *volts*.
V_b	volume of a particle, m^3.
W_p	weight of particles inside confined space, *grams*.
x_o	maximum displacement of vibro-fluidizing system, *m*.
Y	response ratio (see Eq. 4.6), dimensionless.
y	half of the height-difference of two ends of manometer, *m*.
z	a constant (see Eq. 2.34), dimensionless.
α	constant in determining pressure recovery ratio, dimensionless.
α_1	constant in the calculation of u_{mf}, dimensionless.
α_2	constant in the calculation of u_{mf}, dimensionless.
β	ratio of orifice diameter to bed diameter, dimensionless.

Symbol	Definition
β	a constant in determining pressure recovery ratio, dimensionless.
ΔP	pressure drop across a fluidized bed, $\frac{N}{m^2}$.
ΔT	temperature difference between heat-transfer surface and fluidized bed, K.
δ_f	thickness of the gas film, m.
δ_L	extent of the contact zone adjacent to the heat surface, m.
δ_o	a constant (see Eq. 7.4), dimensionless.
δ_R	ratio of particle diameter versus bed diameter, dimensionless.
δP	pressure drop across a bed, $\frac{N}{m^2}$.
δP_m	pressure difference in manometer, $\frac{N}{m^2}$.
Γ	dimensionless group in Eq. 3.12, dimensionless.
Γ'	dimensionless group in Eq. 3.11, dimensionless.
ε	voidage of fluidized bed, dimensionless.
ε_f	voidage of fluidized bed, dimensionless.
ε_{mf}	voidage of a bed at minimum fluidizing condition, dimensionless.
ε_{sl}	voidage in a slugging bed, dimensionless.
ρ_e	density of the packet of emulsion, $\frac{kg}{m^3}$.
ρ_f	density of the fluid, $\frac{kg}{m^3}$.
ρ_g	density of the gas, $\frac{kg}{m^3}$.
ρ_m	density of the fluid in manometer, $\frac{kg}{m^3}$.
ρ_{mx}	density of the solid-gas mixture, $\frac{kg}{m^3}$.
ρ_r	density ratio ($= \frac{\rho_s - \rho_g}{\rho_g}$), dimensionless.

Symbol	Definition
ρ_s	density of solids, $\frac{kg}{m^3}$.
λ	particle shape factor, dimensionless.
Φ	a pseudo-constant defined in Eq. 3.7, dimensionless.
Φ'	a constant (see Eq. 3.4), dimensionless.
$\Phi(t)$	frequency of packets' occurrence (see Eq. 2.21), $\frac{1}{s}$.
Φ_f	stream function around a bubble, dimensionless.
φ_s	particle sphericity, dimensionless.
σ	a constant (see Eq. 3.14), dimensionless.
σ_k	a constant (see Eq. 4.7), dimensionless.
θ	a constant defined in Eq. 4.5, dimensionless.
τ	contacting time between particle and heat surface, *s*.
τ	time constant (see Eq. 4.5), *s*.
	thermal time constant (see Eq. 2.22), *s*.
τ_w	shear stress between particles and bed wall, $\frac{N}{m^2}$.
μ_f	viscosity of fluid, $\frac{N\,s}{m^2}$.
μ_g	viscosity of gas, $\frac{N\,s}{m^2}$.
μ_f	viscosity of the fluid inside a manometer, $\frac{N\,s}{m^2}$.
ω	angular velocity of vibro-fluidizing system, *s*.

Appendices

Appendix A. Pressure drop across a multi-staged shallow fluidized-bed system

As mentioned earlier in the discussion of the pressure recovery (Chapter 4), an advantage of shallow fluidized beds is their ability to reduce the total pressure drop in a multi-staged operation. A simulation has been carried out to prove that the total pressure of a fluidized-bed system decreases as the number of stages dividing the system increases.

[I]. SIMULATING CONDITIONS:

Particles:

particle density = 1000 Kg/m^3.

particle diameter = 500 μm.

static voidage = 0.4

minimum fluidizing velocity $\cong$ 0.10 m/s.

Fluidizing conditions:

distributor open area = 15%

bed diameter = .1016 m (4 inches)

gas velocity = 0.5 m/s

The amount of particles required (for the whole bed):

= 2000 mm of static bed height.

[II]. The equations used for the simulation

(see Chapter 4 for the details.)

[1] the pressure drop across a distributor:

$$P_d = [\frac{u}{A_r \times 4.034 \times C_o}]^2 \qquad [C.1]$$

where $C_o = 0.8$; A_r is the open area ratio of the distributor.

[2] the pressure drop across the bed:

$$P_b = P_{wt} \times PR \qquad [C.2]$$

Where P_{wt} is the total weight of the particles in a bed divided by the cross area of the bed.

$$PR = \alpha - \frac{\beta}{H_s} \qquad [C.3]$$

$$\alpha = 1 - \frac{\tau_w}{\rho_p R_h (1 - \varepsilon_f)} \qquad [C.4]$$

$$\beta = \frac{f_d}{\rho_p (1 - \varepsilon_s)} \qquad [C.5]$$

and,

$$f_d = 471.54 + 111.05 \times Re + 0.1572 \times F_r \qquad [C.6]$$

where F_r = Froude number for the particle-fluid system, and can be calculated by --

$$F_r = (\frac{u_o^2}{gD})(\frac{\rho_p - \rho_f}{\rho_f})$$

Re = Reynold number for particle near the distributor, usually defined by --

$$Re = \frac{\rho_f d_p u_o}{\mu_f}$$

ρ_f = density of the fluid, Kg/m^3

μ_f = viscosity of the fluid, Kg/m s

g = gravitational constant, 9.8 for S.I. units.

$$\tau_w = 6.49 \times 10^{-5} \rho_r^{1.286} \qquad [C.7]$$

where

$\rho_r = (\rho_p - \rho_f) / \rho_f$ = density ratio.

For details of the above equations, see Chapter 4.

[III]. Results and discussions:

We can divide the fluidized bed into many stages and obtain a smaller total pressure drop across the system. Table A-1 lists the pressure drop across the system and across a single stage versus the number of stages while Figure A-1 gives the plots. Some conclusions can be summarized according to hydrodynamic theory in conjunction with the data presented in the figure and table:

1. Dividing the deep bed into 40 stages of shallow beds will reduce the total pressure drop by about 43%. This has been one of the advantages of shallow beds (with 40 stages) over the deep bed (only one stage).

2. For catalytical reactions, the use of multi-stage operation will also eliminate the by-pass problem caused by gas bubbles in many deep beds.

3. The multi-stage operation allows us to control the bed temperature more precisely.

Table A-1. The pressure drop across a multi-staged shallow fluidized-bed system

(pressure in mm of water)

No. of stages	Pressure drop for one stage (including distributor)	pressure drop across the system
1	1119.7	1119.7
2	553.7	1107.4
4	270.7	1082.8
8	129.2	1033.6
12	82.1	985.2
16	58.5	936.0
20	44.3	886.0
24	34.9	837.6
28	28.1	786.8
32	23.1	739.2
36	19.2	691.2
40	16.0	640.0

Figure A-1. The number of stages versus the pressure drop across the multi-staged shallow fluidized-bed system

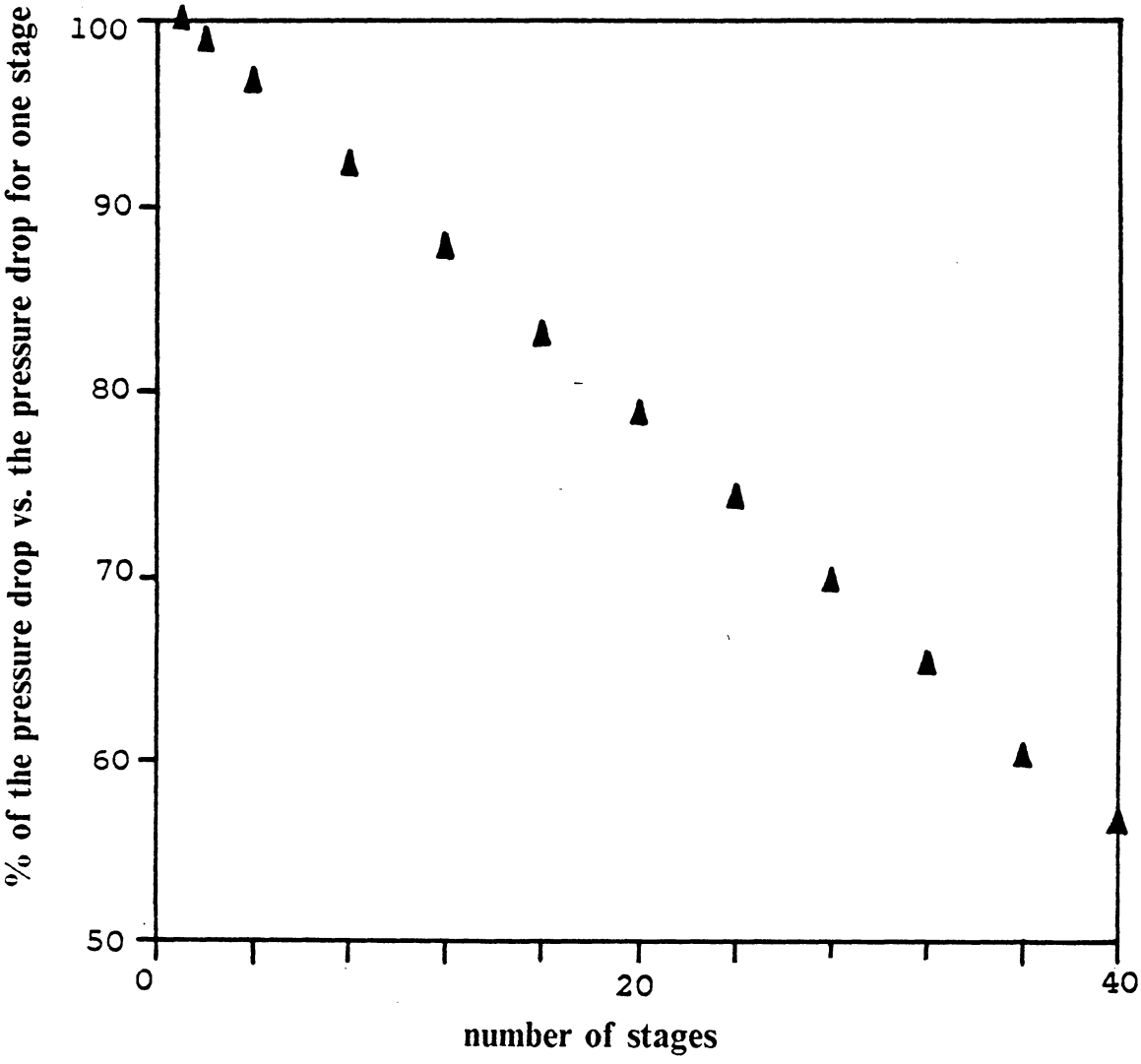

APPENDIX B. BASIC program for the DT2801 data acquistion board in IBM PC

```
10  ''
20  '' THE DT2801 INTERFACING COMMANDS FOR GETTING DATA FROM AN
30  '' LIGHT PROBE.  -- USING CHANNEL 0 ALL THE WAYS
40  ''
50    DEFINT A-Z
60    BASE.ADDRESS       = &H2EC
70    COMMAND.REGISTER   = BASE.ADDRESS + 1
80    STATUS.REGISTER    = BASE.ADDRESS + 1
90    DATA.REGISTER      = BASE.ADDRESS
100    COMMAND.WAIT       = &H4
110    WRITE.WAIT         = &H2
120    READ.WAIT          = &H5
130    CSTOP              = &HF
140    CCLEAR             = &H1
150    CERROR             = &H2
160    CCLOCK             = &H3
170    CSAD               = &HD
180    CRAD               = &HE
190    EXT.CLOCK          = &H40
200    EXT.TRIG           = &H80
210    DIM ADL(3000),ADH(3000)
220    DIM VA#(3000),IS(20),BB#(20)
230    DIM X#(500),Y#(500)
240    INPUT "DOING THE CALIBRATION";CA$
250    IF CA$="Y" OR CA$="Y" THEN VO#=10 ELSE VO#=MEAN#
260 VCL#=10/VO#
270    IF CA$="Y" OR CA$="Y" THEN GOTO 370
280 PRINT
290 PRINT "PROGRAM  #1,  SAMPLING RATE= 600 HZ, 10 VOLT MAX."
300 PRINT
310 INPUT "WHAT KIND OF PARTICLE";G1$
320 INPUT "WT. OF PARTICLES( GRAMS)";G2$
330 INPUT "THE SIZE OF PARTICLES (MICRON)";G3$
340 INPUT "THE GAS VELOCITY (M/S)";G4$
350 INPUT "THE PROBE HT. (MM)";G5$
360 INPUT "THE DISTRIBUTOR LABEL";G6$
370 PERIOD#=400000!/600
380 ''
390 '' CHECK FOR LEGAL STATUS REGISTER.
400 ''
410    STATUS = INP(STATUS.REGISTER)
420    IF NOT((STATUS AND &H70) = 0) THEN GOTO 2000
430 ''
440 '' STOP AND CLEAR THE DT2801.
450 ''
460    OUT  COMMAND.REGISTER, CSTOP
470    TEMP = INP(DATA.REGISTER)
480    WAIT STATUS.REGISTER,  COMMAND.WAIT
490    OUT  COMMAND.REGISTER, CCLEAR
```

(continued)

```
500 ''
510 '' WRITE SET CLOCK PERIOD COMMAND.
520 ''
530    WAIT STATUS.REGISTER,  COMMAND.WAIT
540    OUT  COMMAND.REGISTER, CCLOCK
550 ''
560 '' WRITE HIGH AND LOW BYTES OF PERIOD%.
570 ''
580    PERIODH = INT(PERIOD%/256)
590    PERIODL = PERIOD% - PERIODH * 256
600    WAIT STATUS.REGISTER,  WRITE.WAIT, WRITE.WAIT
610    OUT  DATA.REGISTER,    PERIODL
620    WAIT STATUS.REGISTER,  WRITE.WAIT, WRITE.WAIT
630    OUT  DATA.REGISTER,    PERIODH
640 ''
650 '' GET A/D GAIN.
660 ''
670 '' GET NUMBER OF CONVERSIONS TO DO.
680    PRINT
690    INPUT "         NUMBER OF CONVERSION = ";NUM.CONV
700 ''
710 '' SET A/D PARAMETERS COMMAND TO SET UP THE A/D CONVERTER.
720 '' WRITE SET A/D PARAMETERS COMMAND.
730 ''
740    WAIT STATUS.REGISTER,  COMMAND.WAIT
750    OUT  COMMAND.REGISTER, CSAD
760 ''
770 '' WRITE A/D GAIN BYTE.
780 ''
790    WAIT STATUS.REGISTER,  WRITE.WAIT, WRITE.WAIT
800    OUT  DATA.REGISTER,    GAIN.CODE
810 ''
820 '' WRITE A/D START CHANNEL BYTE.
830 ''
840    WAIT STATUS.REGISTER,  WRITE.WAIT, WRITE.WAIT
850    OUT  DATA.REGISTER,    START.CNL
860 ''
870 '' WRITE A/D END CHANNEL BYTE.
880 ''
890    WAIT STATUS.REGISTER,  WRITE.WAIT, WRITE.WAIT
900    OUT  DATA.REGISTER,    END.CNL
910 ''
920 '' WRITE HIGH AND LOW BYTES OF NCONVERSIONS%.
930 ''
940    NUMBERH = INT(NUM.CONV/256)
950    NUMBERL = NUM.CONV - NUMBERH * 256
960    WAIT STATUS.REGISTER,  WRITE.WAIT, WRITE.WAIT
970    OUT  DATA.REGISTER,    NUMBERL
980    WAIT STATUS.REGISTER,  WRITE.WAIT, WRITE.WAIT
990    OUT  DATA.REGISTER,    NUMBERH
```

(continued)

```
1000 '' WRITE READ A/D COMMAND.
1010 ''
1020 PRINT: PRINT
1030 ''
1040    WAIT STATUS.REGISTER,  COMMAND.WAIT
1050    OUT  COMMAND.REGISTER, CRAD
1060 ''
1070 FOR LOOP=1 TO NUM.CONV : WAIT STATUS.REGISTER,  READ.WAIT
1080 ADL(LOOP)=INP(DATA.REGISTER) : WAIT STATUS.REGISTER,READ.WAIT
1090 ADH(LOOP)=INP(DATA.REGISTER) : NEXT LOOP
1100 ''
1110 '' CHECK FOR ERROR.
1120 ''
1130 WAIT STATUS.REGISTER,COMMAND.WAIT : STATUS=INP(STATUS.REGISTER)
1140    IF (STATUS AND &H80) THEN GOTO 1760
1150 ''
1160 '' CALCULATE AND PRINT THE A/D READINGS IN VOLTS.
1170 ''
1180    NCHAN=1
1190    PRINT
1200    SUMVOL#=0!
1210   PRINT: PRINT "   VOLTAGES -----: "
1220 PRINT
1230    APR#=.0459
1240    FOR LOOP = 1 TO NUM.CONV
1250    DATA.VALUE#  = ADH(LOOP) * 256 + ADL(LOOP)
1260 IF DATA.VALUE#>32767 THEN DATA.VALUE#=DATA.VALUE#-65536!
1270 ''
1280    VOLTS# =VCL#*DATA.VALUE#/409.6
1290    VTS#=VOLTS#/10
1300    IF VOLTS# < 7.7 THEN GOTO 1330
1310    DV#=.7173*(1-VTS#^APR#)
1320    GOTO 1390
1330    IF VOLTS# < .1 THEN GOTO 1360
1340    DV#=.00284*EXP(.4793*(10-VOLTS#))
1350    GOTO 1390
1360    DV#=.00284*EXP(.4793*(10-VOLTS#))*(1.8093-8.093*VOLTS#)
1370    IF CNL >= NUMBER.CNLS THEN CNL = CNL - NUMBER.CNLS
1380 ''
1390 ''PRINT USING "####.###";VOLTS#;
1400    IF CA$="Y" OR CA$="Y" THEN VV#=VOLTS# ELSE VV#=DV#
1410    VA#(LOOP)=VV#
1420   SUMVOL#=SUMVOL#+VV#
1430    NEXT LOOP
1440    MEAN#=SUMVOL#/NUM.CONV
1450 '' ASK IF MORE CONVERSIONS ARE DESIRED.
1460 ''
1470 PRINT
1480 PRINT "         MEAN VALUE=" USING "#####.###";MEAN#
1490    IF CA$="Y" OR CA$="Y" THEN GOTO 240
1500 BEEP
1510 PRINT
```

(continued)

```
2000 ''
2010 '' ILLEGAL STATUS REGISTER.
2020 ''
2030    PRINT
2040    PRINT "FATAL ERROR - ILLEGAL STATUS REGISTER VALUE"
2050    PRINT "STATUS REG. VALUE=";HEX$(STATUS);" HEXIDECIMAL"
2060    BEEP : BEEP
2070 ''
2080    PRINT : PRINT
2090 ''
2100   INPUT "          RUN PROGRAM AGAIN (Y/N)";Y$
2110   IF Y$ = "Y" OR Y$ = "Y" THEN RUN
2120   END
2130 SCREEN 1
2140 COLOR 9,1
2150 KEY OFF
2160 CLS
2170 LINE(40,150)-(280,150)
2180 FOR IA=1 TO 10
2190 IA1=24*(IA-1)+46
2200 IA2=IA1+6
2210 IA3=IA2+6
2220 IA4=IA3+6
2230 IAX=IA*4
2240 IP=0
2250 IF IA >2 THEN GOTO 2270
2260 IP=1
2270 IPX=IP+IA*3+4
2280 LOCATE 20,IPX
2290 PRINT IAX
2300 LINE(IA1,148)-(IA1,150)
2310 LINE(IA2,148)-(IA2,150)
2320 LINE(IA3,148)-(IA3,150)
2330 LINE(IA4,146)-(IA4,150)
2340 NEXT IA
2350 FOR IB=1 TO 5
2360 IVY=150-20*IB
2370 IVY1=160-20*IB
2380 LINE(40,IVY1)-(43,IVY1)
2390 LINE(40,IVY)-(45,IVY)
2400 NEXT IB
2410 LOCATE 7,1
2420 PRINT " 1.0"
2430 LOCATE 12,2
2440 PRINT "DV"
2450 LOCATE 22,13
2460 IF YKK=10 THEN GOTO 2490
2470 PRINT "TIME IN .01 SEC."
2480 GOTO 2500
2490 PRINT "TIME IN .1 SEC."
2500 LINE(40,50)-(40,150)
```

(continued)

```
1520    INPUT "DRAW THE FIGURE FOR 0.1 SEC. SCALE ";T$
1530    YKK=10
1540    IF T$="Y" OR T$="Y" THEN GOSUB 2130
1550    KK$=INKEY$
1560    IF KK$="" GOTO 1550
1570    CLS
1580    SCREEN 0,0,0
1590    INPUT "DRAW THE FUGURE FOR 0.01 SEC. SCALE ";T$
1600    YKK=1
1610    IF T$="Y" OR T$="Y" THEN GOSUB 2130
1620    JJ$=INKEY$
1630    IF JJ$="" GOTO 1620
1640    CLS
1650    SCREEN 0,0,0
1660 PRINT
1670    INPUT "MORE CONVERSION WITH THE SAME SAMPLING RATE ";Y$
1680 ''
1690    IF Y$="N" OR Y$= "N" THEN GOTO 1710
1700    IF Y$ = "Y" OR Y$ = "Y" THEN GOTO 640
1710    INPUT "MORE CONVERSION AND CHANGE THE SAMPLING RATE ";Y$
1720    IF Y$="Y" OR Y$= "Y" THEN GOTO 280
1730    PRINT : PRINT : PRINT "     _    READ A/D OPERATION COMPLETE"
1740    GOTO 2080
1750 ''
1760 ''
1770 '' FATAL BOARD ERROR.
1780 ''
1790    PRINT
1800    PRINT "FATAL BOARD ERROR"
1810    PRINT "STATUS REGISTER VALUE IS ";HEX$(STATUS);" HEXIDECIMAL"
1820    PRINT : BEEP : BEEP : GOSUB 1870
1830    PRINT "ERROR REGISTER VALUES ARE:"
1840    PRINT "      BYTE 1 -   ";HEX$(ERROR1);"  HEXIDECIMAL"
1850    PRINT "      BYTE 2 -   ";HEX$(ERROR2);"  HEXIDECIMAL"
1860    PRINT : GOTO 2080
1870 ''
1880 '' READ THE ERROR REGISTER.
1890 ''
1900    OUT  COMMAND.REGISTER, CSTOP : TEMP = INP(DATA.REGISTER)
1910 ''
1920    WAIT STATUS.REGISTER, COMMAND.WAIT
1930    OUT COMMAND.REGISTER, CERROR
1940 ''
1950    WAIT STATUS.REGISTER, READ.WAIT
1960    ERROR1 = INP(DATA.REGISTER)
1970    WAIT STATUS.REGISTER, READ.WAIT
1980    ERROR2 = INP(DATA.REGISTER)
1990    RETURN
```

(continued)

```
2510 X%(1)=40
2520 Y%(1)=150-VA%(1)*100
2530 FOR LK=2 TO 241
2540 LS=LK-1
2550 X%(LK)=LS+40
2560 LKS=LK*YKK
2570 Y%(LK)=150-VA%(LKS)*100
2580 LINE(X%(LS),Y%(LS))-(X%(LK),Y%(LK))
2590 NEXT LK
2600 LOCATE 24,6
2610 PRINT "PARTICLE DENSITIES IN S.F.B.S";
2620 LOCATE 2,7: PRINT G2$;" GRAMS OF ";G3$;" MICRON ";G1$
2630 LOCATE 3,7: PRINT "GAS VELOCITY: "G4$;" M/S"
2640 LOCATE 4,7: PRINT "PROBE HEIGHT: "G5$;" MM"
2650 LOCATE 5,7: PRINT "DISTRIBUTOR : ";G6$
2660 RETURN
```

Appendix C. Derivation of the theoretical calibration curve for the light probe

Assumptions for the calibration

1. Light rays are parallel between LED and photo transistor.

2. There is no deflection of light.

3. The output voltage is linearly proportional to the intensity of the light passing through the particles.

Derivation for the equations

For a small volume of $A_p \times d_p$, the number of particles can be confined inside is --

$$n = \frac{\text{volume that can be occupied}}{\text{volume of one particle}} = \frac{A_p \times d_p \times (1 - \varepsilon)}{(\pi \times d_p^3)/6}$$

The overall projected area for those particles toward the photo transistor is--

$$n \times a = n \times [(\pi d_p^2)/4] = 1.5 \times A_p (1 - \varepsilon)$$

Therefore, the area ratio not covered by the particles in a small distance d_p will be --

$$1 - 1.5(1 - \varepsilon) = 0.5(3\varepsilon - 1)$$

The total area ratio not covered by the particles for the distance between the LED and the photo transistor can be expressed by --

$$[0.5 (3\varepsilon - 1)]^{L/d_p}$$

The output voltage from the photo transistor is 10 Volts when the space between the LED and the transistor is full open and 0 when the space is full closed. By assuming that the output voltage is linearly proportional to the intensity of the light passing through the particles, we can with --

$$V = 10 \times [0.5 (3\varepsilon -)]^{L/d_p}$$

After rearrangement --

$$\varepsilon = \frac{2(0.1V)^{d_p/L} + 1}{3}$$

or,

$$d_v = 1 - \varepsilon = (\frac{2}{3}) \times [1 - (0.1V)^{n_p}]$$

where

$$n_p = \frac{L}{d_p}$$

APPENDIX D. The Pattern search program for the calibration of light probe

```
C*********************************************************************
C                                                                     *
C           FORTRAN PROGRAM USED FOR THE CALCULATION OF               *
C           CALIBRATIONAL FUNCTION OF LIGHT PROBE BY                  *
C           UTILIZING THE PATTERN SEARCH TECHNIQUE                    *
C                                                                     *
C*********************************************************************
C
      DIMENSION MA(13),MT(10,13),WT(10),X(2)
C
C+++++++++++++++++++++++++++++++++++++++++++++++++++++++++++++++++++++
C     READ IN THE DATA FOR THE CALIBRATION                           +
C+++++++++++++++++++++++++++++++++++++++++++++++++++++++++++++++++++++
C
      DO 100 I=1,10
      READ(5,*) WT(I)
      READ(5,*) (MT(I,K),K=1,13)
  100 CONTINUE
C
C+++++++++++++++++++++++++++++++++++++++++++++++++++++++++++++++++++++
C     ASSIGN THE INITIAL GUESS FOR A AND B (X(1) & X(2) HERE         +
C+++++++++++++++++++++++++++++++++++++++++++++++++++++++++++++++++++++
C
      READ(5,*) X(1),X(2)
C
C+++++++++++++++++++++++++++++++++++++++++++++++++++++++++++++++++++++
C     CALL THE PATTERN SEARCH PROGRAM TO FIND THE OPTIMAL VALUES OF  +
C     A AND B                                                        +
C+++++++++++++++++++++++++++++++++++++++++++++++++++++++++++++++++++++
C
      CALL SQPAT(X,MT,WT)
      WRITE(6,200) X(1),X(2)
  200 FORMAT(2X,F9.5,2X,F9.5)
      STOP
      END
      SUBROUTINE SQPAT(X,MY,Z)
C
C  **********************************************************************
C  *  THIS SUBROUTINE IS USED TO FIND OUT THE LEAST SQUARE FITTING      *
C  *  CALIBRATIONAL FUNCTION FOR THE LIGHT PROBE.                       *
C  *  PATTERN( HOOKES AND JEEVE'S) SEARCH METHOD IS USED HERE.          *
C  *  THE FITTING FUNCTION IS:                                          *
C  *                              DV=A*EXP(B*V)                         *
C  *                                                                    *
C  **********************************************************************
```

(continued)

```
C
      DIMENSION DELTA(2),EPSI(2),X(2),MY(10,13),Z(10)
C
C+++++++++++++++++++++++++++++++++++++++++++++++++++++++++++++++++++++++++++++
C     ASSIGN INITIAL GUESS VALUES.                                          +
C+++++++++++++++++++++++++++++++++++++++++++++++++++++++++++++++++++++++++++++
C
      DELTA(1)=0.0002
      DELTA(2)=0.01
      EPSI(1)=0.00002
      EPSI(2)=0.0001
      N=2
      OPT=DIRECT(N,X,DELTA,EPSI,MY,Z)
      RETURN
      END
C
C*****************************************************************************
C*****************************************************************************
C
      FUNCTION F(X,MY,WT)
      DIMENSION MY(10,13),WT(10)
      DIMENSION MA(13),X(2)
      WF=0.0
      DO 200 L=1,10
      DO 150 KK=1,13
      MA(KK)=MY(L,KK)
  150 CONTINUE
      A=X(1)
      B=X(2)
C
C+++++++++++++++++++++++++++++++++++++++++++++++++++++++++++++++++++++++++++++
C     CALL THE SUBROUTINE TO EVALUATE THE TOTAL WEIGHT OF PARTICLES  +
C+++++++++++++++++++++++++++++++++++++++++++++++++++++++++++++++++++++++++++++
C
      CALL FINT(A,B,MA,WWT)
      WW=WWT-WT(L)
      WS=WW*WW
      WF=WF+WS
  200 CONTINUE
      F=WF
      RETURN
      END
      SUBROUTINE FINT(A,B,MA,WWT)
C
C*****************************************************************************
C                                                                            *
C     SUBROUTINE USED TO EVALUATE THE TOTAL AMOUNT OF PARTICLES BY   *
C     USING THE GIVEN DATA FORM THE OUTPUT OF LIGHT PROBE.           *
C                                                                            *
C*****************************************************************************
C
```

(continued)

```
      DIMENSION MA(13),DV(13)
      DO 100 I=1,13
      BV=B*MA(I)/1000.0
      E=EXP(BV)
      DV(I)=A*E
  100 CONTINUE
C
C+++++++++++++++++++++++++++++++++++++++++++++++++++++++++++++++++++++++++++++
C     SIMPSON RULE IS USED HERE FOR THE INTEGRATION.                        +
C     NOTES:                                                                +
C           1. 13 DATA POINT ARE FIXED AT BED HEIGHT = 1.0 1.5 2.0          +
C              2.5,3,4,5,6,7,8,9,10,11.                                     +
C           2. THE DATA AT 0.0 AND 0.5 ARE INTERPERATED BY USING THE        +
C              VALUE AT 1.0.                                                +
C+++++++++++++++++++++++++++++++++++++++++++++++++++++++++++++++++++++++++++++
C
      WA=7.0*DV(1)+4.0*DV(2)+2.0*DV(3)+4.0*DV(4)+DV(5)
      WB=DV(5)+2.0*(DV(7)+DV(9)+DV(11))+4.0*(DV(6)+DV(8)+DV(10)+DV(12))+
     *DV(13)
      WV=WA/6.0+WB/3.0
      WWT=WV*3.68*81.0732
      RETURN
      END
C
C*************************************************************************
C*************************************************************************
C
      FUNCTION DIRECT(N,X,DELTA,EPSI,MY,Z)
C
C  ***********************************************************************
C  *  THIS FUNCTION IMPLEMENTS THE DIRECT SEARCH METHOD TO FIND A        *
C  *  MINIMUM VALUE FOR THE FUNCTION F, GIVEN APPROPRIATE STARTING       *
C  *  VALUES X, INCREMENTS DELTA, AND TOLERANCES EPSI.                   *
C  ***********************************************************************
C
      DIMENSION X(N),DELTA(N),EPSI(N),B1(20),B2(20),T(20)
      DIMENSION MY(10,13),Z(10)
C
C+++++++++++++++++++++++++++++++++++++++++++++++++++++++++++++++++++++++++++++
C     SET BASE POINT B1 AND CALCULATE FUNCTION VALUE                        +
C+++++++++++++++++++++++++++++++++++++++++++++++++++++++++++++++++++++++++++++
C
      DO 10 I=1,N
   10 B1(I)=X(I)
      FB1=F(B1,MY,Z)
C
C+++++++++++++++++++++++++++++++++++++++++++++++++++++++++++++++++++++++++++++
C     CHECK STARTING POINT FOR FEASIBILITY                                  +
C+++++++++++++++++++++++++++++++++++++++++++++++++++++++++++++++++++++++++++++
C
```

(continued)

```
      IF(FB1.LT.1.E34) GO TO 20
      DIRECT=1.E35
      RETURN
C
C+++++++++++++++++++++++++++++++++++++++++++++++++++++++++++++++++++++++++++++
C     MAKE PATTERN SEARCH AT B1 TO GET B2 AND FB2                           +
C+++++++++++++++++++++++++++++++++++++++++++++++++++++++++++++++++++++++++++++
C
   20 FB2=EXPLOR(N,FB1,B1,DELTA,B2,MY,Z)
C
C+++++++++++++++++++++++++++++++++++++++++++++++++++++++++++++++++++++++++++++
C     CHECK FB1 AND FB2 FOR SUCCESSFUL PATTERN SEARCH                       +
C+++++++++++++++++++++++++++++++++++++++++++++++++++++++++++++++++++++++++++++
C
      IF(FB1.NE.FB2) GO TO 60
C
C+++++++++++++++++++++++++++++++++++++++++++++++++++++++++++++++++++++++++++++
C     PATTERN SEARCH FAILED.  CHECK CONVERGENCE CRITERIA                    +
C+++++++++++++++++++++++++++++++++++++++++++++++++++++++++++++++++++++++++++++
C
      DO 30 I=1,N
      IF(DELTA(I).GT.EPSI(I)) GO TO 40
   30 CONTINUE
C
C+++++++++++++++++++++++++++++++++++++++++++++++++++++++++++++++++++++++++++++
C     ALL DELTA(I) ARE SMALLER THAN EPSI(I). SEARCH IS OVER                 +
C+++++++++++++++++++++++++++++++++++++++++++++++++++++++++++++++++++++++++++++
C
      GO TO 100
C
C+++++++++++++++++++++++++++++++++++++++++++++++++++++++++++++++++++++++++++++
C     SEARCH INCOMPLETE.  HALVE THE DELTA(I) ANC CONTINUE                   +
C+++++++++++++++++++++++++++++++++++++++++++++++++++++++++++++++++++++++++++++
C
   40 DO 50 I=1,N
   50 DELTA(I)=DELTA(I)/2.0
      GO TO 20
C
C+++++++++++++++++++++++++++++++++++++++++++++++++++++++++++++++++++++++++++++
C     MAKE A PATTERN MOVE FROM B1 THROUGH B2 TO T, FIND FT                  +
C+++++++++++++++++++++++++++++++++++++++++++++++++++++++++++++++++++++++++++++
C
   60 DO 70 I=1,N
   70 T(I)=2.0*B2(I)-B1(I)
      FT=F(T,MY,Z)
C
C+++++++++++++++++++++++++++++++++++++++++++++++++++++++++++++++++++++++++++++
C     CHECK FT AND FB2 FOR SUCCESSFUL PATTERN MOVE                          +
C+++++++++++++++++++++++++++++++++++++++++++++++++++++++++++++++++++++++++++++
C
      IF(FT.LT.FB2) GO TO 90
C
```

(continued)

```
C++++++++++++++++++++++++++++++++++++++++++++++++++++++++++++++++++++++++++++++
C     PATTERN MOVE FAILED.  RESET B1 AND START OVER                          +
C++++++++++++++++++++++++++++++++++++++++++++++++++++++++++++++++++++++++++++++
C
      DO 80 I=1,N
   80 B1(I)=B2(I)
      FB1=FB2
      GO TO 20
C
C++++++++++++++++++++++++++++++++++++++++++++++++++++++++++++++++++++++++++++++
C     MAKE A PATTERN SEARCH AT B2 TO GET T AND FT                             +
C++++++++++++++++++++++++++++++++++++++++++++++++++++++++++++++++++++++++++++++
C
   90 FB2=EXPLOR(N,FT,T,DELTA,B2,MY,Z)
      GO TO 60
C
C++++++++++++++++++++++++++++++++++++++++++++++++++++++++++++++++++++++++++++++
C     SET COORDIANTES OF EXTREME POINT.  RETURN MINIMUM VALUE                 +
C++++++++++++++++++++++++++++++++++++++++++++++++++++++++++++++++++++++++++++++
  100 DO 110 I=1,N
  110 X(I)=B1(I)
      DIRECT=FB1
      RETURN
      END
C
C*******************************************************************************
C*******************************************************************************
C
      FUNCTION EXPLOR(N,FP1,P1,DELTA,P2,MY,Z)
C
C  ***************************************************************************
C  *  THIS FUNCTION CARRIES OUT A PATTERN SEARCH ABOUT THE POINT             *
C  *  P1 WITH FUNCTION VALUE FB1.  THE INCREMENT IN VARIABLE I IS            *
C  *  GIVEN BY DELTA(I),AND THE FINAL POINT IS P2                            *
C  ***************************************************************************
C
      DIMENSION P1(N),P2(N),DELTA(N),MY(10,13),Z(10)
C
C++++++++++++++++++++++++++++++++++++++++++++++++++++++++++++++++++++++++++++++
C     INITIALIZE P2 AS P1,  SET SAVE=FP1                                      +
C++++++++++++++++++++++++++++++++++++++++++++++++++++++++++++++++++++++++++++++
C
      DO 10 I=1,N
   10 P2(I)=P1(I)
      SAVE=FP1
C
C++++++++++++++++++++++++++++++++++++++++++++++++++++++++++++++++++++++++++++++
C     INCREMENT P1(I) BY DELTA(I)                                             +
C++++++++++++++++++++++++++++++++++++++++++++++++++++++++++++++++++++++++++++++
C
```

(continued)

```
      DO 40 I=1,N
      P2(I)=P2(I)+DELTA(I)
      FP2=F(P2,MY,Z)
C
C+++++++++++++++++++++++++++++++++++++++++++++++++++++++++++++++++++++++++++++++
C     CHECK FOR BETTER FUNCTION VALUE                                         +
C+++++++++++++++++++++++++++++++++++++++++++++++++++++++++++++++++++++++++++++++
C
      IF(FP2.GE.SAVE) GO TO 20
C
C+++++++++++++++++++++++++++++++++++++++++++++++++++++++++++++++++++++++++++++++
C     BETTER VALUE FOUND                                                      +
C+++++++++++++++++++++++++++++++++++++++++++++++++++++++++++++++++++++++++++++++
C
      SAVE=FP2
      GO TO 40
C
C+++++++++++++++++++++++++++++++++++++++++++++++++++++++++++++++++++++++++++++++
C     FAILURE.   TRY DECREMENTING P1(I) BY DELTA(I)                           +
C+++++++++++++++++++++++++++++++++++++++++++++++++++++++++++++++++++++++++++++++
C
   20 P2(I)=P2(I)-2.0*DELTA(I)
      FP2=F(P2,MY,Z)
C
C+++++++++++++++++++++++++++++++++++++++++++++++++++++++++++++++++++++++++++++++
C     CHECK FOR BETTER FUNCTION VALUE                                         +
C+++++++++++++++++++++++++++++++++++++++++++++++++++++++++++++++++++++++++++++++
C
      IF(FP2.GE.SAVE) GO TO 30
C
C+++++++++++++++++++++++++++++++++++++++++++++++++++++++++++++++++++++++++++++++
C     BETTER VALUE FOUND                                                      +
C+++++++++++++++++++++++++++++++++++++++++++++++++++++++++++++++++++++++++++++++
C
      SAVE=FP2
      GO TO 40
C
C+++++++++++++++++++++++++++++++++++++++++++++++++++++++++++++++++++++++++++++++
C     RESTORE ORIGINAL VALUE OF P1(I)                                         +
C+++++++++++++++++++++++++++++++++++++++++++++++++++++++++++++++++++++++++++++++
C
   30 P2(I)=P2(I)+DELTA(I)
   40 CONTINUE
C
C+++++++++++++++++++++++++++++++++++++++++++++++++++++++++++++++++++++++++++++++
C     RETURN FUNCTIONAL VALUE AT P2                                           +
C+++++++++++++++++++++++++++++++++++++++++++++++++++++++++++++++++++++++++++++++
C
      EXPLOR=SAVE
      RETURN
      END
```

Appendix E. Error analysis for heat-transfer measurements

Some experiments have been carried out to estimate the possible error caused by heat losses through supporting rods and Lexan rings. Table E-1 lists all of the experimental data for this analysis.

Before installing the supporting Lexan rings, the heat-transfer coefficient was determined between the heat probe and the still air surrounding the probe. First column of Table E-1 gives the surface temperature of the probe, temperature of the air, and the power supplied to the probe. Since both ends of the probe were well-insulated, the heat-transfer coefficient can be calculated as --

$$h^* = \frac{Q}{A\,\Delta T}$$

The surface area of the probe is 0.0031919 m^2 (with a 12.7-mm O.D., and 80 mm in length). Therefore --

$$h^* = 15.947\ W/m^2K$$

The same test was repeated after Lexan rings and supporting rods were installed. Two thermocouples inserted on Lexan rings show that the temperature of Lexan rings was very uniform. It was found that most of the heat lost toward Lexan rings would be transferred to the supporting rods and dissipate gradually. With the assumption that the copper section will have the same heat-transfer coefficient as when the rings are absent, the heat lost from the copper section will be --

$$Q^* = 15.947 \times 0.0031919 \times (83.0 - 31.9) = 2.601\ (W)$$

The second column of Table E-1 shows that the heat supplied to the probe is 2.676 *W*. Therefore, the heat lost through Lexan rings will be 0.075 *W* (2.676 - 2.601). We can estimate a heat-transfer coefficient, *U*, between copper section and Lexan ring; thus --

$$U = \frac{Q}{A\Delta T} = \frac{.075}{[\frac{(.0127)^2\pi}{2}](83.0 - 31.9)} = 5.79(W/m^2K)$$

The third column of Table E-1 lists a set of typical heat-transfer data from our study. It has been found that the heat-transfer coefficient between the heat probe and the fluidized bed is 310.4 W/m^2K, neglecting the heat lost toward Lexan rings and supporting rods. However, by assuming that the heat-transfer coefficient between the copper tube and Lexan rings is constant, the heat lost can be estimated as --

$$Q_{lost} = A \times \Delta T \times 5.79 = .027\,(W)$$

By neglecting this heat lost, the error of the heat-transfer coefficient will be --

$$\frac{0.027}{32.5 - 0.027} = 0.0008$$

which is small. This analysis provides only an order of magnitude of the error; but since this error is always smaller than a probable error in reading thermocouples (about .1°*C* reading error for a temperature difference of 30 to 45 °*C*), we can conclude that the error caused by the heat loss to Lexan rings can be neglected.

However, if we assume that the heat transfer between Lexan rings and fluidized bed do exist. The heat-transfer coefficient will be --

$$\frac{0.075}{(\pi \times 0.009 \times 0.0127 \times 2)\,(56.3 - 31.9)} = 4.28\ W/m^2K$$

where (0.009 m) is the length of one Lexan ring.

By assuming the ratio of the heat-transfer coefficient increased for the copper tube and Lexan rings remains constant after particles are added to the bed. The error percentage caused by the Lexan rings can be calculated as --

$$\frac{4.28 \times (0.009 \times 2)}{15.974 \times 80} \times 100\% = 6\%$$

This is relative high in comparing with the previous analysis. Fortunately, that error percentage remains consistent throughout our heat-transfer study. Therefore, our qualitative analysis of the heat-transfer coefficient will not be affected by the heat lost. The correlation we proposed for the heat-transfer coefficient will only be shifted by a factor after the error caused by the heat lost is taken into consideration.

Table E-1 Data from measurements for the error analysis in the heat-transfer study

The error caused by the heat loss toward two ends of the heat probe:

	no particle no support	no particle with support	with particles and support
temperature of the probe	83.1 C	83.0 C	82.5 C
temperature of the surrounding	32.1 C	31.9 C	49.7 C
temperature of the support	----	56.3 C	63.8 C
power input	2.596 W	2.676 W	32.50 W
heat-transfer coefficient (W/sq.m. K)	15.947	15.947	310.4

Appendix F. Experimental conditions for study of pressure drop across shallow beds

Data and experimental conditions for the study of pressure drop across shallow beds

particle	d_p (μm)	*distr.*	A_r	u(m/s)	α	β	R^2
P-A-2	630	D-1	5.6	0.5	0.9623	-0.4333	0.9920
P-A-2	630	D-1	5.6	1.0	0.9634	-0.3817	0.9918
P-A-2	630	D-1	5.6	1.5	0.9435	-0.3571	0.9857
P-A-2	630	D-1	5.6	2.0	0.9325	-0.3995	0.9855
P-A-2	630	D-1	5.6	2.5	0.9441	-0.5662	0.9874
P-A-3	335	D-1	5.6	0.5	0.9692	-0.3831	0.9922
P-A-3	335	D-1	5.6	1.0	0.9387	-0.3477	0.9737
P-A-3	335	D-1	5.6	1.5	0.9104	-0.3248	0.9578
P-A-3	335	D-1	5.6	2.0	0.9241	-0.4057	0.9197
P-S-1	630	D-1	5.6	0.5	0.9627	-0.3502	0.9819
P-S-1	630	D-1	5.6	1.0	0.9234	-0.3083	0.9836
P-S-1	630	D-1	5.6	1.5	0.8937	-0.3312	0.9762
P-S-2	359	D-1	5.6	0.5	0.9082	-0.2390	0.9727
P-C-1	630	D-1	5.6	0.5	0.9475	-0.4685	0.9920
P-G-1	842	D-1	5.6	1.0	0.9523	-0.2769	0.9919
P-G-1	842	D-1	5.6	1.5	0.9511	-0.3672	0.9927
P-G-1	842	D-1	5.6	2.0	0.9428	-0.5928	0.9942
P-G-2	705	D-1	5.6	0.5	0.9684	-0.2995	0.9940
P-G-2	705	D-1	5.6	1.0	0.9608	-0.3795	0.9929
P-G-2	705	D-1	5.6	1.5	0.9302	-0.3959	0.9900
P-G-3	484	D-1	5.6	1.0	0.9200	-0.2816	0.9877
P-G-3	484	D-1	5.6	1.5	0.9015	-0.3138	0.9783
P-G-3	484	D-1	5.6	2.0	0.9049	-0.4277	0.9715
P-G-4	353	D-1	5.6	0.5	0.9334	-0.3151	0.9657
P-G-4	353	D-1	5.6	1.0	0.9087	-0.3038	0.9498
P-A-1	1260	D-2	3.6	1.0	0.9746	-0.4430	0.9916
P-A-1	1260	D-2	3.6	1.5	0.9787	-0.4373	0.9924
P-A-1	1260	D-2	3.6	2.0	0.9728	-0.5949	0.9949
P-A-1	1260	D-2	3.6	2.5	0.9576	-0.8787	0.9970
P-A-1	1260	D-2	3.6	3.0	0.9629	-1.4116	0.9973
P-A-2	630	D-2	3.6	0.5	0.9620	-0.3204	0.9790
P-A-2	630	D-2	3.6	1.0	0.9584	-0.3106	0.9888
P-A-2	630	D-2	3.6	1.5	0.9534	-0.4056	0.9911
P-A-2	630	D-2	3.6	2.0	0.9431	-0.5721	0.9920
P-A-2	630	D-2	3.6	2.5	0.9490	-0.9008	0.9960
P-A-3	335	D-2	3.6	0.5	0.9642	-0.3158	0.9797
P-A-3	335	D-2	3.6	1.0	0.9389	-0.3320	0.9762
P-A-3	335	D-2	3.6	1.5	0.9203	-0.4088	0.9737
P-A-3	335	D-2	3.6	2.0	0.9243	-0.6175	0.9825

(continue --)

particle	d_p (μm)	*distr.*	A_r	u(m/s)	α	β	R^2
P-A-2	630	D-6	9.0	1.0	0.9345	-0.2178	0.9704
P-A-2	630	D-6	9.0	1.5	0.9078	-0.1530	0.9067
P-A-2	630	D-6	9.0	2.0	0.9055	-0.1218	0.8249
P-A-3	335	D-6	9.0	0.5	0.9089	-0.2789	0.9929
P-A-3	335	D-6	9.0	1.0	0.8880	-0.1961	0.9313
P-A-3	335	D-6	9.0	1.5	0.8747	-0.1488	0.8335
P-S-1	630	D-6	9.0	1.0	0.9090	-0.2020	0.9333
P-S-1	630	D-6	9.0	1.5	0.8907	-0.1709	0.9259
P-G-1	842	D-6	9.0	1.0	0.9431	-0.3249	0.9968
P-G-1	842	D-6	9.0	1.5	0.9338	-0.2984	0.9842
P-G-1	842	D-6	9.0	2.0	0.9342	-0.3086	0.9861
P-G-2	705	D-6	9.0	1.0	0.9324	-0.3234	0.9916
P-G-2	705	D-6	9.0	1.5	0.9105	-0.2573	0.9795
P-G-4	353	D-6	9.0	0.5	0.8927	-0.2662	0.9918
P-G-4	353	D-6	9.0	1.0	0.8373	-0.1694	0.9176
P-A-2	630	D-7	15.0	1.0	0.9185	-0.2214	0.9901
P-A-2	630	D-7	15.0	1.5	0.9165	-0.2107	0.9493
P-A-2	630	D-7	15.0	2.0	0.9062	-0.1809	0 9403
P-A-3	335	D-7	15.0	1.0	0.8744	-0.1525	0.9202
P-A-3	335	D-7	15.0	1.5	0.8658	-0.1514	0.7514
P-S-1	630	D-7	15.0	1.0	0.8998	-0.1934	0.9899
P-S-1	630	D-7	15.0	1.5	0.8875	-0.1786	0.9769
P-G-1	842	D-7	15.0	1.0	0.9539	-0.3341	0.9958
P-G-1	842	D-7	15.0	1.5	0.9398	-0.2797	0.9925
P-G-1	842	D-7	15.0	2.0	0.9316	-0.2462	0.9930
P-G-2	705	D-7	15.0	1.0	0.9337	-0.1673	0.8873
P-G-2	705	D-7	15.0	1.5	0.9126	-0.1930	0.9754
P-A-2	630	D-8	18.0	1.0	0.8980	-0.2571	0.9870
P-A-2	630	D-8	18.0	1.5	0.8912	-0.2187	0.9834
P-A-2	630	D-8	18.0	2.0	0.8870	-0.2059	0.9817
P-A-3	335	D-8	18.0	1.0	0.8509	-0.2102	0.9435
P-A-3	335	D-8	18.0	1.5	0.8402	-0.1728	0.8504
P-S-1	630	D-8	18.0	1.0	0.8976	-0.2777	0.9926
P-S-1	630	D-8	18.0	1.5	0.8842	-0.2448	0.9797
P-G-1	842	D-8	18.0	1.0	0.9430	-0.3560	0.9927
P-G-1	842	D-8	18.0	1.5	0.9231	-0.2745	0.9945
P-G-1	842	D-8	18.0	2.0	0.9115	-0.2220	0.9817
P-G-2	705	D-8	18.0	1.0	0.9139	-0.2809	0.9861
P-G-2	705	D-8	18.0	1.5	0.9000	-0.2406	0.9741

(continue --)

particle	d_p (μm)	*distr.*	A_r	u(m/s)	α	β	R^2
P-S-1	630	D-2	3.6	0.5	0.9702	-0.4704	0.9953
P-S-1	630	D-2	3.6	1.0	0.9401	-0.4420	0.9801
P-S-2	359	D-2	3.6	0.5	0.9337	-0.3908	0.9814
P-C-1	630	D-2	3.6	0.5	0.9541	-0.5217	0.9938
P-G-1	842	D-2	3.6	1.0	0.9745	-0.4115	0.9957
P-G-1	842	D-2	3.6	1.5	0.9912	-0.5307	0.9823
P-G-1	842	D-2	3.6	2.0	0.9924	-0.8509	0.9767
P-G-2	705	D-2	3.6	0.5	0.9921	-0.4008	0.9872
P-G-2	705	D-2	3.6	1.0	0.9631	-0.3912	0.9737
P-G-2	705	D-2	3.6	1.5	0.9705	-0.5248	0.9743
P-G-3	484	D-2	3.6	0.5	0.9758	-0.3525	0.9954
P-G-3	484	D-2	3.6	1.0	0.9565	-0.3680	0.9858
P-G-3	484	D-2	3.6	1.5	0.9572	-0.4068	0.9737
P-G-4	353	D-2	3.6	0.5	0.9234	-0.2989	0.9553
P-G-4	353	D-2	3.6	1.0	0.9251	-0.3864	0.9406
P-A-1	1260	D-3	2.1	1.0	0.9614	-0.6110	0.9804
P-A-1	1260	D-3	2.1	1.5	0.9019	-0.7466	0.9682
P-A-1	1260	D-3	2.1	2.0	0.8972	-1.0421	0.9920
P-A-2	630	D-3	2.1	0.5	0.9469	-0.5062	0.9634
P-A-2	630	D-3	2.1	1.0	0.9205	-0.5869	0.9470
P-A-2	630	D-3	2.1	1.5	0.8783	-0.7492	0.9628
P-A-2	630	D-3	2.1	2.0	0.8801	-1.0664	0.9970
P-A-3	335	D-3	2.1	0.5	0.9265	-0.4927	0.9345
P-A-3	335	D-3	2.1	1.0	0.8598	-0.4469	0.9108
P-A-3	335	D-3	2.1	1.5	0.7992	-0.4984	0.9539
P-S-1	630	D-3	2.1	0.5	0.9494	-0.6284	0.9812
P-S-1	630	D-3	2.1	1.0	0.9125	-0.7916	0.9710
P-S-2	359	D-3	2.1	0.5	0.9100	-0.5695	0.9933
P-C-1	630	D-3	2.1	0.5	0.9538	-0.9666	0.9970
P-G-1	842	D-3	2.1	1.0	0.9505	-0.6798	0.9926
P-G-1	842	D-3	2.1	1.5	0.9637	-1.0178	0.9671
P-G-1	842	D-3	2.1	2.0	0.8913	-1.2610	0.9927
P-G-2	705	D-3	2.1	0.5	0.9734	-0.4980	0.9940
P-G-2	705	D-3	2.1	1.0	0.9421	-0.5985	0.9950
P-G-3	484	D-3	2.1	0.5	0.9495	-0.3758	0.9828
P-G-3	484	D-3	2.1	1.0	0.8846	-0.4337	0.9615
P-G-3	484	D-3	2.1	1.5	0.8063	-0.5278	0.9506
P-G-4	353	D-3	2.1	0.5	0.9232	-0.4666	0.9029
P-G-4	353	D-3	2.1	1.0	0.8755	-0.7579	0.9775

Bibliography

1. Abu Bakar, M. Y., M. A. Bergougnou, J. D. Tarasuk, and J. L. Sullivan, "Local Heat Transfer Coefficients Around a Horizontal Tube in a Shallow Fluidized Bed", **Journal of Powder and Bulk Solids Technology** , vol. 4, p. 11 (1980).

2. Abu Bakar, M. Y., "Heat Transfer Studies between a Horizontal Tube and a Shallow Fluidized Bed", Ph.D. Dissertation, The University of Western Ontario, London, Canada, June (1981).

3. Abu Bakar, M. Y., J. D. Tarasuk, M. A. Bergougnou and J. L. Sullivan, "Local and Overall Heat Transfer Coefficients on a Horizontal Tube inside a Shallow Gas Fluidized Bed by Means of a New Two-Sector Heat Transfer Probe", **4th Intern. Fluidization Conference** , Kashikojima, Japan, May (1983).

4. Adams, R. L. and J. R. Welty, "A Gas Convection Model of Heat Transfer in Large Particle Fluidized Beds", **AIChE Journal** , vol. 25, No. 3, p. 395 (1979).

5. Aerojet Energy Conversion Corporation, "Evaluation of Fluid-Bed Heat Exchanger Optimization Parameters", Final Report, U.S. Dept. of Energy, Contract No. DE-AC22-78ET11343, March (1980).

6. Agarwal, J. C., W. L. Davis and D. T. King, "Fluidized-Bed Coal Dryer", **Chem. Eng. Prog.** , vol. 58, No. 11, p. 85 (1962).

7. Agarwal, S. C. and E. N. Ziegler, "Surface to Fluidized-Bed Transport Processes", **Chem. Eng. Prog. Symp. Ser.** , vol. 66, No. 105, p. 68 (1970).

8. Ainshtein, V. G., "An Investigation of Heat Transfer Processes between Fluidized Beds and Single Tubes Submerged in the Beds", Kand. Diss., Lomonosova, Moscow (1959).

9. Ainshtein, V. G. and N. I. Gel'perin, "Heat Transfer between a Fluidized Bed and a Surface", **Int. Chem. Eng.** , vol. 6, No. 1, p. 67 (1966).

10. Al Ali, B. M. A. and J. Broughton, "Shallow Fluidized-Bed Heat Transfer", **Applied Energy** , vol. 3, p. 101 (1977).

11. Andeen, B. R. and L. R. Glicksman, "Heat Transfer to Horizontal Tubes in Shallow Fluidized Beds", ASME Paper 76-HT-67, presented ASME-AIChE Heat Transfer Conference, St. Louis, Missouri (1976).

12. Andeen, B. R., Glicksman, L. R., and R. Bowman, "Heat Transfer from Flattened Horizontal Tubes", **Fluidization** , J. F. Davidson and D. Keairns (editors), Cambridge University Press, p. 345 (1978).

13. Atkinson, G. A., "Extended-Surface Fluidized-Bed Heat Transfer", Ph.D. Thesis, University of Aston in Birmingham, England, Oct. (1974).

14. Atkinson, G. A., "Extended-Surface Fluidized-Bed Heat Transfer", **Proceedings of the Fifth Canadian Congress of Applied Mechanics** , University of New Brunswick, Fredericton, p. 603, May (1975).

15. Baeyens, J. and W. R. A. Goosens, "Some Aspects of Heat Transfer between a Vertical Wall and a Gas Fluidized Bed", **Powder Technology** , vol. 8, p. 91 (1973).

16. Bakker, P. J. and P. M. Heertjes, "Porosity Distributions in a Fluidized Bed", **Chem. Eng. Sci.** , vol. 12, p. 260 (1960).

17. Barker, R. P. and J. C. Chen, "Heat Transfer from a Horizontal Tube in Shallow Fluidized Beds", Report TS-752, Dept. of Mechanical Engineering and Mechanics, Lehigh University, June (1975).

18. Baskakov, A. P. "The Mechanism of Heat Transfer between a Fluidized Bed and a Surface", **Int. Chem. Eng.** , vol. 4, No. 2, P. 320, (1964).

19. Baskakov, A. P. and V. M. Suprun, "The Determination of the Convective Component of the Coefficient of Heat Transfer to a Gas in a Fluidized Bed", **Int. Chem. Eng.** vol. 12, No. 1, p. 53, (1972).

20. Bazaraa, M. S. and C. M. Shetty,"Nonlinear Programming - Theory and Algorithms", John Wiley & Sons, p. 274 (1979).

21. Basov, V. A., V. I. Markhevka, T. Kh. Melik-Akhnazarov and D. I. Orochko, "Investigation of the Structure of a Nonuniform Fluidized Bed", **Int. Chem. Eng.** , vol. 9, No. 2, p. 263 (1969).

22. Beeken, D. W., **British Chem. Eng.** , vol. 5, p. 484 (1960).

23. Behie, L. A., M. A. Bergougnou, C. G. J. Baker and W. Bulani, "Jet Momentum Dissipation at a Grid of a Large Gas Fluidized Bed", **Can. J. Chem. Eng.** , vol. 48, p. 158 (1970).

24. Behie, L. A., M. A. Bergougnou, C. G. J. Baker and T. E. Base, "Further Studies on Momentum Dissipation of Grid Jets in a Gas Fluidized Bed", **Can. J. Chem. Eng.** , vol. 49, p. 557 (1971).

25. Behie, L. A. and P. Kehoe, "Grid Region in a Fluidized Bed Reactor", **AIChE Journal**, vol. 19, p. 1070 (1973).

26. Botterill, J. S. M. and J. R. Williams, "The Mechanism of Heat Transfer to Gas-Fluidized Beds", **Trans. Inst. Chem, Engrs,** , vol. 41, p. 217 (1963).

27. Bird, R. B., W. E. Stewart and N. Lightfoot, **Transport Phenomena** , Wiley, New York (1960).

28. Botterill, J. S. M., M. H. D. Butt, G. L. Cain, R. Chandrasekhar, and J. R. Williams, **International Symposium on Fluidization** , p. 442 (1967).

29. Botterill, J. S. M., M. van der Kolk, D. E. Elliott, S. McGuigan, "The Flow of Fluidized Solids,", **Powder Technology** , vol. 6, p. 343 (1972).

30. Botterill, J. S. M., **Fluid-Bed Heat Transfer** , Academic Press, New York (1975).

31. Botterill, J. S. M., Y. Teoman and K. R. Yuregir, "Temperature Effects on the Heat Transfer Behavior of Gas Fluidized Beds", **AIChE. Symp. Ser.** , vol. 77, No. 208, p. 330 (1981).

32. Broughton, J. and J. R. Howard, "Combustion of Coal in Fluidized Beds", in **Fluidized Beds: Combustion and Applications** , edited by J. R. Howard, Applied Science Publishers, p. 37 (1983).

33. Brusenback, R. A., Ph.D. Dissertation, Northwestern Univ., Evanston, Illinois (1963).

34. Catipovic, N. M., T. J. Fitzgerald, A. H. George and J. R. Welty, "Experimental Validation of the Adams-Welty Model for Heat Transfer in Large Particle Fluidized Beds", **AIChE Journal** , vol. 28, No. 5, p. 714 (1982).

35. Chandran, R., J. C. Chen and F. W. Staub, "Local Heat Transfer Coefficient around Horizontal Tubes in Fluidized Beds', **Transactions of the ASME** , vol. 102, p. 152 (1980).

36. Chen, J. C. and J. G. Withers, "An Experimental Study of Heat Transfer From Plain and Finned Tubes in Fluidized Beds", **AIChE Symp. Ser.** , vol. 74, No. 174, p. 327 (1978).

37. Clift, R., J. R. Grace and M. E. Weber, **Bubbles, Drops and Particles** , Academic Press, New York, (1978).

38. Coughanowr, D. R. and L. B. Koppel, **Process Systems Analysis and Control** , McGraw-Hill, New York, (1975).

39. Davidson, J. F. and D. Harrison, **Fluidised Particles** , Cambridge University Press (1963).

40. Davidson, J. F. and D. Harrison, "The Behaviour of a Continuously Bubbling Fluidised Bed", **Chem. Eng. Sci.** , vol. 21, p. 731 (1966).

41. Decker, N. A. and L. R. Glicksman, "Conduction Heat Transfer at the Surface of Bodies Immersed in Gas Fluidized Bed of Spherical Particles", **AIChE. Symp. Ser.** , vol. 77, No. 208, p. 341 (1981).

42. Engineering Equipment Users Association, "Pneumatic Handling of Powdered Materials", Constable and Company, London (1963).

43. Denloye, A. O. Q. and J. S. M. Botterill, "Bed-to-Surface Heat Transfer in a Fluidized Bed of Large Particles", **Powder Technology** , vol. 19, p. 197 (1978).

44. Dow, W. M. and M. Jakob, "Heat Transfer between a Vertical Tube and a Fluidized Air-Solid Mixture", **Chem. Eng. Prog.** , vol. 47, No. 12, p. 637 (1951).

45. Dutta, S. and C. Y. Wen, "A Simple Probe for Fluidized Bed Measurements", **Can. J. Chem. Eng.** , vol. 57, p. 115 (1969).

46. Elliott, D. E., "Possible Use of Fluidized-Bed Combustion and Heat Transfer", Paper 22, The Total Energy Conference, The Institute of Fuel, Bringhton, England, November (1971).

47. Ergun, S., "Fluid Flow through Packed Columns", **Chem. Eng. Prog.** , vol. 48, p. 89 (1952).

48. Ernst, R., "Warmeubergang an Warmeaustaushern in Moving Bed", **Chemie-Ingenieur-Technik** , vol. 32, p. 17 (1960).

49. Fakhimi, S. and D. Harrison, **Inst. Chem. Eng. Symp. Ser.** , vol. 23, p. 29 (1971).

50. Fan, L. T., T. C. Ho, N. Yutani, and W. P. Walawender, in **Fluidization** , D. Kunii and R. Toei (editors), Engineering Foundation, New York, p. 15 (1984).

51. Filla, M. and L. Massimilla, "Analysis of the Variables Controlling Gas Jet Penetration in Fluidized Beds", **Ind. Eng. Chem. Fundam.** , vol. 23, p. 131 (1984).

52. Filla, M., L. Massimilla and S. Vaccaro, **Can. J. Chem. Eng.** , vol. 61, p. 370 (1983).

53. Gabor, J. D., "Wall-to-Bed Heat Transfer in Fluidized and Packed Beds", **AIChE Symp. Ser.** , vol. 66, No. 105, p. 76 (1970).

54. Geldart, D., "Types of Gas Fluidization", **Powder Technology** , vol. 7, p. 285 (1973).

55. Geldart, D. and A. R. Abrahamsen, in **Fluidization** , edited by J. R. Grace and J. M. Matsen, Plenum, new York, p. 453 (1980).

56. Gel'perin, N. I. and V. G. Einstein, "Heat Transfer in Fluidized Beds", in **Fluidization** , edited by J. F. Davidson and D. Harrison, Ch. 10., p. 471 (1971).

57. Gel'perin, N. I., V. G. Ainshtein, and A. V. Zaikovskii, "Variation of Heat Transfer Intensity Around the Perimeter of a Horizontal Tube in a Fluidized Bed", **J. Eng. Phys.** , vol. 10, No. 6, p. 4173, (1966).

58. Groosens, W. R. A. and L. Hellinckx, **Fluidisation et ses Applications** , Toulouse, Societe Chemie Indust., p. 303 (1973).

59. Grace, J. R. and D. Harrison, "The Behaviour of Freely Bubbling Fluidised Beds', **Chem. Eng. Sci.** , vol. 24, p. 497 (1969).

60. Grace, J. R., and R. Clift, "On the Two-Phase Theory of Fluidization", **Chem. Eng. Sci.** , vol. 29, p. 327 (1974).

61. Grewal, N. S. and S. C. Saxena, "Effect of Surface Roughness on Heat Transfer from Horizontal Immersed Tubes in a Fluidized Bed", **J. Heat Trans.** , vol. 101, p. 397 (1979).

62. Grewal, N. S. and S. C. Saxena, "Maximum Heat Transfer Coefficient between a Horizontal Tube and a Gas-Solid Fluidized Bed", **Ind. Eng. Prog. Chem, Proc. Des. Dev.** , vol. 20, No. 1, p. 108 (1981).

63. Grewal, N. G. and S. C. Saxena, "Experimental Studies of Heat Transfer Between a Bundle of Horizontal Tubes and a Gas-Solid Fluidized Bed of Small Particles", **Int. Eng. Chem. Process** , vol. 22, No. 3 (1983).

64. Gutfinger, C. and N. Abuaf, 'Heat Transfer in Fluidized Beds", **Advances in Heat Transfer** , vol, 10, p. 167 (1974).

65. Hanway, J. E., "Industrial Scale-Up of Fluidized-Bed Systems for Incineration of Spent Pulping Effluents", **Chem. Eng. Prog. Symp. Ser.** , vol. 66, No. 105, p. 253 (1970).

66. Harrison, D., J. F. Davidson and J. W. de Kock, "On the Nature of Aggregative and Particulate Fluidization", **Trans. Inst. Chem. Eng.** , vol. 39, p. 202 (1961).

67. Heywood, H., in **Symposium on the Interaction between Fluids and Solids** , edited by P. A. Rottenburg, Institution of Chem. Engrs., p. 1 (1962).

68. Hirt, D. E., "Heat Transfer Between a Supernatant Gas and a Flowing Vibrofluidized Bed of Solids", M.S. Thesis, Virginia Tech, Blacksburg, Virginia, July (1984).

69. Huang, H., "Heat Transfer Between a Shallow Fluidized Bed and a Single Horizontal Tube Immersed in the Bed", M.S. Thesis, Virginia Tech, Blacksburg, Virginia, July (1983).

70. Juveland, A. C., J. E. Dougherty, and H. P. Deinken, "Particle-to-Gas Heat Transfer in Fluidized Beds", **Ind. Eng. Chem. Fund.** , vol. 5, No. 3, p. 439 (1966).

71. Kehoe, P. W. K. and J. F. Davidson, "Continuously Slugging Fluidized Beds", **Inst. Chem, Engrs, Symp. Ser.** , vol. 33, p. 97, (1970).

72. Koppel, L. B., R. D. Patel and J. T. Holmes, "Statistical Models for Surface Renewal in Heat and Mass Transfer", **AIChE Journal** , vol. 16, No. 3, p. 456 (1970).

73. Kunii, D. and O. Levenspiel, **Fluidization Engineering** , Wiley, New York (1969).

74. Lanneau, K. P., "Gas-Solid Contacting in Fluidized Beds", **Trans Inst. Chem. Eng.** , vol. 38, p. 125 (1960).

75. Leva, M., **Fluidization** , McGraw-Hill, New York (1959).

76. Levenspiel, O. and J. S. Walton, "Bed-Wall Heat Transfer in Fluidized Systems", **Chem. Eng. Prog. Symp. Ser.** , vol. 50, No. 9, p. 1 (1954).

77. Lewis, W. K., E. R. Gilliland and H. Girouard., "Heat Transfer and Solids Mixing in Beds of Fluidized Solids", **Chem. Eng. Prog. Symp. Ser.** , vol. 58, No. 38, p. 87 (1962).

78. Liu, Y. and D. Gidaspow, "Solid Mixing in Fluidized Beds -- a Hydrodynamic Approach", **Chem. Eng. Sci.** , vol. 36, p. 539, (1981).

79. Liu, Y. A. and A. M. Squires, countercurrent Heat-Exchange Between a Gas and a vibrofluidized Solid, Technical Progress Report for the Period of September 1, 1984 to March 31, 1985, DOE grant No. DE-FG07-83ID12428, Idaho Operation Office, Idaho Falls (1985).

80. Liu, Y. A., A. M. Squires and K. Konrad, "Fischer-Tropsch Synthesis from a Low H_2:CO Gas in a Dry Fluidized-Bed System", Technical Report for the Period of Sept. 1, 1982 to Mar. 31, 1983, DOE Grant No. DE-FG-82P50791, Report No. DOE/PC/50791T1 (DE83011185) DOE Technical Information Center, Oak Ridge, TN (1983).

81. Lockett, M. J., J. F. Davidson and D. Harrison, "On the Two-Phase Theory of Fluidisation", **Chem. Eng. Sci.** , vol. 22, p. 1059, (1967).

82. Markhevka, V. I., V. A. Basov, T. Kh. Melik-Akhnazarov and D. I. Orochko, **Theor. Found. Chem. Eng.** , vol. 5, p. 81 (1971).

83. McGuigan, S. J., "The Flow Behaviour of Shallow Fluidised Beds", Ph.D. Thesis, The University of Aston in Birmingham, England, June, (1975).

84. Martin, H., "Heat and Mass Transfer in Fluidized Beds", **Int. Chem. Eng.** , vol. 22, No. 1. p. 30 (1982).

85. May, W. G., "Fluidized-Bed Reactor Studies", **Chem. Eng. Prog.** , vol. 55, No. 12, p. 49 (1959).

86. McCabe, W. L. and J. C. Smith, **Unit Operations of Chemical Engineering** , McGraw-Hill, New York (1981).

87. Merry, J. M. D., "Penetration of Vertical Jets into Fluidized Beds", **AIChE Journal** , vol. 21, No. 3, p. 507 (1975).

88. Merry, J. M. D. and J. F. Davidson, "Gulf Stream Circulation in Shallow Fluidized Beds", **Trans. Inst. Chem. Eng.** , vol. 51, p. 361 (1973).

89. Mickley, H. S. and D. F. Fairbanks, "Mechanism of Heat Transfer to Fluidized Beds", **AIChE Journal** , vol. 1, p. 374 (1955).

90. Mickley, H. S., D. F. Fairbanks and R. D. Hawthorn, "The Relation between the Heat Transfer Coefficient and Thermal Fluctuations in Fluidized-Bed Heat Transfer", **CEP Symp. Ser.** , vol. 57, No. 32, p. 51 (1961).

91. Nienow, A. W. and P. N. Rowe, "Particle Growth and Coating in Gas-Fluidized Beds", in **Fluidization** , edited by J. F. Davidson, D. Harrison and R. Clift, Academic Press, New York (1985).

92. Patterson, R. G. and M. L. Jackson, "Shallow Multistage Fluidized Beds for Particle Collection", **AIChE Symp. Ser.** , vol. 73, No. 161, p. 64 (1977).

93. Petrie, J. C., W. A. Freeby, and J. A. Buckham, "In-Bed Exchangers", **Chem. Eng. Prog.** , vol. 54, No. 7, p. 45 (1968).

94. Pillai, K. K., "Heat Transfer to a Sphere Immersed in a Shallow Fluidized Bed", **Letter in Heat Mass. Trans.** , vol. 3, p. 131, (1976).

95. Potter. O. E., "Mixing in Fluidization", in **Fluidization** , edited by J. F. Davidson and D. Harrison, Academic Press, New York (1971).

96. Richardson, R. J. and N. Zaki, "Sedimentation and Fluidization", **Trans. Inst. Chem. Eng.** , vol. 32, p. 35 (1954).

97. Romero, J. B. and L. N. Johanson, "Factors Affecting Fluidized Bed Quality", **Chem. Eng. Prog. Symp. Ser.** , vol. 58, No. 38, p. 28 (1962).

98. Rowe, P. N., H. J. MacGillivray and D. J. Cheesman, **Trans. Inst. Chem. Eng.** , vol. 57, p. 194 (1979).

99. Rudnicki, M. I., C. S. Mah and H. W. Williams, "Status of Fluidized-Bed Waste Heat Recovery", in **Heat Exchanger: Theory and Practice** , edited by J. Taborek, G. F. Hewitt and Afgan, Hemisphere Publishing Corp., Washington, DC. (1983).

100. Simpson, H. C. and B. W. Rodger, "The Fluidization of Light Solids by Gases under Pressure and Heavy Solids by Water", **Chem. Eng. Sci.** , vol. 16, p. 153 (1961).

101. Smith, T. N., "Limiting Volume Fractions in Vertical Pneumatic Transport", **Chem. Eng. Sci.** , vol. 33, p. 745 (1978).

102. Sprung, R., B. Thomas, Y. A. Liu and A. M. Squires, Shallow Vibrobeds of 'Master Beads', Paper to be presented in **Proceedings** , Fifth Engineering Foundation Conference on Fluidization, Elsinore, Denmark, May 18-23, (1986).

103. Squires, A. M., "Applications of Fluidized Beds in Coal Technology", in **Alternative Energy Sources** , edited by J. P. Hartnett, Academic Press, New York, p. 59 (1976).

104. Squires, A. M., K. C. Lee and R. Pfeffer, "The Panel Bed: A Fluid-Solid Contacting Device Exploiting a New Mode of Soil Failure", **POWTECH 81**, Birmingham, England, march (1981).

105. Squires, A. M., "Contribution toward a History of Fluidization", **Proceedings of the Joint Meeting of American Institute of Chemical Engineers and Chemical Industry and Engineering Society of China** , Beijing, vol. 1, p. 322, September (1982).

106. Squires. A. M., "Three Bold Exploiters of Coal Gasification: Winkler, Godel and Porta", in **Fluidized Beds: Combustion and Applications** , edited by J. R. Howard, Applied Science Publishers, p. 277 (1983).

107. Squires, A. M., **Proc. J. Meet. Chem. Eng. Chem. Ind. Eng. Soc. China Am. Inst. Chem. Eng.** , p. 392 (1984).

108. Squires, A. M., M. Kwauk and A. A. Avidan, "Fluid Beds: At Last, Challenging Two Entrenched Practices", **Science** , vol. 23, p. 1329, December (1985).

109. Staub, F. W. and G. S. Canada, "Effect of Tube Bank and Gas Density on Flow Behavior and Heat Transfer in Fluidized Beds:, in **Fluidization** , Proceedings of 2nd Engineering Foundation International Conference on Fluidization, p. 339 (1978).

110. Thiel, W. J. and O. E. Potter, "Slugging in Fluidized Beds", **Ind. Eng. Chem. Fundam.** , vol. 16, p. 242 (1977).

111. Twoomey, R. D. and H. F. Johnston, "Gaseous Fluidization of Solid Particles", **Chem. Eng. Prog.** , vol. 48, No. 5. p. 220, (1952).

112. Vakhrushev, I. A., Ya. A. Botnikov and N. G. Zenchenkov, "Heat Transfer from a Fluidized Bed of Hot Coke to the Surface of Horizontal Tubes", **Inter. Chem. Eng.** , vol. 3. No. 2, p. 207 (1963).

113. Van Deemter, J. J. "Mixing", in **Fluidization** , edited by J. F. Davidson, D. Harrison and R. Clift, Academic Press, New York (1985).

114. Van Heerden, C., A. P. P. Nobel and D. W. van Krevelen, "Mechanism of Heat Transfer in Fluidized Beds", **Ind. Eng. Chem.** , vol. 45, No. 6, p. 1234 (1953).

115. Vreedenberg, H. A., "General Discussion on Heat Transfer", **Inst. Mech. Eng.** , (London), p. 373 (1951).

116. Vreedenberg, H. A., "Heat Transfer between a Fluidized Bed and a Horizontal Tube", **Chem. Eng. Sci.** , vol. 9, p. 52 (1958).

117. Wall, C. J., J. T. Graves, and E. J. Roberts, **Chem. Eng.** (London), p. 77 (1975).

118. Wallis, G. B., **One-Dimensional Two-Phase Flow** , McGraw-Hill, New York (1969).

119. Wasan, D. T. and M. S. Ahluwalia, "Consecutive Film and Surface Renewal Mechanism for Heat or Mass Transfer From a Wall", **Chem. Eng. Sci.** , vol. 24, p. 1535, (1969).

120. Wen, C. Y., N. R. Deole and L. H. Chen, "A Study of Jets in a Three-Dimensional Gas Fluidized Bed", **Powder Technology** , vol. 31, p. 175 (1982).

121. Whithead, A. B., "Some Problems in Large-Scale Fluidized Beds", in **Fluidization** , edited by J. F. Davidson and D. Harrison, Academic Press, London (1971).

122. Whiting, G. K., "Development of a Microreactor System for Unsteady-State Fischer-Tropsch Synthesis", Ph.D. Dissertation, Virginia Tech, Blacksburg, Virginia, March (1985).

123. Wiche, E. and F. Fetting, "Heat Transfer in Fluidized Beds", **Chem. Ing. Techn.** , vol. 26, p. 301 (1954).

124. Wilhelm, R. H. and M. Kwauk, "Fluidization of Solid Particles", **Chem. Eng. Prog.** , vol. 44, p. 201 (1948).

125. Xavier, A. M. and J. F. Davidson, "Heat Transfer to Surface Immersed in Fluidized Beds, Particularly Tube Arrays", in **Fluidization** , Proceedings of 2nd Engineering Foundation International Conference on Fluidization, p. 333 (1978).

126. Xavier, A. M. and J. F. Davidson, "Heat Transfer to Surfaces Immersed in Fluidized Beds and in the Freeboard Region", **AIChE Symp. Ser.** , vol. 77, No. 208, p. 368 (1981).

127. Yagi. S. and D. Kunii, "Studies on Heat-Transfer Near Wall Surface in Packed Beds", **AIChE Journal** , vol. 6, p. 97 (1960).

128. Yan, Z., J. Z. Yao, W. L. Wang, S. J. Liu and M. Kwauk, "Cocurrent Shallow Multistage Fluid-Bed Reactor", **4th Intern. Fluidization Conf.** , Kashikojima, Japan, May (1983).

129. Yang, W. C., and D. L. Keairns, "Estimation the Jet Penetration Depth of Multiple Vertical Grid Jets", **Ind. Eng. Chem. Fundam.** , vol. 18, p. 317 (1979).

130. Yang, W. and D. L. Keairns, "Solid Entrainment Rate into Gas and Gas-Solid, Two-Phase Jets in a Fluidized Bed", **Powder Technology** , vol. 33, p. 89 (1982).

131. Yasutomi, T. and T. Yokota, "Heat Transfer from the Surface of a Body Fixed in a Fluidized Bed", **Heat Transfer - Japanese Research** , vol. 6, No. 3, p. 26, (1977).

132. Yates, J. G., **Fundamentals of Fluidized-Bed Chemical Processes** , Butterworths, London (1983).

133. Yerushalmi, J. and A. Avidan, "High-Velocity Fluidization", in **Fluidization** , edited by J. F. Davidson, R. Clift and D. Harrison, Academic Press, Ch. 7, p. 225 (1985).

134. Yoshida, K., D. Kunii and O. Levenspiel, "Heat Transfer Mechanisms between Wall Surface and Fluidized Bed", **Int. J. Heat Mass. Trans.** , vol. 12, p. 529 (1969).

135. Yuditskii, V. I. and S. S. Zabrodsky, "Some Peculiarities of Heat Tranfer between a Thin Fluidized Bed and a Surface Immersed in the Bed", (translated), ARNL-TRANS-587, Argonne National Laboratory (1966).

136. Zabrodsky, S. S., **Hydrodynamics and Heat Transfer in Fluidized Beds** , MIT Press, Cambridge, MA (1966).

137. Zabrodsky, S. S., **Int. J. Heat and Mass Transfer** , vol. 15, p. 241 (1973).

138. Zenz, F. A. and D. F. Othmer, **Fluidization and Fluid-Particle Systems** , Reinhold, New York (1960).

139. Ziegler, E. N. and W. T. Brazelton, "Mechanism of Heat Transfer to a Fixed Surface in a Fluidized Bed", **Ind. Eng. Chem. Fundamentals** , vol. 3, p. 94 (1964).

The vita has been removed from the scanned document